Institut für Theoretische Chemie
Universität Ulm

# Non-adiabatic Effects in the Dissociative Adsorption of $O_2$ on Aluminum (111) Surfaces

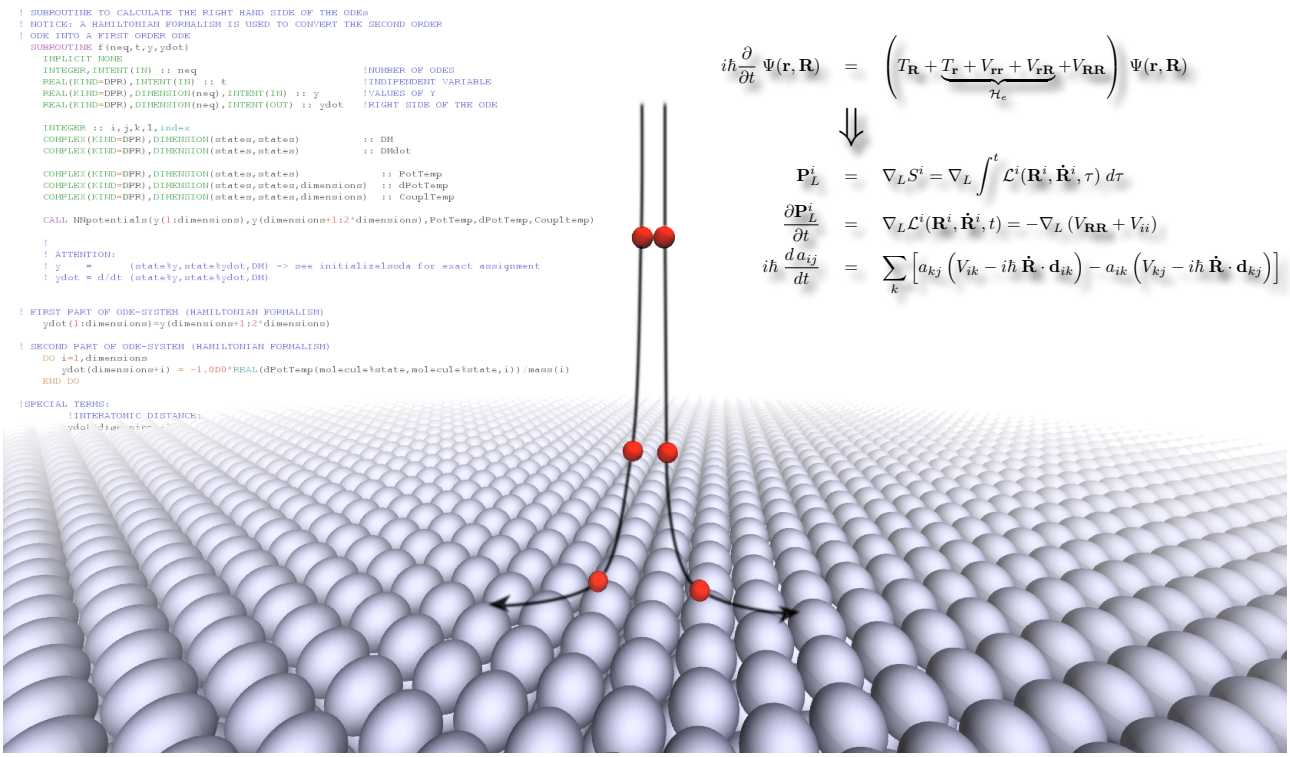


Dissertation zur Erlangung des Doktorgrades Dr. rer. nat.
der Fakultät für Naturwissenschaften der Universität Ulm

vorgelegt von Christian Carbogno aus Bozen, Italien, 2009

**Amtierender Dekan der Fakultät für Naturwissenschaften der Universität Ulm bei der Eröffnung des Promotionsverfahrens:**

*Prof. Dr. Peter Bäuerle,*
Institut für Organische Chemie II und Neue Materialien,
Universität Ulm

**Amtierender Dekan der Fakultät für Naturwissenschaften der Universität Ulm beim Abschluss des Promotionsverfahrens:**

*Prof. Dr. Axel Groß,*
Institut für Theoretische Chemie,
Universität Ulm

**Erstgutachter:**

*Prof. Dr. Axel Groß,*
Institut für Theoretische Chemie,
Universität Ulm

**Zweitgutachter:**

*Prof. Dr. Joachim Ankerhold*
Institut für Theoretische Physik
Universität Ulm

**Drittgutachter:**

*Prof. Dr. Peter Saalfrank*
Lehrstuhl für Theoretische Chemie
Institut für Chemie - Universität Potsdam

**Tag der Promotion:** *20. Oktober 2009*

# Abstract

Metal oxidation processes are of outstanding importance in various industrial and scientific applications. Therefore, this research field has attracted huge scientific interest over the last decades. In spite of that, there still exist some not yet elucidated phenomena, even for systems that appear utterly simple at first sight. One of the most prominent and intriguing examples for them is the oxidation of the lowest energy (111) surface of aluminum. For a long time, theoretical state-of-the-art investigations [1, 2] were unable to reproduce or even to explain the low adsorption probability for thermal $O_2$ molecules found in experiments [3]. The mysterious dynamics of this system was recently related to spin selection rules, which hinder a spin transition from the initial $O_2$ gas-phase triplet state to the singlet state of the adsorbed O atoms [4]. Thereby, a constrained Density Functional Theory approach [5] was employed to compute the Potential Energy Surfaces of $O_2$ in different spin-configurations, and the lowered adsorption probability was calculated when restricting [6] the $O_2$ molecule to move on the spin-triplet Potential Energy Surface only. In spite of the good agreement with the experiment, this model lacks credibility, since under the employed restriction the $O_2$ molecule is also not able to relax to the correct final singlet state of the adsorbed atoms either. To overcome this deficiency, we extend these studies by considering the dissociation dynamics on multiple spin Potential Energy Surfaces, allowing transitions between them within the mixed quantum-classical fewest switches algorithm as proposed by Tully [7], which has been applied to various molecule-surface processes [8, 9] before.

After first reviewing the historical progress achieved in the experimental and theoretical study of chemical dynamics in Chap. 1, the analytical theories and numerical techniques, on which this work relies, are introduced in Chap. 2. Then the electronic structure of the $O_2$ molecule is discussed in detail in Chap. 3, whereby special attention is drawn to the nature of the excited states and to their correct theoretical description. The thereby computed Spin-Orbit Interaction of the isolated molecule allows to introduce a lower boundary for the non-adiabatic coupling between the different electronic states that play a role in the reaction dynamics. Conversely, also an upper bound for the non-adiabatic coupling elements is extracted from the unconstrained adiabatic potential by inverse diagonalization with respect to the triplet and to the singlet Potential Energy Surface. For both this maximal and the minimal coupling strength the adsorption process is inspected in Chap. 4, both as a function of the incident kinetic energy, of the incidence angle and of the initial electronic state. Thereby we critically discuss the effects of the approximate non-adiabatic couplings, the role of the involved excited states and the uncertainties underlying the Potential Energy Surfaces. Obtaining good agreement with experiment for the dissociation probability, we also examined the underlying adsorption and scattering dynamics and mechanisms in more detail. On the basis of these studies we propose experiments [10] that are able to inspect and to quantify the non-adiabaticity of this system's dynamics. In this context, the feasibility of such experiments, which would be the first proof that hindered spin transitions can play a role in heterogeneous chemical reactions, is critically scrutinized. Last but not least, the main results of this work are summarized in Chap. 5 and their validity for other chemical reactions is discussed.

# Zusammenfassung

Die Oxidation von Metalloberflächen spielt eine herausragende Rolle in vielen industriellen und wissenschaftlichen Anwendungen, so dass dieser Thematik in den letzten Jahrzehnten viel Aufmerksamkeit gewidmet wurde. Dennoch bietet dieses Forschungsgebiet immer noch ungeklärte Fragen selbst für chemische Prozesse, die auf den ersten Blick verblüffend einfach erscheinen. Ein sehr bekanntes und faszinierendes Beispiel dafür ist die Oxidation der (111) Oberfläche des Aluminiums: Die experimentell bestimmte [3], sehr niedrige Adsorptionswahrscheinlichkeit thermischer $O_2$ Moleküle hat sich lange Zeit einer Erklärung im Rahmen der modernen Festkörper- und Molekültheorie entzogen [1, 2]. Erst kürzlich [4] wurde diese bisher unverstandene Reaktionsdynamik mit Spin-Auswahlregeln in Verbindung gebracht, die einen Spin-Übergang vom Triplet-Grundzustand des $O_2$ Moleküls in der Gasphase in den Singlet-Grundzustand der adsorbierten O Atome verhindern. Untermauert wurde diese Hypothese mit Dichtefunktionaltheorie-Rechnungen unter Einbezug von elektronischen Randbedingungen [5], die es erlauben, die Potentialenergie-Hyperflächen für $O_2$ in verschiedenen Spin-Konfigurationen zu berechnen. In anschließenden Simulationen, in denen die Bewegung des $O_2$ auf die Spin-Triplet Potentialenergie-Hyperfläche eingeschränkt [6] wurde, konnte dann auch die niedrige Adsorptionswahrscheinlichkeit des Experiments reproduziert werden. Trotzdem leidet die Glaubwürdigkeit dieser Simulationen unter der Tatsache, dass es in dieser Modellierung dem $O_2$ nicht möglich ist, in den korrekten elektronischen Endzustand, d.h. in den Singlet-Grundzustand zweier einzelner adsorbierten O Atome, zu relaxieren. Um diese gravierende Schwäche der bisherigen Untersuchungen zu beseitigen, wird in dieser Arbeit die Dissoziationsdynamik des Sauerstoffs auf mehreren Potentialenergie-Hyperflächen betrachtet: Übergänge zwischen den beteiligten elektronischen Zuständen werden dabei anhand der gemischt quantenmechanisch-klassischen, von Tully [7] eingeführten “fewest switches” Methode, die schon früher erfolgreich für verschiedenste Molekül-Obeflächenreaktionen eingesetzt wurde [8, 9], explizit berücksichtigt.

Nachdem in Kap. 1 zuallererst die historische Entwicklung der für die chemische Dynamik relevanten experimentellen und theoretischen Untersuchungsmethoden skizziert wird, werden in Kap. 2 die dieser Arbeit zu Grunde liegenden Theorien und numerischen Techniken ausführlich vorgestellt. Daraufhin wird in Kap. 3 die elektronische Struktur des $O_2$ Moleküls im Detail diskutiert, wobei ein besonderes Augenmerk auf dessen angeregte Zustände und deren korrekte Beschreibung geworfen wird. Auf Grund der dabei berechneten Spin-Bahn Wechselwirkung des isolierten Moleküls wird dann eine untere Schranke für das nicht-adiabatische Kopplungselement zwischen den jeweiligen Spin-Zuständen eingeführt. Für ebendieses Kopplungselement wird des weiteren auch eine obere Schranke definiert, die aus dem adiabatischen Potential durch inverse Diagonalisierung der Triplet und Singlet Hyperflächen extrahiert wird. Sowohl für diese maximale als auch für die minimale Kopplungsstärke wird in Kap. 4 der Adsorptionsprozess in Abhängigkeit der Einschussenergie, des Einschusswinkels und des anfänglichen elektronischen Zustands ausführlich untersucht. Der Einfluss der nur näherungsweise bekannten Kopplungselemente, die Rolle der beteiligten elektronischen Zustände und mögliche systematische Fehler in der Berechnung der der Dynamik zu Grunde liegenden Potential-Hyperflächen werden hierbei

eingehend diskutiert. Die gute Übereinstimmung mit allen bisher bekannten experimentellen Daten [3, 11] erlaubt es uns, weitere Messungen [10] vorzuschlagen, die den nicht-adiabatischen Charakter dieser Reaktion eindeutig nachweisen und genau charakterisieren können. Insbesondere die Machbarkeit solcher Experimente, die erstmals einen wesentlichen Einfluss von Spin-Auswahlregeln auf heterogene chemische Reaktionen nachweisen könnten, wird in diesem Rahmen kritisch hinterfragt. Zu guter Letzt werden die wichtigsten Schlussfolgerungen dieser Arbeit in Kap. 5 nochmals zusammengefasst und deren Übertragbarkeit auf andere chemische Reaktionen wird abschließend diskutiert.

# Contents


**1 Introduction** **1**

**2 Theory** **9**
2.1 The Born-Oppenheimer Approximation . . . . . 9
2.1.1 Adiabatic and Diabatic Representations . . . . . 12
2.2 Electronic Structure Theory . . . . . 14
2.2.1 Quantum Chemistry . . . . . 15
2.2.2 Density Functional Theory . . . . . 24
2.3 Interpolation Methods . . . . . 32
2.3.1 Neural Networks . . . . . 34
2.4 Nuclear Dynamics . . . . . 37
2.4.1 Molecular Dynamics . . . . . 37
2.4.2 Quantum Dynamics . . . . . 38
2.4.3 Mixed Quantum-Classical Dynamics . . . . . 40

**3 The Oxygen Molecule** **51**
3.1 Qualitative Discussion of the Electronic Structure . . . . . 51
3.2 Quantum Chemical Calculations . . . . . 55
3.2.1 Calculational Details . . . . . 55
3.2.2 Results & Discussion . . . . . 61
3.3 Density Functional Theory Calculations . . . . . 80
3.3.1 The non-interacting Reference System . . . . . 80
3.3.2 Calculational Details . . . . . 82
3.3.3 Results & Discussion . . . . . 89

**4 Reaction Dynamics of the $O_2$/Al(111) System** **97**
4.1 Introduction . . . . . 97
4.2 The Potential Energy Surfaces . . . . . 101
4.2.1 Calculational Details . . . . . 101
4.2.2 The Inspected Electronic States . . . . . 103
4.3 The Coupling . . . . . 109
4.4 Results & Discussion . . . . . 115
4.4.1 The Sticking Coefficient . . . . . 115
4.4.2 The Vibrational Enhancement . . . . . 120
4.4.3 The Normal Energy Scaling . . . . . 124
4.4.4 High Energy Effects . . . . . 133
4.4.5 The Dynamics of Singlet $O_2$ . . . . . 142
4.4.6 The Frozen Substrate Approximation and its Limits . . . 149

**5 Conclusion & Outlook** **157**

**Appendix** **160**

**A The Many-Electron Spin Problem** **161**
A.1 The Spin Operators $\mathbf{S}^2$ and $S_z$ . . . . . 161
A.2 Generic Eigenfunctions of $\mathbf{S}^2$ . . . . . 163
A.2.1 High-Spin Configurations . . . . . 164
A.2.2 Closed Shell Configurations . . . . . 164

**B Convergence Studies** **167**
B.1 Quantum Chemical Calculations . . . . . 167
B.2 Density Functional Theory Calculations . . . . . 174

**Bibliography** **181**

**Acknowledgements** **203**

# Chapter 1

# Introduction

Great scientific effort has been made over the last centuries to understand and to actively control the velocity of chemical reactions. As early as in 1835 J. J. Berzelius discovered that certain substances speed up specific reactions significantly, and he coined the name *catalysis* for this phenomenon. Nevertheless, the basic laws governing the velocity of chemical reactions were formulated not until decades later by S. Arrhenius and J. H. van 't Hoff, who thus founded the field of reaction kinetics [12]. Essentially, the kinetic picture (see Fig 1.1) provides a model on the basis of energetic differences between educt, transition state and product for thermal equilibrium situations. Hence, by measuring the change of concentration over time, it was experimentally possible to determine the energetic barrier of the reaction and to determine its type and order [13]. By this means, W. Ostwald could explain the hitherto mysterious catalysis as a decrease (or contrariwise as an increase) of the effective barrier by a substance that is not altered in the reaction [14]. The desire for energy saving and fast, but also highly selective chemical synthesis led to the discovery of a multitude of catalytic processes of outstanding industrial and scientific importance during the first part of the last century [15, 16].

Significant progress was also achieved in measuring reaction rates, allowing scientists to study both extremely slow and extremely fast reactions. Nevertheless, the exact nature of the measured barriers could not be investigated by means of experiments, since—according to the laws of thermodynamics—both the velocities of the molecules and their orientation in a gas or a liquid are randomly distributed. Therefore, the details of the reaction become blurred and it is hardly possible to study which molecular features and which degrees of freedom are actually relevant for the velocity of the reaction. In the chemistry Nobel prize presentation speech in 1986 [17] this problem was brilliantly compared with the performance of a radical shortened drama: By just knowing the beginning of the first act and the last minutes of the finale, it will be almost impossible for a spectator to guess the complete plot. The development of the (crossed) molecular beam and the infrared-chemiluminescence techniques, honored with the already mentioned Nobel prize for D. R. Herschbach, Y. T. Lee and J. C. Polanyi [17], allowed some first glimpses at the intermediate acts of the "reaction drama", thereby actually founding the research field of chemical dynamics. Molecular beams are well-defined with respect to many molecular parameters

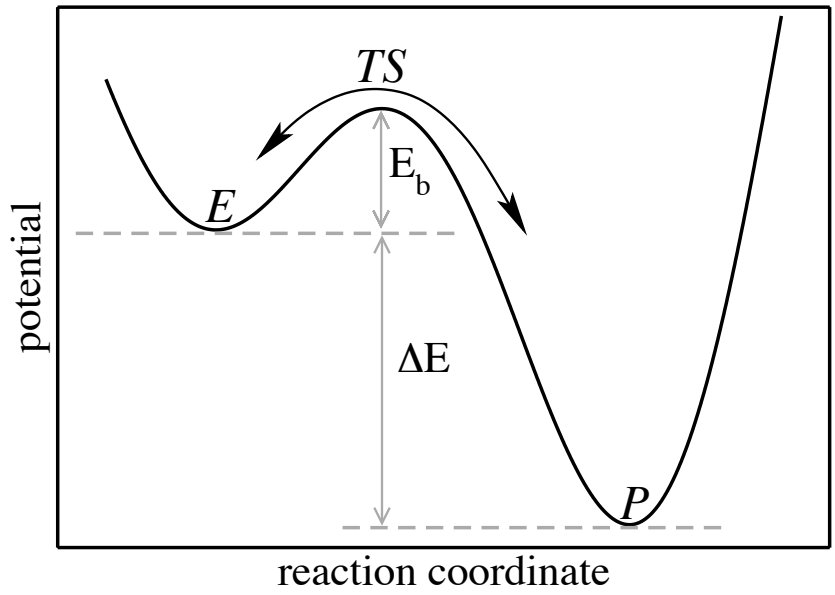


Figure 1.1: Schematic *kinetic* picture of a chemical reaction, showing the barrier $E_b$ at the transition state $TS$ and the energy difference $\Delta E$ between educt $E$ and product $P$.

as the kinetic energy, hence enabling studies of chemical reactions in dependence of these molecular degrees of freedom. Furthermore, the measurement of the infrared light released by the products gives some indirect but essential information about the nature of the occurring electronic rearrangement. Nowadays it is possible to produce molecular beams of unprecedented sharpness even with respect to vibrational and rotational degrees of freedom [18]. When working with pulsed beams, one can also employ mass spectrometers to detect the products, thus enabling the measurement of their time-of-flight and their kinetic energy. In addition, various spectroscopic techniques as infrared, microwave and *Resonance-enhanced-Multi-Photon-Ionization* [19] spectroscopy allow the detection of the products' population in the miscellaneous vibrational, rotational and electronic states. Scientific progress has not only been made in the characterization of educt and product but also in the measurement of the transition state (see Fig 1.1): The development and use of laser flashes pulsed on a timescale comparable to that of atomic motion, commonly known as femtosecond spectroscopy [20], made it possible to detect intermediate states and actually follow the movement of the single atoms a molecule consists of during the chemical reactions. These experimental techniques as a whole allowed to figure out a large amount of mechanisms underlying chemical reactions. Even industrial catalytic processes occurring under ill-defined conditions could be understood on the basis of their elementary steps analyzed in "clean" laboratory setups, as G. Ertl [21] successfully demonstrated.

Hand in hand with these experimental achievements the understanding of chemical reactions from a theoretical point of view made progress, but a rather small one. The simple Arrhenius equation, which works for gases, was generalized in

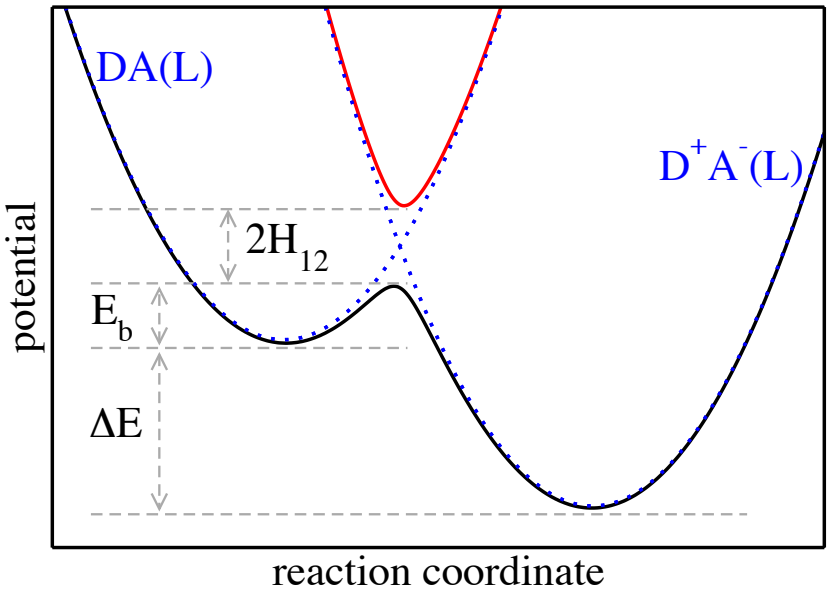


Figure 1.2: An electron-transfer reaction in the Marcus picture: The Potential Energy Surfaces for the neutral ($DA(L)$) and for the ionic ($D^+A^-(L)$) donor-acceptor-liquid system and the basic parameters entering the *Marcus Theory* are shown.

order to be applied as well to solution and mixed phase reactions by H. Eyring, M. G. Evans and M. Polanyi [22] as early as in 1935. This allowed the experimental determination of the involved barrier in this type of reactions as well, whereas its calculation still was a formidable problem. In between 1956 and 1965, R. A. Marcus elaborated a mathematical model to describe the probably most simple chemical reaction, where no bond is broken but one single electron is transferred from one reaction partner to the other within a liquid environment. This framework, commonly known as *Marcus Theory* [23], allows to calculate the barriers of such processes on the basis of some reaction parameters like ionic radii and charges. Under the assumption that the Potential Energy Surface of both the neutral and the ionic donor-acceptor system is parabolic near their relative equilibrium point (blue curves in Fig. 1.2), one can determine the crossing point between them. Actually the height of the barrier $E_b$ is lowered with respect to the crossing point, since the intersection is "avoided" (solid lines) due to the interaction $H_{12}$ among the two electronic configurations. When artificially increasing the energy difference $\Delta E$ between the educt and the product state by shifting one of the parabolas vertically, the crossing point slips to the left, the barrier $E_b$ decreases and thus the actual reaction velocity increases. At a certain value of $\Delta E$ the crossing point coincides with the equilibrium position and the barrier vanishes completely. So far, the Marcus theory is consistent with one's chemical intuition that the more exothermic a chemical reaction is, the faster it occurs. However, if $\Delta E$ is further increased, the barrier rises again, since the crossing point is now located on the left wing of the parabola. As a result—in contrast to one's expectations—the reaction rate should decrease in this *inverted Marcus region*. This long disputed prediction was finally proved

experimentally in the mid '80s [24].

Although the fundamental equations governing chemical reactions were fully known since the development of quantum mechanics, their mathematical complexity prevented their solution. Consequently—as in the Marcus model—just a qualitative insight based on strong approximations, but no general quantitative description or prediction could be provided by theory. This rather frustrating situation changed dramatically with the development and availability of high-performance computers, which allowed to solve the quantum mechanical equations numerically without the use of parameters or strongly limiting approximations. These calculational approaches, which just rely on fundamental physical constants, are referred to as *ab initio* methods and laid the foundation for all further simulation techniques in chemistry. However, they are still pretty costly, even for small molecules. That is why huge efforts have been made both to increase the performance of the solving algorithms as well as to reformulate quantum mechanics to make its numerical treatment more efficient. In combination with the enormous growth of computer power during the last decades, this technical progress established *computational chemistry* as a state-of-the-art technique to understand, reproduce and even predict experiments. In 1998 W. Kohn and J. A. Pople, the intellectual fathers of Density Functional Theory and the Quantum Chemistry methods respectively, were awarded the Nobel prize for this huge achievement [25].
Without going into details about the mentioned methods, since they are discussed extensively in Chap. 2, we will examine their application to chemical reactions qualitatively. As the atomic motion in general occurs on a larger timescale than the electronic, the two motions are treated consecutively in the commonly known Born-Oppenheimer approximation (see Sec. 2.1). First, *ab initio* calculations are employed to solve the Schrödinger equation for fixed nuclei, thus resulting in a complete description of the electronic state for the given geometry. The obtained total energy of the system, corresponding to one point of the black solid lines in Fig. 1.1 and 1.2, and its derivatives can be used in an iterative optimization algorithm to find the local minima of this (in general high dimensional) Potential Energy Surface and thus the educt and product equilibrium states. More elaborate and expensive optimization schemes [26] also allow to locate the transition state. Furthermore, chemical dynamics, i.e., the explicit motion of the atoms during a reaction, can be simulated by coupling an ordinary Molecular Dynamics (MD) algorithm [27] for the nuclei with an *ab initio* method, which determines the electronically induced forces on the fly. Apart from computationally cheap systems (single molecules [28] or $H_2$ on Pd(100) [29] for instance) this state-of-the-art approach is still too costly to simulate a sufficient number of trajectories to cover the huge phase space of a polyatomic system. If so, one can still apply the *Divide and Conquer* technique as proposed by, e.g., A. Groß and M. Scheffler [30]: By restricting the motion to the most relevant degrees of freedom, e.g. the molecular[1] ones in a heterogeneous reaction, it is possible to map the significant part of the Potential Energy Surface by combining the results of *ab initio* calculations with multi-dimensional interpolation methods. The smooth hypersurface obtained therewith can be used in a MD or wave packet [31] simulation to calculate a huge number of trajecto-

[1] This restriction is commonly known as *frozen substrate approximation*.

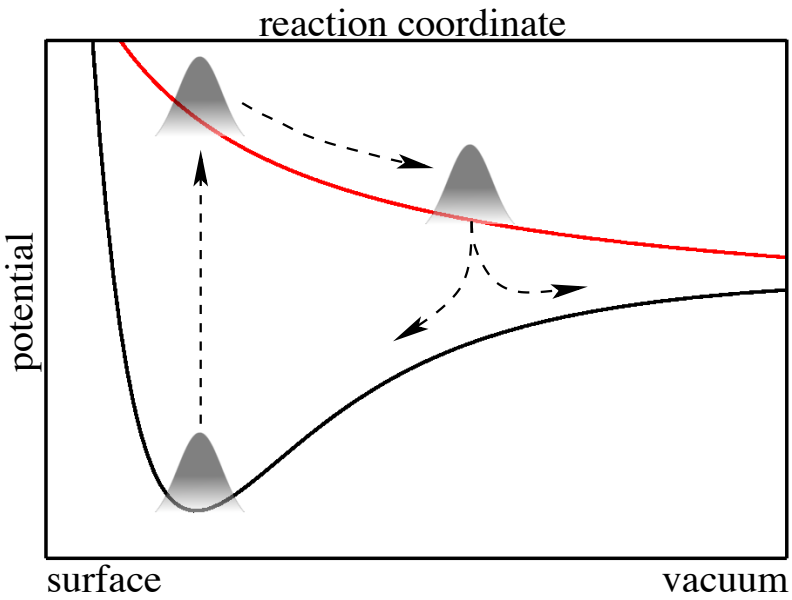


Figure 1.3: Desorption induced by electronic transitions in the *Menzel-Gomer-Redhead* model [34, 35]: The molecule is excited from its equilibrium absorption well to a repulsive excited potential (black and red curves respectively), where it is accelerated away from the surface, until it relaxes back into its electronic ground state by photon emission. Whether it desorbs or not, depends upon the amount of kinetic energy the molecule has gained in the excited state.

ries, hence allowing the determination of thermodynamically averaged reaction rates. Last but not least, one might be interested in processes occurring on a macroscopic timescale, like the diffusion driven island formation of adsorbates on a surface. On the basis of barriers determined in an *ab initio* fashion, it is also possible to reproduce this kind of processes [32] within a *kinetic* (also known as *dynamic*) *Monte Carlo* approach [33]. As varied as the applications of *ab initio* techniques are, as manifold are their scientific achievements: On the one hand, the calculational approach allows to examine all variables of a dynamic process, in particular those not observable by experiment, and thus it reveals the entire plot of the "chemical reaction drama". On the other hand, it facilitates the interpretation and generalization of experimental results, since all input parameters (mass, charge and geometry) can be varied independently.

However, all listed methods are based on the Born-Oppenheimer approximation, i.e., the separation of the dynamics into two parts, an electronic and a nuclear one, which are treated consecutively (see Sec. 2.1). Therefore the calculation of the electronic ground state within *ab initio* methods leads to a Potential Energy Surface describing smooth transitions among the individual electronic configurations (the black curve in Fig. 1.2), since the electrons are allowed to relax to their relative ground state in each individual nuclear geometry. Hence the Born-Oppenheimer approximation allows to describe a chemical reaction, a process including distinct electronic states by definition, on one Potential Energy

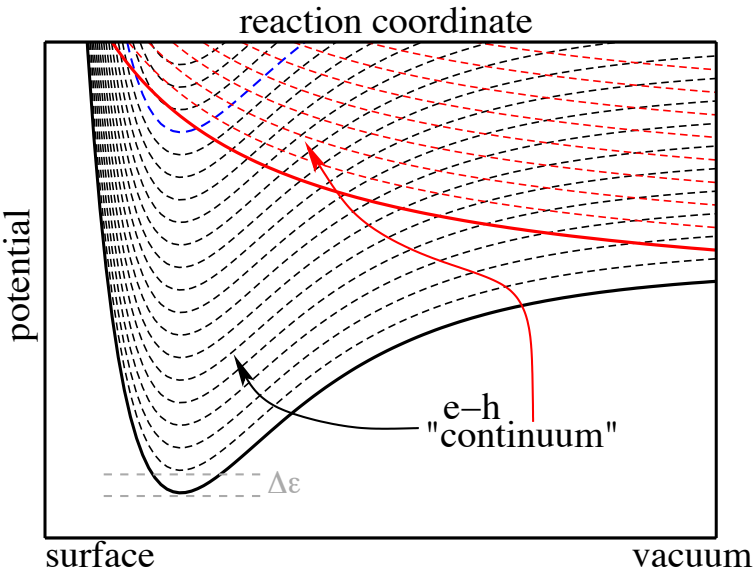


Figure 1.4: Effect of electronic excitations in the metal upon a molecule-surface reaction: Each (molecular) Potential Energy Surface (solid lines) spawns an infinite set of excited hypersurfaces, separated from each other by the constant amount of energy $\Delta\epsilon$ needed to create an electron-hole pair in the bulk. Potential Energy Surfaces associated with a strong bulk excitation (exemplarily shown as blue curve) exhibit intersections with the molecular excited state near their own minima.

Surface, whose underlying electronic character changes *adiabatically*. Obviously, this approximation breaks down for reactions, as for example in the case of a desorption induced by electronic transitions, where transitions to and out of excited molecular states and their exact occurrence during the molecular motion play the main role (see Fig. 1.3). For reactions among a metal surface and a molecule, the electronic excitation of the bulk leads to a connatural effect (see Fig. 1.4). The resulting pseudo-continuum of excited states constitutes an additional energy dissipation channel for the molecule and can therefore be successfully described within a friction model [36] for instance. During adsorption, excess kinetic energy of the molecule may thereby[2] leak, which results in an increased reaction rate. Desorption can also be induced by this means: A strong (local) excitation of the electron gas—as generated by a laser pulse—can trigger an excitation of the molecule (see blue curve in Fig. 1.4) and thus the desorption process [39].

Aside from these mechanisms, the *non-adiabaticity* of which is self-evident due to the explicit role electronic excitations play, a breakdown of the Born-Oppenheimer approximation may manifest itself in a more subtle manner: The electronic transition from the educt state to the product state may be so strongly suppressed due to selection rules, that the electrons are not able to relax within the

[2]However the importance of this dissipation channel depends strongly on the studied system [37, 38].

timescale of nuclear motion. In the limit of a totally forbidden transition, the nuclei would then not move on the (black) adiabatic potential in the Marcus picture (see Fig. 1.2) but rather on distinct parabolas (blue). Hence non-adiabatic effects of this kind can entirely alter the character of a system, leading to dramatically reduced reaction rates. The dissociative adsorption of $O_2$ on Al(111), a process that is supposed to be strongly determined by such a mechanism [4], is the main topic of this thesis, which is structured as follows:

(*a*) In the theory part (Chap. 2) we will first discuss the Born-Oppenheimer approximation on a stringent mathematical basis (Sec. 2.1) and introduce the Surface Hopping method (SH) chosen in this work to extend MD simulations beyond their limits (Sec. 2.4.3.2). The *ab initio* techniques employed to derive the data underlying the dynamics are also summarized briefly in Sec. 2.2.1 and 2.2.2.

(*b*) The oxygen molecule and its peculiarities are discussed in chapter 3. An in-depth study of the molecular oxygen's electronic structure (Sec. 3.2 and 3.3) is presented and compared to experimental and theoretical results in literature to substantiate the validity of the *ab initio* approach.

(*c*) In chapter 4 the $O_2$/Al(111) system is introduced first. Then MD and SH simulations for this system are presented, whereby the dependence on the topology of the underlying Potential Energy Surfaces and the thereto associated electronic states is analyzed extensively. Finally, the chosen approach is critically discussed by comparing these studies to various experimental evidences.

(*d*) In chapter 5 the most relevant results of this work are summarized: Further experiments to validate the theoretical findings as well as computational approaches to improve the description of the non-adiabatic effects are proposed.

# Chapter 2

# Theory

In this work we will focus on (bound) electron-nuclear systems as atoms, molecules, bulks and their surfaces. Hence one has to deal with a Hamiltonian $\mathcal{H}$, which depends both on the electronic and on the nuclear degrees of freedom, here denoted by lower ($\mathbf{r}$) and upper case ($\mathbf{R}$) letters, respectively. The terms entering the Hamiltonian are the nuclear and the electronic kinetic energies ($T_{\mathbf{R}}, T_{\mathbf{r}}$) as well as the relative electrostatic potentials: the electron-electron repulsion $V_{\mathbf{rr}}$, the nuclei-nuclei repulsion $V_{\mathbf{RR}}$ and the electron-nuclei attraction $V_{\mathbf{rR}}$. Generally, all other forces—i.e. the gravitational, the strong and the weak interaction [40]—can be safely neglected, although there are speculations whether the electroweak force could influence the stability of one enantiomer over another [41]. Since relativistic effects[1] do not play a relevant role for light systems [42] either, the solution of the following Schrödinger equation has to be found:

$$\mathcal{H}\,\Psi\left(\mathbf{r},\mathbf{R}\right) = \left(T_{\mathbf{R}} + T_{\mathbf{r}} + V_{\mathbf{rr}} + V_{\mathbf{RR}} + V_{\mathbf{rR}}\right)\,\Psi\left(\mathbf{r},\mathbf{R}\right) = E\,\Psi\left(\mathbf{r},\mathbf{R}\right). \tag{2.1}$$

Due to the enormous mass difference between nuclei and electrons ($M_{\mathrm{H}} \approx 1800\,m$), one expects the nuclear and the electronic motion to occur on different timescales. This assumption implies that the electrons adjust *instantaneously*, whenever the forces acting on them are altered due to the nuclear motion, and thus stay *adiabatically* in their ground state. As shown formally in the next section, this allows to split Eq. (2.1) in two parts, which have to be tackled subsequently: first one for the electrons, then one for the nuclei.

## 2.1 The Born-Oppenheimer Approximation

In a first step we will inspect the Schrödinger equation for a set of immobile nuclei, which enter Eq. (2.1) as a set of parameters $\{\mathbf{R}\}$:

$$\overbrace{\left(T_{\mathbf{r}} + V_{\mathbf{rr}} + V_{\mathbf{r}\{\mathbf{R}\}} + V_{\{\mathbf{R}\}\{\mathbf{R}\}}\right)}^{\mathcal{H}_e}\,\Phi_i\left(\mathbf{r},\{\mathbf{R}\}\right) = \varepsilon_i \Phi_i\left(\mathbf{r},\{\mathbf{R}\}\right). \tag{2.2}$$

[1] The spin, which might be regarded as a relativistic effect, enters the Schrödinger equation indirectly, as seen in Sec. 3.

Thereby the terms in the *electronic Hamiltonian* $\mathcal{H}_e$ expand to:

$$\mathcal{H}_e = \underbrace{-\frac{\hbar^2}{2m}\sum_l \nabla_l^2}_{T_r} + \underbrace{\frac{1}{2}\sum_{l\neq m}\frac{e^2}{|\mathbf{r}_l-\mathbf{r}_m|}}_{V_{\mathbf{rr}}} \underbrace{-\sum_{l,M}\frac{Z_M e^2}{|\mathbf{r}_l-\mathbf{R}_M|}}_{V_{\mathbf{r}\{\mathbf{R}\}}} + \underbrace{\frac{1}{2}\sum_{L\neq M}\frac{Z_L Z_M e^2}{|\mathbf{R}_L-\mathbf{R}_M|}}_{V_{\{\mathbf{R}\}\{\mathbf{R}\}}}. \tag{2.3}$$

Although Eq. (2.2) already represents a formidable problem, the solution of which will be addressed separately in Sec. 2.2, we will assume that the eigenvalues $\varepsilon_i$ and the eigenfunctions $\Phi_i(\mathbf{r},\{\mathbf{R}\})$ of the electronic Hamiltonian $\mathcal{H}_e$ are known at this point. For any given set of coordinates $\{\mathbf{R}\}$, these eigenfunctions $\Phi_i(\mathbf{r},\{\mathbf{R}\})$ constitute a complete orthonormal basis set. Thus the complete solution $\Psi(\mathbf{r},\mathbf{R})$ of Eq. (2.1) is expanded in terms of solutions of the immobile nuclei problem:

$$\Psi(\mathbf{r},\mathbf{R}) = \sum_j C_j(\mathbf{R})\ \Phi_j(\{\mathbf{R}\},\mathbf{r}) \stackrel{!}{=} \sum_j C_j|j\rangle. \tag{2.4}$$

Reinserting the expansion (2.4) in the original Schrödinger equation (2.1) and multiplying it by $\langle i|$ from the left, leads to the following relation:

$$\langle i|T_{\mathbf{R}}\sum_j C_j|j\rangle + \underbrace{\sum_j C_j\langle i|\overbrace{(T_{\mathbf{r}}+V_{\mathbf{rr}}+V_{\mathbf{rR}})}^{\mathcal{H}_e}|j\rangle}_{C_i\varepsilon_i} + V_{\mathbf{RR}}C_i = EC_i. \tag{2.5}$$

The matrix elements of the total nuclear kinetic energy operator

$$T_{\mathbf{R}} = -\sum_L \frac{\hbar^2}{2M_L}\nabla_L^2, \tag{2.6}$$

which contains one kinetic energy term for each nucleus $\mathbf{R}_L$, are then expressed as

$$\begin{aligned}
\langle i|T_{\mathbf{R}}\sum_j C_j|j\rangle &= \langle i|\left(\sum_L -\frac{\hbar^2}{2M_L}\nabla_L^2\right)\sum_j C_j|j\rangle \\
&= \sum_j\langle i|\left(\sum_L -\frac{\hbar^2}{2M_L}\nabla_L^2 C_j\right)|j\rangle \\
&+ \sum_j\langle i|C_j\left(-\sum_L\frac{\hbar^2}{2M_L}\nabla_L^2|j\rangle\right) \\
&+ \sum_j\langle i|\left(\sum_L -\frac{\hbar^2}{2M_L}\cdot 2\cdot(\nabla_L C_j)\cdot(\nabla_L|j\rangle)\right) \\
&= T_{\mathbf{R}}C_i \\
&+ \sum_j C_j\langle i|T_{\mathbf{R}}|j\rangle - \sum_{j,L}\frac{\hbar^2}{M_L}(\nabla_L C_j)\langle i|\nabla_L|j\rangle.
\end{aligned} \tag{2.7}$$

This leads to the following equation for the nuclear wave function $C_i(\mathbf{R})$:

$$\left( T_{\mathbf{R}} + \underbrace{\varepsilon_i + V_{\mathbf{RR}}}_{v^i_{\text{eff}}(\mathbf{R})} - E \right) C_i = \sum_{j,L} \frac{\hbar^2}{M_L} (\nabla_L C_j) \langle i| \nabla_L |j\rangle - \sum_j C_j \langle i| T_{\mathbf{R}} |j\rangle . \tag{2.8}$$

The left-hand side of Eq. (2.8) corresponds to a Schrödinger equation for nuclei moving in the effective potential $v^i_{\text{eff}}(\mathbf{R})$, which we usually refer to as the *Potential Energy Surface* (PES) associated to the electronic state $i$. It includes both the nuclear repulsion term $V_{\mathbf{RR}}$ as well as the potential $\varepsilon_i(\{\mathbf{R}\})$ induced by the electronic rearrangement. The right-hand side of Eq. (2.8) can be estimated qualitatively:

($a$) Due to

$$\langle i| \nabla_L |i\rangle = \frac{1}{2} \nabla_L \langle i|i\rangle = 0$$

the diagonal terms $\langle i| \nabla_L |i\rangle$ in the first sum vanish exactly.

($b$) The diagonal terms $\langle i| T_{\mathbf{R}} |i\rangle$ in the second sum, also known as the *Diagonal Born-Oppenheimer Corrections* [43], describe the kinetic energy the electrons gain due to the nuclear motion. In the extreme, they may follow the nuclei without any delay or distortion, which results in a kinetic energy gain in the order of

$$\langle i| T_{\mathbf{R}} |i\rangle \approx \frac{m}{M_L} \langle i| T_{\mathbf{r}} |i\rangle = \frac{m}{M_L} E^e_{\text{kin}}.$$

Indeed, these corrections basically describe the *reduced mass effect* and can be approximated by using atomic instead of nuclear masses in Eq. (2.8). A more accurate treatment of these diagonal terms may be necessary for high-accuracy calculations (e.g. isotope effects) of extreme light molecules, as molecular hydrogen [44] for instance.

($c$) The non-diagonal terms, i.e. $\langle i| T_{\mathbf{R}} |j\rangle$ and the *non-adiabatic coupling vector* $\langle i| \nabla_L |j\rangle$, describe the electronic transitions between state $i$ and $j$ induced by the nuclear motion. They are by far harder to estimate without any deeper knowledge of the system, since they depend on the nature of the actual transition (e.g. gradual electron transfer, abrupt spin flips). Generally, one expects such transitions to occur on the same timescale as the electronic motion itself.

In the *Born-Oppenheimer approximation*, formally introduced by Max Born and Robert J. Oppenheimer [45] in the early days of quantum mechanics, the electronic transitions (c) are completely neglected: The nuclei are assumed to move in the electronic potential $\varepsilon_0(\{\mathbf{R}\})$, as if the electrons were staying adiabatically in their relative ground state. The diagonal corrections (b) are addressed by using atomic instead of nuclear masses in the nuclear kinetic energy operator $T_{\mathbf{R}} \to T^{\text{at.}}_{\mathbf{R}}$, which leads to

$$\left( T^{\text{at.}}_{\mathbf{R}} + \underbrace{\varepsilon_0 + V_{\mathbf{RR}}}_{v^0_{\text{eff}}(\mathbf{R})} - E \right) C_0 = 0. \tag{2.9}$$

The solution of this *nuclear* Schrödinger equation can be further simplified for heavy systems ($M \gg M_{\mathrm{H_2}}$) by neglecting quantum mechanical effects (see Sec. 2.4.1), thus leading to a classical Equation of Motion on one Potential Energy Surface $v^0_{\mathrm{eff}}(\mathbf{R})$ for the nuclei:

$$M_L^{\mathrm{at.}} \ddot{\mathbf{R}}_L = -\nabla_L \, v^0_{\mathrm{eff}}(\mathbf{R}). \tag{2.10}$$

Although the Born-Oppenheimer approximation may seem crude from a formal point of view due to the lack of arguments in point (c), its intent is plausible: Indeed almost all atomic, molecular, solid state and surface physics theories successfully rely on it [46, 43, 47, 48]. Nevertheless, the Born-Oppenheimer approximation may break down in specific situations, a few of them are already mentioned in the introduction (Chap. 1).

### 2.1.1 Adiabatic and Diabatic Representations

In the derivation of the Born-Oppenheimer approximation we expanded the total wave function in the Hilbert space spanned by the solutions of the electronic Schrödinger equation (2.2). This complete orthonormal basis set is commonly referred to as *adiabatic*. However, a more general expansion in terms of generic functions $|i\rangle = |i\,(\mathbf{r}, \{\mathbf{R}\})\rangle$ comes in handy when dealing with electronic transitions. Accordingly, Eq. (2.8) also assumes a more generic shape

$$\begin{aligned}(T_{\mathbf{R}} + V_{\mathbf{RR}} - E)C_i + \sum_j \underbrace{\langle i| \, \mathcal{H}_e \, |j\rangle}_{V_{ij}(\mathbf{R})} C_j = \\ \sum_{j,L} \frac{\hbar^2}{M_L} (\nabla_L C_j) \, \langle i| \, \nabla_L \, |j\rangle - \sum_j C_j \, \langle i| \, T_{\mathbf{R}} \, |j\rangle \,, \end{aligned} \tag{2.11}$$

whereby the eigenvalues of the electronic Hamiltonian $\mathcal{H}_e$ have been replaced by a potential energy matrix $V_{ij}$. In this representation its non-diagonal elements, i.e. the *diabatic coupling*, account for the transitions from state $i$ to state $j$ (and vice versa) as well. Obviously, one re-obtains Eq. (2.8), when using the appropriate adiabatic basis set which diagonalizes $V_{ij}$. Then again one could choose the expansion in such a way that the right hand side of Eq. (2.11) vanishes, as achieved by a basis set that does not depend on the nuclear coordinates $\mathbf{R}$. Such a *crude diabatic* ansatz is helpful to obtain a physical interpretation of the electronic transitions, as exemplified in Fig. 2.1 for the formation of NaCl. There, the electronic configurations chosen for the crude diabatic expansion (solid lines) are the neutral configuration "NaCl"(red) and the ionic configuration "$\mathrm{Na^+Cl^-}$"(black). Thus the resulting diagonal potential matrix elements $V_{ii}\,(\mathbf{R})$ belong to the relative ground states in the educt and product state, respectively. In between, the two diabatic potentials intersect at a well defined *crossing point*, which strictly delimits the region where the pure ionic configuration is energetically favorable from the region where the pure neutral one is favorable. According to the *non-crossing rule*, Potential Energy Curves associated with electronic states of the same symmetry species cannot cross in the adiabatic representation as the intranuclear distance is varied [49]. Consequently, the (blue) adiabatic potentials, which pertain to distinct eigenstates of the electronic Hamiltonian, *avoid* this crossing, which leads to a lowered and

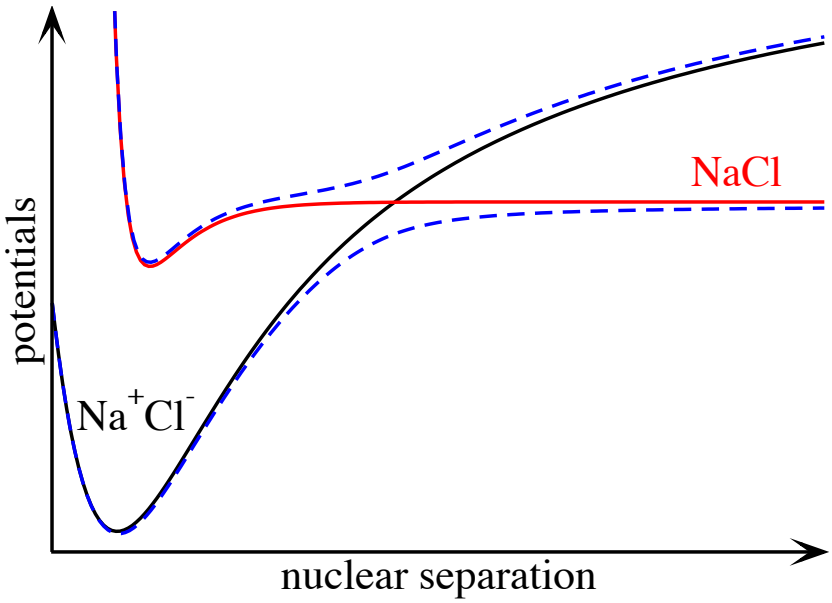


Figure 2.1: Schematic plot of both the crude diabatic (solid) and the adiabatic (dashed) potentials involved in the formation of NaCl. Both the curves for the neutral (red) and for the ionic (black) electronic configuration are shown as a function of the nuclear separation.

an elevated potential respectively. The width of the splitting is determined by the nature of the interaction in between the two configurations. At large nuclear distances a transition from the neutral to the ionic state is obviously just possible due to electron tunneling from the sodium to the chlorine atom. As the nuclei approach each other, however, the orbitals start to overlap and thus the lower adiabatic potential describes atoms changing their electronic character from neutral to ionic when traversing the crossing region. This transition occurs smoothly, since the overlap matrix elements are smooth functions of the nuclear distance as well. Accordingly, the adiabatic potentials show no cusp at the diabatic crossing point. Under the electronic perspective this corresponds to a mixing of the diabatic ionic and the diabatic neutral wave function in variable ratios.

One immediately sees the key benefits of a Born-Oppenheimer description: As long as the nuclear motion is considerably slower than the electron dynamics, the adiabatic assumption holds and hence allows to describe the NaCl formation on **one** Potential Energy Surface, i.e. the lower adiabatic one, without spending a thought on the electronic character of the wave function in the crossing region. Indeed, such an analysis on the nature of the involved electronic states, often referred to as *diabatization*, can be performed in hindsight. Still, apart from being an interpretation aid, the diabatic potentials can be useful: In the—in this case unrealistic—high energy limit, where the nuclei move orders of magnitude faster than the electrons, the Born-Oppenheimer approximation breaks down. As the electrons are no longer able to adjust to the changing external forces fast enough,

the nuclei indeed move on the respective crude diabatic potential, e.g. on the neutral one (red solid line) when approaching each other. Still, just one Potential Energy Surface has been considered in this Gedankenexperiment. For a realistic description of the dynamics in between the Born-Oppenheimer approximation and the high energy limit, i.e. in the case of comparable timescales for nuclear and electronic motion, one has to solve Eq. (2.11) on **multiple** Potential Energy Surfaces and to take account of the electronic transitions explicitly. Since the basis set chosen for an expansion has no influence on the quantum dynamics itself as long as all relevant states are included, one might choose a basis set, beside the adiabatic and crude diabatic one, which minimizes the right-hand side of Eq. (2.11) and which is thus specially suited for the inspected problem. Hence a whole series of different basis set expansions, irritatingly all referred to as diabatic in literature, can be found. In scattering theory for example, one tries to minimize the number of non-vanishing elements in the scattering matrix and therefore chooses a basis set which diagonalizes the generalized momentum and angular momentum matrices [50]. In contrast thereto, a basis set is called diabatic in the Quantum Chemistry community, if in addition to minimizing the right hand side of Eq. (2.11), it can be generated by an orthogonal transformation of the adiabatic basis. As a matter of fact, such a basis set can be defined for diatomic molecules, but does not exist in general for larger systems [51]. In this work we will stick to the adiabatic and crude diabatic basis. The latter will be simply referred to as diabatic, as usually done in the Surface Hopping community [7].

## 2.2 Electronic Structure Theory

In electronic structure theory one tries to find solutions to the electronic Schrödinger equation for a set of fixed[2] nuclear coordinates, as introduced in Sec. 2.1:

$$\overbrace{\left(T_{\mathbf{r}} + V_{\mathbf{rr}} + V_{\mathbf{rR}}\right)}^{\mathcal{H}_e} \Phi_i(\mathbf{r}) = \varepsilon_i \Phi_i(\mathbf{r}). \tag{2.12}$$

The three terms in the electronic Hamiltonian $\mathcal{H}_e$, whose meaning has been already examined (see Eq. (2.3) and its discussion), expand to:

$$\mathcal{H}_e = \underbrace{-\frac{\hbar^2}{2m}\sum_l \nabla_l^2}_{T_r} + \underbrace{\frac{1}{2}\sum_{l\neq m}\frac{e^2}{|\mathbf{r}_l - \mathbf{r}_m|}}_{V_{\mathbf{rr}}} \underbrace{-\sum_{l,M}\frac{Z_M e^2}{|\mathbf{r}_l - \mathbf{R}_M|}}_{V_{\mathbf{rR}}}. \tag{2.13}$$

To solve this equation the *Rayleigh-Ritz minimization principle* [52]

$$\varepsilon_0 = E[\Phi_0] \leq E[\psi] = \frac{\langle\psi|\,\mathcal{H}_e\,|\psi\rangle}{\langle\psi|\psi\rangle} \tag{2.14}$$

is taken advantage of. It states that the total energy functional $E[\psi]$ of normalized trial wave functions $\psi$ exhibits an absolute minimum for the correct

[2] In contrast to Eq. (2.2), the nuclear repulsion term $V_{\mathbf{RR}}$ is omitted, because it just results in a constant energy shift. The $\{\mathbf{R}\}$ notation employed in the previous section to discriminate in between parameters and variables is unnecessary here and has therefore been abandoned for the sake of readability.

electronic ground state $\Phi_0(\mathbf{r})$ with its respective eigenvalue $\varepsilon_0$. Consequently, one can transform the eigenvalue problem (2.12) into a formally simpler minimization one (2.14). Still, its solution is far from being trivial due to the huge Hilbert space that is spanned by a many-electron problem. In the next section 2.2.1 general ansätze for the trial wave function $\psi$ and the way the resulting functional $E[\psi]$ is efficiently evaluated are discussed. The many-body trial wave function used in these so called *wave function based* methods explicitly depends on all electronic degrees of freedom, i.e., on $3N$ coordinates in the case of a $N$-electron system. Therefore the numerical evaluation of the numerator in Eq. (2.14), which includes one- and two-center integrals, becomes numerically prohibitively expensive, the larger the number of electrons is. In *Density Functional Theory* Eq. (2.14) is formally rewritten as a functional of the electronic density $\rho(\mathbf{r})$, which only depends on three spatial coordinates regardless of the actual number of electrons the simulated system includes. Thereby, the evaluation of the numerator in Eq. (2.14) can be significantly sped up, as will be seen in Sec. 2.2.2.

### 2.2.1 Quantum Chemistry

The term "Quantum Chemistry" usually refers to a whole class of computational techniques used to solve the many-electron Schrödinger equation. All of them are wave function based *ab initio* approaches, which solve Eq. (2.12) by varying the trial wave function $\psi$ without employing additional empirical data or approximations. As a matter of fact, the methods discussed within this section just differ in the complexity—and hence in the generality—of the ansatz for $\psi$.

#### 2.2.1.1 Independent Particle Model

In a first step we discuss the "Independent Particle Model", wherein the electron-electron interaction $V_{\mathbf{rr}}$ in Eq. (2.13) is neglected. Although not useful for practical purposes, its solution is very instructive to analyze the role the electron-electron interaction plays in the exact problem.

The Hamiltonian for this "Independent Particle" model $\tilde{\mathcal{H}}_e$ can actually be rewritten as a sum over identical single-electron Hamiltonians $\mathbf{h}_l$:

$$\tilde{\mathcal{H}}_e = \sum_l \mathbf{h}_l = \sum_l \left( -\frac{\hbar^2}{2m}\nabla_l^2 - \sum_M \frac{Z_M e^2}{|\mathbf{r}_l - \mathbf{R}_M|} \right). \tag{2.15}$$

This separation drastically reduces the complexity of the task: Instead of tackling the $N$ electron problem, one simply has to solve a **one**-particle Schrödinger equation

$$\mathbf{h}\,\varphi = \left( -\frac{\hbar^2}{2m}\nabla^2 - \sum_J \frac{Z_J e^2}{|\mathbf{r} - \mathbf{R}_J|} \right) \varphi = \lambda\,\varphi \tag{2.16}$$

and combine its eigenstates $\varphi_i$ to a many-body wave function. Thereby the electronic spin states $|\uparrow\rangle$ and $|\downarrow\rangle$, which do not occur in the Schrödinger equation explicitly, are taken into account in hindsight by introducing *spinorbitals* $\phi_i$ via tensor multiplication:

$$\phi_i = (\varphi_1, \cdots, \varphi_i, \cdots) \otimes (|\uparrow\rangle, |\downarrow\rangle). \tag{2.17}$$

An antisymmetric wave function for the entire system, as demanded by the Pauli principle (see Appendix A), can be constructed by combining $n$ spinorbitals into a Slater Determinant [53]

$$\begin{aligned}\psi^{SD}(\mathbf{r}_1,\ldots,\mathbf{r}_n) &= \frac{1}{\sqrt{n!}}\begin{vmatrix}\phi_1(\mathbf{r}_1) & \phi_1(\mathbf{r}_2) & \cdots & \phi_1(\mathbf{r}_n)\\ \phi_2(\mathbf{r}_1) & \phi_2(\mathbf{r}_2) & \cdots & \phi_2(\mathbf{r}_n)\\ \vdots & \vdots & \ddots & \vdots\\ \phi_n(\mathbf{r}_1) & \phi_n(\mathbf{r}_2) & \cdots & \phi_n(\mathbf{r}_n)\end{vmatrix}\\ &= \frac{1}{\sqrt{n!}}\,\epsilon^{\mathbf{r}_1\cdots\mathbf{r}_n}\phi_1(\mathbf{r}_1)\cdots\phi_i(\mathbf{r}_l)\cdots\phi_n(\mathbf{r}_n), \qquad (2.18)\end{aligned}$$

whereby the *Einstein summation notation* and the *Levi-Civita Symbol* $\epsilon^{\mathbf{r}_1\cdots\mathbf{r}_n}$ are employed in the last step. The latter formulation highlights the character of the many-body wave function as sum over all possible permutations of the electrons: Each of them occurs in each of the $n$ spinorbitals once for each of the $(n-1)!$ permutations of the remaining $(n-1)$ electrons. For the expectation value of the one-particle Hamiltonian this wave function leads to

$$\begin{aligned}\left\langle\psi^{SD}\right|\mathbf{h}\left|\psi^{SD}\right\rangle &= \frac{1}{n!}\left(\lambda_0+\lambda_1+\cdots+\lambda_n\right)(n-1)! \qquad (2.19)\\ &= \frac{1}{n}\sum_j^n \lambda_j. \qquad (2.20)\end{aligned}$$

Hence the total energy of the system is just the sum of the $n$ single *spinorbital energies* $\lambda_j$

$$\varepsilon = \left\langle\psi^{SD}\right|\tilde{\mathcal{H}}_e\left|\psi^{SD}\right\rangle = \sum_j^n \lambda_j, \qquad (2.21)$$

as one would intuitively expect. Accordingly, the ground state wave function can be constructed by employing the $n$ spinorbitals $\phi_j$ with the lowest energies $\lambda_j$ in the Slater Determinant (2.18).

Formally similar relations, which will be useful in the next section, can be derived for generic operators: As a consequence of the spinorbital's orthogonality, the inner product of different permutations of $|\phi_1(\mathbf{r}_1)\cdots\phi_i(\mathbf{r}_i)\cdots\phi_n(\mathbf{r}_n)\rangle$ vanishes, as exemplarily shown for the exchange of $\mathbf{r}_1$ with $\mathbf{r}_2$:

$$\begin{aligned}&\langle\phi_1(\mathbf{r}_1)\cdot\phi_2(\mathbf{r}_2)\cdots\phi_n(\mathbf{r}_n)|\phi_1(\mathbf{r}_2)\cdot\phi_2(\mathbf{r}_1)\cdots\phi_n(\mathbf{r}_n)\rangle =\\ &\qquad\underbrace{\langle\phi_1(\mathbf{r}_1)|\phi_2(\mathbf{r}_1)\rangle}_{=0}\cdot\underbrace{\langle\phi_2(\mathbf{r}_2)|\phi_1(\mathbf{r}_2)\rangle}_{=0}\cdot 1\cdots 1 = 0. \qquad (2.22)\end{aligned}$$

Analogously, such inner products occurring in the expectation value of any **one-electron** operator

$$\begin{aligned}&\langle\phi_1(\mathbf{r}_1)\cdot\phi_2(\mathbf{r}_2)\cdots\phi_n(\mathbf{r}_n)|f(\mathbf{r}_1)|\phi_1(\mathbf{r}_2)\cdot\phi_2(\mathbf{r}_1)\cdots\phi_n(\mathbf{r}_n)\rangle =\\ &\qquad\langle\phi_1(\mathbf{r}_1)|f(\mathbf{r}_1)|\phi_2(\mathbf{r}_1)\rangle\cdot\underbrace{\langle\phi_2(\mathbf{r}_2)|\phi_1(\mathbf{r}_2)\rangle}_{=0}\cdot 1\cdots 1 = 0 \qquad (2.23)\end{aligned}$$

vanish as well. For the total Slater Determinant these two relations lead to:

$$\langle \psi^{SD} | \psi^{SD} \rangle = \frac{1}{n} \sum_{i=1}^{n} \langle \phi_i | \phi_i \rangle = 1 \quad \text{and} \tag{2.24}$$

$$\langle \psi^{SD} | f(\mathbf{r}_1) | \psi^{SD} \rangle = \frac{1}{n} \sum_{i=1}^{n} \langle \phi_i(\mathbf{r}_1) | f(\mathbf{r}_1) | \phi_i(\mathbf{r}_1) \rangle. \tag{2.25}$$

However, this does **not** apply to generic **two-electron** operators:

$$\begin{aligned} &\langle \phi_1(\mathbf{r}_1) \cdot \phi_2(\mathbf{r}_2) \cdots \phi_n(\mathbf{r}_n) | f(\mathbf{r}_1, \mathbf{r}_2) | \phi_1(\mathbf{r}_2) \cdot \phi_2(\mathbf{r}_1) \cdots \phi_n(\mathbf{r}_n) \rangle = \\ &\quad \langle \phi_1(\mathbf{r}_1) | f(\mathbf{r}_1, \mathbf{r}_2) | \phi_2(\mathbf{r}_1) \rangle \cdot \langle \phi_2(\mathbf{r}_2) | f(\mathbf{r}_1, \mathbf{r}_2) | \phi_1(\mathbf{r}_2) \rangle \cdot 1 \cdots 1 \neq 0. \end{aligned} \tag{2.26}$$

This fact gives rise to an additional term in the expectation value of such operators

$$\begin{aligned} &\langle \psi^{SD} | f(\mathbf{r}_1, \mathbf{r}_2) | \psi^{SD} \rangle = \\ &\quad \frac{1}{n(n-1)} \sum_{i \neq j} \big( \langle \phi_i(\mathbf{r}_1) \phi_j(\mathbf{r}_2) | f(\mathbf{r}_1, \mathbf{r}_2) | \phi_i(\mathbf{r}_1) \phi_j(\mathbf{r}_2) \rangle \\ &\qquad - \langle \phi_i(\mathbf{r}_1) \phi_j(\mathbf{r}_2) | f(\mathbf{r}_1, \mathbf{r}_2) | \phi_j(\mathbf{r}_1) \phi_i(\mathbf{r}_2) \rangle \big) \end{aligned} \tag{2.27}$$

with unique features:

($a$) It vanishes for spinorbitals with *different* spins, as can be easily seen. Thus it *correlates* electrons in **different** orbitals which share the **same** spin.

($b$) It **lowers** the expectation value, since the *Levi-Civita symbol* in Eq. (2.18) yields a factor of $(-1)$. Thereby it can stabilize certain electronic configurations, as discussed in detail in the next section.

#### 2.2.1.2 Hartree-Fock Theory

In Hartree-Fock Theory one assumes that the exact $n$-electron wave function can be approximated by **one Slater-Determinant** $\psi^{SD}$ of $n$ spinorbitals $\phi_i$. Beside the spinorbital energies discussed in the independent particle model

$$\langle \phi_j | \, \mathbf{h} \, | \phi_j \rangle = \lambda_j, \tag{2.28}$$

two new terms appear in the total energy expectation value $\langle \psi^{SD} | \, \mathcal{H}_e \, | \psi^{SD} \rangle$ of the exact Hamiltonian $\mathcal{H}_e$ (2.13) due to the two-electron operator

$$V_{\mathbf{rr}}(\mathbf{r}_l, \mathbf{r}_m) = \frac{e^2}{|\mathbf{r}_l - \mathbf{r}_m|}. \tag{2.29}$$

The *Coulomb Integrals*, which describe the classical repulsion between two charge distributions $|\phi_i(\mathbf{r}_l)|^2$ and $|\phi_j(\mathbf{r}_m)|^2$, arise from the terms with the same permutation on both sides of $V_{\mathbf{rr}}$:

$$\begin{aligned} &\langle \phi_i(\mathbf{r}_l) \phi_j(\mathbf{r}_m) | \, V_{\mathbf{rr}}(\mathbf{r}_l, \mathbf{r}_m) \, | \phi_i(\mathbf{r}_l) \phi_j(\mathbf{r}_m) \rangle = \\ &\qquad e^2 \iint \frac{\phi_i^*(\mathbf{r}_l) \phi_i(\mathbf{r}_l) \; \phi_j^*(\mathbf{r}_m) \phi_j(\mathbf{r}_m)}{|\mathbf{r}_l - \mathbf{r}_m|} d\mathbf{r}_l d\mathbf{r}_m. \end{aligned} \tag{2.30}$$

In addition, the permutation of $\mathbf{r}_l$ with $\mathbf{r}_m$ (see Eq. (2.26)) on one side of the operator gives rise to

$$\langle\phi_i(\mathbf{r}_l)\phi_j(\mathbf{r}_m)|\, V_{\mathbf{rr}}(\mathbf{r}_l,\mathbf{r}_m)\,|\phi_i(\mathbf{r}_m)\phi_j(\mathbf{r}_l)\rangle = e^2 \iint \frac{\phi_i^*(\mathbf{r}_l)\phi_j(\mathbf{r}_l)\;\phi_j^*(\mathbf{r}_m)\phi_i(\mathbf{r}_m)}{|\mathbf{r}_l-\mathbf{r}_m|} d\mathbf{r}_l d\mathbf{r}_m, \quad (2.31)$$

i.e. the so called *Exchange Integrals* (see Eq. (2.27)), which have no classical analogon. Most conveniently, the total energy is then rewritten in operator notation

$$\left\langle \psi^{SD}\right|\mathcal{H}_e\left|\psi^{SD}\right\rangle = \sum_j^n \langle\phi_j|\,\mathbf{h}\,|\phi_j\rangle + \frac{1}{2}\sum_{i,j}\left(\langle\phi_j|\,\mathbf{J}_i\,|\phi_j\rangle - \langle\phi_j|\,\mathbf{K}_i\,|\phi_j\rangle\right), \quad (2.32)$$

whereby

$$\mathbf{J}_i\;|\phi_j(\mathbf{r}_2)\rangle = \langle\phi_i(\mathbf{r}_1)|\,\frac{e^2}{|\mathbf{r}_1-\mathbf{r}_2|}\,|\phi_i(\mathbf{r}_1)\rangle\;\;|\phi_j(\mathbf{r}_2)\rangle \quad (2.33)$$

denotes the *Coulomb Operator* and

$$\mathbf{K}_i\;|\phi_j(\mathbf{r}_2)\rangle = \langle\phi_i(\mathbf{r}_1)|\,\frac{e^2}{|\mathbf{r}_1-\mathbf{r}_2|}\,|\phi_j(\mathbf{r}_1)\rangle\;\;|\phi_i(\mathbf{r}_2)\rangle \quad (2.34)$$

the *Exchange Operator*[3]. According to the Rayleigh-Ritz principle (2.14) one minimizes Eq. (2.32) under the constraint of orthogonal and normalized orbitals [55] and thus gains the final set of *Hartree-Fock equations*

$$\underbrace{\left(\mathbf{h}+\sum_j^n(\mathbf{J}_j-\mathbf{K}_j)\right)}_{\mathbf{F}}\phi_i = \sum_j^n \Lambda_{ij}\phi_j, \quad (2.35)$$

where the *Fock Operator* $\mathbf{F}$ and the Lagrange-multipliers $\Lambda_{ij}$ have been introduced. Through a unitary transformation of the $\phi_i$ into so called *canonical orbitals* $\hat{\phi}_i$ Eq. (2.35) can be further simplified to

$$\mathbf{F}\hat{\phi}_i = \Lambda_i\hat{\phi}_i. \quad (2.36)$$

Still, this pseudo-eigenvalue equation is not accessible straightforwardly due to the dependence of the Fock operator $\mathbf{F}$ on all eigenfunctions $\hat{\phi}_j$ via the Coulomb and Exchange operators (Eq. (2.33) and (2.34)). Thus an iterative approach is employed to solve this problem: From a reasonable initial set of orbitals $\hat{\phi}_i^0$ the *Fock Matrix*

$$\mathbf{F}_{ij}^n = \left\langle\hat{\phi}_i^n\right|\mathbf{F}\left|\hat{\phi}_j^n\right\rangle \quad (2.37)$$

is computed and diagonalized. The resulting eigenfunctions $\hat{\phi}_i^1$ are now used as an improved set for the construction of a new Fock matrix. This procedure is repeated until the solution $\hat{\phi}_i^n$ in iteration $n$ does not differ from the one in

[3]The single Molecular Orbitals $\phi_i$ are eigenfunctions to $\mathbf{h}_i$ and $\mathbf{J}_i$, but not to $\mathbf{K}_i$. Thus no separation into single electron problems—as usual in the Hartree ansatz [54]—is possible here.

the previous step to a certain numeric extent. Therefore one also refers to the Hartree-Fock approach as the *Self Consistent Field* (SCF) method.

Finally, the total energy as given in Eq. (2.32) can be expressed as:

$$\varepsilon = \sum_{j}^{n} \Lambda_j - \frac{1}{2} \sum_{i,j} \left( \left\langle \hat{\phi}_j \middle| \mathbf{J}_i \middle| \hat{\phi}_j \right\rangle - \left\langle \hat{\phi}_j \middle| \mathbf{K}_i \middle| \hat{\phi}_j \right\rangle \right) \tag{2.38}$$

$$= \sum_{j}^{n} \lambda_j + \frac{1}{2} \sum_{i,j} \left( \left\langle \hat{\phi}_j \middle| \mathbf{J}_i \middle| \hat{\phi}_j \right\rangle - \left\langle \hat{\phi}_j \middle| \mathbf{K}_i \middle| \hat{\phi}_j \right\rangle \right). \tag{2.39}$$

In contrast to the independent particle model, the total energy is not a simple sum over spinorbital energies—neither over $\lambda_j$ nor over $\Lambda_j$. Thereby the Pauli Principle, i.e. the Exchange Operator $\mathbf{K}_i$ in Eq. (2.39) as its manifestation, leads to a reduction of the total energy, since electrons that share the same spin are forced to avoid each other. Although formally not included in the definition of the *correlation* energy (2.45), the exchange energy is thus in principle also a *statical correlation* effect (see Sec. 2.2.1.4).

#### 2.2.1.3 Basis Set Approximation

The depicted Hartree-Fock equations can indeed be solved by mapping the wave functions on a set of grid points in real space as long as low-dimensional systems are studied. In practice, it is numerically more profitable to expand the *Molecular Orbitals* $\phi_i$ in terms of a semi-orthonormal[4] basis set

$$\phi_i = \sum_{\beta}^{m} c_{\beta i} \chi_\beta, \tag{2.40}$$

whereas the expansion coefficients $c_{\beta i}$ have to obey the usual normalization constraints. By inserting this expansion in Eq. (2.37) and by multiplication with $\langle \chi_\alpha |$ from the left, one obtains the *Roothan-Hall* equation

$$\mathbf{FC} = \mathbf{SC}\varepsilon, \tag{2.41}$$

in which the Fock matrix $F_{\alpha\beta} = \langle \chi_\alpha | \mathbf{F} | \chi_\beta \rangle$ and the overlap matrix $S_{\alpha\beta} = \langle \chi_\alpha | \chi_\beta \rangle$ in the atomic orbital representation have been introduced. Since both the integrals in $\mathbf{F}$ as well as in $\mathbf{S}$ are performed in the basis set's Hilbert space, the **functional form of the orbitals** chosen for the expansion considerably affects the performance of the (numerical or analytical) integration. Moreover, the number of integrals that need to be evaluated is in principle infinite, as the number of terms in the expansion (2.40) principally is. In practice, this sum is truncated and just a small **number of orbitals** $m$ is considered. Still, the performance of the Hartree-Fock method (and all other QC methods) scales with at least a factor of $m^4$ [56]. Thus an easy to integrate basis set, which additionally describes the Molecular Orbitals correctly within the fewest number of expansion terms, has to be found. There is no silver bullet for this formidable

[4] Atomic orbitals—as usually employed in the expansion—belonging to one and the same atom are indeed orthogonal to each other, but those belonging to different atoms can result in non-vanishing overlap matrix elements.

task: Rather a whole zoo of specific basis sets—each of them specially suited for certain problems—is available. Its complete description would go beyond the scope of this thesis, but the most important considerations and their conclusions shall be discussed:

**Type of orbitals:** In the spirit of LCAO (Linear Combination of Atomic Orbitals) and MO (Molecular Orbital) theory *atomic orbitals*—centered at the respective nuclei—are usually employed in Quantum Chemical simulations. The inherent affinity to the solution of the problem suggests a fast *convergence* with respect to the size of the basis set. Furthermore this basis set permits an arbitrary, *a priori* specification of molecular quantum numbers ($\mathbf{S}^2$, $S_z$, $\mathbf{L}^2$,...) for which the minimum energy configuration has to be found: By means of group theory, the electronic wave function can be constrained to the given state by specifically selecting, excluding and constraining certain atomic orbitals in the expansion. Formally this corresponds to a generalization of the Rayleigh-Ritz principle, which originally applies to searches for the absolute ground state in the complete Slater Determinant's Hilbert space. The respective minimum in one of its subspaces is found by employing a *symmetry constrained search* instead. Accordingly, both the molecular ground state as well as specific excited states and spin configurations—one in each symmetry group—can be accessed in this fashion.

**Functional form of the orbitals:** The denomination *atomic orbitals* erroneously suggests that the functional form of the basis set corresponds to the exact analytical solutions of the *Hydrogen Problem*. However, there is no need for such numerically demanding functions, which are not the exact solution of the atomic Hartree-Fock problem either. Instead, simpler functional forms, which resemble the basic features of the hydrogen wave functions but are by far easier to handle when integrated, are constructed on top of the spherical harmonics $Y_{lm}(\theta, \phi)$ to cut the computational costs. In practice, the so called *Slater Type Orbitals* (STOs [57])

$$\chi_{nlm\zeta}(r, \theta, \phi) = n\, Y_{lm}(\theta, \phi)\, r^{n-1}\, e^{-\zeta r} \tag{2.42}$$

are used for high accuracy simulations of atomic and diatomic systems due to their fast convergence with respect to the basis set size. Three and four center integrals cannot be solved analytically when employing STOs, hence *Gaussian Type Orbitals* (GTOs [58])

$$\chi_{nlm\zeta}(r, \theta, \phi) = n\, Y_{lm}(\theta, \phi)\, r^{2n-l-2}\, e^{-\zeta r^2} \tag{2.43}$$

are usually utilized for bigger systems. GTOs can indeed be easily integrated analytically, but they do not reproduce all relevant features of the hydrogen wave functions as good as STOs do. Thus a larger basis set is needed to reach a comparable accuracy.

**Number of atomic orbitals:** The minimal number of atomic orbitals one has to employ is obviously equal to the total number of electrons present, e.g., one $1s$ function for hydrogen or one $1s$, one $2s$ and one set of $2p$ functions ($2p_x, 2p_y, 2p_z$)

for second row elements. Such a *minimal basis set*—corresponding to a zero-order expansion—could only provide correct results, if the chosen atomic orbitals already coincided with the exact solution of the Hartree-Fock problem. In more generic expansions the functions already present[5] in the minimal basis set are included twice (DZ: *Double Zeta* basis set), three times (TZ: *Triple Zeta* basis set) or even more often. Physically these extra functions account for the participation of one atomic orbital in multiple, different bonds (or MOs) as for example in Hydrogen Cyanide:




There, the $2p$ electrons of the carbon contribute both to the $\sigma$ bonding with the hydrogen and to the $\pi$ bonding with the nitrogen. Obviously, the different characters of these two bonds cannot be allowed for within a single $2p$ function set. However, bigger basis sets account for the dependence of the electron distribution on different directions and bond partners. Additionally, *polarization* or *diffuse* functions can be included to incorporate wave function features not present in the original basis set: Once again, the alignment of the $\sigma$ bond in HCN is not reproduced by the spherically symmetric $1s$ orbitals of the hydrogen but deserves an auxiliary $p_z$ polarization term centered there.

**Further basis sets:** When treating the electronic structure of bulks and surfaces, especially of metals, a finite set of atomic orbitals is both numerically expensive and not suitable to describe the long range periodic delocalization of valence electrons. Indeed, the Bloch theorem [59] predicts a wave function of the form

$$\Psi(\mathbf{r}) = \sum_{\mathbf{k}} u_{\mathbf{k}}(\mathbf{r}) e^{i\mathbf{kr}}, \tag{2.44}$$

whereby the coefficients $u_{\mathbf{k}}(\mathbf{r})$ exhibit the same periodicity of the bulk. Hence for such systems, whose infinite extent is achieved by means of periodic boundary conditions, an expansion in terms of plane waves is numerically favorable (also see Sec. 3.3.2).

#### 2.2.1.4 Deficiencies of the Hartree-Fock method

The Hartree-Fock method is pretty efficient and successful in describing molecules in their equilibrium state. For a large enough basis set it indeed requires just one simple assumption: The wave function has to be representable as a **single** Slater Determinant. Accordingly, just a reasonable subspace of the complete $n$-electron Hilbert space is inspected. The consequences of this approximation are not self-evident. One prominent example is the failure of Hartree-Fock in correctly describing chemical reactions, especially dissociations. In the limit of an infinite separation, two reaction partners behave independently, each with its own Slater Determinant type electronic structure. Thus the wave function

[5] As a matter of fact, the additional basis functions are **not** exactly identical to the already included ones: They indeed exhibit the same atomic orbital character but differ in their exponent $\zeta$, which describes their diffuseness (see Eq. (2.42) and (2.43)).

of a system that undergoes such a dissociation progressively resembles two individual Slater Determinants, the more the respective chemical bond is stretched. Hartree-Fock—being limited to a single Determinant by definition—cannot take account[6] of such effects. Thus the transition states and energies, which usually rely on contributions both from the product and the educt state, are typically overestimated [60, 61].

As seen in Sec. 2.2.1.2, the inclusion of the Pauli Principle, which forces the electrons that share the same spin to avoid each other, leads to a reduction of the total energy in the Hartree-Fock method (*exchange energy*). Analogously, spin or geometric symmetries can lead to similar additional constraints under certain circumstances (see Sec. 3.1) and thus to a lowering of the total energy as well. These effects, which are not included in the Hartree-Fock formalism, since they deserve a description in terms of multiple Slater Determinants, are referred to as *statical correlation*. In contrast thereto, also *dynamical correlation*, which is also missing in Hartree-Fock, exists: In a time dependent formalism also electrons with opposite spin can lower the overall electron-electron repulsion by dynamically avoiding each other in a correlated motion, whereas in Hartree-Fock theory each electron just feels the time averaged field the whole electronic distribution generates. This *mean field approximation* is **not** a consequence of the stationarity of the approach [62] but an outcome of the wave function being forced to consist of $n$ totally (integer) occupied MOs [63]. As a matter of fact, both the statical and the dynamical correlation can be obtained in stationary calculations as well by allowing a fractional, non-integer occupation of excited Slater Determinants, as can be seen in the next section. The therein discussed exact solution of the many-body Schrödinger equation is formally often used to define the *total correlation energy*

$$E_{\text{corr}} = E_{\text{exact}} - E_{\text{HF}} \tag{2.45}$$

as the energy difference between the exact solution and the Hartree-Fock solution of one and the same system. The exchange energy, which is in principle the most basic statical correlation effect, is not included in this definition of correlation.

#### 2.2.1.5 The Exact Solution: Full Configuration Interaction

The discussed flaws of Hartree-Fock theory can be tackled by employing multiple Slater Determinants, which are referred to as *configurations* $\Psi_i$. They are constructed by "exciting" electrons from occupied into unoccupied MOs of a *reference* Hartree-Fock wave function $\Psi_0$ (see Fig. 2.2). The total trial wave function in such *Configuration Interaction* (CI) approaches

$$\Psi = a_0\Psi_0 + \sum_{i=1} a_i\Psi_i \tag{2.46}$$

is accordingly written as a sum over all possible configurations, whereby fractional occupation coefficients $a_i$, which are subject to the usual normalization constraint, are introduced. Analogously to the derivation of the Hartree-Fock

[6] Still, the individual fragments can be addressed with Hartree-Fock in independent calculations, e.g., to determine the binding energy.

equation (2.35), a variational approach for this kind of trial wave function leads to the *CI secular equation* [55]:

$$\begin{pmatrix} H_{00}-E & H_{01} & \cdots & H_{0k} \\ H_{10} & H_{11}-E & \cdots & \vdots \\ \vdots & \vdots & \ddots & \vdots \\ H_{k0} & \cdots & \cdots & H_{kk}-E \end{pmatrix} \cdot \begin{pmatrix} a_0 \\ a_1 \\ \vdots \\ a_k \end{pmatrix} = \begin{pmatrix} 0 \\ 0 \\ \vdots \\ 0 \end{pmatrix}. \tag{2.47}$$

Thereby the entries $H_{ij} = \langle \Psi_i | \mathbf{H} | \Psi_j \rangle$ in the *CI matrix* are evaluated as done in the Hartree-Fock method. In the limit of a complete basis set this equation yields the **exact** solution [64]. Unfortunately, this approach is numerically too expensive for almost all systems of chemical interest: Although the majority of the CI matrix elements vanish according to *Slater's Rules* (or *Slater-Condon* rules) [53, 65], the number of possible excited Slater Determinants $\Psi_i$ in the expansion (2.46) is prohibitively large. For a system with $m$ basis functions (2.40) and $n$ electrons, there exist

$$k = \binom{m}{n} - 1 = \frac{m!}{n! \cdot (m-n)!} - 1 \tag{2.48}$$

possible configurations. Due to this factorial dependence on the number of basis functions it is utopistic to include all possible Determinants (*Full CI*) in an approximately complete basis set—even for small systems. In practice the phase space is thus generally restricted to the most important configurations (*truncated CI*), which are originated by single(S), double(D) or triple(T) excitations of the reference state (see. Fig. 2.2).

#### 2.2.1.6 Approximative High Level Quantum Chemistry Methods

Though in principle exact, a Full CI treatment is generally not feasible except for pretty small systems. Truncated CI however suffers some serious drawbacks, as missing size consistency and extensivity [55], resulting in less and less dynamical correlation recovered as the system grows larger. Thus several approximative methods, as *Many-Body Perturbation Theory* in its various fashions [66], are employed in practice to obtain the lion's share of correlation within considerably less numerical effort. However, CI-type methods still play an important role to describe statical correlation and thus to gain a reference wave function featuring the correct total spin and symmetry. This wave function can then serve as a starting point for further perturbative calculations instead of a genuine Hartree-Fock reference. In *Complete Active Space SCF* (CASSCF) techniques, not the number of excitations as in truncated CI but the number of involved MOs is restricted by defining an *active space* (see Fig. 2.2), wherein a Full CI is performed. Thereby, the basis set expansion coefficients $c_{\beta i}$ of the reference state and the CI coefficients $a_i$ are optimized simultaneously[7]. However, the active space—usually consisting of the lowest unoccupied and highest occupied MOs—has to be chosen by hand, which obviously requires a profound *a priori* understanding of the system. If given, decent results can be achieved with comparably small numerical effort (see Sec 3). Furthermore, the CASSCF simulations can serve

[7] Generally, algorithms optimizing both the basis set expansion coefficients $c_{\beta i}$ as well as the CI coefficients $a_i$ are referred to as *Multi-Configuration SCF* (MCSCF) methods.

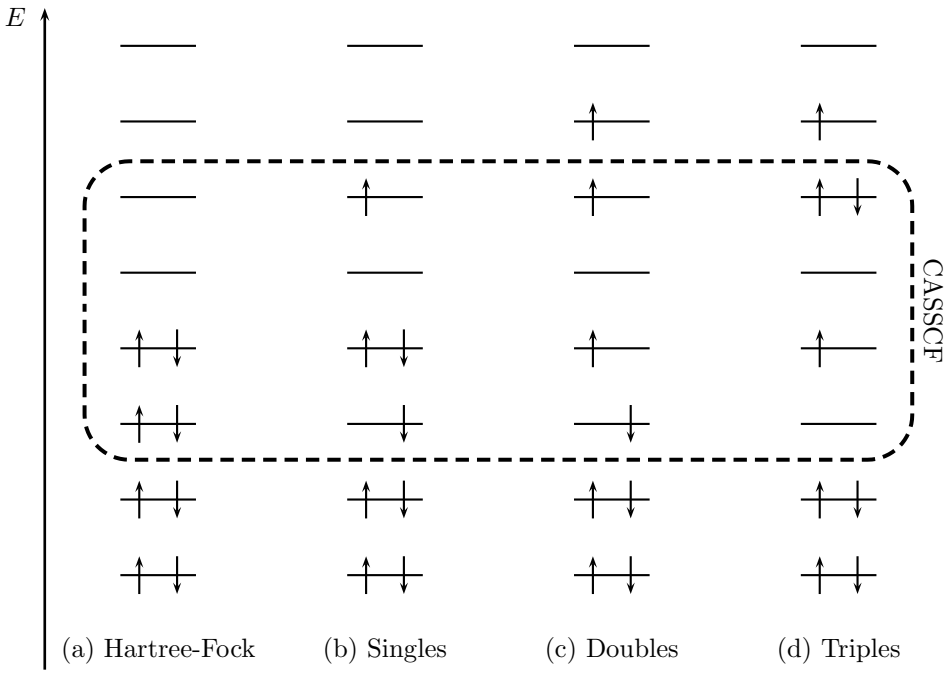


Figure 2.2: Classification of Slater Determinants employed in truncated CI methods: With respect to the reference configuration (a), wherein all the lowest energy states are populated, new configurations are generated by respectively exciting one ("Singles"), two ("Doubles") or three ("Triples") electrons to unoccupied MOs. The dashed box exemplifies a possible *active space* for CASSCF calculations as discussed in Sec. 2.2.1.6.

as a refined starting point for the extension of the truncated CI approach. In such *Multireference CI* (MRCI) calculations the single (double,...) excitations out of **all** the Slater Determinants included in the CASSCF wave function are considered. Such an approach—when computationally feasible—is able to describe a system exactly to a large extent, as the comparison to Full CI [67] and *coupled cluster* calculations [68] shows. In particular, this technique is required when chemical reactions, i.e. complete Potential Energy Surfaces, are studied. In the case of bond breaking, many excited states can collapse into the ground state in the dissociation limit. Accordingly, excitations out of these excited states can become as relevant as excitations out of the ground state, whenever chemical bonds are distorted or stretched. Hence, restricting the description to excitations out of one of these Slater Determinants significantly influences bond breaking, the related barriers and the electron affinities [69, 70, 71].

### 2.2.2 Density Functional Theory

*Density Functional Theory* (DFT) is an alternative *ab initio* electronic structure theory, which—in contrast to the hitherto discussed approaches—is not based on

the $n$-electron wave function $\Psi(\mathbf{r}_1, \cdots, \mathbf{r}_n)$, but on the overall electron density

$$\rho(\mathbf{r}) = \rho(\mathbf{r}_1)|_{\mathbf{r}_1=\mathbf{r}} = n \cdot \int \Psi^*(\mathbf{r}_1, \cdots, \mathbf{r}_n)\Psi(\mathbf{r}_1, \cdots, \mathbf{r}_n)\, d\mathbf{r}_2 \cdots d\mathbf{r}_n, \qquad (2.49)$$

whereby the integration occurs over all except one arbitrary electron coordinate $\mathbf{r}_1$. Although this degree of freedom can be freely chosen, the given definition is still unique due to the total antisymmetry of wave functions with respect to the particle exchange operator.

For a single Slater-Determinant $\Psi^{SD}$ the density is given by

$$\rho(\mathbf{r}) = n \cdot \frac{1}{n}(\phi_1^*(\mathbf{r}_1)\phi_1(\mathbf{r}_1) + \cdots + \phi_n^*(\mathbf{r}_1)\phi_n(\mathbf{r}_1))\Big|_{\mathbf{r}_1=\mathbf{r}} = \sum_{i=1}^{n} \phi_i^*(\mathbf{r})\phi_i(\mathbf{r}), \quad (2.50)$$

i.e. just the sum over the $n$ occupied Molecular Orbitals $\phi_i$. Conversely, any density of this shape is the result of a single Determinant wave function [72]. More general densities that are based on more than one Determinant can be formulated by extending this sum—in a CI like fashion—to an infinite number of terms

$$\rho(\mathbf{r}) = \sum_i d_i \phi_i^*(\mathbf{r})\phi_i(\mathbf{r}), \qquad (2.51)$$

whereby—analogously to Eq. (2.46)—fractional occupation numbers $d_i$ are employed to fulfill the normalization constraint

$$n = \int \rho(\mathbf{r})\, d\mathbf{r}. \qquad (2.52)$$

#### 2.2.2.1 The Hohenberg-Kohn Theorems

Already in the early days of quantum mechanics there have been attempts, for example in the Thomas-Fermi theory [73, 74], to express the quantum mechanical many-body problem, i.e. the Schrödinger equation or the Rayleigh-Ritz principle, in terms of the electron density. Such an approach can significantly reduce the task's complexity: The number of considered degrees of freedom is drastically lowered from $3n$ for a wave function $\Psi(\mathbf{r}_1, \cdots, \mathbf{r}_n)$ to 3 for the density $\rho(\mathbf{r})$ ansatz—independently from the actual number of electrons $n$. Not until decades later, P. Hohenberg and W. Kohn were able to prove the existence of such an unique mapping in between the ground-state density of a gas of interacting electrons and the applied external potential [75]. The resulting unambiguous *functional* relation

$$E[\rho(\mathbf{r})] = T_{\mathbf{r}}[\rho(\mathbf{r})] + V_{\mathbf{rr}}[\rho(\mathbf{r})] + V_{\mathbf{rR}}[\rho(\mathbf{r})] \qquad (2.53)$$

in between the total energy $E$ and the electron density $\rho(\mathbf{r})$ is usually referred to as the *First Hohenberg-Kohn Theorem*. Furthermore, the properties of this functional under variation are addressed in analogy to the Rayleigh-Ritz principle (2.14) in the *Second Hohenberg-Kohn Theorem*: Within the correct normalization constraint (2.52) the total energy $E[\rho(\mathbf{r})]$ indeed exhibits an absolute minimum for the correct ground-state density. Hence minimization techniques, as employed in the Quantum Chemistry methods to determine the correct wave

function, are in principle also applicable to the total energy functional for finding the correct density. However, the exact analytical form of the total energy functional is hitherto unknown. In spite of that the Hohenberg-Kohn theorems can be used to derive one-particle equations—the famous *Kohn-Sham equations*—that in principle yield the exact solution as discussed below. In their derivation we will not follow the original formalism that mainly focuses on the electron density [75, 76]. Rather, the Molecular Orbital based framework already employed in the discussion of the Quantum Chemical methods serves as a starting point in this work[8]. By this means the similarities and differences between DFT and Quantum Chemistry algorithms can be outlined most efficiently. Thus, in a first step, we will try to express the Rayleigh-Ritz minimization principle (2.14), i.e. the therein occurring expectation value of the electronic Hamiltonian (2.13), as functional of the electron density. Its nuclear attraction term, which is referred to as *external potential* $v_{ext}(\mathbf{r})$ in the original Hohenberg-Kohn publication, can indeed be reformulated this way by replacing the $3n$-dimensional integral over the electronic coordinates with an integration over the three-dimensional electron density (2.49):

$$\begin{aligned}
\langle\Psi|\, V_{\mathbf{rR}}\,|\Psi\rangle &= -\int \Psi^*(\mathbf{r}_1,\cdots,\mathbf{r}_n)\sum_{i,M}\frac{Z_M e^2}{|\mathbf{r}_i-\mathbf{R}_M|}\,\Psi(\mathbf{r}_1,\cdots,\mathbf{r}_n)\,d\mathbf{r}_1\cdots d\mathbf{r}_n \\
&\overset{\mathbf{r}_i=\mathbf{r}}{=} -\int\sum_{M}\frac{Z_M e^2}{|\mathbf{r}-\mathbf{R}_M|}\cdot\rho(\mathbf{r})\,d\mathbf{r} \\
&= -\int v_{ext}(\mathbf{r})\cdot\rho(\mathbf{r})\,d\mathbf{r} = V_{\mathbf{rR}}[\rho(\mathbf{r})]. \qquad (2.54)
\end{aligned}$$

However, first problems already arise in the analogous derivation of the expectation value for the electronic repulsion:

$$\begin{aligned}
\langle\Psi|\, V_{\mathbf{rr}}\,|\Psi\rangle = e^2\int\frac{\rho(\mathbf{r})\cdot\rho(\mathbf{r}')}{|\mathbf{r}-\mathbf{r}'|}\,d\mathbf{r}d\mathbf{r}' + NC[\rho(\mathbf{r})] = \\
= J[\rho(\mathbf{r})] + NC[\rho(\mathbf{r})] = V_{\mathbf{rr}}[\rho(\mathbf{r})]\,. \qquad (2.55)
\end{aligned}$$

Beside the "classical" electrostatic repulsion $J[\rho(\mathbf{r})]$, which is indeed expressible as density functional, also a "non-classical" term $NC[\rho(\mathbf{r})]$ appears. It contains the exchange-energy $K$, which has been already discussed for single Slater-Determinants in Sec. 2.2.1.2, as well as further two-electron integrals which arise due to the multiple Determinant character of the correlated wave function $\Psi$. Accordingly, also the kinetic energy

$$T_{\mathbf{r}} = -\frac{\hbar^2}{2m}\sum_i d_i\,\langle\phi_i|\,\nabla_i^2\,|\phi_i\rangle \qquad (2.56)$$

comprehends an **infinite** number of terms and is thus also not easily expressible as a density functional. Historically, huge effort has been put into finding the exact functionals or at least good approximations thereto already before the development of the Hohenberg-Kohn theorems as, e.g., first in Thomas-Fermi theory [73, 74] and then with the Slater-Dirac functional for exchange [77, 78,

[8] Such an approach is often found in textbooks that concentrate on the simulation of molecular properties as [55, 72] for instance.

54] or with the Weizäcker functional for the kinetic energy [79]. However, all direct approaches—commonly known as *orbital-free DFT*—that aim at a direct minimization of Eq. (2.53) have not yielded any satisfactory results until very recently [80, 81], primarily due to the lack of an appropriate kinetic energy functional. This problem is circumvented in an elegant fashion in the Kohn-Sham equations, as discussed below.

#### 2.2.2.2 The Kohn-Sham Equations

The derivation of the well celebrated *Kohn-Sham* equations [76], which yield the correct solution to the interacting many-body problem, is based upon the Hohenberg-Kohn theorems and the respective total energy functional (2.53), which was formally introduced in the previous section but whose exact terms are still unknown. At the price of reintroducing orbitals and thus making the problem dependent on the number of electrons $n$ once again, a set of numerically solvable independent single-particles equations can be found. In a first step towards their formulation the kinetic energy (2.56) is decomposed into the kinetic energy

$$T_{\mathbf{r}}^s = -\frac{\hbar^2}{2m}\sum_{i=1}^{n}\left\langle \hat{\phi}_i \middle| \nabla_i^2 \middle| \hat{\phi}_i \right\rangle \tag{2.57}$$

that pertains to a system of non-interacting electrons with the exact same density[9]

$$\hat{\rho}(\mathbf{r}) = \sum_{i=1}^{n}\langle\hat{\phi}_i|\hat{\phi}_i\rangle \stackrel{!}{=} \rho(\mathbf{r}) \tag{2.58}$$

and a not yet specified remaining part $C[\rho(\mathbf{r})]$:

$$T_{\mathbf{r}} = T_{\mathbf{r}}^s + C[\rho(\mathbf{r})] = -\frac{\hbar^2}{2m}\sum_{i=1}^{n}\left\langle \hat{\phi}_i \middle| \nabla_i^2 \middle| \hat{\phi}_i \right\rangle + C[\rho(\mathbf{r})]. \tag{2.59}$$

The terms in the total energy functional can now be rearranged

$$E[\rho(\mathbf{r})] = T_{\mathbf{r}}^s + V_{\mathbf{rR}}[\rho(\mathbf{r})] + J[\rho(\mathbf{r})] + XC[\rho(\mathbf{r})], \tag{2.60}$$

whereby both the previously undetermined parts $NC[\rho(\mathbf{r})]$ and $C[\rho(\mathbf{r})]$ have been summarized into one *exchange-correlation* functional $XC[\rho(\mathbf{r})]$. Analogously to the definition of the correlation energy (2.45), this is a formally exact definition of the *exchange-correlation* energy as the difference between exact (but unknown) and known functionals:

$$XC[\rho(\mathbf{r})] = T_{\mathbf{r}}[\rho(\mathbf{r})] - T_{\mathbf{r}}^s[\rho(\mathbf{r})] + V_{\mathbf{rr}}[\rho(\mathbf{r})] - J[\rho(\mathbf{r})]. \tag{2.61}$$

Its functional derivative defines the as well unknown *exchange-correlation potential*

$$v_{xc}(\mathbf{r}) = \frac{\delta}{\delta\rho(\mathbf{r})}\left(T_{\mathbf{r}}[\rho(\mathbf{r})] - T_{\mathbf{r}}^s[\rho(\mathbf{r})] + V_{\mathbf{rr}}[\rho(\mathbf{r})] - J[\rho(\mathbf{r})]\right). \tag{2.62}$$

[9] Densities that can be decomposed that way are called *non-interacting v-representable*. See the end of this section for a further analysis of this property.

A variational minimization, which also fulfills the density's normalization by employment of a Lagrangian multiplier $\mu$, results in the *Euler-Lagrange* equation

$$\begin{aligned}\mu = \frac{\delta E[\rho(\mathbf{r})]}{\delta\rho(\mathbf{r})} &= \frac{\delta T^s_{\mathbf{r}}[\rho(\mathbf{r})]}{\delta\rho(\mathbf{r})} + \frac{\delta V_{\mathbf{rR}}[\rho(\mathbf{r})]}{\delta\rho(\mathbf{r})} + \frac{\delta J[\rho(\mathbf{r})]}{\delta\rho(\mathbf{r})} + \frac{\delta XC[\rho(\mathbf{r})]}{\delta\rho(\mathbf{r})} \\ &= \frac{\delta T^s_{\mathbf{r}}[\rho(\mathbf{r})]}{\delta\rho(\mathbf{r})} + v_{ext}(\mathbf{r}) + \int \frac{\rho(\mathbf{r}')}{|\mathbf{r}-\mathbf{r}'|} d\mathbf{r}' + v_{xc}(\mathbf{r}) \\ &= \frac{\delta T^s_{\mathbf{r}}[\rho(\mathbf{r})]}{\delta\rho(\mathbf{r})} + v_{eff}(\mathbf{r}), \end{aligned} \tag{2.63}$$

whereby the effective potential $v_{eff}(\mathbf{r})$ has been introduced. Remarkably, the same approach to the *independent particle problem*[10]

$$\tilde{E}[\rho(\mathbf{r})] = T^s_{\mathbf{r}} + V_{\mathbf{rR}}[\rho(\mathbf{r})] \tag{2.64}$$

leads to an Euler-Lagrange equation of the same structure as (2.63):

$$\begin{aligned}\mu = \frac{\delta \tilde{E}[\rho(\mathbf{r})]}{\delta\rho(\mathbf{r})} &= \frac{\delta T^s_{\mathbf{r}}[\rho(\mathbf{r})]}{\delta\rho(\mathbf{r})} + \frac{\delta V_{\mathbf{rR}}[\rho(\mathbf{r})]}{\delta\rho(\mathbf{r})} \\ &= \frac{\delta T^s_{\mathbf{r}}[\rho(\mathbf{r})]}{\delta\rho(\mathbf{r})} + v_{ext}(\mathbf{r}). \end{aligned} \tag{2.65}$$

This correspondence allows to map—generally and in principle exactly—the problem of $n$ interacting particles in an external field $v_{ext}(\mathbf{r})$ onto the problem of $n$ non-interacting particles in a different external field $v_{eff}(\mathbf{r})$. As delineated in Sec. 2.2.1.1, the latter is by far simpler to handle, since its exact solution is a single Slater Determinant

$$\frac{1}{\sqrt{n!}} \begin{vmatrix} \phi^{KS}_1(\mathbf{r}_1) & \phi^{KS}_1(\mathbf{r}_2) & \cdots & \phi^{KS}_1(\mathbf{r}_n) \\ \phi^{KS}_2(\mathbf{r}_1) & \phi^{KS}_2(\mathbf{r}_2) & \cdots & \phi^{KS}_2(\mathbf{r}_n) \\ \vdots & \vdots & \ddots & \vdots \\ \phi^{KS}_n(\mathbf{r}_1) & \phi^{KS}_n(\mathbf{r}_2) & \cdots & \phi^{KS}_n(\mathbf{r}_n) \end{vmatrix} \tag{2.66}$$

of *Kohn-Sham orbitals* $\phi^{KS}_i$, which can be derived from the one-particle Hamiltonian:

$$\tilde{h}_{ks}\phi^{KS} = \left(-\frac{\hbar^2}{2m}\nabla^2 + v_{eff}(\mathbf{r})\right)\phi^{KS}. \tag{2.67}$$

Since the effective potential appearing therein

$$v_{eff}(\mathbf{r}) = v_{ext}(\mathbf{r}) + \int \frac{\rho(\mathbf{r}')}{|\mathbf{r}-\mathbf{r}'|} d\mathbf{r}' + v_{xc}(\mathbf{r}) \tag{2.68}$$

still depends on the density, the problem has to be solved self-consistently as done in Hartree-Fock Theory before (see Sec. 2.2.1.2). Likewise, the Kohn-Sham orbitals are expanded in a suitable basis set (see Sec. 2.2.1.3)

$$\phi^{KS}_i = \sum_{\beta}^{m} c_{\beta i}\chi_\beta$$

[10] Obviously, neither exchange nor correlation terms appear if the electron-electron repulsion is neglected. Accordingly, also the kinetic energy is described exactly by the $n$ terms of $T^s_{\mathbf{r}}$ (see Eq. (2.59)) in this case.

with the resulting density

$$\rho(\mathbf{r}) = \sum_{\beta}^{m} \sum_{i}^{n} c_{\beta i}^{*} c_{\beta i} \chi_{\beta}^{*} \chi_{\beta}.$$

Thereby, the occupation numbers $n_\beta = \sum_i^n c_{\beta i}^* c_{\beta i}$ in the corresponding orbitals $\chi_\beta$ are adjusted in each iteration step until convergence is reached.

Although rather simple in its structure, DFT also provides plenty of opportunities of misinterpretation:

**Total energy of the system:** Although the correct density is calculated by solving the corresponding independent particle problem, the total energy of the system is **not** just the sum over the Kohn-Sham orbital energies $\varepsilon_i$ like for any one-particle formalism (compare Eq. (2.21) and (2.53)). Indeed, the correct total energy is:

$$\begin{aligned} E &= T_{\mathbf{r}}^{s} + V_{\mathbf{rR}}[\rho(\mathbf{r})] + J[\rho(\mathbf{r})] + XC[\rho(\mathbf{r})] \\ &= \sum_{i}^{n} \varepsilon_i - \frac{1}{2} \int \frac{\rho(\mathbf{r})\rho(\mathbf{r}')}{|\mathbf{r} - \mathbf{r}'|} d\mathbf{r} d\mathbf{r}' + XC[\rho(\mathbf{r})] - \int v_{xc}(\mathbf{r})\rho(\mathbf{r}) d\mathbf{r}. \end{aligned} \tag{2.69}$$

**Nature of the Kohn-Sham orbitals:** The probably most fascinating feature of DFT is the apparently lossless mapping in between the real wave function (2.51), consisting of an infinite number of MOs, and the $n$ Kohn-Sham orbitals. Hence, in a first step, one is inclined to overestimate their significance: As a matter of fact they are just a set of orthonormal functions able to reproduce the correct density and thus have in principle no physical reality of their own. In spite of that, physical observables that depend on the Molecular Orbitals and on their eigenvalues, e.g., the ionization energy, can be derived from the Kohn-Sham orbitals under certain conditions [82] as well.

**Universality of the functional:** The proof of the Hohenberg-Kohn Theorems as given in [75] relies on the fact that the densities are *v-representable*, i.e. that they are associated with the ground state wave function of a Hamiltonian

$$H_{vr} = T_{\mathbf{r}} + V_{\mathbf{rr}} + \sum_{i}^{n} v(\mathbf{r}_i), \tag{2.70}$$

whereby $v(\mathbf{r})$ has not even to be coulombic. However, apart from some special cases [83], the conditions for a given density to be v-representable are still unknown. Indeed, many "reasonable" densities have been proved to be not v-representable, e.g., the density of certain multiple degenerate ground states [84, 85]. Furthermore, the second Hohenberg-Kohn Theorem ceases to apply to such non v-representable trial densities as well. Fortunately, both theorems can be reformulated so that only a weaker prerequisite needs to be fulfilled, i.e. the density has to be derived from some antisymmetric wave function. This *n-representability* condition, which allows for the description of any reasonable density, is satisfied in practice by constraining [84] the variational search to

antisymmetric wave functions $\Psi$:

$$\min_{\rho(\mathbf{r})} E[\rho(\mathbf{r})] \longrightarrow \min_{\Psi \to \rho(\mathbf{r})} E[\Psi]. \tag{2.71}$$

A similar line of reasoning is followed in the mathematical proof of the Kohn-Sham equations: The decomposition of the kinetic energy in Eq. (2.59) requires the density to be *non-interacting v-representable*, thus to be the ground state of

$$H_{nivr} = T_{\mathbf{r}} + \sum_{i}^{n} v(\mathbf{r}_i). \tag{2.72}$$

Analogously, an implementation of this restriction is achieved by constraining the search to antisymmetric wave functions [84, 85, 86]. This results in a slight but remarkable practical consequence: While the combination of the $n$ Kohn-Sham orbitals with the lowest eigenvalues $\varepsilon_i$ with respect to $\tilde{h}_{ks}$ usually yields the lowest total energy (2.69), this does not apply to densities that are not non-interacting v-representable. In such a case a wave function corresponding to an excited state of $\tilde{h}_{ks}$ may result in the lowest total energy [87, 72].

To draw a bottom line: Density Functional Theory has some remarkable properties, which are best outlined with respect to the wave function based methods discussed in Sec. 2.2.1: On the one hand, DFT is in principle exact as a Full CI approach. On the other hand, it dramatically reduces the numerical effort, even with respect to the—approximative by definition—Hartree-Fock method, since no nonlocal potential occurs in $v_{eff}(\mathbf{r})$. However, these statements just hold for the exact exchange-correlation potential $v_{xc}(\mathbf{r})$ which is hitherto unknown. Various approximations thereto and their influence on the quality and on the numerical costs of DFT calculations shall be shortly discussed in the next section.

#### 2.2.2.3 Exchange-Correlation Functionals

The search for the exact exchange-correlation functional is one of the most ambitious and complex topics of scientific research in modern solid state theory and theoretical chemistry. Up to the present, a variety of different approximate expressions for both the exchange and the correlation part have been proposed. An exhaustive discussion of their individual properties would go far beyond the scope of this work. Nevertheless, a short description of the most important functionals and functional classes employed herein is given.

**Local Density Approximation (LDA):** The LDA functional has its roots in the Thomas-Fermi theory [73, 74] and is thus derived under the assumption of a homogenous electron gas. While the exchange interaction can be formulated analytically within this model (*Dirac exchange-energy functional* [77, 78]), the correlation terms have been calculated by means of *Quantum Monte Carlo* techniques [88]. Although the LDA is based on this rather crude assumption, it works remarkably well in many solid state systems in practice, presumably due to positive error cancellation. However, binding is usually overestimated, resulting in too small bond lengths and lattice constants [89].

**General Gradient Approximation (GGA):** In the spirit of perturbation theory, functionals that also depend on the gradient of the density have been introduced to overcome the often unsatisfactory outcomes of LDA. A straightforward Taylor-expansion like approach is foredoomed, since—in contrast to the LDA—it violates some of the basic properties the exact exchange-correlation functional has to fulfill [90]. Hence more complex functionals, which depend on the gradient of the density, but also satisfy various sum and scaling rules and reproduce the correct asymptotic behavior as well, have been introduced under the umbrella term *general gradient approximation* (GGA) functionals. The PW91 functional proposed by Perdew and Wang [91] and the PBE functional formulated by Perdew, Bunke and Ernzerhof [92] are the most common GGA functionals nowadays in solid state physics and surface science, both leading to similar results with an accuracy generally sufficient for the description of most chemical reactions. In this thesis an additional functional, the *Revised PBE* (RPBE) functional [93], which differs from the PBE functional only in the functional form of the local exchange enhancement (see Sec. 3.3.2), is also widely used (see Sec. 3.3 for details).

**Further functionals:** Although the GGA functionals work satisfactorily well in general, they can still fail under certain mostly unforeseeable circumstances. Hence their systematic stepwise improvement as first delineated by Perdew [94, 95] is highly desirable. The proposed "Jacob's ladder" towards exactness basically extends the expansion concept already underlying the GGAs' development. Accordingly, its first two rungs are the already discussed LDA and GGA functionals. The next one is the consideration of supplementary dependencies, e.g., on the Laplacians of the density in a first step, to incorporate nonlocal effects in the so called *meta-GGAs*. The inclusion of known key properties of the exact-exchange functional in their construction has not yielded completely satisfactory solutions to this formidable task so far. As an alternative approach the fitting of parameters to Quantum Chemical calculations generated the so called *semi-empirical meta-GGAs*. They have excellent modeling capabilities when applied to systems similar to the ones they have been fitted to, but may also drastically fail otherwise. Hence the average gain in accuracy for both types of meta-GGAs is rather small when compared to GGA results [96]. A concurring approach to the functional's improvement ignores the exchange-correlation dependence on higher order derivatives of the density and directly tackles the next rung in the ladder: the inclusion of *exact-exchange* [97]. As the *adiabatic connection fluctuation-dissipation theorem* [98] reveals, the correct functional should incorporate a fraction of the LDA exchange as well as a fraction of the Hartree-Fock exchange (2.31). In so called *hybrid functionals* variable parts of both of them and also portions of other exchange-correlation functionals are included. Again, these relative fractions are either determined by fitting to a certain set of systems (e.g. B3LYP [99] to Pople's G1/G2 [100, 101] test sets) or non-empirically (e.g. PBE0 [102]). These functionals are still topic of scientific debate: Whereas they are widely and successfully used to address molecules, there exist only few systematic studies with respect to extended systems due to the functionals' huge numerical demands in periodic or quasi-periodic codes. However, the average gain in accuracy does not legitimate the increased computational costs in most cases. Especially the semi-empirical hybrid functionals

seem to lack the ability to reproduce effects they have not been fitted to [103], as it is the case for the semi-empirical meta-GGAs discussed above. Eventually, the complete evaluation of the adiabatic connection fluctuation-dissipation theorem includes both the exact exchange and the nonlocal correlation effects. First promising but prohibitively expensive attempts [104] show that by this means even the Van der Waals interaction governing noble gas solids can be reproduced from first principles.

#### 2.2.2.4 Deficiencies of DFT

Besides the flaws of approximated functionals, DFT also exhibits certain methodological shortcomings. Ironically enough, these limitations are inherently related to this theory's greatest asset: the mapping of the exact wave function via its density onto the $n$ Kohn-Sham orbitals. Chemical properties not directly derivable from the electron density, which thus require the knowledge of the complete wave function, cannot be calculated on the basis of the Kohn-Sham orbitals, since their physical significance is strongly limited (see Sec. 2.2.2.2). Accordingly, the strategies employed in wave function based methods to access excited states pertaining to a different symmetry state (see Sec. 2.2.1.3) cannot be applied one-to-one in DFT calculations either. Various techniques [105, 106, 107, 108, 109] to circumvent this restriction have been proposed for atoms and molecules. However, they cannot be applied straightforwardly to calculate the band gaps in the bulk for instance due to the strong many-body-character of the involved excitations. Such quasi-particle energies can be derived by utilizing Green's function methods in various approximative species (*GW*, *GW0* or *Bethe-Salpeter* approximation [110, 111, 112]) on top of the DFT calculations. These approaches also benefit from improvements on the functional, as e.g., the inclusion of exact-exchange [113, 114]. Finally, the evolution of an electronic state can be described by introducing time dependence as done in *time-dependent DFT* (TD-DFT) [115]. In addition to its obvious application in dynamic processes [116], this technique also accounts for excitation effects [117]. Unfortunately, all these approaches also increase the computational costs significantly. Thus their usefulness in dynamical surface science problems, which already hit the limits of what is feasible anyway, is still limited.

## 2.3 Interpolation Methods

After determining the total energy of a certain nuclear geometry with an electronic structure method described in Sec. 2.2, the forces acting on the nuclei have still to be computed and to be handed over to the algorithm controlling the nuclear dynamics. Thereto no approximate three-point estimation for determining differences, which would require additional electronic structure calculations, is needed, since the forces can be evaluated directly and exactly from the electronic wave function by means of the *Hellmann-Feynman theorem* [118] for a basis that does not depend on the atomic positions [119]. However, a complete QC or DFT calculation is required in each step of the nuclear dynamics: For the system of interest in this work such a *direct method* is prohibitively expen-

sive and thus mostly inapplicable (see Sec. 4.4.6.1). This basically practical problem can be circumvented by introducing approximative Potential Energy Surfaces (PES) as proposed by, e.g., Groß and Scheffler [30]. For nuclear geometries in the range of interest a whole series of electronic structure calculations is performed and their outcome $v^i_{eff}(\mathbf{R})$ (as defined in Eq. (2.8)) interpolated. Thereby only the most relevant degrees of freedom, i.e. the six coordinates of the oxygen molecule in this special case, are varied, whereas the positions of the aluminum atoms are kept fixed (*Frozen Substrate Approximation*). The necessary number of electronic minimizations thus just depends on the number of degrees of freedom considered and on the range they span but not on the number of nuclear trajectories simulated in the dynamic's part. Whenever a large amount of them is needed, the numerical effort can be significantly lowered by this means. However, the error introduced by the limitation on certain degrees of freedom cannot be estimated in general but strongly depends on the system and on the dynamical process of interest. Fortunately, the accuracy of the method can be systematically probed by comparison with direct methods and thus also improved by stepwise considering additional degrees of freedom. Supplementary electronic structure calculations also enhance the quality of the high-dimensional interpolation, which is indeed a formidable problem:

(*a*) It is possible to rely on an analytical, physically motivated model and fit its parameters to the *ab initio* data. Thereby many properties of the system, e.g. the correct long-range behavior, are reproduced automatically since they are inherently included in the ansatz. However, this is also the main drawback of this approach: Effects not already considered in the model are likely to be ignored.

(*b*) The physical notion of the system's properties can also be ignored: Then a pure numerical technique, e.g. splines [120], is employed to fit the *ab initio* data. Indeed, such approaches allow a general description of Potential Energy Surfaces with the possibility to methodically refine the numerical error. The price to pay in return is high: The huge amount of free parameters that have to be determined leads to a drastic increase of necessitated *ab initio* calculations. Furthermore, these algorithms usually lack generalization properties, i.e. the ability to predict features beyond the boundaries of the data that they have been fitted to.

(*c*) Last but not least a mixed ansatz, which employs physically motivated models for certain degrees of freedom and general numerical methods for others, can be utilized as well, e.g. the *Corrugation Reduction Procedure* (CRP) [121]. Such algorithms combine both the assets and the drawbacks of the previously discussed techniques to the best advantage: The amount of electronic structure calculations needed to construct a PES is significantly reduced with respect to a pure numerical method. However, the validity of the physical restrictions imposed on the system by the employed models has to be critically cross-checked as the case arises.

To stretch the accuracy to the utmost only numerical methods out of class (b) are used in spite of their cost within this work: For one- and two-dimensional data *splines*, which can be found in any numeric's textbook [120], are employed, whereas the six dimensional PES of the $O_2$/Al(111) system is interpolated by

means of a *Neural Network*, as first applied to this class of problems by Doren *et al.* [122].

### 2.3.1 Neural Networks

Inspired by the mechanism governing biological information transmission, *Neural Networks* have been first proposed in the middle of the 20th century to model neurologic systems by essentially reproducing their underlying cell structure [123]. Their elementary component is the node or *perceptron* [124], a simplistic model of a neuron, which features outgoing and incoming connections to other perceptrons. The basic *binary* perceptron possesses two states: "firing" and "not firing" (or "0" and "1" in a less biological vocabulary). It "senses" all its input connections, i.e. the state of the nodes linked as input, and switches itself to "firing" as soon as the sum over the inputs exceeds a certain critical threshold. Thereby the value passed on by the perceptron $i$ to the perceptron $j$ is additionally rescaled by a given weight $w_{ij}$. These weights are the actual free parameters that have to be determined in the fitting process.

The designation *Neural Network* indeed refers to the weighted web of perceptrons as a whole without any restriction on its topology. The ones employed in this work, so called *multi-layer forward feed networks*, can be subdivided in different *layers*, whereby each perceptron output in a certain layer is connected to each perceptron input of the next layer, as shown in Fig. 2.3. Accordingly, the signal processing has a specified direction: It starts from an *input* layer, which consists of perceptrons whose state is defined by the user, continues over a certain arbitrary number of *hidden* layers, and ends in an *output* layer, whose state is returned to the user. In the considered application as interpolation technique the nodes in the input layer represent the degrees of freedom of interest, whereas the output layer should yield the fitted potential energy values at the end. For the description of such a steady hypersurface no binary nodes can be employed reasonably. *Activated* perceptrons are used instead: A sigmoidal *activation function* $f_a$, which is applied to the sum of the input values, replaces the Heaviside step function (i.e. the critical threshold) employed in the binary model to determine a perceptron's state. As a consequence, the nodes can adopt any value in between zero and one. Furthermore, a sigmoidal activation function also introduces non-linearity in the network and thus allows to reproduce arbitrary functional shapes. This flexibility can be further increased by adding a *constant bias* to all perceptrons to force the nodes to work in the most sensible and non-linear region of the activation function. Eventually, the value of the $i^{th}$ node ${}^{k}y_i$ in the $(k+1)^{th}$ layer can be determined recursively from the values of the perceptrons in the preceding layer and the respective bias weight ${}^{k}w_{0i}$:

$$ {}^{k+1}y_i = f_a\left({}^{k}w_{0i} + \sum_j ({}^{k}w_{ji} \cdot {}^{k}y_j)\right). \tag{2.73} $$

By this means an analytic formula for the output layer can be constructed and even differentiated with respect to both the input values and the weights, as long as the activation function is differentiable itself. Evidently Eq. (2.73) also illustrates how arbitrary complex functional shapes can be generated by putting one layer of perceptrons after the other. Thereby the number of layers and nodes

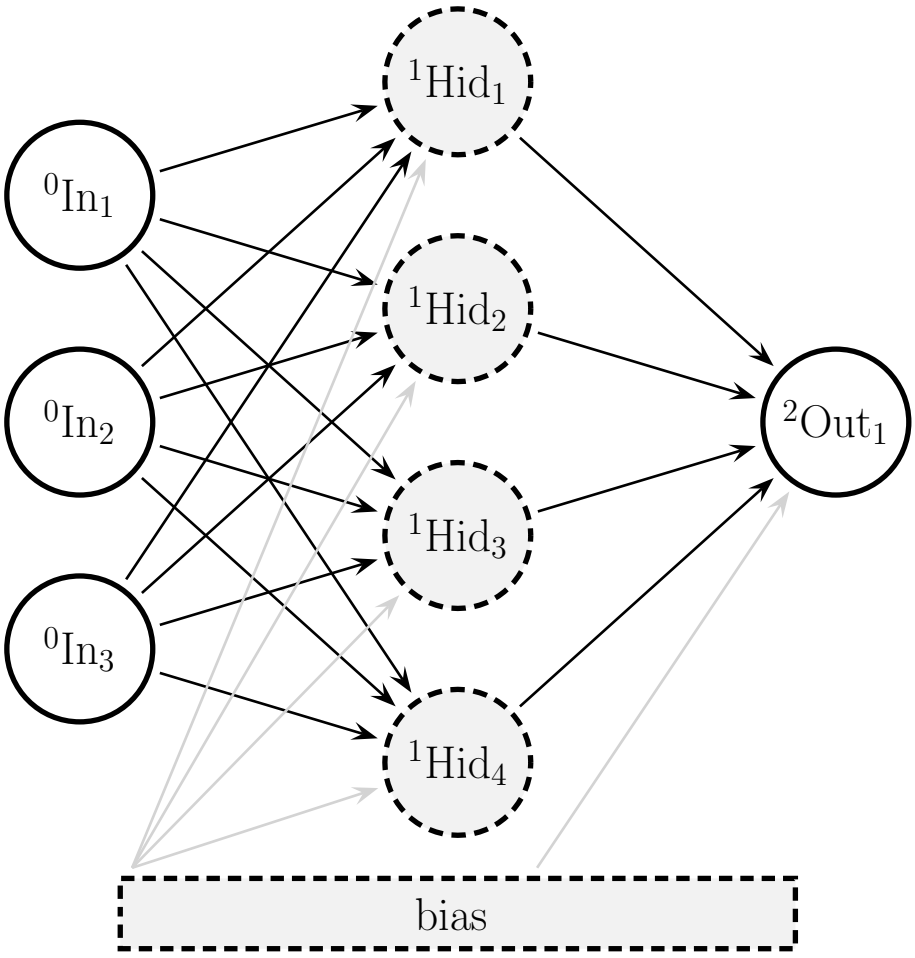


Figure 2.3: Schematic sketch of a *multi-layer feed forward* Neural Network with three input ($^0\mathrm{In}_i$) and one output ($^2\mathrm{Out}_1$) nodes. In between them, a layer with four perceptrons ($^1\mathrm{Hid}_i$) is hidden. The value adopted by the single nodes can be calculated by recursively applying Eq. (2.73), whereby the constant bias depicted in the figure is considered as well.

necessary for a specific Potential Energy Surface is not known *a priori*, but has to be determined during the fitting process: On the one hand, an insufficient number of perceptrons leads to an artificial smoothing of the input data and thus to a loss of relevant physical information. On the other hand a surplus of nodes results in overfitting artifacts as well as to an increased amount of free parameters that have to be determined. Accordingly, the number of *ab initio* data points needed for convergence also rises. In our special case **two** hidden layers, each of them consisting of **38** perceptrons for the singlet PES and **40** perceptrons for the triplet and adiabatic ones have been used (see Sec. 3 for details on the electronic states). The output layer obviously just consists of one node representing the total energy. As activation function a hyperbolic tangent is chosen in the hidden, a linear function in the output perceptrons. Although

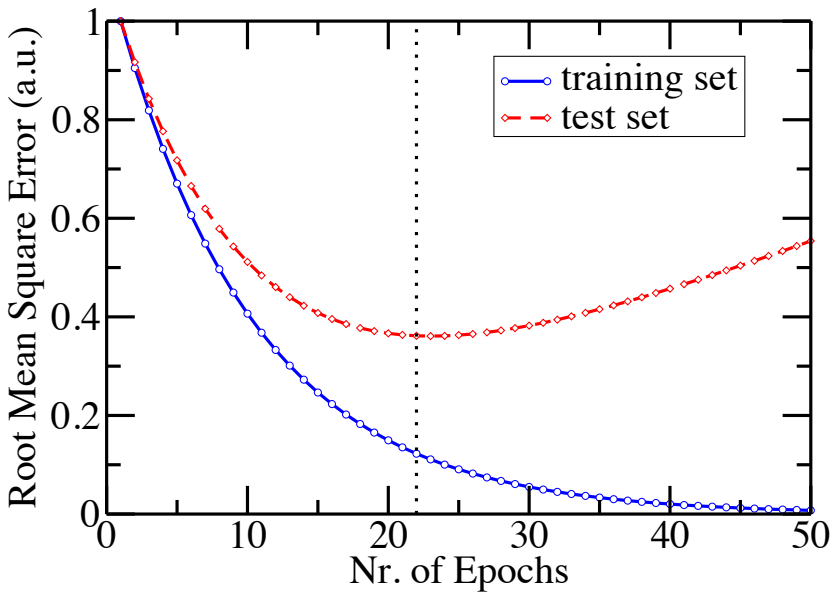


Figure 2.4: Schematic plot of the root mean square error for a Neural Network fit: With respect to the training data the error monotonically decreases with increasing number of epochs, whereas it has a well defined minimum with respect to the test set. The optimum fit for this special case is indicated by the dotted line. Commonly a "test error" that still is approximately twice as large as the "training error" is achievable.

the energy is solely mapped as a function of the six $O_2$ molecules' degrees of freedom, a total of **11** input nodes is employed to achieve faster convergence. Indeed, the input is presented to the network redundantly in terms of *symmetry functions*, which mirror all the inherent (translational and rotational) symmetries of the molecule-surface system [125]. The respective weights have been determined during the fitting process, which is referred to as *learning* or *training* in the Neural Network's community. Thereby a whole series of input-output pairs as obtained by the *ab initio* calculation is fed to the network and the resulting root mean square deviation between the presented data and the output perceptron is evaluated. Needless to say, the Neural Network performs poorly in the beginning. However, the error (or *cost* function) can be minimized [126] due to the differentiability of Eq. (2.73). Thereby the weights are optimized in a *steepest descent*, *conjugate gradient* or *quasi-Newtonian* algorithm as usual in fitting approaches [120]. The described learning process, which is referred to as *epoch*, is iteratively repeated so that the fit improves. In spite of that, its generalization properties deteriorate at a certain point: In such an *overtrained* network the error with respect to the already presented data tends to zero, although the price to pay is the introduction of undesirable high-frequency artifacts, which result in an unphysical PES. To avoid such overfitting effects, the available data is split up in two classes: the usually larger *training set*, employed to optimize the weights, and the *test set*, which is solely used to sense the network's generalization ability and thus to detect overtraining. However, a compromise in between the accuracy with respect to the training and with

respect to the test set has to be found by hand (see Fig. 2.4).

Nevertheless, this section considers just the basics of Neural Networks, as needed for the understanding of this thesis, but omits many of the fascinating details. The interested reader can find an in-depth introduction to the various numerical techniques, network architectures and applications in [127]. Regarding their utilization in Surface Science, the original implementation [122, 128] and its application to the topic of this thesis [125] are suggested for reading, as well as further publications of the same author [129].

## 2.4 Nuclear Dynamics

Last but not least the actual dynamic's calculation—our original topic of interest—has to be performed on the basis of the obtained interpolated data. Once again, various approaches with different assets and drawbacks exist.

### 2.4.1 Molecular Dynamics

The most crude and simple, but also the most flexible and efficient starting point is the **classical** Equation of Motion (2.10) on one PES

$$M_L^{\text{at.}} \ddot{\mathbf{R}}_L = -\nabla_L \, v^i_{\text{eff}}(\mathbf{R}), \tag{2.74}$$

in which each electronic state $i$ of the system is characterized by a distinct Potential Energy Surface $v^i_{\text{eff}}(\mathbf{R})$ (see Sec. 2.1). Starting from an arbitrary set of initial conditions $\{\mathbf{R}_L(0), \mathbf{V}_L(0)\}$ there are many different ways to stepwise integrate the classical Equation of Motion. One simple and still reliable algorithm is the *Verlet* algorithm [27], here in its *Velocity Verlet* formulation [130]

$$\begin{aligned} \mathbf{R}_L(t+h) &= \mathbf{R}_L(t) + h\mathbf{V}_L(t) + \frac{h^2}{2}\frac{\mathbf{F}^i_L(t)}{M_L} + \mathcal{O}(h^4) \\ \mathbf{V}_L(t+h) &= \mathbf{V}_L(t) + h\frac{\mathbf{F}^i_L(t+h) + \mathbf{F}^i_L(t)}{2M_L}, \end{aligned} \tag{2.75}$$

whereby the respective forces are supplied by the interpolated Potential Energy Surface:

$$\mathbf{F}^i_L(t) = -\nabla_{\mathbf{R}_L} \, v^i_{eff}(\mathbf{R}_1, \cdots, \mathbf{R}_N). \tag{2.76}$$

The *relative time step* $h$, which determines the numerical efficiency and preciseness of the integration, is typically fine-tuned by counterchecking the accuracy of the total energy conservation. As a rule of thumb, a time step around a tenth of the system's shortest period has been found to yield satisfactory results in practice. Beside the *Microcanonical*, also the *Canonical* or the *Grand Canonical Ensemble* can be sampled by coupling the system to a heat and a particle bath [130]. By this means millions of atoms can be included [131] and simulated under realistic conditions for several hundreds of nanoseconds [132], thus even allowing theoretical studies of biological relevant processes as e.g. protein folding.

### 2.4.2 Quantum Dynamics

Obviously a Molecular Dynamics approach cannot allow for the quantum mechanical character of the nuclear wave function, which manifests itself in various fashions [133]: Zero Point Energies, Resonances, Tunneling and Interference. As expected, these effects play a role in the chemistry of light elements [134], but they can also affect extended systems [135]. Although excited state dynamics on one specific PES can be assessed in Molecular Dynamics, non-adiabatic effects, which require the consideration of motion on multiple Potential Energy Surfaces, cannot be included by this means either. A full quantum mechanical approach to the problem is advisable in such cases if feasible: As a matter of fact, such a *Quantum Dynamics* treatment increases the numerical costs significantly and, as if this limitation was not bad enough already, it makes high demands on the involved Potential Energy Surfaces. According to the basic laws of quantum mechanics as derived e.g. from *Heisenberg's Uncertainty Principle* [136], the wave function can spread out in energetically forbidden regions of the PES. Thus the phase space that has to be considered in the interpolation is massively inflated, especially if numerical interpolation methods that lack generalization properties are employed (see Sec. 2.3). Additionally, this can lead to instabilities [48] in the direct numerical integration of the **nuclear** Schrödinger equation

$$\left( T_{\mathbf{R}}^{\text{at.}} + \underbrace{\varepsilon_i + V_{\mathbf{RR}}}_{v_{\text{eff}}^i(\mathbf{R})} - E \right) C_i = 0. \tag{2.77}$$

However, efficient and reliable algorithms[11] have been developed to solve both the *time-dependent* and the *time-independent* formulation of Eq. (2.77). Since both approaches have to yield equivalent results as a matter of principle [62], the choice which simulation technique to employ is basically a matter of personal preference.

**Stationary Approach:** The first crucial step in a time-independent approach is the choice of a reaction path coordinate $s$ and the respective transformation of the Schrödinger equation:

$$\left( T_{\mathbf{R}}^{s} + \underbrace{T_{\mathbf{R}}^{\text{at.}} - T_{\mathbf{R}}^{s} + v_{\text{eff}}^{i}(\mathbf{R})}_{V_i} - E \right) C_i = 0. \tag{2.78}$$

The wave function perpendicular to the reaction path is expanded in a suitable **s-independent** orthonormal basis set $|I\rangle$, so that the total wave function can be written as:

$$C_i(\mathbf{R}) = C_i(s, \ldots) = \sum_J \gamma_J^i(s) \, |J\rangle \, . \tag{2.79}$$

The insertion of this expansion in Eq. (2.78) and multiplication with $\langle I|$ results in a *Coupled-Channel* equation set:

$$\sum_J \left\{ (T_{\mathbf{R}}^s - E)\delta_{IJ} + \langle I| \, V_i \, |J\rangle \right\} \gamma_J^i(s) = 0. \tag{2.80}$$

[11] For the solution of Eq. (2.77) a variety of different methods exists, a complete discussion of which would go beyond the scope of this thesis. Consequently, we will just exemplarily introduce two possible methods.

In practice, this still unstable *boundary problem* can be first transformed into a stable *initial value* problem [137, 138, 139] and then solved numerically. This method can also be generalized to incorporate non-adiabatic effects, as done for conceptually similar approaches [140, 141]: In such a case the diabatic Equation of Motion (see Sec. 2.1.1)

$$(T_{\mathbf{R}} + V_{\mathbf{RR}} - E)C_i + \sum_j \underbrace{\langle i| \mathcal{H}_e |j\rangle}_{V_{ij}(\mathbf{R})} C_j = 0 \tag{2.81}$$

replaces Eq. (2.77) in the beginning of the derivation.

**Non-Stationary Approach:** In a time dependent approach a well defined wave packet $\{C_i(\mathbf{R}, t=0)\}$ serves as a starting point. In principle, the quantum-mechanical *time propagation operator* $\mathcal{T}(t)$ can be employed to determine the states' time evolution [142]:

$$\begin{pmatrix} C_0(\mathbf{R},t) \\ C_1(\mathbf{R},t) \\ \vdots \\ C_M(\mathbf{R},t) \end{pmatrix} = \underbrace{\exp\left(-\frac{i\,\mathbf{H}\,t}{\hbar}\right)}_{\mathcal{T}(t)} \begin{pmatrix} C_0(\mathbf{R},0) \\ C_1(\mathbf{R},0) \\ \vdots \\ C_M(\mathbf{R},0) \end{pmatrix}. \tag{2.82}$$

Thereby non-adiabatic transitions have been fully included on the basis of Eq. (2.81) so that the exponential of a *Hamiltonian Matrix*

$$\mathbf{H}_{ij} = (T^{\text{at.}}_{\mathbf{R}} + V_{\mathbf{RR}})\delta_{ij} + V_{ij}(\mathbf{R}) = T^{\text{at.}}_{\mathbf{R}}\delta_{ij} + V^{\text{eff}}_{ij} \tag{2.83}$$

appears in the time-propagation operator. In the *Split Operator* method [143, 144] described below the kinetic energy contribution

$$\mathbf{O}_T = \exp\left(-\frac{i\,t}{\hbar}\, T^{\text{at.}}_{\mathbf{R}}\delta_{ij}\right) \tag{2.84}$$

is approximately separated from the potential energy contribution

$$\mathbf{O}_V = \exp\left(-\frac{i\,t}{\hbar}\, V^{\text{eff}}_{ij}\right). \tag{2.85}$$

For small discrete time-steps $\Delta t$ this leads to a propagation operator of the form

$$\begin{aligned} \mathcal{T}(\Delta t) &= \sqrt{\mathbf{O}_T}\cdot\mathbf{O}_V\cdot\sqrt{\mathbf{O}_T} + \mathcal{O}(\Delta t^3) \\ &= \sqrt{\mathbf{O}_V}\cdot\mathbf{O}_T\cdot\sqrt{\mathbf{O}_V} + \mathcal{O}(\Delta t^3). \end{aligned} \tag{2.86}$$

Accordingly, the repeated application of $\mathcal{T}(\Delta t)$ results in an approximative[12] description of the wave packet's dynamics. Thereby the potential energy contributions $\mathbf{O}_V$ are evaluated by diagonalizing the potential matrix $V^{\text{eff}}_{ij}$, whereas the kinetic energy part

$$\mathbf{O}_T = \mathfrak{F}^{-1}\cdot\exp\left(-i\,\Delta t\,\frac{\hbar k^2}{2M_{\text{at.}}}\right)\cdot\mathfrak{F} \tag{2.87}$$

[12]The accuracy of the approximative time propagation operator can be systematically increased by reducing the time step $\Delta t$ and/or by adding additional terms to the expansion (2.86).

is evaluated in reciprocal space by means of the *(Fast) Fourier Transformation* (FFT) [120] operator $\mathfrak{F}$.

Both the stationary and the time-dependent approach require a computational power orders of magnitude greater than the one needed for a simple MD algorithm: Thus just low-dimensional systems or a few dimensions of a high-dimensional system can be treated reasonably. In the latter case the restriction to specific degrees of freedom can influence the dynamics to a greater extent than the quantum-mechanical effects do (compare [145] with [146]). Obviously, there is no alternative to Quantum Dynamics under certain circumstances, e.g., when investigating the motion of hydrogen atoms or molecules [147, 30]. Then again, effects like Tunneling and the Zero Point Energy affect the dynamics of heavier molecules in a quantitative fashion at the utmost, whereas non-adiabatic transition might still play a relevant role in this case. For such systems the question begs to be asked, if Molecular Dynamics and Quantum Dynamics could be combined to the best advantage[13]: Such algorithms, referred to as *mixed quantum-classical* in literature, are discussed in the next section.

### 2.4.3 Mixed Quantum-Classical Dynamics

The fundamental idea underlying mixed quantum-classical algorithms is the partitioning of the degrees of freedom into **fast** electronic ones, which deserve a quantum-mechanical treatment, and **slow** nuclear ones, which can be accurately described classically. In contrast to the Born-Oppenheimer Approximation (see Sec. 2.1), this mixed quantum-classical separation is **not** aimed at resulting into two decoupled problems that can be solved consecutively. Rather, the two types of dynamics are explicitly coupled to one another so that the electrons react properly to the nuclear motion and so that the nuclei respond correctly on time-dependent electronic changes. This mutual feedback is crucial for a correct description of non-adiabatic effects: Therefore, approaches that do not achieve self-consistency, as e.g. the *Redfield approach* [150, 151] or the *classical path method* [152, 153], are not taken into account in this thesis. However, there is no unique way to combine the quantum and the classical dynamics self-consistently. Thus just the two major approaches, which are antithetical in their character and application, are first introduced and then critically compared as follows.

#### 2.4.3.1 Mean Field Approach

The derivation of the *Mean Field* or *Ehrenfest* method starts again with the complete Hamiltonian (2.1) introduced in the discussion of the Born-Oppenheimer Approximation:

$$\mathcal{H} = T_{\mathbf{R}} + \underbrace{T_{\mathbf{r}} + V_{\mathbf{rr}} + V_{\mathbf{rR}}}_{\mathcal{H}_e} + V_{\mathbf{RR}}. \tag{2.88}$$

[13] A comparison of the mixed quantum-classical approach with semiclassical methods, which are not discussed in this thesis, can be found in [148, 149].

For the **total** wave function, a product ansatz, i.e. a factorization into nuclear and electronic parts, is employed

$$\Psi\left(\mathbf{r},\mathbf{R},t\right) = C\left(\mathbf{R},t\right) \cdot \Phi(\mathbf{r},t) \cdot \exp\left(\frac{i}{\hbar}\gamma(t)\right), \tag{2.89}$$

whereby a yet unspecified time-dependent *phase factor* $\gamma$ is introduced. Insertion into the *time-dependent Schrödinger* equation leads to

$$\begin{aligned} i\hbar\frac{\partial\Phi}{\partial t} = \\ \left[T_{\mathbf{r}} + V_{\mathbf{rr}} + \dot{\gamma} + \int C^* \left(T_{\mathbf{R}} + V_{\mathbf{RR}} + V_{\mathbf{rR}} - i\hbar\frac{\partial}{\partial t}\right) C\, d\mathbf{R}\right] \Phi \end{aligned} \tag{2.90a}$$

and

$$\begin{aligned} i\hbar\frac{\partial C}{\partial t} = \\ \left[T_{\mathbf{R}} + V_{\mathbf{RR}} + \dot{\gamma} + \int \Phi^* \left(T_{\mathbf{r}} + V_{\mathbf{rr}} + V_{\mathbf{rR}} - i\hbar\frac{\partial}{\partial t}\right) \Phi\, d\mathbf{r}\right] C, \end{aligned} \tag{2.90b}$$

depending on whether a multiplication with $C^*$ and a subsequent integration over the nuclear degrees of freedom $\mathbf{R}$ or a multiplication with $\Phi^*$ and a subsequent integration over the electronic degrees of freedom $\mathbf{r}$ is performed. The expectation value for the total energy can then be simplified by making use of Eq. (2.90a) and (2.90b):

$$\begin{aligned} E_{\text{tot}} = \langle\Psi|\,\mathcal{H}\,|\Psi\rangle = \\ = \int C^*\ \left(T_{\mathbf{R}} + V_{\mathbf{RR}}\right)\ C\, d\mathbf{R} + \int C^*\Phi^*\ \mathcal{H}_e\ C\Phi\ d\mathbf{r}\, d\mathbf{R} = \\ = \underbrace{\int C^*\ i\hbar\frac{\partial}{\partial t}\ C\ d\mathbf{R}}_{E(t)} + \underbrace{\int \Phi^*\ i\hbar\frac{\partial}{\partial t}\ \Phi\ d\mathbf{r}}_{\epsilon(t)} - \dot{\gamma} = \langle\Psi|\, i\hbar\frac{\partial}{\partial t}\,|\Psi\rangle\,. \end{aligned} \tag{2.91}$$

Although the last equation, i.e. energy conservation, constitutes an essential constraint on the phase factor, it does not[14] result in a unique definition of $\gamma$. This so called *phase invariance* can be exploited to transform the Mean Field equations into a more convenient form by assuming without loss of generality [154]:

$$E(t) \quad \stackrel{!}{=} \quad \iint C^*\,\Phi^*\ \ \mathcal{H}\ \ C\,\Phi\ d\mathbf{R}\, d\mathbf{r} = E_{\text{tot}} \tag{2.92}$$

$$\epsilon(t) \quad \stackrel{!}{=} \quad \iint C^*\,\Phi^*\ \ \mathcal{H}_e\ \ C\,\Phi\ d\mathbf{R}\, d\mathbf{r} \tag{2.93}$$

$$\Longrightarrow \gamma(t) \quad \stackrel{!}{=} \quad \int_0^t \epsilon(\tau)\ \ d\tau. \tag{2.94}$$

[14] As known from basic quantum mechanics, charge conservation, i.e. the conservation of the integrated probability distribution in the continuity equation, requires the wave function to be independent from an overall phase factor. Thus no obligatory initial condition exists for the differential Eq. (2.91).

Accordingly, Eq. (2.90a) and Eq. (2.90b) can be further simplified in a next step:

$$i\hbar\frac{\partial\Phi}{\partial t} = \left[T_{\mathbf{r}} + V_{\mathbf{rr}} + \int C^*\, V_{\mathbf{rR}}\, C\, d\mathbf{R}\right]\, \Phi \tag{2.95a}$$

$$i\hbar\frac{\partial C}{\partial t} = \left[T_{\mathbf{R}} + V_{\mathbf{RR}} + \int \Phi^*\, \mathcal{H}_e\, \Phi\, d\mathbf{r}\right]\, C. \tag{2.95b}$$

In comparison to the Born-Oppenheimer Equation of Motion (2.9), the nuclei do not sense the potential of a single electronic state $\varepsilon_i$, i.e. one single **eigenvalue** of $\mathcal{H}_e$, in Eq. (2.95b). Rather, the **expectation value** of $\mathcal{H}_e$, i.e. the occupation averaged potential over all electronic states

$$V^{\mathrm{MF}}(\mathbf{R}) = \int \Phi^*\, \mathcal{H}_e\, \Phi\, d\mathbf{r}\,, \tag{2.96}$$

determines the nuclear motion instead. Analogously, the electrons feel the averaged effect of the nuclei in Eq. (2.95a) as well: hence the name *Mean Field approach*.

To finally obtain a classical Equation of Motion for the nuclei, the classical limit $\hbar \to 0$ has to be taken. Following Messiah [155], the **nuclear** wave function is first separated into a real valued amplitude and a real valued phase:

$$C(\mathbf{R}, t) = A(\mathbf{R}, t) \cdot \exp\left(\frac{i}{\hbar} S(\mathbf{R}, t)\right). \tag{2.97}$$

Insertion in Eq. (2.95b) and subsequent determination of the classical limit leads to one equation for the real and one for the imaginary part of the wave function respectively:

$$\frac{\partial S}{\partial t} + \sum_L \frac{(\nabla_L S)^2}{2M_L} + V_{\mathbf{RR}} + V^{\mathrm{MF}} = -\frac{1}{A}\, T_{\mathbf{R}}\, A \xrightarrow{\hbar\to 0} 0 \tag{2.98a}$$

$$\frac{\partial A}{\partial t} + \sum_L \frac{1}{2M_L}\left[A(\nabla_L^2 S) + 2(\nabla_L A)(\nabla_L S)\right] = 0. \tag{2.98b}$$

The resulting Eq. (2.98a) is the classical *Hamilton-Jacobi* equation

$$H\left(\mathbf{R}, \mathbf{P}, t\right) + \frac{\partial S}{\partial t} = \sum_L \frac{1}{2M_L}\mathbf{P}_L^2 + V_{\mathbf{RR}} + V^{\mathrm{MF}} + \frac{\partial S}{\partial t} = 0, \tag{2.99}$$

in which the *generalized momentum*

$$\mathbf{P}_L = \nabla_L S = \nabla_L \int^t \mathcal{L}(\mathbf{R}, \dot{\mathbf{R}}, \tau)\, d\tau \tag{2.100}$$

$$\frac{\partial \mathbf{P}_L}{\partial t} = \nabla_L \mathcal{L}(\mathbf{R}, \dot{\mathbf{R}}, t) = -\nabla_L\left(V_{\mathbf{RR}} + V^{\mathrm{MF}}\right) \tag{2.101}$$

is formally introduced. Consequently, $S(\mathbf{R}, t)$ constitutes the classical *action*, i.e. the time integral of the system's *Lagrangian* $\mathcal{L}(\mathbf{R}, \dot{\mathbf{R}}, t)$.

The remaining Eq. (2.98b) is then multiplied with $2A$ so that it results into a *continuity equation* [149] for the nuclear probability density $A^2$:

$$\frac{\partial A^2}{\partial t} + \sum_L \nabla_L \cdot \left( A^2 \frac{\nabla_L S}{M_L} \right) = \frac{\partial A^2}{\partial t} + \operatorname{div} \left( A^2 \cdot \dot{\mathbf{R}} \right) = 0. \tag{2.102}$$

Integration over $\mathbf{R}$ with the help of the *divergence* (or *Gauss'*) *theorem* yields

$$\frac{d}{dt} \int A^2(\mathbf{R}, t)\, d\mathbf{R} = 0 \tag{2.103}$$

and thus norm conservation over time for the nuclear wave function.

Eventually, the electronic Mean Field equation (2.95a) has to be adapted to the classical limit as well. Thereto the nuclear probability density $A^2 = C^* C$ is replaced with a Delta-distribution at the classical trajectory' position. The subsequent integration for the potential term results in a time dependent electronic Schrödinger equation

$$i\hbar \frac{\partial \Phi}{\partial t} = \left[ T_{\mathbf{r}} + V_{\mathbf{rr}} + V_{\mathbf{rR}} \left( \mathbf{R}(t) \right) \right] \Phi, \tag{2.104}$$

in which the actual potential depends upon the classical trajectory $\mathbf{R}(t)$. Altogether, Eq. (2.99) and Eq. (2.104), which are typically solved by expanding the electronic wave function in an appropriate basis set, embody the Mean Field (or Ehrenfest) approach.

#### 2.4.3.2 Surface Hopping

In contrast to the Mean Field method, no simple product ansatz (2.89) is used for the wave function in Surface Hopping methods, but a correct time-dependent *multiple electronic states* expansion

$$\Psi(\mathbf{r}, \mathbf{R}, t) = \sum_j C_j(\mathbf{R}, t)\ \Phi_j(\mathbf{R}, \mathbf{r}) \overset{!}{=} \sum_j C_j \left| j \right\rangle, \tag{2.105}$$

which was already employed in the derivation of the Born-Oppenheimer approximation in Sec. 2.1, is utilized instead. For a general orthonormal basis set $|j\rangle$ insertion into the time-dependent Schrödinger equation and multiplication with $\langle i|$ from the left results in

$$\begin{aligned} \left( T_{\mathbf{R}} + V_{\mathbf{RR}} - i\hbar \frac{\partial}{\partial t} \right) C_i + \sum_j \underbrace{\langle i | \mathcal{H}_e | j \rangle}_{V_{ij}(\mathbf{R})} C_j = \\ \sum_{j,L} \frac{\hbar^2}{M_L} (\nabla_L C_j) \langle i | \nabla_L | j \rangle - \sum_j C_j \langle i | T_{\mathbf{R}} | j \rangle, \end{aligned} \tag{2.106}$$

which is just the explicitly time-dependent formulation of the already discussed Eq. (2.11). Once again, the nuclear wave function is first separated[15] into am-

[15] In contrast to the Mean Field method, neither the amplitude nor the phase have to be real valued in this case due to the differing outcome of the normalization constraint on the two types of wave functions (2.89) and (2.105).

plitude and phase:

$$C_i(\mathbf{R},t) = A_i(\mathbf{R},t)\cdot\exp\left(\frac{i}{\hbar}S_i(\mathbf{R},t)\right) \tag{2.107}$$

and then inserted in Eq. (2.106). This procedure yields an equation for the real valued part and an equation for the imaginary part respectively:

$$\frac{1}{A_i}\left(T_{\mathbf{R}}A_i\right) + \sum_L \frac{(\nabla_L S_i)^2}{2M_L} + V_{\mathbf{RR}} + \frac{\partial S_i}{\partial t} + V_{ii} = \sum_{j,L}\frac{\hbar^2}{M_L}\frac{(\nabla_L A_j)}{A_i}e^{\frac{i}{\hbar}(S_j-S_i)}\langle i|\nabla_L|j\rangle - \sum_j \frac{A_j}{A_i}e^{\frac{i}{\hbar}(S_j-S_i)}\langle i|T_{\mathbf{R}}|j\rangle \tag{2.108a}$$

$$\sum_L \frac{1}{2M_L}\left(2(\nabla A_i)(\nabla S_i) + (\nabla^2 S_i)A_i\right) + \frac{\partial A_i}{\partial t} + \frac{1}{\hbar}\sum_{j\neq i} V_{ij}A_j e^{\frac{i}{\hbar}(S_j-S_i)} = -\sum_{j,L}\frac{1}{M_L}A_j(\nabla_L S_j)\langle i|\nabla_L|j\rangle e^{\frac{i}{\hbar}(S_j-S_i)}. \tag{2.108b}$$

The classical limit $\hbar\to 0$ for Eq. (2.108a) results in

$$H\left(\mathbf{R}^i,\mathbf{P}^i,t\right) + \frac{\partial S_i}{\partial t} = \sum_L \frac{(\nabla_L S_i)^2}{2M_L} + V_{\mathbf{RR}} + V_{ii} + \frac{\partial S_i}{\partial t} = 0, \tag{2.109}$$

which is again a *Hamilton-Jacobi* equation for the generalized momentum:

$$\mathbf{P}_L^i = \nabla_L S^i = \nabla_L \int^t \mathcal{L}^i(\mathbf{R}^i,\dot{\mathbf{R}}^i,\tau)\,d\tau \tag{2.110}$$

$$\frac{\partial \mathbf{P}_L^i}{\partial t} = \nabla_L \mathcal{L}^i(\mathbf{R}^i,\dot{\mathbf{R}}^i,t) = -\nabla_L\left(V_{\mathbf{RR}} + V_{ii}\right). \tag{2.111}$$

In contrast to the Mean Field method, in which the nuclei feel the averaged electronic potential $V^{\text{MF}}$ (2.96) of all electronic states, only the potential $V_{ii}$ associated to a specific electronic state $|i\rangle$ acts on the nuclei in this case. However, there is also a distinct trajectory $\mathbf{R}^i$ for each one of these states. A deeper comprehension on how these trajectories interact with each other, can be gained by rewriting Eq. (2.108b) into a continuity equation, as done for the respective Mean Field equation (2.98b) before:

$$\frac{\partial|A_i|^2}{\partial t} + \sum_L \nabla_L\cdot\left(|A_i|^2\frac{\nabla_L S_i}{M_L}\right) = -2\sum_{j\neq i}A_i^*A_j\left[\frac{1}{\hbar}V_{ij} - \sum_L\frac{\nabla_L S_j}{M_L}\langle i|\nabla_L|j\rangle\right]e^{\frac{i}{\hbar}(S_j-S_i)}. \tag{2.112}$$

In contrast to the connatural equation for the Mean Field method (2.102), the right hand side does not vanish in this case. As a consequence, there is no norm conservation for the probability density $|A_i|^2 = A_i^*A_i$ in any specific[16] state $|i\rangle$.

[16] For the overall wave function norm conservation still applies, as can be seen by taking the sum over the continuity equations for all states.

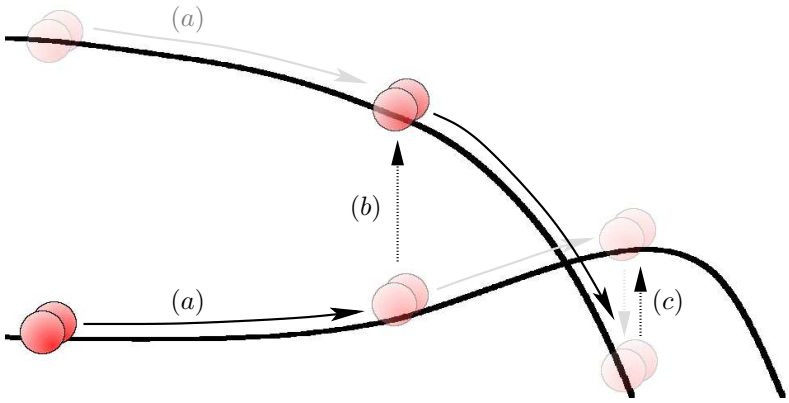


Figure 2.5: Schematic drawing of a trajectory in the Surface Hopping method: The depicted oxygen molecule starts in the ground state at the far left and moves towards the barrier in step (*a*). At the same time, the density matrix for the total two-state system is integrated, as if the trajectory would also evolve in the excited state. During this motion, the probability for the occupation of the excited state rises so that a stochastic surface hop—here shown exemplarily at the position (*b*)—occurs. Henceforward the trajectory evolves in the potential of the excited state. Still, the total density matrix is integrated along this pathway so that further switches, at position (*c*) for instance, can occur.

Thus, while the single trajectories $\mathbf{R}^i$ evolve simultaneously, the right hand side of Eq. (2.112) describes the probability flux between them. Unfortunately, a practical algorithm to solve Eq. (2.109) and (2.112) directly has not been found to date due to the difficulties associated with the non-local coupling terms present in the continuity equation [154, 156]. In *Surface Hopping* methods, however, these pitfalls are avoided by inspecting a single trajectory $\mathbf{R}^i \rightarrow \mathbf{R}$ that is in a single electronic state at each time step. Due to this approximation, the classical action $S_i \rightarrow S$ becomes independent on the actual electronic state as well and thus leads to a simplified continuity equation:

$$\frac{\partial |A_i|^2}{\partial t} + \operatorname{div}\left(A_i^2 \cdot \dot{\mathbf{R}}\right) = -2 \sum_{j \neq i} A_i^* A_j \left[\frac{1}{\hbar} V_{ij} - \sum_L \dot{\mathbf{R}}_i \cdot \langle i | \nabla_L | j \rangle\right]. \quad (2.113)$$

For the *occupation numbers* $a_{ii}(t) = \langle A_i | A_i \rangle$ along the trajectory, this equation then translates into

$$\frac{d\, a_{ii}}{dt} = -2 \sum_{j \neq i} a_{ij} \left[\frac{1}{\hbar} V_{ij} - \sum_L \dot{\mathbf{R}}_i \cdot \underbrace{\langle i | \nabla_L | j \rangle}_{\mathbf{d}_{ij}}\right]. \quad (2.114)$$

Analogously, a more general set of time dependent differential equations can be derived for the rest of the *density matrix elements*:

$$i\hbar \frac{d\, a_{ij}}{dt} = \sum_k \left[a_{kj}\left(V_{ik} - i\hbar\, \dot{\mathbf{R}} \cdot \mathbf{d}_{ik}\right) - a_{ik}\left(V_{kj} - i\hbar\, \dot{\mathbf{R}} \cdot \mathbf{d}_{kj}\right)\right]. \quad (2.115)$$

As a consequence, the classical Hamilton-Jacobi equations of motion (2.109) and the quantum mechanical density matrix along this trajectory (2.115) can be stepwise integrated simultaneously. By this means, the actual occupation probability for **all** included electronic states can be determined, in spite of the fact that the trajectory evolves in the potential of a **single** electronic state at each time step. This fact is cleverly exploited in Surface Hopping methods: If along this pathway another electronic state gains importance, a stochastic *surface hop or switch*, i.e. an instantaneous change of the electronic state $i \rightarrow j$, is applied to model the undergoing *electronic transition*. Accordingly, the potential of the new electronic state $V_{jj}$ determines the evolution of the classic trajectory henceforward, as sketched in Fig. 2.5. Again, both the classical Equation of Motion and the density matrix along the trajectory are integrated after the surface hop so that further switches can occur. Because of the random character of these hops, the evolution of the classical trajectory is not deterministic anymore: As a matter of fact, even switches into states with almost no occupation probability can occur. Accordingly, a large number of trajectories $N$ has to be computed for each set of initial conditions to determine the behavior of the system. Thus, in contrast to the Mean Field method, in which the potential is averaged over the electronic states, the averaging is performed over multiple trajectories in Surface Hopping methods. Thereby the switching algorithm must be designed in such a way that for a large number of trajectories the fraction of trajectories assigned to a certain electronic state is approximately equal to its respective occupation number at any time step. However, this boundary condition does not determine the occurrence of switches uniquely so that a variety of different implementations exists [157, 158, 159, 160, 161, 162, 163, 164, 165, 156, 166].

Throughout this work, *Tully's Fewest Switches* [7] algorithm, which ensures the fulfillment of the boundary condition mentioned above within the **fewest** possible number of switches, is employed. As shown in the flow chart 2.6, the probabilities

$$P_{i\rightarrow j} = -\frac{2a_{ji}\left[\frac{1}{\hbar}V_{ji} - \dot{\mathbf{R}}\cdot\mathbf{d}_{ji}\right]}{a_{ii}}\Delta t \tag{2.116}$$

for a switch from the actual state $i$ to another state $j \neq i$ are calculated[17] after each time step $\Delta t$. Then a dice is thrown to decide if a switch takes place or not in a *Metropolis* [167] like fashion. In the affirmative case, the kinetic energy of the molecule has to be adjusted to ensure energy conservation, since such electronic transitions do not just occur at the crossing seam of the respective Potential Energy Surfaces but virtually anywhere along the pathway. Thereby the change in potential energy $\Delta V = V_{ii} - V_{jj}$ due to the surface hop is counterbalanced by rescaling the velocity vector in the direction of the non-adiabatic coupling vector $\mathbf{d}_{ij}$

$$\frac{M\,\dot{\mathbf{R}}^2}{2} - \frac{M\,\left(\dot{\mathbf{R}} + \lambda\,\mathbf{d}_{ij}\right)^2}{2} + \Delta V = 0, \tag{2.117}$$

since semiclassical studies [140, 141] suggest that the driving force of such transi-

[17] As the comparison of Eq. (2.116) with the continuity equation (2.114) shows, these probabilities can be interpreted as the appropriately time-scaled probability flux from state $i$ to state $j$ per trajectory in state $i$.

tions typically acts in its direction. However, the quadratic Eq. (2.117) generally yields two solutions for $\lambda$, which can even be complex. Therefore, two additional rules apply for the velocity rescaling procedure:

- In the case of complex solutions, the surface hop is rejected, since energy conservation interdicts the transition: Typically, the available kinetic energy is not sufficient to bridge the gap for an excitation into a higher energy state. Whereas quantum mechanics explicitly allows for such *tunneling* processes, there is no correspondent mechanism in classical theory. Modifications [166] of the Surface Hopping algorithm, which try to account for such tunneling effects approximatively, exist. For the system of interest in this work (see Sec. 4), such processes play a negligible role and thus no such modified algorithm has been employed.
- In most cases, Eq. (2.117) yields two real solutions, which can be assigned to a mostly forward or a mostly backscattering event respectively [168]. In this context one has to realize that both of these velocity adjustments break the *momentum conservation* of the system: While in nature a spontaneous photon emission compensates for these effects in the momentum balance, no such mechanism is included in Surface Hopping algorithms. Notwithstanding, the employment of the solution with the smaller change in momentum—as done throughout this work—seems reasonable against this background.

After the velocity rescaling procedure or if no switch occurred at all, the algorithm checks if any of the breaking conditions is fulfilled. In the affirmative case, the calculation stops, whereas the algorithm continues with the integration to the next time step in the negative case. As shown in the flow chart in Fig. 2.6, this procedure is repeated for a large number of trajectories $N$ that share the same initial conditions. Additionally, a sampling over different initial conditions can be performed as well (see Sec. 4.4.2 for instance).

The described *Surface Hopping* algorithm has a decisive advantage over the *Mean Field* method when applied to surface science problems as dissociative adsorption for instance: Typically, the pathway of the molecule is barrier free in one electronic state and activated in the other state for such systems. In a Mean Field description of the dynamics [169] on such potentials, the nuclei will always feel a certain barrier, which is lowered with respect to the original one due to the averaging process. Accordingly, for a given set of initial conditions that exhibit a total energy which is lower than that barrier, no dissociation can occur. In contrast thereto, the Surface Hopping method explicitly allows for bifurcations: Thus for the exact same set of initial conditions a fraction of trajectories will be repelled in one electronic state, whereas there will also be a fraction of molecules able to dissociate in the other state [149]. Notwithstanding, the approximations used in the derivation of the *Surface Hopping* method also lead to some shortcomings:

- As mentioned before, *tunneling* effects are not accounted for in this algorithm to ensure energy conservation for the classical trajectory. However, such effects should play only a subordinate role in the system of interest in this work.

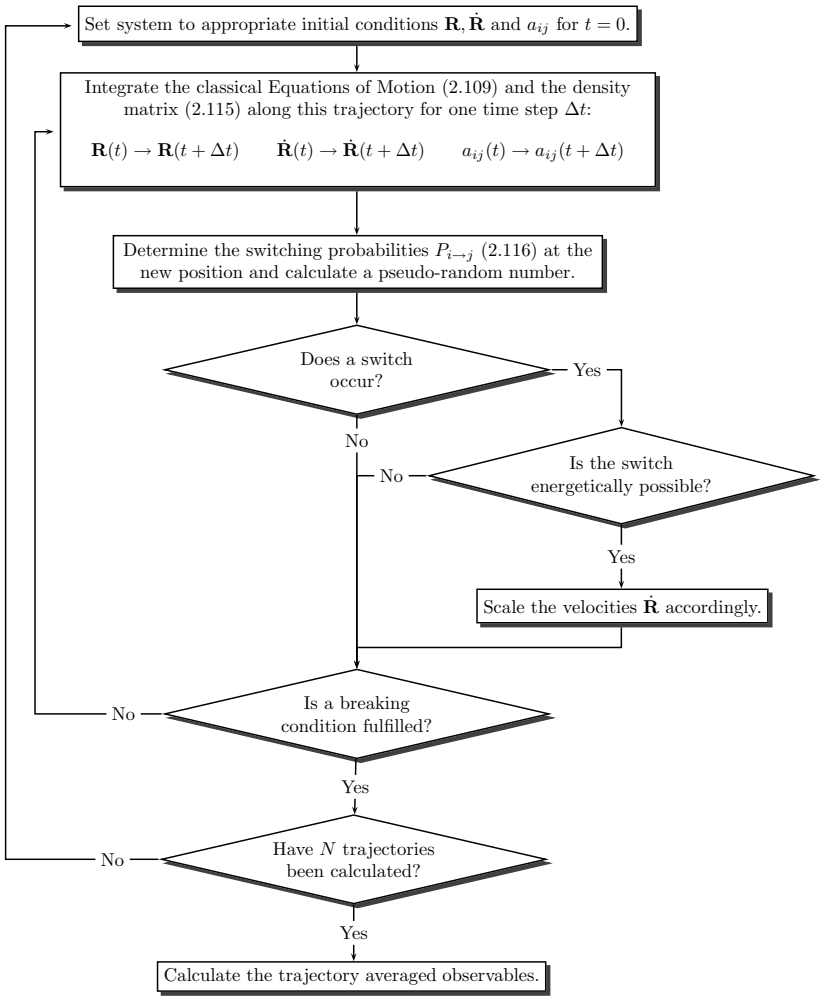


Figure 2.6: Program flow chart of *Tully's Fewest Switches Algorithm* [7] as implemented in this work.

- Furthermore, interference effects are solely reproduced qualitatively, especially if the involved Potential Energy Surfaces differ strongly from each other: In the case of a double curve crossing occurring on the molecules pathway (or a twice trespassed crossing in scattering processes for instance), a quantum mechanical wave packet typically branches off at the first crossing seam. Henceforward, the two packets evolve **independently** on distinct potentials, but can collide at the second crossing. There, the phase difference accumulated on their pathways plays a decisive role, since it determines if the superposition leads to a constructive or a destructive interference. In the Surface Hopping method, however, the trajectory is always in one well defined electronic state. The phase difference to the other states is calculated under the assumption that the motion on the other potentials **mimics** the motion on the actual potential exactly. Obviously this approximation fails, whenever the respective potentials differ

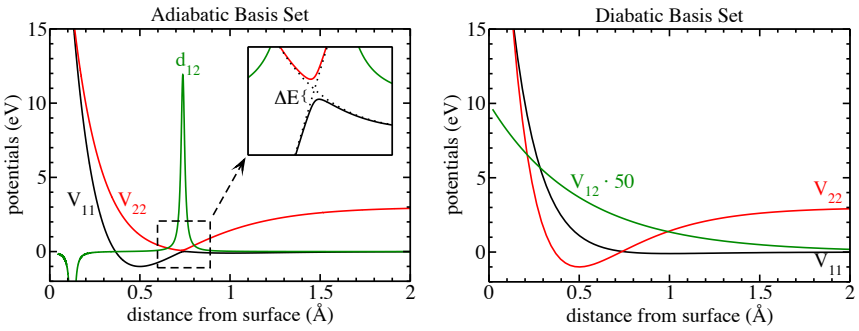


Figure 2.7: One-dimensional adiabatic and diabatic potentials for the scattering of neutral and anionic iodine on a diamond surface [8].

too strongly. In spite of that, the Surface Hopping method still reproduces the interference patterns in a qualitative manner [7], whereby a phase shift with respect to the interference patterns yielded by full quantum mechanical calculations [8] usually occurs. Again, such effects play a relevant role in low-dimensional systems but not in extended multi-dimensional surface science ones, in which the phase coherence is quickly lost [170] anyway.

- Last but not least, one has to realize that the outcome of the Surface Hopping method—in contrast to the Mean Field method—often depends upon the chosen expansion for the electronic states, i.e. if a diabatic or an adiabatic representation is employed (see Fig. 2.7). First, the terms entering the probability (2.116) and the right hand side of Eq. (2.115) differ: Whereas solely the non-adiabatic coupling vector $\mathbf{d}_{ij}$, which is strongly localized at the crossing seams, plays a role in the adiabatic case, only the smooth non-diagonal coupling matrix elements $V_{ij}$ enter the equations in the diabatic case (see Sec. 2.1.1). As a consequence, the adiabatic basis leads to switches that mainly occur in the region of the curve crossings, while the diabatic representation yields surface hops that occur virtually everywhere along the pathway and thus also more often [7]. In the latter case, phase coherence is thereby additionally diminished and thus the concordance with full quantum mechanical results is also worse [8]. Fortunately, such interference effects just play a role in low-dimensional systems so that diabatic and adiabatic basis sets could be expected to yield the same results for the system of interest in this work. However, this is not the case (see Sec. 4.3), since there is another subtle difference: If there is a curve crossing point at the barrier position, i.e. when the motion on one of the potentials is energetically hindered, the effective barrier that the nuclei experience differs: While in the diabatic case the barrier is given by the exact value of the curve crossing, this amount is lowered in the adiabatic basis set due to the avoided crossing, as shown in the inlet of Fig. 2.7. The influence of such effects, especially which representation and which coupling one has to choose, will be extensively discussed in Sec. 4.3.

# Chapter 3

# The Oxygen Molecule

## 3.1 Qualitative Discussion of the Electronic Structure

It is a very well known fact that the $O_2$ molecule plays a prominent role in the circle of life as a highly available oxidation partner. This extraordinary position is determined by its unique electronic structure, which results in a combination of molecular properties not found elsewhere in nature. Noteworthy enough, it behaves rather inertly in the gas-phase in spite of its open-shell triplet (diradical) character, if the other reactant and the product are spin singlets. Obviously this peculiarity of the oxygen molecule can be understood by the laws of quantum mechanics, in this special case by the constraint of overall spin conservation as first formulated by Wigner [171]. For the quantification of this phenomenon, however, there is a *caveat*: The oxygen molecule's atypical electronic structure deserves particular attention, since it is not straightforwardly accessible by the most common approximative methods as will be discussed below. Thus, in a first step, we will inspect the ground state and the excited states of $O_2$ qualitatively in terms of *Molecular Orbitals* (MOs), i.e. linear combinations[1] of the orbitals of single oxygen atoms.

The electronic configuration of a single oxygen atom is $1s^2 2s^2 2p^4$, which according to Hund's rules [172] leads to a $^3P$ ground state. In an oxygen molecule energy split bonding and antibonding MOs are formed (see Fig. 3.1) that are symmetric and antisymmetric combinations of the respective oxygen atomic orbitals (AOs). Thereby the combinations of AOs that carry no angular momentum along the molecular axis, i.e. the z-axis without loss of generality, result in MOs not carrying any angular momentum either, e.g., $1s - 1s \rightarrow 1\sigma$ and $1p_z + 1p_z \rightarrow 1\sigma^*$. In contrast thereto, the remaining $2p_x$ and $2p_y$ orbitals couple to two-fold degenerate bonding $2\pi_p$ and antibonding $2\pi_p^*$ Molecular Orbitals, whose angular momentum along the bond does not vanish [173]. For the energetically lowest lying electronic states of the $O_2$ molecule all MOs up to the $2\pi_p^*$ level are completely filled, while the $2\pi_p^*$ MOs that comprise the two degenerate orbitals $\phi_x \sim 2p_x - 2p_x$ and $\phi_y \sim 2p_y - 2p_y$ are half filled.

[1] Formally, these are the correct solutions of the corresponding non-interacting system, in which the electron-electron repulsion term $V_{\mathbf{rr}}$ is neglected.

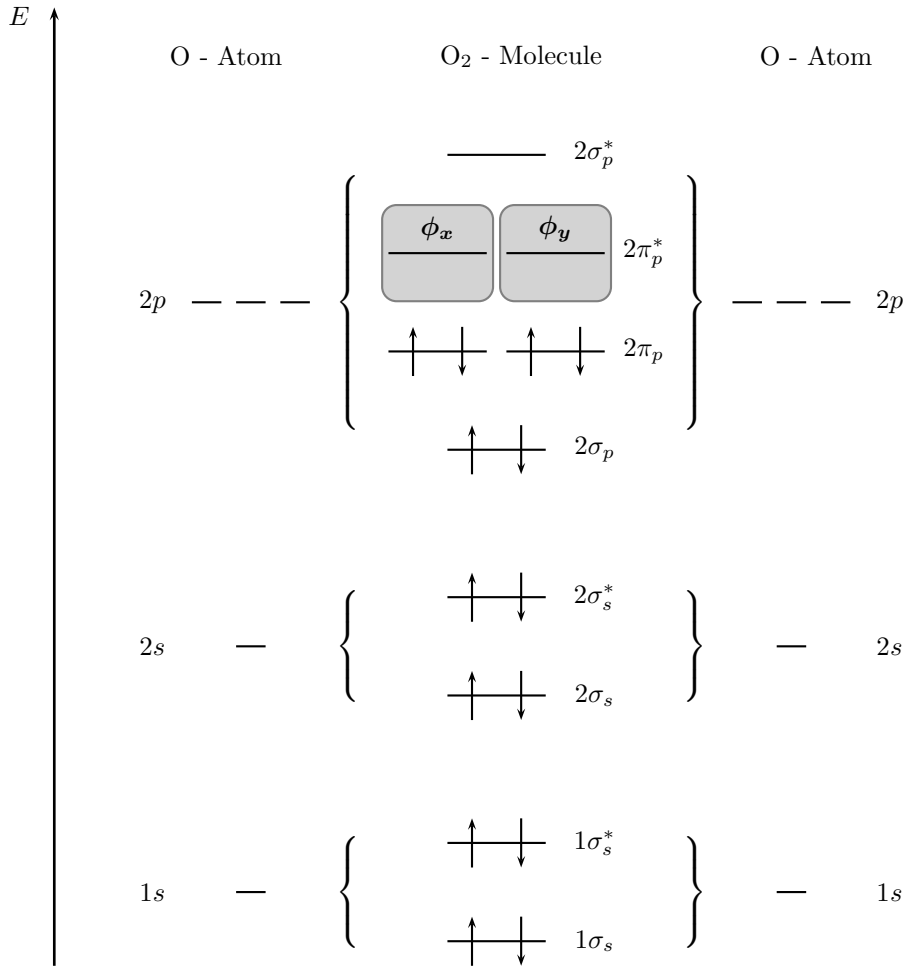


Figure 3.1: Sketch of the $O_2$'s Molecular Orbitals in energetic order as obtained from the symmetric and antisymmetric combination of the single oxygen's orbitals. All MOs up to the two-fold degenerate $2\pi_p$ orbitals are completely filled, whereas the two-fold degenerate, gray shaded antibonding $2\pi_p^*$ orbitals are half filled.

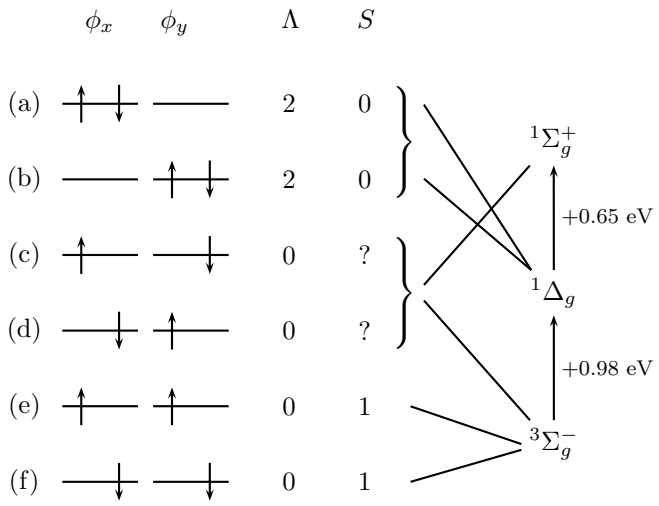


Figure 3.2: The six possible configurations of two electrons in the four $2\pi_p^*$ spinorbitals of the oxygen molecule. Their quantum numbers of the projected angular momentum $\Lambda$ and of the total spin $S$ are also given if possible. Finally, the pairs of Determinants which have to be combined to yield correct electronic states are also denoted.

Therefore, the lowest lying electronic states of the oxygen molecule are uniquely identified by the occupation of these four valence spinorbitals $\phi_x|\uparrow\rangle$, $\phi_x|\downarrow\rangle$, $\phi_y|\uparrow\rangle$ and $\phi_y|\downarrow\rangle$. As shown schematically in Fig. 3.2, there are obviously six distinct possibilities to arrange the two residual valence electrons in these $2\pi_p^*$ orbitals. Formally, these occupation patterns (a)-(f) result in the following six *Slater Determinants*

$$\Psi_a = \frac{1}{\sqrt{2}}\begin{vmatrix}\phi_x|\uparrow\rangle(1) & \phi_x|\downarrow\rangle(1)\\ \phi_x|\uparrow\rangle(2) & \phi_x|\downarrow\rangle(2)\end{vmatrix} = \frac{1}{\sqrt{2}}\phi_x\phi_x(|\uparrow\downarrow\rangle - |\downarrow\uparrow\rangle)\,, \tag{3.1a}$$

$$\Psi_b = \frac{1}{\sqrt{2}}\begin{vmatrix}\phi_y|\uparrow\rangle(1) & \phi_y|\downarrow\rangle(1)\\ \phi_y|\uparrow\rangle(2) & \phi_y|\downarrow\rangle(2)\end{vmatrix} = \frac{1}{\sqrt{2}}\phi_y\phi_y(|\uparrow\downarrow\rangle - |\downarrow\uparrow\rangle)\,, \tag{3.1b}$$

$$\Psi_c = \frac{1}{\sqrt{2}}\begin{vmatrix}\phi_x|\uparrow\rangle(1) & \phi_y|\downarrow\rangle(1)\\ \phi_x|\uparrow\rangle(2) & \phi_y|\downarrow\rangle(2)\end{vmatrix} = \frac{1}{\sqrt{2}}\left(\phi_x\phi_y|\uparrow\downarrow\rangle - \phi_y\phi_x|\downarrow\uparrow\rangle\right)\,, \tag{3.1c}$$

$$\Psi_d = \frac{1}{\sqrt{2}}\begin{vmatrix}\phi_x|\downarrow\rangle(1) & \phi_y|\uparrow\rangle(1)\\ \phi_x|\downarrow\rangle(2) & \phi_y|\uparrow\rangle(2)\end{vmatrix} = \frac{1}{\sqrt{2}}\left(\phi_x\phi_y|\downarrow\uparrow\rangle - \phi_y\phi_x|\uparrow\downarrow\rangle\right)\,, \tag{3.1d}$$

$$\Psi_e = \frac{1}{\sqrt{2}}\begin{vmatrix}\phi_x|\uparrow\rangle(1) & \phi_y|\uparrow\rangle(1)\\ \phi_x|\uparrow\rangle(2) & \phi_y|\uparrow\rangle(2)\end{vmatrix} = \frac{1}{\sqrt{2}}(\phi_x\phi_y - \phi_y\phi_x)|\uparrow\uparrow\rangle\,, \tag{3.1e}$$

$$\Psi_f = \frac{1}{\sqrt{2}}\begin{vmatrix}\phi_x|\downarrow\rangle(1) & \phi_y|\downarrow\rangle(1)\\ \phi_x|\downarrow\rangle(2) & \phi_y|\downarrow\rangle(2)\end{vmatrix} = \frac{1}{\sqrt{2}}(\phi_x\phi_y - \phi_y\phi_x)|\downarrow\downarrow\rangle\,, \tag{3.1f}$$

whereby the usual shortened textbook notation

$$\phi_x\phi_y|\uparrow\downarrow\rangle \stackrel{!}{=} \phi_x(1)\phi_y(2)|\uparrow(1)\rangle|\downarrow(2)\rangle \tag{3.2}$$

has been employed. Undoubtedly, all these wave functions fulfill the antisymmetry criterion with respect to particle exchange *by construction*. However, the

correct wave functions have to be eigenfunctions of the total spin momentum operator $\mathbf{S}^2$ as well. This condition—as discussed extensively in Sec. A—makes additional demands on the structure of the wave functions. Actually, the wave function **must not** change when any two antiparallel spins are pairwise flipped in the valence orbitals:

- The two high-spin wave functions $\Psi_e$ (3.1e) and $\Psi_f$ (3.1f) fulfill this prerequisite and thus indeed represent the correct structure which the triplet ground state wave functions of the oxygen molecule must assume.
- Contrariwise, this is not the case for the Slater Determinants $\Psi_c$ (3.1c) and $\Psi_d$ (3.1d) as elucidated in Sec. A. Notwithstanding, the symmetric and antisymmetric linear combination of $\Psi_e$ and $\Psi_f$ yields eigenfunctions of $\mathbf{S}^2$ to a low-spin triplet and a singlet state respectively, as also shown in Sec. A.
- For the two Slater Determinants $\Psi_a$ (3.1a) and $\Psi_b$ (3.1b) this problem does not arise, since they are indeed correct singlet eigenfunctions of $\mathbf{S}^2$.

The latter two Slater Determinants $\Psi_a$ (3.1a) and $\Psi_b$ (3.1b), however, exhibit another kind of flaw: Since the respective orbitals $\phi_x$ and $\phi_y$ are exactly degenerate, the electrons can switch between these two configurations [109] and thereby lower the electronic repulsion. A further pairwise symmetric and antisymmetric combination of the respective Slater Determinants accounts for this *static correlation* without altering the already correct spin part. Finally, the correct set of wave functions for the oxygen molecule is:

$$\text{a) } {}^1\Delta_g: \quad \Psi_1^s = \frac{1}{\sqrt{2}}(\Psi_a - \Psi_b) = \frac{1}{2}(\phi_x\phi_x - \phi_y\phi_y)(|\uparrow\downarrow\rangle - |\downarrow\uparrow\rangle) \tag{3.3a}$$

$$\text{b) } {}^1\Delta_g: \quad \Psi_2^s = \frac{1}{\sqrt{2}}(\Psi_a + \Psi_b) = \frac{1}{2}(\phi_x\phi_x + \phi_y\phi_y)(|\uparrow\downarrow\rangle - |\downarrow\uparrow\rangle) \tag{3.3b}$$

$$\text{c) } {}^1\Sigma_g^+: \quad \Psi_3^s = \frac{1}{\sqrt{2}}(\Psi_c - \Psi_d) = \frac{1}{2}(\phi_x\phi_y + \phi_y\phi_x)(|\uparrow\downarrow\rangle - |\downarrow\uparrow\rangle) \tag{3.3c}$$

$$\text{d) } {}^3\Sigma_g^-: \quad \Psi_4^t = \frac{1}{\sqrt{2}}(\Psi_c + \Psi_d) = \frac{1}{2}(\phi_x\phi_y - \phi_y\phi_x)(|\uparrow\downarrow\rangle + |\downarrow\uparrow\rangle) \tag{3.3d}$$

$$\text{e) } {}^3\Sigma_g^-: \quad \Psi_5^t = \frac{1}{\sqrt{2}}(\phi_x\phi_y - \phi_y\phi_x)|\uparrow\uparrow\rangle \tag{3.3e}$$

$$\text{f) } {}^3\Sigma_g^-: \quad \Psi_6^t = \frac{1}{\sqrt{2}}(\phi_x\phi_y - \phi_y\phi_x)|\downarrow\downarrow\rangle \tag{3.3f}$$

As long as the Spin-Orbit Coupling is neglected, these **six** wave functions correspond to **three** energetically distinct electronic states: the threefold degenerate triplet ground state ${}^3\Sigma_g^-$, the twofold degenerate first excited singlet state ${}^1\Delta_g$ and the second excited singlet state ${}^1\Sigma_g^+$. Their respective experimental energies and quantum numbers $\Lambda$, $S$ and $S_z$ are summarized in Tab. 3.1. The dissociation limit, i.e. the electronic state of the two oxygen atoms in the limit of large bond lengths, is ${}^3\mathrm{P}+{}^3\mathrm{P}$ for all of these states, since all the $2\sigma_p$, $2\pi_p$, $2\pi_p^*$ and $2\sigma_p$ orbitals collapse into the three degenerate $2p_x$, $2p_y$ and $2p_z$ orbitals of the isolated oxygen atom upon bond elongation. This also applies to the next three excited states of the oxygen molecule, namely a ${}^1\Sigma_u^-$, a ${}^3\Delta_u$ and a ${}^3\Sigma_u^+$ state, which can be constructed by excitation of one of the $2\pi_p$ electrons into

| | $\Psi$ | $\Lambda$ | $S$ | $S_z$ | $i$ | $\sigma_v$ | $\mathbf{\Delta E}$ (eV) |
|---|---|---|---|---|---|---|---|
| $^1\Delta_g$ | $\Psi_1^s$ | 2 | 0 | 0 | +1 | ±1 | 0.975 |
| $^1\Delta_g$ | $\Psi_2^s$ | 2 | 0 | 0 | +1 | ±1 | 0.975 |
| $^1\Sigma_g^+$ | $\Psi_3^s$ | 0 | 0 | 0 | +1 | −1 | 1.624 |
| $^3\Sigma_g^-$ | $\Psi_4^t$ | 0 | 1 | 0 | +1 | +1 | 0.00 |
| $^3\Sigma_g^-$ | $\Psi_5^t$ | 0 | 1 | +1 | +1 | +1 | 0.00 |
| $^3\Sigma_g^-$ | $\Psi_6^t$ | 0 | 1 | −1 | +1 | +1 | 0.00 |

Table 3.1: Spectroscopic symbols, quantum numbers, symmetry with respect to inversion $i$ (*parity*), symmetry with respect to reflection $\sigma_h$ at the planes including the molecular axis and relative experimental excitation energies [174] of the discussed electronic states of the oxygen molecule.

the $2\pi_p^*$ orbital (see Fig. 3.8). These states—as well as certain triplet and singlet $\Pi$ states—lie more than 6 eV higher in energy with respect to the ground state and have thus not been explicitly addressed in these reference studies. However, they play an important role in the determination of *transition rates* and are thus discussed in Sec. 3.2.2.

## 3.2 Quantum Chemical Calculations

### 3.2.1 Calculational Details

Almost all Quantum Chemical calculations presented in this chapter have been calculated with routines provided by the simulation package MOLPRO [175] due to the extensive possibilities it offers. *Correlation Consistent Dunning Basis Sets*, which guarantee a smooth convergence towards the infinite basis set limit, have been used with additional polarized [176], diffusive [177] and core-core/core-valence [178] functions up to a sextuple-zeta [179, 180] level of accuracy. However, all results presented in this section are calculated with a quintuple V5Z basis without any additional functions and with MOLPRO's default numerical thresholds. As discussed in Sec. B.1, this ensures convergence with respect to relative energies and furthermore with respect to the equilibrium properties of the oxygen molecule to a large extent.

To check the quality of the respective methods we compared miscellaneous simulated features of the molecule with their experimental values and with previously published theoretical studies. In a first step a whole set of *ab initio* calculations with varying oxygen-oxygen distance was performed in the proximity of the experimental bond length—starting at 0.75 Å and ending at 3.5 Å in

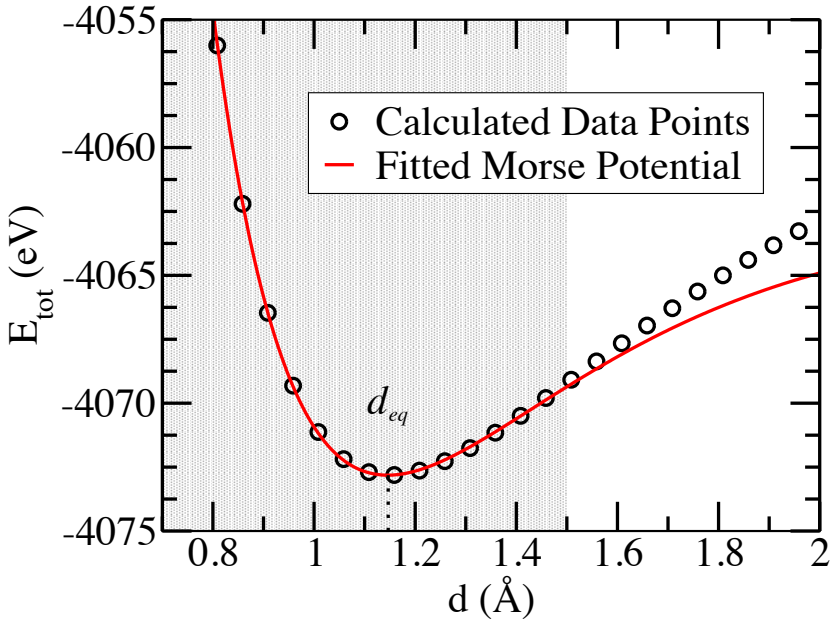


Figure 3.3: Total energy $E_{tot}$ of the oxygen molecule calculated by the Restricted Open-Shell Hartree-Fock method in a V5Z basis set: The open circles show the simulated values, the solid line a fit to a Morse Potential (3.4) in the region in between 0.7 Å and 1.5 Å (shaded grey area).

steps of 0.05 Å. The obtained data was fitted with a *Morse Potential* [181]

$$E_{tot}(d) = D \cdot \left(1 - \exp^{-a(d-d_{\mathrm{eq}})}\right)^2 + D_\infty \tag{3.4}$$

to determine the equilibrium state of the molecule, i.e. its equilibrium bond length $d_{\mathrm{eq}}$ and its equilibrium total energy $E_{\mathrm{eq}} = E_{tot}(d_{\mathrm{eq}})$. The fitting was only performed in the proximity of the equilibrium state, i.e. in the region in between 0.7 Å and 1.5 Å, where the approximations underlying the Morse Potential are expected to hold (see Fig. 3.3). Indeed, relative errors in the order of magnitude of 0.0001% are achieved after the root mean square error minimization in the region of interest. A further trimming of this interval just virtually changes the outcome of the fitting process, as also inspected. The resulting equilibrium bond lengths $d_{\mathrm{eq}}$ and the equilibrium total energies $E_{\mathrm{eq}}$ have then been used to determine the molecule's binding energy

$$E_{\mathrm{b}} = E_{\mathrm{eq}} - 2 \cdot E_{\mathrm{O}}. \tag{3.5}$$

For the evaluation of Eq. (3.5) the total energy of a single oxygen atom $E_{\mathrm{O}}$ is required as well: A straightforward calculation with the same method and the same class of basis set, e.g. Hartree-Fock/V5Z, results in a systematic error, the so called *Basis Set Superposition Error* (BSSE). Due to the effectively different number of basis functions employed for the $O_2$ molecule and the O atom—the number of functions for an $O_2$ is twice as large in the same class of basis

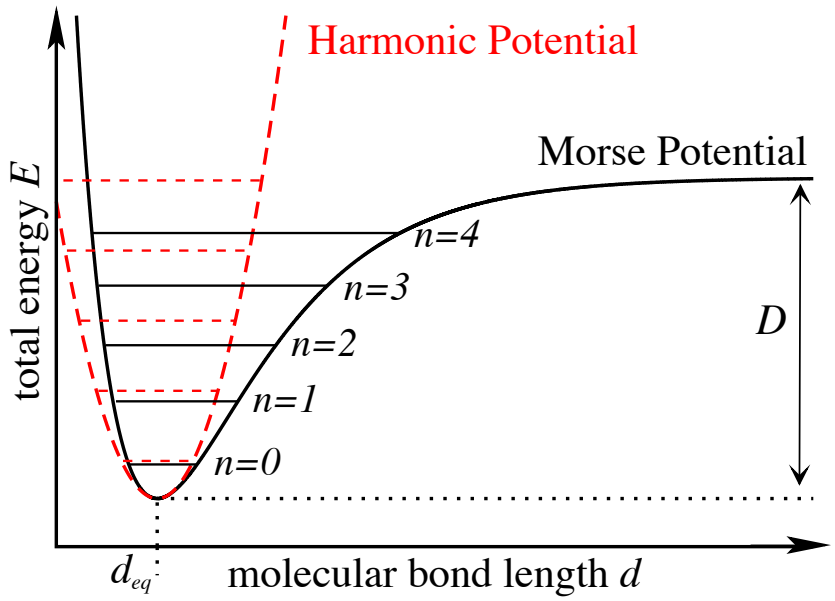


Figure 3.4: Schematic comparison of a *Morse Potential* with a *Harmonic Potential*: The lower vibrational states, which are not energetically equidistant for the Morse Potential, are also shown.

set—the two total energy values are not directly comparable. *Counterpoise Corrections* (CP), i.e. calculations for a single oxygen atom in the basis set of an oxygen molecule, have thus been applied to get rid of this artifact. Thereto also the symmetry operations used to construct the MOs have to be altered by artificially reducing the point group of the system from $D_{2h}$ to $C_{2v}$. Molecular Orbitals constructed under assumption of a mirror plane perpendicular to the molecular axis $\sigma_h$ can obviously not describe a single oxygen atom correctly. The influence of this symmetry reduction on the energy of the $O_2$ molecule has been inspected as well, but it has been found to be vanishingly small (approximately $40 \cdot 10^{-9}$ eV in the V5Z basis set) and thus irrelevant for our calculations.

Furthermore, the effectively measured binding energy is lowered with respect to Eq. (3.5) by the *Zero Point Energy* (ZPE) of the molecule. To account for this effect and to correct the calculated binding energy (3.5) accordingly, the vibrational spectrum of the molecule must be known. Instead of calculating the bond's vibrational frequency $\omega_o$ in the harmonic approximation by the use of analytical derivatives, central differences [175] or even more elaborate methods [182], we take advantage of the already determined Morse Potential fit. The analytic solution of the stationary Schrödinger equation in this kind of potential results [181] in a spectrum of eigenvalues

$$E_{\text{vib}}(n) = \hbar\omega_o \left(n + \frac{1}{2}\right) - \frac{\hbar^2\omega_o^2}{4D}\left(n + \frac{1}{2}\right)^2, \tag{3.6}$$

which—in contrast to the harmonic case—are not equidistant (see Fig. 3.4). For

a molecule with the reduced mass $m$, the vibrational frequency

$$\omega_o = a\sqrt{\frac{2D}{m}} \tag{3.7}$$

can be directly calculated on the basis of the parameters $a$ and $D$ determined in the fitting process. Thus the binding energy including Zero Point Energy Corrections is expressed as

$$E_{\mathrm{b}} = E_{\mathrm{eq}} - 2 \cdot E_{\mathrm{O}} + \frac{\hbar\omega_o}{2} - \frac{\hbar^2\omega_o^2}{16D}, \tag{3.8}$$

whereby anharmonic effects are also included approximatively by this means.

Last but not least also the quality of the excited states' simulation was inspected: Both the resulting energetic gap in between the ${}^3\Sigma_g^-$ and the ${}^1\Delta_g$ configuration, referred to as triplet-singlet gap $\Delta E_{\mathrm{TS}}^{\Delta}$ hereinafter, and the gap in between the ${}^3\Sigma_g^-$ and the ${}^1\Sigma_g^+$ state, referred to as triplet-singlet gap $\Delta E_{\mathrm{TS}}^{\Sigma}$ hereinafter, have been examined. Thereto the total energies of the respective electronic states $E_\Delta/E_\Sigma$ at the equilibrium bond length of the triplet state have been calculated. Equally, Zero Point Energy Corrections for the excitation energies have been considered by determining the vibrational frequencies $\omega_\Delta$ and $\omega_\Sigma$ of the excited states as already done for the ground state. Accordingly, the excitation energies are:

$$\Delta E_{\mathrm{TS}}^{\Delta} = E^{\Delta}(d_{\mathrm{eq}}) - E_{\mathrm{eq}} + \frac{\hbar(\omega_\Delta - \omega_o)}{2} - \frac{\hbar^2\left(\omega_\Delta^2 - \omega_o^2\right)}{16D} \tag{3.9}$$

$$\Delta E_{\mathrm{TS}}^{\Sigma} = E^{\Sigma}(d_{\mathrm{eq}}) - E_{\mathrm{eq}} + \underbrace{\frac{\hbar(\omega_\Sigma - \omega_o)}{2} - \frac{\hbar^2\left(\omega_\Sigma^2 - \omega_o^2\right)}{16D}}_{\text{ZPE corrections}} \tag{3.10}$$

**Hartree-Fock Theory:** Since in nature the vast majority of stable molecules exhibits a closed-shell electronic structure, in which each orbital up to a certain energetic level is fully occupied, a straightforward stratagem is generally employed to halve the amount of memory and computation time needed for a simulation: Instead of addressing each single electron, the respective spin up and spin down electrons that share the same orbital are combined in a lot. This so called *Restricted Hartree-Fock* (RHF) method obviously only allows for the simulation of such closed-shell singlet structures. For the more general case also an *Unrestricted Hartree-Fock* (UHF) method exists, wherein each electron is indeed addressed individually. This approach, however, exhibits serious flaws whenever there is a different number of up and down electrons present: The *exchange-interaction* (see Sec. 2.2.1.2), which lowers the total energy for electrons that share the same spin, results in a relative energetic shift between up and down orbitals in such cases (see Fig. 3.5). Due to this lift of degeneracy, the total wave function is **not** an eigenfunction of the total spin operator $\mathbf{S}^2$ anymore (see Sec. A) and thus contains various portions of different spin configurations. This effect, commonly known as *spin-contamination*, can distort the results considerably, even if the spin-contamination is minuscule (see Sec. 3.2.2). To avoid such artifacts, the *Restricted Open-Shell Hartree-Fock* (ROHF) method is applied: Therein the electrons are still treated individually, but the respective

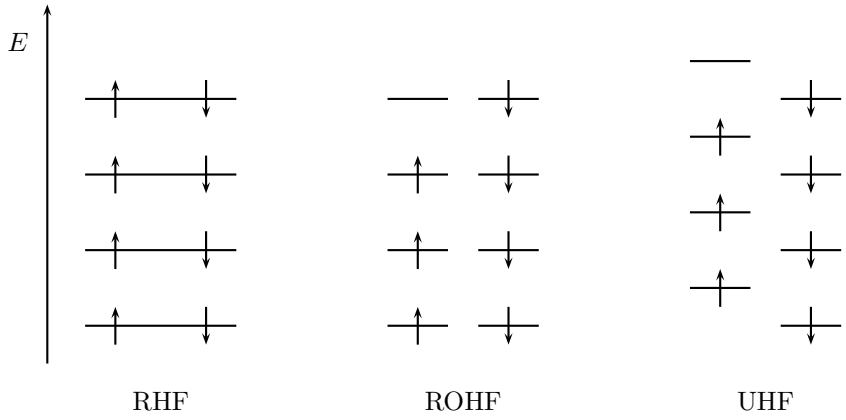


Figure 3.5: Schematic Sketch of the energetic constraints put on up and down spinorbitals in the *Restricted Hartree-Fock* (RHF), *Restricted Open-Shell Hartree-Fock* (ROHF) and in the *Unrestricted Hartree-Fock* (UHF) methods.

up and down orbitals are forced to be equal although not equally occupied. In this work, both the Unrestricted and the Restricted Open-Shell Hartree-Fock method are employed to address the open-shell structure of the oxygen molecule.

**MCSCF & CASSCF:** As discussed in Sec. 3.1, a single Slater Determinant is not sufficient to reproduce the correct wave function structure that the excited singlet states of the oxygen molecule exhibit. Thus, instead of employing Determinants, *Configuration State Functions* (CSFs), i.e. symmetry adapted linear combinations of Slater Determinants that are also eigenfunctions of $\mathbf{S}^2$, are utilized in the *Multiconfiguration SCF* method. The simplest case is to restrict the electronic optimization to one single CSF for each electronic state, i.e. exactly to one of the wave functions (3.3a)-(3.3f). Such simulations, referred to as *MCSCF* hereinafter, allow to sense the role and importance that *statical correlation* plays. Furthermore, a portion of *dynamical correlation* can also be recovered by including additional excited CSFs with the same symmetry and the same spin configuration. For linear molecules MOLPRO allows the auxiliary specification of the total orbital angular momentum of the CSFs, thus permitting to discriminate *a priori* between the $^1\Delta_g$ and the $^1\Sigma_g^+$ state. The *active space* (see Sec. 2.2.1.6) is then further restricted by forcing the $1\sigma_s$ and the $1\sigma_s^*$ orbital to be fully occupied in each of the CSFs. Calculations with such a setup are referred to as *CASSCF* hereinafter.

**FVCI, CISD & MRCI:** To recover additional *dynamic correlation*, single-reference Configuration Interaction calculations have been performed on the basis of the ROHF wave functions. In a first step just the single and double excitations of the two valence electrons, an approach commonly known as *Full Valence CI* (FVCI) [183], have been allowed for. Thereby the core $1\sigma_s$ and $1\sigma_s^*$ electrons have been "frozen" to their Hartree-Fock orbitals in all Slater Determinants and are thus not correlated at all. All other closed orbitals ($2\sigma_s$, $2\sigma_s^*$, $2\sigma_p$

and $2\pi_p$) are explicitly correlated but only through *internal* single and double excitations [175]. Finally, all possible excitations[2] of the two valence electrons in the additionally available orbitals (173 in the V5Z basis set) have been included. In practice, this results in 28 "internal" CSFs, 72 "singly-excited" CSFs and 81 "doubly excited" CSFs for the triplet ground state—constructed on the basis of the single ROHF Slater Determinant.
In a second step, also the dynamical correlation of the inner electrons was accounted for by including all their single and double excitations in the CISD runs. Under the constraint of still "frozen" core $1\sigma_s$ and $1\sigma_s^*$ orbitals, this results in 21 "internal" CSFs, 138 "singly-excited" CSFs and 263 "doubly-excited"CSFs for the triplet ground state.
Additionally, Multireference Configuration Interaction calculations with single and double excitations (MRCI) (see Sec. 2.2.1.6), whose starting point are the six multiple Determinant CASSCF wave functions for the three discussed electronic states, have been performed as well. Still, the core $1\sigma_s$ and $1\sigma_s^*$ electrons have been assumed to be "frozen" in their Hartree-Fock orbitals, as already done in the underlying CASSCF calculations. However, all remaining orbitals are "active" in this case. One has to realize that the reference CASSCF wave functions for the various electronic states do not just differ in the outer, open $2\pi^*$ orbitals but also slightly in the closed inner shells, whose relaxation depends on the valence electrons as well. Thus the CASSCF method yields not, e.g., one single $2\sigma_s$ MO as the ROHF references but a whole set of them: one for each of the electronic states. If combined with each other, they yield the 60 basis reference CSFs, out of which 336 "internal", 1008 "singly-excited" and 2448 "doubly-excited" CSFs are constructed.

[2]For this system with two "active" electrons, the single and double excitations are indeed all possible excitations.

### 3.2.2 Results & Discussion

**The Ground State Properties:**

In a first step, the key properties of the ground state, i.e. the equilibrium oxygen-oxygen distance $d_{eq}$ (summarized in Tab. 3.2) and the vibrational frequency $\omega_o$ (summarized in Tab. 3.3) have been analyzed. Although the Hartree-Fock methods exhibit a typical overbinding, they reproduce the molecular bond length already quite satisfactorily. This is not too surprising due to the Single Determinant character of the $O_2$ ground state. Accordingly, the single CSF in the MCSCF method coincides with the single Determinant in the ROHF method and thus the two algorithms yield identical results. The same line of reasoning applies to the vibrational frequency, which is in the right order of magnitude, but—due to its higher sensitivity on the shape of the Potential Energy Curve—exhibits a larger relative error. In the end, the stepwise introduction of further dynamical correlation in the FVCI, CISD, CASSCF and MRCI methods gives almost a perfect agreement with the experimental data for both discussed molecular properties. Correspondence to previously published theoretical studies is excellent as well: Indeed, the occurring numerical deviations with respect to literature can be traced back to the different types and levels of basis sets employed in the various studies.

| $d_{eq}$ (Å) | Reference | |
|---|---|---|
| 1.153 | UHF | this work |
| 1.146 | ROHF | this work |
| 1.146 | MCSCF | this work |
| 1.213 | CASSCF | this work |
| 1.177 | FVCI | this work |
| 1.187 | CISD | this work |
| 1.204 | MRCI | this work |
| 1.207 | experiment | [184] |
| 1.163 | Hartree-Fock | [185] |
| 1.168 | Hartree-Fock | [186] |
| 1.246 | Møller Plesset order 2 | [186] |
| 1.242 | Møller Plesset order 2 | [185] |
| 1.211 | Møller Plesset order 3 | [185] |
| 1.278 | Minimal basis / Full Valence CI | [183] |
| 1.236 | First Order CI | [187] |
| 1.206 | CI with Singles and Doubles | [185] |
| 1.221 | Quadratic CI with Singles and Doubles | [186] |
| 1.211 | CASSCF | [188] |
| 1.210 | MRCI | [189] |
| 1.213 | MRCI+Q | [189] |
| 1.193 | Dynamic Monte Carlo | [190] |

Table 3.2: Equilibrium molecular bond length $d_{eq}$ of the $O_2$ molecule in its ${}^3\Sigma_g^-$ ground state at different levels of theory. The values were determined by fitting to a Morse Potential (3.4) as discussed in Sec. 3.2.1.

| $\omega_o$ (cm $^{-1}$) | Reference | |
|---|---|---|
| 2002 | UHF | this work |
| 2045 | ROHF | this work |
| 2045 | MCSCF | this work |
| 1540 | CASSCF | this work |
| 1808 | FVCI | this work |
| 1718 | CISD | this work |
| 1586 | MRCI | this work |
| 1580 | experiment | [184] |
| 1998 | Hartree-Fock | [186] |
| 1413 | Møller Plesset order 2 | [186] |
| 1673 | Minimal basis / Full Valence CI | [183] |
| 1499 | First Order CI | [187] |
| 1639 | Quadratic CI with Singles and Doubles | [186] |
| 1578 | CASSCF | [188] |
| 1558 | MRCI | [189] |
| 1550 | MRCI+Q | [189] |
| 1665 | Dynamic Monte Carlo | [190] |

Table 3.3: Vibrational frequencies $\omega_o$ of the $O_2$ molecule in its $^3\Sigma_g^-$ ground state at different levels of theory. The values were determined by fitting to a Morse Potential (3.4) as discussed in Sec. 3.2.1.

In a next step, the binding energy $E_\mathrm{b}$ (3.5) has been calculated as summarized in Tab. 3.4. The agreement with the experiment is not satisfactory in this case: The pure Hartree-Fock methods fail dramatically—predicting a binding energy almost 4 eV lower than the experimental value. However, the explicit treatment of correlation in the more sophisticated methods yields better but still not "chemical accurate" results. In a first step to improve these calculations, the inherent flaws of the employed methods, i.e. the Basis Set Superposition Error and the Zero Point Energy Corrections, have been addressed to achieve maximal accuracy within the algorithm's boundaries (see Tab. 3.4). While Counterpoise Corrections play just a minor role due to the huge basis set employed (see Sec. B.1), the Zero Point Energy additionally lowers the value of the simulated binding energy and thus makes the discrepancy in between theory and experiment even more evident[3]. Furthermore, neither the explicit inclusion of the $1\sigma_s$ electrons in the MRCI method nor an increased numerical integration accuracy improves the simulated binding energy significantly (see Sec. B.1).

As a matter of fact, this relatively large error in the binding energy is caused by a systematic error of truncated CI methods: the lack of size consistency. A CISD calculation of the oxygen molecule includes configurations that exhibit a single excitation on one fragment (S-Determinants), configurations that exhibit a single excitation on both fragments (D-Determinants) and configurations that exhibit a double excitation on one fragment (also D-Determinants). The respective CISD simulation of an isolated atom yields single and double

[3]The main error source is not the Zero Point Energy Correction, the values of which are in almost perfect agreement with respect to the experiment as discussed above (see Tab. 3.3) but still the underlying total energy values.

| $E_b$ (eV) | Reference | |
|---|---|---|
| -1.566 | UHF | this work |
| -1.566 | UHF, +CP | this work |
| -1.441 | UHF, +CP, +ZPE | this work |
| -1.332 | ROHF | this work |
| -1.323 | ROHF, +CP | this work |
| -1.195 | ROHF, +CP, +ZPE | this work |
| -1.387 | MCSCF | this work |
| -1.323 | MCSCF, +CP | this work |
| -1.195 | MCSCF, +CP, +ZPE | this work |
| -4.047 | CASSCF | this work |
| -4.005 | CASSCF, +CP | this work |
| -3.909 | CASSCF, +CP, +ZPE | this work |
| -3.996 | FVCI | this work |
| -3.970 | FVCI, +CP | this work |
| -3.857 | FVCI, +CP, +ZPE | this work |
| -4.230 | CISD | this work |
| -4.205 | CISD, +CP | this work |
| -4.098 | CISD, +CP, +ZPE | this work |
| -4.688 | MRCI | this work |
| -4.663 | MRCI, +CP | this work |
| -4.564 | MRCI, +CP, +ZPE | this work |
| -4.105 | CASSCF (PEC) | this work |
| -4.010 | CASSCF (PEC), +ZPE | this work |
| -5.030 | MRCI (PEC) | this work |
| -4.933 | MRCI (PEC), +ZPE | this work |
| -5.116 | experiment | [191] |
| -5.123 | experiment | [192] |
| -1.253 | Hartree-Fock | [186] |
| -1.431 | Hartree-Fock, + ZPE | [92] |
| -4.11 | Minimal basis / Full Valence CI | [183] |
| -4.864 | First Order CI | [187] |
| -5.100 | Møller Plesset order 2 | [186] |
| -4.294 | Quadratic CI with Singles and Doubles | [186] |
| -5.200 | Coupled Cluster with Singles and Doubles | [193] |
| -5.065 | MRCI (PEC) | [189] |
| -5.193 | MRCI+Q (PEC) | [189] |
| -4.710 | Quantum Monte Carlo | [190] |
| -4.844 | Quantum Monte Carlo, +ZPE | [194] |

Table 3.4: Binding energy $E_b$ of the $O_2$ molecule as defined in Eq. (3.5) at different levels of theory with additional *Counterpoise Corrections* (CP) and *Zero Point Energy Corrections* (ZPE). All calculations have been done in the V5Z Dunning basis set at the respective equilibrium bond lengths $d_{eq}$ given in Tab. 3.2. For the ZPE Corrections as defined in Eq. (3.8) the respective frequencies $\omega_o$ specified in Tab. 3.3 have been used. Additionally, the binding energies derived from the calculated Potential Energy Curves (PEC) are listed.

excited configurations of the individual oxygen. However, taking this resulting energy twice to describe two oxygen atoms at infinite distance—as done for the calculation of the binding energy (3.5)—implicitly includes configurations that exhibit double excitations on each of the two atoms. Qualitatively, this configuration setup corresponds to a CISDTQ calculation and can thus not be compared energetically to the CISD calculation of the oxygen molecule. This lack of size consistency can be overcome by using *Quadratic CI* [195] or it can be circumvented approximatively[4] by simulating two oxygen atoms at large distances. However, this workaround is not foolproof either, as can be seen in Fig. 3.6, where the Potential Energy Curve (PEC), i.e. the total energy as function of the molecular bond length, is plotted for the various discussed simulation methods. For the description of two almost non-interacting oxygen atoms at large distance from each other within one simulation, at least[5] two independent Slater-Determinants are needed. Hence all single Determinant methods (UHF, ROHF and MCSCF) are doomed to fail in the description of the dissociation process from the beginning: Indeed, all of them exhibit a by far too strong and too long-ranged binding. Analogously, the FVCI and the CISD calculations, which account for multiple Determinants but still for just one ground state reference Determinant (see Sec. 2.2.1.6), do not succeed either. Solely the CASSCF and the MRCI calculations are able to reproduce the bond breaking correctly, whereby only the MRCI simulation results in an acceptable binding energy (see Tab. 3.4). Nevertheless, an absolute error of approximately 0.2 eV (4% of the experimental binding energy) with respect to the experimental value still occurs: An inclusion of higher order excitations can recover this missing portion of correlation, as comparison with literature shows [189].

**The Excited State Properties:**

As discussed in Sec. 3.1, multiple Determinants must necessarily be included in the simulation of the $O_2$'s excited single states to reproduce their correct wave functions. Thus the single Determinant Hartree-Fock method cannot correctly describe these states as a matter of principle. Nevertheless, the energy of the single Slater Determinants (3.1a) and (3.1b) that are used in the construction of the wave function for the $^1\Delta_g$ state can be addressed in spite of that, although they are not the correct wave functions that are sought after. In these two Determinants either the $\phi_x$ or the $\phi_y$ orbital is doubly occupied, which indeed leads to the correct projected angular momentum of $\Lambda = 2$. However, the electrons are not able to avoid each other by occupying both the $\phi_x$ and $\phi_y$ orbitals as it occurs in the correct wave functions (3.3a) and (3.3b) for this electronic state. The thereby generated additional electrostatic repulsion leads to a triplet-singlet gap that is by far too large in the ROHF method (see Tab. 3.5). This triplet-singlet gap is even larger in the UHF calculations: For the singlet state both the UHF and ROHF method yield the same result due to the full occupancy of all orbitals in this configuration. Contrariwise, the UHF energy is lowered with respect to the ROHF value (see Fig. 3.6) for the triplet ground state due to spin-contamination ($S = 1.01427$ instead of $S = 1$ in the V5Z basis

[4] Size extensivity is not guaranteed for truncated CI methods [55] either.

[5] Please note that the Hartree-Fock method is size consistent so that such problems do not arise when addressing the individual dissociation fragments, e.g., to determine the binding energy.

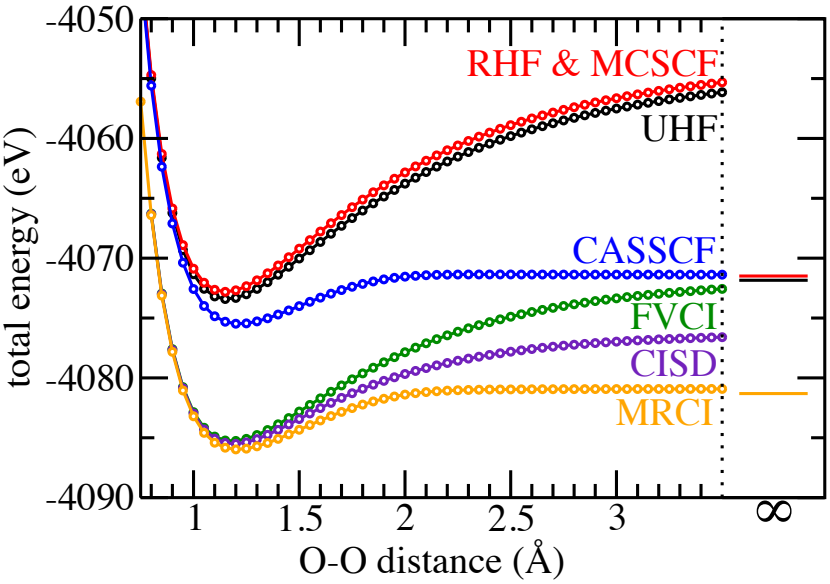


Figure 3.6: Total energy for the $O_2$ molecule in its triplet ground state as function of the oxygen-oxygen distance at different levels of theory. The failure of all single-reference methods in describing bond breaking is self evident. To highlight the effect of size inconsistency, two times the respective energy of a single oxygen atom, as calculated at the same levels of theory with Counterpoise Corrections, is shown on the right hand side "∞". For the CASSCF calculations this value corresponds to the RHF calculation, whereas for the FVCI and CISD calculations this value is virtually indistinguishable from the MRCI value. All simulations have been performed in the V5Z basis set.

set).

The other two available Slater-Determinants (3.1c) and (3.1d) are not accessible straightforwardly in MOLPRO's Hartree-Fock routine, since they are no spin eigenfunctions. Hence MOLPRO refuses its calculation and correctly suggests the utilization of a multiple Determinant technique. Nevertheless, other Quantum Chemical software allows to simulate these Slater Determinants with the UHF method in spite of their inherent spin-contamination[6]. Since such calculations are instructive for the latter discussion of the singlet state's representability in DFT, we additionally used Gaussian [199] to address these special electronic configurations. In a first step, all the triplet ground state properties we have already discussed have been recomputed with Gaussian and have been found to be consistent if not equal to MOLPRO's results (see Sec. B.1). Thereby all calculations have been performed in the V5Z basis set but with additional polarization functions that Gaussian includes by default. The resulting energy gap $\Delta E^C_{\mathrm{TS}}$ in between this special configuration and the triplet ground state at

[6]Actually, the quantum number $S$ that should be zero for a singlet state amounts to 1.0255 in the Gaussian simulations: Even after "annihilation of the first spin-contaminant" [199, 200] a spurious spin-contamination of $S = 0.2044$ remains.

(a) Triplet-Singlet Energy Gap for the $^1\Delta_g$ State

| $\Delta E_{\mathrm{TS}}^{\Delta}$ (eV) | Reference | |
|---|---|---|
| 2.322 [2.323] | UHF | this work |
| 1.723 [1.722] | ROHF | this work |
| 1.287 [1.286] | MCSCF | this work |
| 0.962 [0.956] | CASSCF | this work |
| 1.094 [1.095] | FVCI | this work |
| 0.923 [0.923] | CISD | this work |
| 0.966 [0.961] | MRCI | this work |
| 0.98 | experiment | [184] |
| 0.981 | experiment | [196] |
| 0.975 | experiment | [174] |
| 1.089 | Generalized Valence Bond CI | [197] |
| 0.92 | Minimal basis / Full Valence CI | [183] |
| 1.098 | First Order CI | [187] |
| 1.028 | Spin Corrected Møller Plesset order 4 | [198] |
| 1.134 | CASSCF | [188] |
| 1.025 | MRCI+Q | [189] |

(b) Triplet-Singlet Energy Gap for the $^1\Sigma_g^+$ State

| $\Delta E_{\mathrm{TS}}^{\Sigma}$ (eV) | Reference | |
|---|---|---|
| 0.755 [0.755] | UHF (Gaussian, $\Delta E_{\mathrm{TS}}^{C}$) | this work |
| 1.510 [1.510] | UHF (Gaussian) | this work |
| 2.550 [2.549] | MCSCF | this work |
| 1.488 [1.477] | CASSCF | this work |
| 1.953 [1.953] | FVCI | this work |
| 1.565 [1.576] | CISD | this work |
| 1.622 [1.612] | MRCI | this work |
| 1.624 | experiment | [174] |
| 1.36 | Minimal basis / Full Valence CI | [183] |
| 1.776 | First Order CI | [187] |
| 0.495 | Unrestricted Møller Plesset order 4 | [198] |
| 1.658 | MRCI+Q | [189] |
| 1.766 | CASSCF | [188] |

Table 3.5: Triplet-singlet energy gaps $\Delta E_{\mathrm{TS}}^{\Delta}$ and $\Delta E_{\mathrm{TS}}^{\Sigma}$ for the $^1\Delta_g$ and the $^1\Sigma_g^+$ state respectively. The corresponding Zero Point Energy corrected values are also listed in brackets for the different levels of theory. Almost all calculations have been performed with MOLPRO and a V5Z basis set. Solely for the denoted Gaussian calculations a V5Z basis set with additional polarization functions was employed due to the unavailability of a V5Z basis set in the code.

the equilibrium position, however, is unreasonably small, even smaller than the gap for the $^1\Delta_g$ state (see Tab. 3.5). This is not too surprising, though, since the constructed wave function has been no spin eigenfunction from the beginning. As discussed in Sec. 3.1, the respective wave functions (3.1c) and (3.1d) have to be combined symmetrically and antisymmetrically to yield the low-spin triplet ground state and the $^1\Sigma_g^+$ state respectively. This fact can be exploited to turn the tables and thus to implement a stratagem—commonly known as *projected* Quantum Chemistry [200]—that yields the energy of a multiple Determinant wave function without employing a multiple Determinants method in the simulation:

Indeed, a symmetric or antisymmetric combination of the correct $^1\Sigma_g^+$ wave function (3.3c) with the correct low-spin triplet $^3\Sigma_g^-$ wave function (3.3d) yields the spin-contaminated Slater Determinant (3.1c) again:

$$\Psi_c = \frac{\sqrt{2}}{2} \cdot \left(\Psi_3^s + \Psi_4^t\right). \tag{3.11}$$

However, Eq. (3.11) is still useless in this form, since both wave functions on the right hand side deserve a multiple Determinants ansatz and are thus not accessible in a pure Hartree-Fock type method. However, the calculation of the total energy expectation value of $\Psi_c$ leads to an interesting result:

$$\begin{aligned} E_c = \langle \Psi_c | \, \mathbf{H} \, | \Psi_c \rangle &= \frac{1}{2} \cdot \left(E_\Sigma^s + E_4^t\right) \\ &= \frac{1}{2} \cdot \left(E_\Sigma^s + E\right). \end{aligned} \tag{3.12}$$

Not too surprisingly, the total energy $E_c$ of the Slater Determinant $\Psi_c$ addressed in the Hartree-Fock calculations is just the average of the total energies $E_\Sigma^s$ and $E_4^t$ associated with the singlet $^1\Sigma_g^+$ wave function $\Psi_3^s$ and the low-spin triplet $^3\Sigma_g^-$ wave function $\Psi_4^t$. In the last step, the energy $E_4^t$ of the low-spin triplet state has been replaced with the energy $E$ of the high-spin triplet state[7] that can be and has been addressed correctly with the Hartree-Fock method, since it consists of a single Slater Determinant alone. Thus Eq. (3.12) can now be used to calculate the correct triplet-singlet gap $\Delta E_{\mathrm{TS}}^\Sigma$ for the $^1\Sigma_g^+$ state on the basis of two single Determinant UHF calculations:

$$\begin{aligned} \Delta E_{\mathrm{TS}}^\Sigma &= E_\Sigma^s\left(d_{\mathrm{eq}}\right) - E_{\mathrm{eq}} \\ &= 2 \cdot \left\{E_c\left(d_{\mathrm{eq}}\right) - E_{\mathrm{eq}}\right\}. \end{aligned} \tag{3.13}$$

The thereby calculated energy gap $\Delta E_{\mathrm{TS}}^\Sigma$ is surprisingly good and apparently benefits from some positive error cancellation as the spurious left over spin-contamination after first order annihilation—a wave function projection that works analogously to Eq. (3.12)—suggests[6].

Obviously, this discussed workaround in the Hartree-Fock framework is at most approximative and the correct approach to calculate the triplet-singlet gaps

[7] This substitution does not take into account the level splitting of the ground state due to the Spin-Orbit Coupling. With respect to the accuracy of the Hartree-Fock method, however, this effect is indeed negligible.

| | | exp. | MRCI/V5Z | abs. error | rel. error |
|---|---|---|---|---|---|
| $d_{\text{eq}}$ | (Å) | 1.207 | 1.204 | -0.003 | -0.2% |
| $\omega_o$ | ($\text{cm}^{-1}$) | 1580 | 1586 | +6 | +0.4% |
| $E_{\text{b}}$ | (eV) | -5.123 | -4.933 | +0.190 | +3.7% |
| $\Delta E_{\text{TS}}^{\Delta}$ | (eV) | 0.975 | 0.961 | -0.014 | -1.4% |
| $\Delta E_{\text{TS}}^{\Sigma}$ | (eV) | 1.624 | 1.612 | -0.012 | -0.7% |

Table 3.6: Absolute and relative errors achieved at a MRCI/V5Z level of theory with respect to the key properties of the oxygen molecule.

for this system is to employ a method that allows for multiple Determinants. Already the inclusion of solely the static part of the correlation by using two Determinants in the MCSCF simulations recovers almost 60% of the total correlation effects with respect to the $\Delta E_{\text{TS}}^{\Delta}$ gap. The stepwise inclusion of further dynamical correlation—the static portion is inherently included for CISD and higher level methods—finally yields almost perfect results that smoothly converge towards the experimental value (see Tab. 3.5). This also applies to the simulation of the $^1\Sigma_g^+$ state, whereby dynamical correlation plays an even more significant role due to the absence of closed valence orbitals in this configuration: Whereas the MCSCF calculations are still wrong by more than 0.8 eV, the MRCI simulations eventually reproduce the experimental value almost exactly (also see Tab. 3.5). Finally, also Zero Point Energy Corrections to the triplet-singlet gaps (bracketed values in Tab. 3.5) have been inspected but have been found to be nearly irrelevant since the vibrational frequencies in the various electronic states differ insignificantly.

These extensive simulations of the electronic structure of the $O_2$ clearly show that the MRCI method and a V5Z basis set is best suited to reproduce all the relevant properties of the three energetically lowest lying electronic states. This is substantiated in Tab. 3.6, where apart from all the relevant properties of the molecule also absolute and relative errors with respect to the experimental values are summarized for this specific calculational setup.

**Potential Energy Curves & Transition Probabilities:**

Potential Energy Curves (PECs) on a tight mesh (starting at 0.75 Å and ending at 3.5 Å in steps of 0.025 Å) have been computed at the MRCI/V5Z level of theory for all the discussed states as well (see Fig. 3.7). This figure also shows that all these states approach their correct dissociation limit $^3$P+$^3$P for large oxygen-oxygen distances: Upon bond elongation, all the discussed states, which correspond to all possible electronic rearrangements within a

$$(2\sigma_p)^2\ (2\pi_p)^4\ (2\pi_p^*)^2 \tag{3.14}$$

configuration, collapse into the same ground state of two separate oxygen atoms. This happens due to the fact that the $2\sigma_p$ and $2\pi_p$ Molecular Orbitals—regardless of whether they exhibit bonding or antibonding character—also collapse into the threefold degenerate $2p$ orbitals of the isolated oxygen atom. Analogously, the next three excited states exhibit the same dissociation limit (see Tab. 3.7).

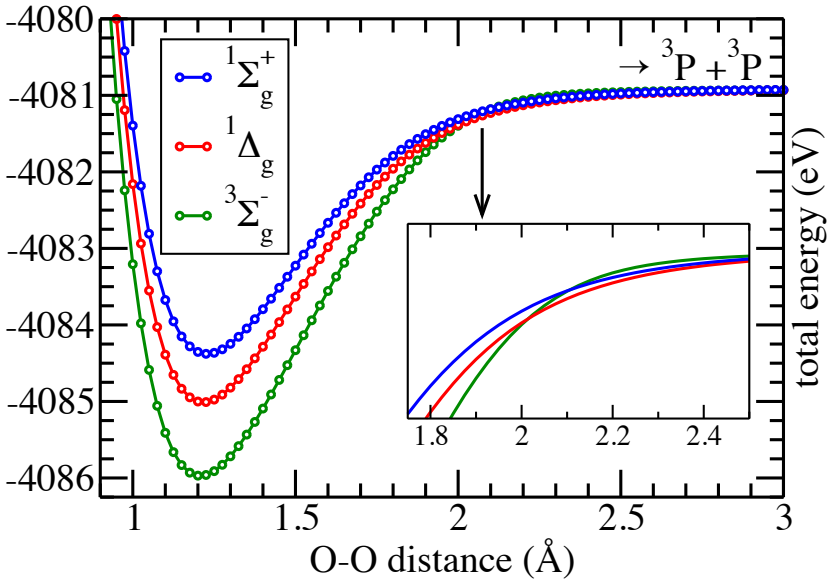


Figure 3.7: Relevant section of the Potential Energy Curves, i.e. the total energy of the three lowest electronic states as function of the oxygen-oxygen distance calculated with MOLPRO at a MRCI/V5Z level of theory. The complete data ranges from 0.75 Å to 3.5 Å, whereby the single data points are separated by 0.025 Å from each other. In the inlet the details of the triplet-singlet curve crossings at approximately 2 Å are shown.

These and the energetically next higher wave functions can be constructed by applying a single electronic excitation to the previously discussed states:

- The first thereby accessible group of states can be constructed by a single excitation from the $2\pi_p$ into the $2\pi_p^*$ orbital. This yields **six** distinct electronic configurations, namely the

  $$^1\Sigma_u^-,\ ^3\Delta_u,\ ^3\Sigma_u^+,\ ^3\Sigma_u^-,\ ^1\Delta_u,\ \text{and the}\ ^3\Sigma_u^+$$

  state (see Tab. 3.7). Because of the wave functions being linear combinations of *ungerade* $2\pi_p$ and *gerade* $2\pi_p^*$ orbitals, all these states change sign under inversion and are therefore *ungerade*.

- The second group of states can be generated by exciting a $2\sigma_p$ electron into the $2\pi_p^*$ orbital. This results in various Π-type configurations with even or odd parity [187]. However, just the energetically lower lying *gerade* states, viz. the

  $$^3\Pi_g \text{ and the } ^1\Pi_g$$

  state, are of interest for the transition rate calculations discussed below. These are also the only Π states that exhibit binding character [188].

The PECs of all these excited states have also been calculated at the MRCI/V5Z level of theory, as shown in Fig. 3.8. There, the Potential Energy Curves for the $\Pi_g$ states exhibit bumps at 1.7 and 1.6 Å respectively due to avoided crossings

| | $\Lambda$ | $S$ | $i$ | $\sigma_v$ | $(2\sigma_p)$ | $(2\pi_p)$ | $(2\pi_p^*)$ | Dissoc. limit | $\Delta E$ (eV) |
|---|---|---|---|---|---|---|---|---|---|
| $^3\Sigma_g^-$ | 0 | 1 | +1 | −1 | 2 | 4 | 2 | $^3$P+$^3$P | 0.000 |
| $^1\Delta_g$ | 2 | 0 | +1 | ±1 | 2 | 4 | 2 | $^3$P+$^3$P | 0.966 |
| $^1\Sigma_g^+$ | 0 | 0 | +1 | +1 | 2 | 4 | 2 | $^3$P+$^3$P | 1.622 |
| $^1\Sigma_u^-$ | 0 | 0 | −1 | −1 | 2 | 3 | 3 | $^3$P+$^3$P | 6.043 |
| $^3\Delta_u$ | 2 | 1 | −1 | ±1 | 2 | 3 | 3 | $^3$P+$^3$P | 6.265 |
| $^3\Sigma_u^+$ | 0 | 1 | −1 | +1 | 2 | 3 | 3 | $^3$P+$^3$P | 6.398 |
| $^3\Sigma_u^-$ | 0 | 1 | −1 | −1 | 2 | 3 | 3 | $^3$P+$^1$D | 9.368 |
| $^1\Delta_u$ | 2 | 0 | −1 | ±1 | 2 | 3 | 3 | $^1$D+$^1$D | 11.592 |
| $^3\Sigma_u^+$ | 0 | 1 | −1 | +1 | 2 | 3 | 3 | $^1$D+$^1$S | 13.222 |
| $^3\Pi_g$ | 1 | 1 | +1 | ±1 | 1 | 4 | 3 | $^3$P+$^3$P | 8.275 |
| $^1\Pi_g$ | 1 | 0 | +1 | ±1 | 1 | 4 | 3 | $^3$P+$^3$P | 9.581 |

Table 3.7: Electronic states of the oxygen molecule: Spectroscopic symbols, quantum numbers, symmetry with respect to inversion $i$, symmetry with respect to reflection $\sigma_h$ at the planes including the molecular axis, occupation numbers, dissociation limits and excitation energies calculated with respect to the equilibrium ground state at a MRCI/V5Z level of theory.

with higher order states of the same symmetry, which have been simulated as well. Contrariwise, all other considered wave functions are orthogonal to each other, as long as the spherical symmetry is not completely restored in the limit of large oxygen-oxygen distances. Thus these electronic states span a diabatic basis in the spirit of the definition given in Sec. 2.1.1. Accordingly, also curve crossings occur as shown exemplarily for the lower lying states in the inlet of Fig. 3.7.

Because of the orthogonality of the addressed electronic states, the mechanism that governs **radiationless** transitions between them must belong to an interaction that has not yet been included in the Quantum Chemical simulations. Furthermore, also **radiative** decay from the lower lying singlet states into the ground state is strongly suppressed due to the $\Delta S = 0$ selection rule that applies to all electromagnetic transitions. Additionally, restrictions for $\Delta \leftrightarrow \Sigma$ and for parity preserving $g \nleftrightarrow u$ transitions exist as well [184]. These selection rules result in experimental lifetimes of about 12 seconds [201] for the $^1\Sigma_g^+$ state and of 72 **minutes** [174] for the $^1\Delta_g$ state. Thus the latter transition is often referred to as the *most forbidden transition in nature* [202]. "Most forbidden" does not mean completely forbidden of course: As a matter of fact, the hitherto ignored interaction of the electron spin with the orbital angular momentum leads to a—usually minute—mixing of certain states with different multiplicity and thus to a partial invalidation of the $\Delta S = 0$ selection rule. This so called Spin-Orbit Coupling (SOC) is not inherently included in the Schrödinger equation but first appears—as the spin degree of freedom itself—in the relativistic, Lorentz-invariant extension of quantum mechanics: the single electron Dirac equation [203, 204] and its many-body generalization [205]. Although there

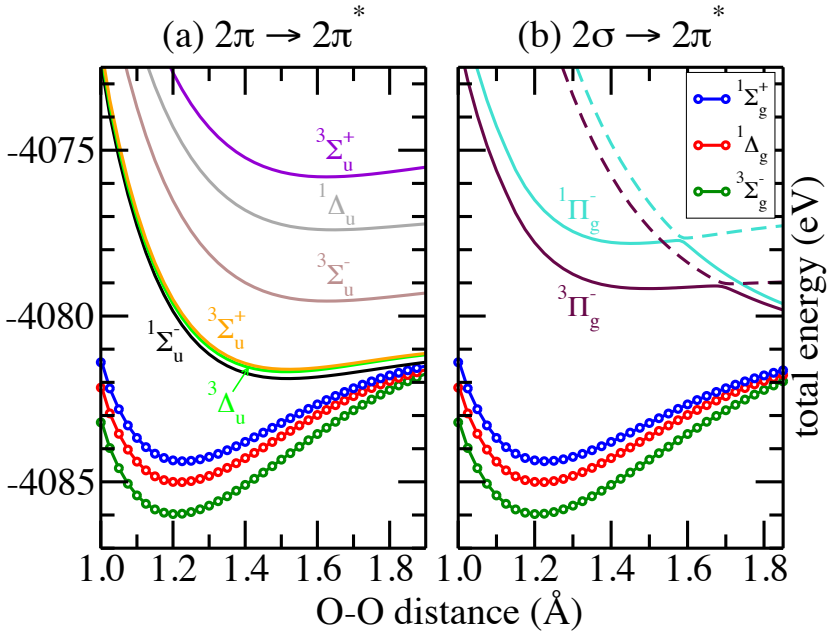


Figure 3.8: Potential Energy Curves for the various electronic states of the oxygen molecule (see Tab. 3.7): Beside the three energetically lowest lying states discussed in detail before (see Fig. 3.7), sub-figure (a) shows the configurations which are yielded by the excitation of a $2\pi_p$ electron into the $2\pi_p^*$ orbital. The states generated by the complementary process—the $2\sigma_p \rightarrow 2\pi_p^*$ transition—are plotted in sub-figure (b). The therein appearing bumps at approximately 1.7 and 1.6 Å are caused by avoided crossings with further Π states, which are also shown as dashed lines. All calculations have been performed with MOLPRO at a MRCI/V5Z level of theory.

are nowadays efficient numerical approaches[8] to the solution of these equations, they are not the method of choice in this case. If just the SOC has to be calculated, but there is no interest in further relativistic effects, such a treatment is a conceptional and numerical overshoot. On this premise a two-component (spin up and spin down) operator, the so called *Breit-Pauli* SOC term [208]

$$V_{\mathrm{SOC}} = \frac{1}{2c^2} \sum_i \left[ \sum_K \frac{Z_K \left(\mathbf{r}_{iK} \times \mathbf{p}_i\right)}{r_{iK}^3} \cdot \mathbf{S}_i - \sum_{i \neq j} \left( \frac{\mathbf{r}_{ji} \times \mathbf{p}_i}{\mathbf{r}_{ij}^3} + 2 \frac{\mathbf{r}_{ij} \times \mathbf{p}_j}{\mathbf{r}_{ij}^3} \right) \cdot \mathbf{S}_i \right], \quad (3.15)$$

can be added to the Hamiltonian of the Schrödinger equation instead. Its point by point derivation, which can be found in several textbooks [209, 210], would

[8] Various extensions both for the Quantum Chemical ansatz, e.g. [206], and for the DFT formalism, e.g. [207], exist.

take us beyond the scope of this thesis. Nevertheless, the derivation's spirit and the thereby employed approximations shall be pointed out in a nutshell:

- The non-relativistic electron-electron interaction $V_{\mathbf{rr}}$ hitherto employed in the Schrödinger equation is spin independent and acts instantaneously. To account for the magnetic interaction and for retardation effects up to the order $1/c^2$, a further term, the so called *Breit Operator* [205], is introduced in the generalization of the Dirac equation for many-body problems.

- The solutions of the Dirac equation consist of four components, as mentioned before: one pair of them corresponds to (spin up and down) eigenstates with positive eigenenergies and the other pair corresponds to (spin up and down) eigenstates with negative eigenenergies [211]. The excitation of one electron from a negative eigenstate into the positive spectrum corresponds to the creation of an electron-positron pair, whereby the vacancy in the negative eigenenergy state describes the antiparticle. Therefore all states with negative eigenenergies have to be filled in the electronic ground state, as long as there is no positron present. This fact implicates that even the single electron Dirac equation represents a many-body problem due to the interaction with this infinite *Fermi sea* of negative energy states. By taking the *Pauli limit* [209], the eigenstates with positive and negative eigenenergies can be decoupled from each other once again. However, this so called *Foldy-Wouthuysen Transformation* [212] solely includes effects up to the order $Z\alpha$ and thus just holds for light atoms and molecules—such as oxygen [208, 213]. Implicitly, this approximation also assumes that the respective application of both $\mathbf{L}$ and $\mathbf{S}$ still results in valid quantum numbers (*Russell-Saunders coupling* [142]).

The resulting Spin-Orbit Coupling (3.15) includes three types of interaction: The first term

$$\sum_K \frac{Z_K \left(\mathbf{r}_{iK} \times \mathbf{p}_i\right)}{r_{iK}^3} \cdot \mathbf{S}_i = \sum_K \frac{Z_K \left(\mathbf{L}_{iK} \cdot \mathbf{S}_i\right)}{r_{iK}^3} \tag{3.16}$$

describes the *Single Electron SOC*, as known from the discussion of the hydrogen atom [142]. There, the orbital angular momentum $\mathbf{L}_{iK}$ of electron $i$ (with respect to the nucleus $K$) couples to the spin of just the same electron $i$. In the many-body problem two additional terms arise due to the additional angular momentum that electrons exhibit with respect to each other. The *Spin-Same Orbit* coupling term

$$\sum_{i \neq j} \frac{\mathbf{r}_{ji} \times \mathbf{p}_i}{\mathbf{r}_{ij}^3} \cdot \mathbf{S}_i = \sum_{i \neq j} \frac{\mathbf{L}_{ij} \cdot \mathbf{S}_i}{\mathbf{r}_{ij}^3} \tag{3.17}$$

describes the interaction of the angular momentum $\mathbf{L}_{ij}$ of electron $i$ with respect to electron $j$ with the spin of electron $i$. Complementarily, the *Spin-Other Orbit* coupling term

$$\sum_{i \neq j} 2\frac{\mathbf{r}_{ij} \times \mathbf{p}_j}{\mathbf{r}_{ij}^3} \cdot \mathbf{S}_i = \sum_{i \neq j} \frac{\mathbf{L}_{ji} \cdot \mathbf{S}_i}{\mathbf{r}_{ij}^3} \tag{3.18}$$

describes the interaction of the angular momentum $\mathbf{L}_{ji}$ of electron $j$ with respect to electron $i$ once again with the spin of electron $i$.

Since the projection of the orbital angular momentum is still a good quantum number in linear systems [173], the effects of the Breit-Pauli term (3.15) can be understood qualitatively by inspecting the single electron case [208]. Under this premise *ladder operators* for the orbital angular momentum $L^{\pm}$ and for the electron spin $S^{\pm}$ (see Sec. A) can be introduced:

$$L^{\pm} = L_x \pm iL_y \tag{3.19a}$$
$$S^{\pm} = S_x \pm iS_y \tag{3.19b}$$

With their help the $\mathbf{L} \cdot \mathbf{S}$ operator can then be simplified to:

$$\mathbf{L} \cdot \mathbf{S} = L_x S_x + L_y S_y + L_z S_z = \frac{1}{4}\left(L^+ S^+ + L^- S^-\right) + L_z S_z. \tag{3.20}$$

All the previously discussed wave functions are eigenfunctions of both the $L_z$ and the $S_z$ operator. Hence the $L_z S_z$ term in Eq. (3.20) provides a coupling mechanism for states that share the same projected angular momentum and the same projected spin, as, e.g., the low-spin triplet ground state ${}^3\Sigma_g^-$ and the ${}^1\Sigma_g^+$ singlet state. Contrariwise the remaining terms in Eq. (3.20) contain ladder operators $L^{\pm}$ and $S^{\pm}$ that either increment or reduce the projected orbital or the projected spin momentum by a single quantum. Thus the first two terms in Eq. (3.20) are responsible for the coupling of states which differ both in their $\Lambda$ and in their $S_z$ quantum number by $\pm 1$. Eventually, this results in the following selection rules:

$$\Delta S = 0 \text{ or } 1 \qquad \Delta S_z = \begin{cases} \pm 1 & \text{if } \Delta\Lambda = \pm 1 \\ 0 & \text{if } \Delta\Lambda = 0 \end{cases} \tag{3.21}$$

In addition, only states with the same parity lead to a nonzero coupling [209].

For the spectrum of electronic states determined before (see Tab. 3.7), these selection rules result in the following matrix elements (see Tab. 3.8):

**$\mathbf{TS_{\Sigma\Sigma}}$**: The low-spin triplet ground state ${}^3\Sigma_{g,0}^-$ ($S_z = 0$) couples to the second excited singlet state ${}^1\Sigma_g^+$. This interaction is crucial for the understanding of the excited states' stability, since it adds a minute portion of singlet character to the ground state.

$TT_{\Sigma\Pi}$: Furthermore, the low-spin triplet ground state interacts with the high-spin triplet ${}^3\Pi_{g,\pm 1}$ configurations, whereas the high-spin states couple to the low-spin triplet ${}^3\Pi_{g,0}$ configuration by exactly the same amount.

$TS_{\Sigma\Pi}$: Additionally, the high-spin states also couple to the singlet ${}^1\Pi_g$ wave function, but not to any of the other energetically lower lying singlet states.

$TS_{\Pi\Delta}$: The ${}^1\Delta_g$ state cannot couple to any $\Sigma$ state due to the too large projected orbital momentum difference. It interacts, however, with the high-spin ${}^3\Pi_{g,\pm 1}$ configurations.

| | $S_z$ | $^3\Sigma_g^-$ +1 | $^3\Sigma_g^-$ 0 | $^3\Sigma_g^-$ -1 | $^1\Delta_g$ 0 | $^1\Sigma_g^+$ 0 | $^3\Pi_g$ +1 | $^3\Pi_g$ 0 | $^3\Pi_g$ -1 | $^1\Pi_g$ 0 |
|---|---|---|---|---|---|---|---|---|---|---|
| $^3\Sigma_g^-$ | +1 | | | | | | | $TT_{\Sigma\Pi}$ | | $TS_{\Sigma\Pi}$ |
| $^3\Sigma_g^-$ | 0 | | | | | $\mathbf{TS_{\Sigma\Sigma}}$ | $TT_{\Sigma\Pi}$ | | $TT_{\Sigma\Pi}$ | |
| $^3\Sigma_g^-$ | -1 | | | | | | | $TT_{\Sigma\Pi}$ | | $TS^*_{\Sigma\Pi}$ |
| $^1\Delta_g$ | 0 | | | | | | $TS_{\Pi\Delta}$ | | $TS^*_{\Pi\Delta}$ | |
| $^1\Sigma_g^+$ | 0 | | $\mathbf{TS^*_{\Sigma\Sigma}}$ | | | | $ST_{\Sigma\Pi}$ | | $ST^*_{\Sigma\Pi}$ | |
| $^3\Pi_g$ | +1 | | $TT^*_{\Sigma\Pi}$ | | $TS^*_{\Pi\Delta}$ | $ST^*_{\Sigma\Pi}$ | | | | |
| $^3\Pi_g$ | 0 | $TT^*_{\Sigma\Pi}$ | | $TT^*_{\Sigma\Pi}$ | | | | | | $TS_{\Pi\Pi}$ |
| $^3\Pi_g$ | -1 | | $TT^*_{\Sigma\Pi}$ | | $TS_{\Pi\Delta}$ | $ST_{\Sigma\Pi}$ | | | | |
| $^1\Pi_g$ | 0 | $TS^*_{\Sigma\Pi}$ | | $TS_{\Sigma\Pi}$ | | | | $TS^*_{\Pi\Pi}$ | | |

Table 3.8: Non-vanishing Spin-Orbit Coupling matrix elements for the $O_2$ molecule: Naming and color coding are consistent with Fig. 3.9, where the triplet-singlet (TS), singlet-triplet (ST) and triplet-triplet (TT) couplings are plotted. Diagonal elements, i.e. self-interaction coupling elements within one electronic state, have been omitted for the sake of clarity.

$ST_{\Sigma\Pi}$: Analogously, the $^1\Sigma_g^+$ singlet state couples to these high-spin $^3\Pi_{g,\pm1}$ configurations in addition to the already mentioned coupling with the triplet ground state.

$TS_{\Pi\Pi}$: Last but not least also the low-spin triplet $^3\Pi_{g,0}$ and the singlet $^1\Pi_g$ state couple to each other.

These SOC matrix elements have all been computed in an *ab initio* fashion by the Spin-Orbit Coupling module provided by MOLPRO [208] in the V5Z basis set, whereby the previously determined MRCI wave functions served as a starting point for the calculation[9]. The absolute values of this matrix elements are plotted in Fig. 3.9. As shown there, the $\mathbf{TS_{\Sigma\Sigma}}$ coupling is a slightly decreasing, almost constant function of the oxygen-oxygen distance. In contrast thereto, all other matrix elements exhibit more or less strong wiggles for distances larger than 1.6 Å. These oscillations and discontinuities are caused by the avoided crossings of the respective Π states, to which all this matrix elements couple.

If we restrict our considerations to the three energetically lowest states of the molecular oxygen, which are of special interest in this work, these constraints result in a nonzero coupling of the triplet ground state $^3\Sigma_g^-$ with the energetically highest singlet state $^1\Sigma_g^+$. Since the Spin-Orbit interaction is minute with respect to the other terms in the Hamiltonian, it can be discussed qualitatively in first order perturbation theory, which results in the following wave functions:

$$\left|^1\Sigma_g^+\right\rangle' = \left|^1\Sigma_g^+\right\rangle + C \cdot \left|^3\Sigma_{g,0}^-\right\rangle \tag{3.22}$$

$$\left|^3\Sigma_{g,0}^-\right\rangle' = \left|^3\Sigma_{g,0}^-\right\rangle - C^* \cdot \left|^1\Sigma_g^+\right\rangle . \tag{3.23}$$

[9] Additionally, simulations based on the CASSCF wave functions have been performed (see Tab 3.9).

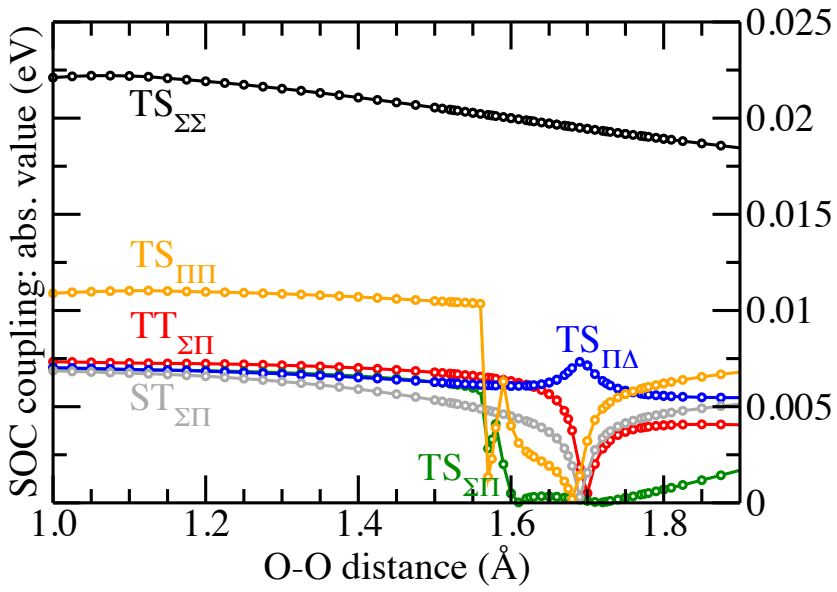


Figure 3.9: Absolute values of the Spin-Orbit Coupling matrix elements: The naming convention and the color coding already employed in the text as well as in Tab. 3.8 have been used. The single data points are separated by 0.025 Å from each other for oxygen-oxygen distances smaller than 1.5 Å and by 0.01 Å for larger distances.

The therein appearing *mixing coefficient* $C$ can be determined by explicitly evaluating the SOC matrix elements

$$C = \frac{1}{\Delta E^{\Sigma}_{\mathrm{TS}}} \mathbf{TS_{\Sigma\Sigma}} = \frac{1}{\Delta E^{\Sigma}_{\mathrm{TS}}} \left\langle {}^3\Sigma^-_g \right| V_{\mathrm{SOC}} \left| {}^1\Sigma^+_g \right\rangle . \tag{3.24}$$

The ${}^1\Delta_g$ singlet state, however, does not couple to any of the other two states due to the too large orbital angular momentum difference $\Delta\Lambda = 2$. There, the $\Pi_g$ states come into play: Since they couple to the ${}^3\Sigma^-_g$, the ${}^1\Sigma^+_g$ and the ${}^1\Delta_g$ configurations, they serve as a bridge between these states. A perturbative treatment of this indirect coupling results in the following wave functions:

$$\left|{}^1\Delta_g\right\rangle' = \left|{}^1\Delta_g\right\rangle + D \cdot \left(\left|{}^3\Pi_{g,+1}\right\rangle + \left|{}^3\Pi_{g,-1}\right\rangle\right) \tag{3.25}$$

$$\left|{}^3\Sigma^-_{g,\pm1}\right\rangle' = \left|{}^3\Sigma^-_{g,\pm1}\right\rangle + E \cdot \left|{}^3\Pi_{g,0}\right\rangle + F \cdot \left|{}^1\Pi_g\right\rangle \tag{3.26}$$

$$\left|{}^3\Sigma^-_{g,0}\right\rangle' = \left|{}^3\Sigma^-_{g,0}\right\rangle + E \cdot \left(\left|{}^3\Pi_{g,+1}\right\rangle + \left|{}^3\Pi_{g,-1}\right\rangle\right) . \tag{3.27}$$

Therein the mixing coefficients are again defined as[10]:

$$D = \frac{TS_{\Pi\Delta}}{E_{{}^3\Pi_g} - E_{{}^1\Delta_g}} , \quad E = \frac{TT_{\Sigma\Pi}}{E_{{}^3\Pi_g} - E_{{}^3\Sigma^-_g}} \text{ and } \quad F = \frac{TS_{\Sigma\Pi}}{E_{{}^1\Pi_g} - E_{{}^3\Sigma^-_g}} . \tag{3.28}$$

[10] A less approximative perturbative calculation of this mixing coefficients can be achieved by diagonalizing the complete SOC matrix. For a qualitative discussion of these effects, however, this approach is sufficient, as substantiated in Tab. 3.9.

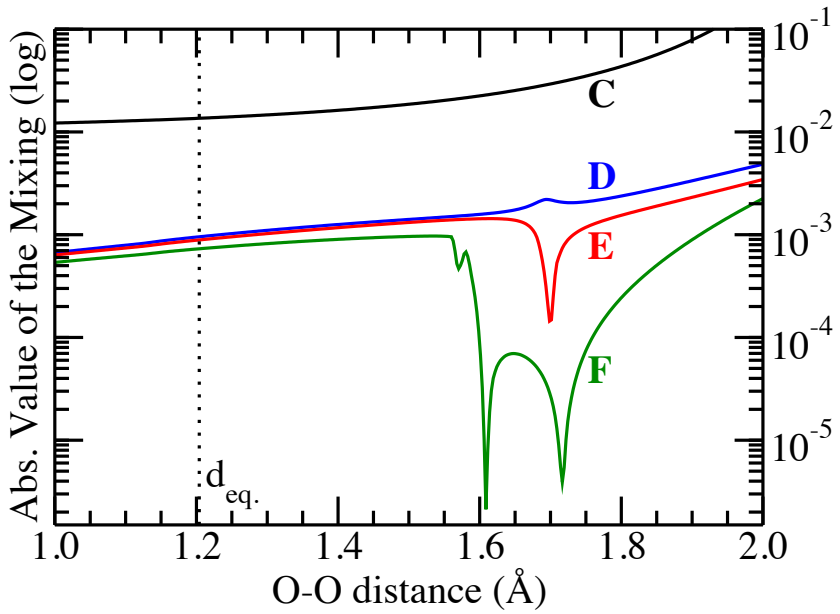


Figure 3.10: Absolute values of the mixing coefficients as function of the oxygen-oxygen distance on a logarithmic scale: The data was obtained by evaluating Eq. (3.24) and Eq. (3.28) respectively. Thereto, the PECs shown in Fig. 3.8 and the Spin-Orbit Coupling matrix elements plotted in Fig. 3.9 have been combined as prescribed.

The simulated values of all these mixing coefficients, which are in excellent agreement with previous studies, are listed in Tab. 3.9 for oxygen at the equilibrium bond length. Additionally, their dependence on the oxygen-oxygen distance is shown in Fig. 3.10. The wiggles and discontinuities already present in the SOC matrix elements in Fig. 3.9 are inherited by the mixing coefficients. Noteworthy enough, there is a huge gap of more than one order of magnitude between $C$ and the other mixing coefficients, since the energy gaps enter their calculation in the denominator of Eq. (3.24) and (3.28). For the same reason, the mixing coefficients increase consistently upon bond elongation, although the underlying SOC couplings decrease.

For the calculation of the excited state's lifetime, the mechanism responsible for the respective radiational transitions has to be identified first. In the Hilbert space spanned by the SOC unperturbed wave functions, both the decay of the $^1\Sigma_g^+$ and the decay of the $^1\Delta_g$ state into the triplet ground state are forbidden due to the $\Delta S = 0$ selection rule that applies to all electromagnetic transitions. For the perturbed wave functions, contrariwise, the Spin-Orbit Coupling results in a mixing of states with different multiplicity ($\Delta S = 0, \pm 1$) and thus into a partial invalidation of the $\Delta S = 0$ selection rule as shown below. However, the SOC does not mix states with different inversion symmetry: Accordingly, electric dipole transitions, which are subject to the $g \leftrightarrow u$ selection rule, are still forbidden for the decays of interest. The next possible parity

| C | D | E | F | Reference | |
|---|---|---|---|---|---|
| 0.0143 | 0.00093 | 0.00087 | 0.00101 | CASSCF, Diag. | this work |
| 0.0136 | 0.00095 | 0.00089 | 0.00073 | MRCI, Eq. (3.24) and (3.28) | this work |
| 0.0136 | 0.00094 | 0.00087 | 0.00103 | MRCI, Diag. | this work |
| 0.0118 | – | – | – | Semiempirical | [214] |
| 0.0117 | – | – | – | One-electron approx. | [174] |
| 0.0114 | – | – | – | INDO | [215] |
| 0.0133 | 0.00096 | 0.00089 | 0.00102 | MRCI | [213] |
| 0.0134 | 0.00092 | 0.00088 | 0.00101 | MRCI | [216] |

Table 3.9: Mixing coefficients at the equilibrium bond length of the oxygen molecule: Both the values obtained from the evaluation of Eq. (3.24) and (3.28) and the values achieved by diagonalizing the complete SOC matrix 3.8 are given. Solely the $F$ coefficient exhibits a significant error when determined approximatively due to thereby neglected interaction of the ${}^3\Pi_g/{}^1\Pi_g$ states.

preserving transition mechanism is described by the *magnetic dipole momentum* operator:

$$\mathbf{M} = \frac{\mu_B}{\hbar}\left(\mathbf{L} + g_e\mathbf{S}\right) = \frac{e}{2m}\left(\mathbf{L} + g_e\mathbf{S}\right). \tag{3.29}$$

Therein $g_e = 2.00231$ is the gyromagnetic *g-factor* for the electron and $\mu_B$ is the Bohr magneton. The selection rules for this process [184], which can be derived analogously to Eq. (3.21), are:

$$\Delta S = 0\,, \quad \Delta\Lambda = 0, \pm 1 \;\text{ and }\; \quad g \nleftrightarrow u. \tag{3.30}$$

For the ${}^1\Sigma_g^+ \to {}^3\Sigma_g^-$ decay, the resulting transition momentum is [11]

$$\left\langle {}^1\Sigma_g^+ \right|' \mathbf{M} \left| {}^3\Sigma_{g,\pm1}^- \right\rangle = \underbrace{\left\langle {}^1\Sigma_g^+ \right| \mathbf{M} \left| {}^3\Sigma_{g,\pm1}^- \right\rangle}_{=0} + C^* \left\langle {}^3\Sigma_{g,0}^- \right| \mathbf{M} \left| {}^3\Sigma_{g,\pm1}^- \right\rangle. \tag{3.31}$$

Although the mixing is minute, this previously strictly forbidden triplet-singlet transition can thereby borrow intensity from the allowed *magnetic dipole transition* ${}^3\Sigma_{g,0}^- \leftrightarrow {}^3\Sigma_{g,\pm1}^-$. Accordingly, we calculated both the orbital momentum and the spin part of the magnetic dipole moment

$$\begin{aligned}\left\langle {}^1\Sigma_g^+ \right|' \mathbf{M} \left| {}^3\Sigma_{g,\pm1}^- \right\rangle = \frac{\mu_B}{\hbar} C^* \left\langle {}^3\Sigma_{g,0}^- \right| \mathbf{L} \left| {}^3\Sigma_{g,\pm1}^- \right\rangle \\ + \frac{\mu_B}{\hbar} C^* g_e \left\langle {}^3\Sigma_{g,0}^- \right| \mathbf{S} \left| {}^3\Sigma_{g,\pm1}^- \right\rangle,\end{aligned} \tag{3.32}$$

whereby the orbital angular momentum contributions are vanishingly small (see Tab. 3.10), in concordance with previous studies [213, 217]. The dominant spin part can be expressed in terms of the respective spin ladder operators (3.19b) and $S_z$:

$$\left\langle {}^3\Sigma_{g,0}^- \right| \mathbf{S} \left| {}^3\Sigma_{g,\pm1}^- \right\rangle = \frac{1}{2} \left\langle {}^3\Sigma_{g,0}^- \right| \begin{pmatrix} S^+ + S^- \\ iS^- - iS^+ \\ 2S_z \end{pmatrix} \left| {}^3\Sigma_{g,\pm1}^- \right\rangle = \frac{1}{2} \begin{pmatrix} \hbar \\ \pm i\hbar \\ 0 \end{pmatrix} \tag{3.33}$$

[11] Contributions due to the mixing of the ${}^3\Sigma_{g,\pm1}^-$ states with the ${}^3\Pi_g$ and ${}^1\Pi_g$ states in Eq. (3.26) are negligible in this case.

| $\langle {}^3\Sigma_g^- \vert L_z \vert {}^1\Sigma_g^+ \rangle$ | $\langle {}^3\Sigma_g^- \vert L_{x,y} \vert {}^3\Pi_g \rangle$ | $\langle {}^1\Delta_g \vert L_y \vert {}^1\Pi_g \rangle$ | Reference | |
|---|---|---|---|---|
| 0.0001 | 1.152 | 1.168 | MRCI | this work |
| $\ll 0.02$ | 1.000 | 1.000 | INDO | [215] |
| – | 1.16 | 1.058 | MRCI | [213] |

Table 3.10: Angular orbital momentum couplings in units of $\hbar$ as determined from *ab initio* calculations at the MRCI/V5Z level of theory.

On the basis of the data hitherto acquired, the transition rate [214]

$$\Gamma = \frac{\alpha^5 \omega^3 \hbar^2 f}{3\mu_B^2} \left| \left\langle {}^1\Sigma_g^+ \right|' \mathbf{M} \left| {}^3\Sigma_{g,\pm 1}^- \right\rangle \right|^2 , \tag{3.34}$$

can be calculated for this process, whereby $\alpha$ designates the fine-structure constant, $\omega$ the transition frequency and $f$ the degeneracy of the final state. The resulting lifetime of 11.16 s, i.e. the inverse of the transition rate, is in excellent agreement with both the experimental value of 11.3 s [174] and previous theoretical studies (see Tab. 3.11).

Analogously, the magnetic dipole transition moment for the the decay of the ${}^1\Delta_g$ state can be calculated by using the perturbed wave functions (3.25) and (3.26):

$$\begin{aligned} \left\langle {}^1\Delta_g \right|' \mathbf{M} \left| {}^3\Sigma_{g,\pm 1}^- \right\rangle' = \overbrace{\left\langle {}^1\Delta_g \right| \mathbf{M} \left| {}^3\Sigma_{g,\pm 1}^- \right\rangle}^{=0} + E^* \left\langle {}^1\Delta_g \right| \mathbf{M} \left| {}^1\Pi_g \right\rangle \\ + D \left\langle {}^3\Pi_{g,\pm 1} \right| \mathbf{M} \left| {}^3\Sigma_{g,\pm 1}^- \right\rangle + DE^* \underbrace{\left\langle {}^3\Pi_{g,\pm 1} \right| \mathbf{M} \left| {}^1\Pi_g \right\rangle}_{=0} . \end{aligned} \tag{3.35}$$

The remaining terms, which do not vanish due to the $\Delta S = 0$ selection rule for magnetic dipole transitions, all exhibit a projected angular momentum difference of $\Delta\Lambda = \pm 1$. Therefore—in contrast to the previously discussed transition—no coupling through the spin part of $M$ is possible in this case and the decay occurs completely due to the angular momentum coupling (see Tab 3.10). Its *ab initio* evaluation yields

$$M = -0.00367 i \mu_B, \tag{3.36}$$

which is in excellent agreement with other theoretical studies [217]. This momentum corresponds to a lifetime (see Tab. 3.11) of 97 minutes, which is in the same order of magnitude as the experimental value of 72 minutes [218]. The deviation from the experiment may seem huge on a first look, especially with respect to the almost perfect results achieved previously for all other quantities. In terms of transition rates, however, these lifetimes translates into absolute errors of 0.00006 $s^{-1}$: an accuracy that is a formidable challenge both for experimentalists and theorists.

Additional contributions to these transition rates, e.g., the one due to *electric quadrupole* interaction that is orders of magnitude smaller [217], have not been considered in this work. Furthermore, corrections due to vibrational effects [214] have not been addressed either, since the exact simulation of radiational decay

| $\tau_\Sigma$ (s) | Reference | |
|---|---|---|
| 11.16 | MRCI | this work |
| 11.11 | MRCI, exp. $\Delta E_{TS}^{\Sigma}$ | this work |
| 11.24 | experiment | [201] |
| 11.3 | experiment | [174] |
| 11.65 | MRCI | [213] |
| 12.59 | CASSCF, linear response theory | [214] |

| $\tau_\Delta$ (s) | Reference | |
|---|---|---|
| 5799.30 | MRCI | this work |
| 5542.48 | MRCI, exp. $\Delta E_{TS}^{\Delta}$ | this work |
| 3875.96 | experiment | [219] |
| 4347.82 | experiment | [218] |
| 5271.48 | MRCI | [213] |
| 5263.16 | MRCI | [217] |

Table 3.11: Lifetimes $\tau_\Sigma$ and $\tau_\Delta$ for the $^1\Sigma_g^+$ and the $^1\Delta_g$ state respectively: All values refer to the decay in the triplet ground state. Additionally, lifetimes calculated by employing the experimental energy gaps are given.

is not the scope of this work. Rather, the presented lifetime calculations shall substantiate the quality of the simulated Spin-Orbit matrix elements, which lay the solid grounding for the Surface Hopping simulations discussed in Sec. 4.

## 3.3 Density Functional Theory Calculations

### 3.3.1 The non-interacting Reference System

As discussed widely in Sec. 2.2.2, the *electron densities*—and not the total wave functions employed in the Quantum Chemical calculations—are the principal quantity that is subject to optimization in DFT algorithms. Thus, in a first step, we will discuss to which densities the previously inspected electronic states of the oxygen molecule (see Sec. 3.1) correspond and how they are best addressed. Thereby we will limit our research to the three lowest lying electronic states, namely the triplet ${}^3\Sigma_g^-$ ground state, the first excited ${}^1\Delta_g$ singlet state and the second excited ${}^1\Sigma_g^+$ singlet state (see Tab. 3.1), which all exhibit the same electronic configuration

$$(1\sigma_s)^2(1\sigma_s^*)^2(2\sigma_s)^2(2\sigma_s^*)^2(2\sigma_p)^2(2\pi_p)^4(2\pi_p^*)^2 \tag{3.37}$$

and just differ in the occupation pattern of the antibonding $2\pi_p^*$ orbital. Since the total electronic density (2.50) solely depends on the occupation numbers, all three states exhibit the exact same density[12]

$$\rho(\mathbf{r}) = \left(\phi_x^*\phi_x + \phi_y^*\phi_y\right). \tag{3.38}$$

At first glance this fact seems to contradict the Hohenberg-Kohn Theorems as introduced in Sec. 2.2.2: Actually, the spin degrees of freedom have hitherto not been considered explicitly in this discussion. Thereby a "closed-shell" configuration, in which each orbital is either completely empty or fully occupied with both a spin up and a spin down electron, was implicitly assumed. For "open-shell" configurations as found for the oxygen molecule, the spin degrees of freedom, which, e.g., determine if there is exchange interaction (2.34) in between two spinorbitals or not, have to be taken into account. For this purpose DFT can be easily generalized to *spin-polarized* DFT [220, 221] by introducing individual *spin up* and *spin down densities*:

$$\rho^{\uparrow}(\mathbf{r}) = n^{\uparrow} \cdot \sum_{\substack{|\uparrow\rangle_{2\dots N} \\ |\downarrow\rangle_{1\dots N}}} \int \Psi^*(\mathbf{r}_1,\cdots,\mathbf{r}_n)\Psi(\mathbf{r}_1,\cdots,\mathbf{r}_n)\, d\mathbf{r}_2\cdots d\mathbf{r}_n \Big|_{\mathbf{r}_1=\mathbf{r}} \tag{3.39a}$$

$$\rho_{\downarrow}(\mathbf{r}) = n_{\downarrow} \cdot \sum_{\substack{|\uparrow\rangle_{1\dots N} \\ |\downarrow\rangle_{2\dots N}}} \int \Psi^*(\mathbf{r}_1,\cdots,\mathbf{r}_n)\Psi(\mathbf{r}_1,\cdots,\mathbf{r}_n)\, d\mathbf{r}_2\cdots d\mathbf{r}_n \Big|_{\mathbf{r}_1=\mathbf{r}} \tag{3.39b}$$

Consequently, the total energy (2.53) is a functional both of the *magnetization density* $m(\mathbf{r})$ and of the *total density* $\rho(\mathbf{r})$:

$$m(\mathbf{r}) = \rho^{\uparrow}(\mathbf{r}) - \rho_{\downarrow}(\mathbf{r}) \tag{3.40a}$$

$$\rho(\mathbf{r}) = \rho^{\uparrow}(\mathbf{r}) + \rho_{\downarrow}(\mathbf{r}). \tag{3.40b}$$

This approach is conceptually comparable to the *Unrestricted Hartree-Fock* method discussed extensively in Sec. 3.2.1, since in both cases the spin up and the spin down electrons are optimized individually.

[12] For the qualitative discussion of the densities, we focus on the twofold degenerate $2\pi_p^*$ valence orbitals $\phi_x$ and $\phi_y$, as done for the examination of the wave functions in Sec. 3.1.

| | | $\boldsymbol{\rho^{\uparrow}}$ $\boldsymbol{(r)}$ | $\boldsymbol{\rho_{\downarrow}(r)}$ | $\boldsymbol{m(r)}$ |
|---|---|---|---|---|
| $^1\Delta_g$ | $\Psi_1^s$ | $\frac{1}{2}\left(\phi_x^*\phi_x+\phi_y^*\phi_y\right)$ | $\frac{1}{2}\left(\phi_x^*\phi_x+\phi_y^*\phi_y\right)$ | 0 |
| | $\Psi_2^s$ | $\frac{1}{2}\left(\phi_x^*\phi_x+\phi_y^*\phi_y\right)$ | $\frac{1}{2}\left(\phi_x^*\phi_x+\phi_y^*\phi_y\right)$ | 0 |
| $^1\Sigma_g^+$ | $\Psi_3^s$ | $\frac{1}{2}\left(\phi_x^*\phi_x+\phi_y^*\phi_y\right)$ | $\frac{1}{2}\left(\phi_x^*\phi_x+\phi_y^*\phi_y\right)$ | 0 |
| $^3\Sigma_g^-$ | $\Psi_4^t$ | $\frac{1}{2}\left(\phi_x^*\phi_x+\phi_y^*\phi_y\right)$ | $\frac{1}{2}\left(\phi_x^*\phi_x+\phi_y^*\phi_y\right)$ | 0 |
| | $\Psi_5^t$ | $\left(\phi_x^*\phi_x+\phi_y^*\phi_y\right)$ | 0 | $\left(\phi_x^*\phi_x+\phi_y^*\phi_y\right)$ |
| | $\Psi_6^t$ | 0 | $\left(\phi_x^*\phi_x+\phi_y^*\phi_y\right)$ | $-\left(\phi_x^*\phi_x+\phi_y^*\phi_y\right)$ |

Table 3.12: Spin up $\rho^{\uparrow}(r)$ and spin down $\rho_{\downarrow}(r)$ densities for the discussed electronic states of the oxygen molecule with respect to the wave functions (3.3a)-(3.3f). Additionally, the resulting magnetization densities $m(\mathbf{r})$ are given.

Within this framework, it is indeed possible to discriminate between the ground state, which exhibits a nonzero magnetization density in the high-spin configurations, and all other states, the magnetization density of which vanishes (see Tab. 3.12). Thus we have found the correct *non-interacting reference* configuration that has to be addressed to describe the triplet ground state. The remaining states, however, are still degenerate: Especially the presence of the low-spin triplet state introduces *spin-contamination* [222] and thus lowers the respective triplet-singlet energy gap consistently (see Sec. 3.3.3), a phenomenon that already occurred in the *Unrestricted Hartree-Fock* calculations discussed before (see Sec. 3.2.2). Analogously, the use of a spin-projection method [223] might seem appealing to partially recover the correct energy differences: However, such an approach might also seriously degrade the quality of the resulting Potential Energy Surfaces [224] and is hence of no use to our purposes.

Nevertheless, the excited singlet states can be accessed in DFT by circumventing the spin-contamination problem in an astute fashion: Let us revert to the standard *spin-unpolarized* formulation of DFT, where a "closed-shell" configuration is inherently presumed. Obviously such an occupation pattern cannot be achieved by distributing the two available valence electrons on the four accessible $2\pi^*$ states. By means of *fractional occupation numbers* [225] such a configuration can be obtained in spite of that. In this case, each of the available states in the $\phi_x$ and $\phi_y$ Molecular Orbitals is occupied with **half** an electron, which results in the following Slater Determinant:

$$\Psi_{\text{Un.Pol.}} = \frac{1}{\sqrt{2}} \begin{vmatrix} \frac{1}{\sqrt{2}}\left(\phi_x \pm \phi_y\right)|\uparrow\rangle\,(1) & \frac{1}{\sqrt{2}}\left(\phi_x \pm \phi_y\right)|\downarrow\rangle\,(1) \\ \frac{1}{\sqrt{2}}\left(\phi_x \pm \phi_y\right)|\uparrow\rangle\,(2) & \frac{1}{\sqrt{2}}\left(\phi_x \pm \phi_y\right)|\downarrow\rangle\,(2) \end{vmatrix}. \tag{3.41}$$

Although such an approach might seem unphysical at first glance, it indeed yields the correct total density (3.38). Furthermore, the employment of spin-unpolarized DFT ensures that the addressed state exhibits a singlet character, since possible contributions from unpaired spins are not even included in the approach itself. Thereby the spin-contamination from the low-spin triplet state can be eliminated. However, the excited singlet states are still degenerate, since

there is no symmetry dependent DFT method available that would be able to discriminate between them. One has to realize that as a consequence also the electronic optimization cannot discriminate between these two states and thus will never yield the correct, lower lying $^1\Delta_g$ state (see Sec. 3.3.3). At present, however, this is still the best possible approach [226].

### 3.3.2 Calculational Details

All results presented in this section have been obtained with the *Vienna ab initio simulation package* VASP [227]. The general considerations discussed below, especially the ones with respect to convergence (see Sec. B.2), strongly differ from the ones presented in the previous section for the Quantum Chemical calculations. There are profound differences, which go far beyond the obvious variance in the treatment of exchange and correlation and which have their origin in the different mathematical description of the electronic structure by the employed simulation packages. One has to realize that MOLPRO [175] focuses on the simulation of **atoms** and **molecules** and thus employs an Atomic Orbital basis set—constructed on its part by Gaussian functions—for the expansion of the wave function (see Sec. 2.2.1.3). This approach has proved itself to be extremely efficient for this particular purpose, since the chosen basis is easy to handle numerically but also resembles the correct solution from the beginning and thus converges within few expansion terms.

In contrast thereto, VASP [228] is tailored to the particular needs encountered in the simulation of (especially metallic) **bulks** and **surfaces** [228], which exhibit a periodic, long-range ordered lattice geometry [47]. This quasi-infinite symmetry is best dealt with by periodic *Born-von Karman* boundary conditions: The resulting wave function $\phi_j$ for the electron $j$ can be written as product of a cell-periodic and a wavelike part [47], a result commonly known as *Bloch's Theorem* [59]

$$\phi_j(\mathbf{r}) = u_j(\mathbf{r}) \cdot e^{i\mathbf{kr}}, \tag{3.42}$$

in which $\mathbf{k}$ denotes a not yet specified wave vector in the first Brillouin zone (see Eq. (3.47) and its discussion). Thereby the cell-periodic part $u_j(\mathbf{r})$ must reflect the symmetry of the crystal and can thus be expanded in a discrete set of Plane Waves [47], whose wave vectors $\mathbf{G}$ are integer linear combinations of the primitive reciprocal vectors $\mathbf{G}_i^0$ of the lattice:

$$u_j(\mathbf{r}) = \sum_{\mathbf{G}} c_{j\mathbf{G}} \cdot e^{i\mathbf{Gr}}. \tag{3.43}$$

Accordingly, the wave function for each of the electrons can be written as

$$\phi_j(\mathbf{r}) = \sum_{\mathbf{G}} c_{j(\mathbf{G}+\mathbf{k})} \cdot e^{i(\mathbf{G}+\mathbf{k})\mathbf{r}}. \tag{3.44}$$

This result makes evident that in this case the most natural basis set for the wave function's expansion is the hereby introduced set of discrete Plane Waves described by the reciprocal lattice vectors. Such an expansion corresponds to a Fourier transformation of the real space wave function, whereby the numerically necessary truncation of the sum (3.44) is dictated by the length scale of the

variation of the wave function [229]. Typically, this *cut-off* procedure is characterized by the Plane Waves' highest kinetic energy included in the expansion, the so called *cut-off energy*

$$E_{\text{co}} = \frac{\hbar^2}{2m} \left|\mathbf{G_{co}} + \mathbf{k}\right|^2, \tag{3.45}$$

which can be gradually increased to study the truncation error, as done analogously in the previous Quantum Chemistry section with the basis set size. When performing such convergence studies, it becomes evident that all-electron calculations unfortunately deserve a prohibitively large cut-off energy: Indeed, the single atomic orbitals with a non-vanishing angular momentum exhibit a pronounced nodal structure close to the nuclei due to the strong attractive coulombic potential in this region. In combination with the orthogonality condition for the various eigenstates this results in rapid oscillations of the respective wave functions, which then actually deserve Plane Waves with large kinetic energies in their expansion. The thereto necessary large cut-off energy can be significantly lowered by an ingenious, but at first sight not obvious detour: As discussed before (see for instance Sec. B.1), the inner core electrons, i.e. the $1s$ electrons for the oxygen atom, are typically not affected by the chemical surrounding and, in return, do not participate in the interaction between atoms. Thus their influence on all other electrons can be described altogether with the coulombic nuclear attraction by the introduction of an *effective potential* so that the calculational effort, which otherwise would be spent in the simulation of the core electrons, can be saved[13]. Furthermore, the constraint of orthogonality between the inner core and the remaining wave functions is lifted by this means so that the actually addressed wave functions can be "smoothed" by mapping them on a set of so called "soft" *pseudowavefunctions*, which are numerically more suitable for a truncated Plane Wave expansion. As a consequence, the external potential $v_{ext}(\mathbf{r})$ that appears in the single electron Kohn-Sham equations (2.67) has to be replaced by a non-local, energy-dependent and element-specific *pseudopotential* [230, 231, 232, 233], which has to be previously determined by precise all-electrons calculations. However, this approach is not unique: Therefore a whole zoo of different techniques for the generation of pseudopotentials exists, which all differ in their relative numerical speed-up and their de facto accuracy. The pseudopotentials employed in this work, which are provided within the VASP suite, are all based on the *Projector Augmented Wave* (PAW) method [234], which ensures high numerical efficiency without abandoning the physics of an all-electron description. VASP also provides *ultra-soft* pseudopotentials [235], which are numerically as efficient as the employed ones, but which unfortunately are solely available for the LDA and the PW91 but not for the PBE and RPBE functional. Since the latter exchange-correlation functional describes the oxygen molecule best, the employment of these ultra-soft pseudopotentials has not been considered in this work.

As soon as the set of Plane Waves has been determined, the Kohn-Sham matrix for the *expansion coefficients* $c_{j(\mathbf{G}+\mathbf{k})}$ can be constructed. Most efficiently, this operation is performed by means of a *Fast Fourier Transformation* [120]

[13] Thus far this approach is identical to the *effective core potential* approach and also inherently related to the *frozen core approximation*, which are both employed in Quantum Chemical methods (see Sec. 3.2.1).

into reciprocal space, where the Kohn-Sham equations (2.67) exhibit an utterly appealing simplicity[14]:

$$\sum_{\mathbf{G}'} \underbrace{\left( -\frac{\hbar^2}{2m} \left|\mathbf{G}+\mathbf{k}\right|^2 \delta_{\mathbf{G}\mathbf{G}'} + \tilde{v}_{eff}(\mathbf{G}-\mathbf{G}') \right)}_{\tilde{h}_{ks}^{pw}} c_{j(\mathbf{G}'+\mathbf{k})} = \tilde{\varepsilon}_j(\mathbf{k})\; c_{j(\mathbf{G}+\mathbf{k})}. \quad (3.46)$$

The resulting matrix $\tilde{h}_{ks}^{pw}$, the size of which is determined by the cut-off energy value, can then be efficiently diagonalized by various problem-specific techniques [89, 227] for a specific wave vector $\mathbf{k}$. Thus we have transformed the problem of finding an infinite number of wave functions for the infinite number of electrons in a bulk to the problem of finding a finite number of wave functions for the finite number of electrons in the unit cell. However, the previously well defined KS-orbital energies $\varepsilon_j$ are now a function of the wave vector $\mathbf{k}$, whose possible values have not yet been specified: Again, the *Born-von Karman* periodic boundary conditions dictate [47] their allowed values

$$\mathbf{k} = \sum_{i=1}^{3} \frac{M_i}{N_i} \mathbf{G}_i^0 \quad (3.47)$$

with respect to the primitive reciprocal lattice vectors $\mathbf{G}_i^0$. Thereby $N = N_1 N_2 N_3$ designates the total number of primitive unit cells in the crystal and $M_i$ is an arbitrary integer value smaller than $N_i$. Hence, for a quasi-infinite bulk, this results in an in principle infinite number of $\mathbf{k}$-points and thus in an in principle infinite number of equations (3.46) that have to be solved. Accordingly, also the KS-orbital energies $\varepsilon_j$ in the calculation of the total energy (2.69) must be replaced by so called *band energies* that are integrals over the first *Brillouin Zone*[15]:

$$\sum_{j}^{n} \varepsilon_j \longrightarrow \sum_{j} \frac{V}{2\pi^3} \int\limits_{1.\ \mathrm{B.Z.}} \tilde{\varepsilon}_j(\mathbf{k}) \cdot \Theta\left(\tilde{\varepsilon}_j(\mathbf{k}) - \mu\right)\, d\mathbf{k}. \quad (3.48)$$

Since the electronic *dispersion relation* $\tilde{\varepsilon}_j(\mathbf{k})$ is a rather smooth function—at least in comparison with densities or wave functions—this integral can be approximated by a discrete sum (3.49) over $\mathbf{k}$-points, which are weighted by a symmetry factor $w_{\mathbf{k}}$. If chosen with care, e.g., by employing a *Monkhorst-Pack grid* [236] or connatural methods, the total number of necessary $\mathbf{k}$-point calculations can be drastically reduced with respect to an equally spaced grid. However, there is no intrinsic physical limit to the number of $\mathbf{k}$-points includable in a calculation so that again convergence with respect to this value can be inspected by gradual variation thereof. For metals, or more generally for any not completely filled bands, the convergence of this sum and thus the convergence in the electronic self consistency cycles is exceedingly slow due to the abrupt drop in the occupancies at the *Fermi edge* $\mu$, as described by the Heaviside step function $\Theta\left(\tilde{\varepsilon}_j(\mathbf{k}) - \mu\right)$. By replacing this discontinuous function with a smooth **smearing** function $f_s\left(\sigma_s,\, \tilde{\varepsilon}_j(\mathbf{k}) - \mu\right)$, e.g., with a Fermi-Dirac function in the limit of vanishing broadness $\sigma_s$, the convergence process can be significantly

[14] Especially, the kinetic energy operator, which basically consists of a Laplacian in real space, is a simple multiplication in reciprocal space.

[15] The variable $V$ appearing in Eq. (3.48) is the volume of the unit cell.

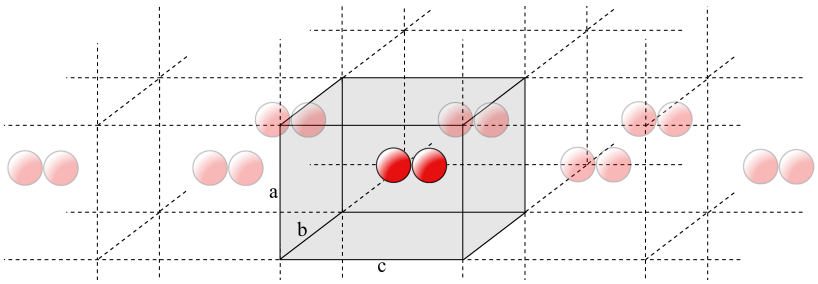


Figure 3.11: Sketch of the geometric setup for the simulation of the isolated $O_2$ molecule with three-dimensional periodic boundary conditions.

sped up without altering the accuracy of the sum:

$$\int_{1.\ \mathrm{B.Z.}} \tilde{\varepsilon}_j(\mathbf{k}) \cdot \Theta\left(\tilde{\varepsilon}_j(\mathbf{k}) - \mu\right) d\mathbf{k} \approx \sum_{\mathbf{k}\text{-points}} w_{\mathbf{k}} \cdot \tilde{\varepsilon}_j(\mathbf{k}) \cdot \Theta\left(\tilde{\varepsilon}_j(\mathbf{k}) - \mu\right)$$
$$\approx \lim_{\sigma_s \to 0} \sum_{\mathbf{k}\text{-points}} w_{\mathbf{k}} \cdot \tilde{\varepsilon}_j(\mathbf{k}) \cdot f_s\left(\sigma_s,\ \tilde{\varepsilon}_j(\mathbf{k}) - \mu\right). \quad (3.49)$$

The thereby introduced *partial occupancies* [237] can also be exploited to describe systems at nonzero temperatures [39]. In the usual case of 0 K electronic structure calculations, however, the convergence with respect to the broadness $\sigma_s$ has to be scrutinized carefully.

For the calculation of the oxygen molecule a monoclinic unit cell with edge lengths of $a = 11.0$ Å, $b = 13.0$ Å and $c = 17.0$ Å has been chosen to avoid the introduction of any artificial symmetries. Thereby the oxygen molecule was positioned in the middle of the unit-cell with the molecular axis aligned to the $c$-axis (see Fig. 3.11). Since the properties of the isolated molecule and not a periodic structure is addressed, the calculation can be performed for a single $\mathbf{k}$-point, the $\Gamma$-point. Thereby a Gaussian-type smearing function with a width of 0.01 eV is used to resemble the sharp energy peaks of Molecular Orbitals in reciprocal space. Eventually, a cut-off energy $E_{\mathrm{co}}$ of 400 eV has been used, as also suggested by the generators of the employed PAW pseudopotential. As substantiated in Sec. B.2, the convergence of the calculations at these parameters has been extensively tested for all four different exchange-correlation functionals employed in this work:

**LDA:** The *Local Density Approximation* functional is the correct functional for a homogeneous electron gas (also see Sec. 2.2.2.3). Its exchange energy is described exactly by the *Dirac exchange-energy* functional [77, 78]

$$E_X^{LDA} = \int \left\{\rho^{\uparrow} \cdot \epsilon_x^{LDA}(\rho^{\uparrow}) + \rho_{\downarrow} \cdot \epsilon_x^{LDA}(\rho_{\downarrow})\right\} d\mathbf{r}^3$$
$$= -\frac{3}{2}\left(\frac{3}{4\pi}\right)^{\frac{1}{3}} \int \left\{\left[\rho^{\uparrow}\right]^{\frac{4}{3}} + \left[\rho_{\downarrow}\right]^{\frac{4}{3}}\right\} d\mathbf{r}^3, \quad (3.50)$$

which can be derived analytically, whereas the correlation part of the functional

$$E_C^{LDA} = \int \rho \cdot \epsilon_C^{LDA}\left(\rho^{\uparrow}, \rho_{\downarrow}\right)\ d\mathbf{r}^3 \tag{3.51}$$

is determined by fitting a functional form for $\epsilon_C^{LDA}\left(\rho^{\uparrow}, \rho_{\downarrow}\right)$, e.g. the *Vosko-Wilk-Nusair interpolation* [238], to the outcome of *Quantum Monte Carlo* simulations for a homogenous electron gas [88].

The below discussed *Generalized Gradient Approximation* (GGA) functionals (also see Sec. 2.2.2.3) are designed to fulfill certain *sum-rules* [90] that the exact exchange-correlation functional is known to satisfy. For instance, the exchange-energy must obey the *spin-scaling relationship* [239]

$$E_X^{GGA,SP}\left[\rho^{\uparrow}, \rho_{\downarrow}\right] = \frac{1}{2}E_X^{GGA}\left[2\rho^{\uparrow}\right] + \frac{1}{2}E_X^{GGA}\left[2\rho_{\downarrow}\right], \tag{3.52}$$

whereby the exchange energy for the respective single spin species is defined as:

$$E_X^{GGA}\left[\rho\right] = \int \rho \cdot \epsilon_x^{LDA}(\rho) \cdot F(s)\ d\mathbf{r}^3 = -\frac{3}{2}\left(\frac{3}{4\pi}\right)^{\frac{1}{3}} \int \left[\rho\right]^{\frac{4}{3}} \cdot F(s)\ d\mathbf{r}^3. \tag{3.53}$$

The thereby introduced *local exchange enhancement factor* $F(s)$, which makes the difference with respect to the Dirac exchange-energy functional, depends upon the *generalized density gradient*:

$$s\left(\mathbf{r}\right) = \frac{|\nabla\rho|}{2 \cdot (3\pi^2)^{1/3}\left[\rho\right]^{4/3}}. \tag{3.54}$$

This quantity, that also gave the name to the functionals, also enters the additional GGA correlation potential $H\left(\rho^{\uparrow}, \rho_{\downarrow}, s\right)$ that appears in the correlation energy:

$$E_C^{GGA}\left[\rho^{\uparrow}, \rho_{\downarrow}\right] = \int \rho \cdot \left[\epsilon_C^{LDA}\left(\rho^{\uparrow}, \rho_{\downarrow}\right) + H\left(\rho^{\uparrow}, \rho_{\downarrow}, s\right)\right]\ d\mathbf{r}^3. \tag{3.55}$$

Its exact functional form is rather complex and thus neither given nor discussed herein. As a matter of fact we will rather focus on the exchange part of the functional when discussing the calculations in Sec. 3.3.3, since—as will be seen below—it is the interaction that is actually responsible for the largest portion of uncertainty in the simulation of the oxygen molecule.

**PW91:** The PW91 (or PW-GGA II) functional [91] proposed by J. P. Perdew and Y. Wang was one of the first parameter-free GGA functionals designed to fulfill as many *sum-rules* [90] as possible. The thereby derived local exchange enhancement factor is

$$F_{PW91}(s) = \frac{1 + A\sinh^{-1}(Bs) \cdot s + (C - De^{-Es^2}) \cdot s^2}{1 + A\sinh^{-1}(Bs) \cdot s + F \cdot s^4}, \tag{3.56}$$

whereby the variables $A$-$F$ designate positive constants, whose value can be found in [91]. As this equation already forebodes, the formulation of the PW91 functional is rather complex and thus suffers some technical drawbacks, as, e.g. overparametrization.

**PBE:** On the basis of the experience gained with the "Byzantine" PW91 functional, a simpler functional, "easier to understand, apply and perhaps to improve" was suggested. Again, all parameters in this so called *Perdew-Burke-Ernzerhof* functional [92] are derived non-empirically from fundamental constants due to the constraints imposed by *sum-rules*. However, a semi-local functional that just depends on the density and its generalized gradient cannot satisfy all *sum-rules* of the correct functional by construction. Therefore some of the imposed restrictions, which are known to affect the total energy of a system just slightly or not at all, have been dropped for the sake of simplicity (for further details see [92] and references therein). Conversely, two additional constraints, which correct for two severe flaws that had been discovered in the PW91 functional, have been accounted for: scaling at the high-density limit and linear-response at small generalized gradients. The latter characteristics—already present in the LDA functional—is just realized approximatively in the PW91 functional. To fix this deficiency, the local exchange enhancement factor $F(s)$ for the PBE functional has been defined as:

$$F_{PBE}(s) = 1 + \kappa - \frac{\kappa}{1 - \frac{\mu s^2}{\kappa}} \stackrel{s\to 0}{\longrightarrow} 1 + \mu s^2. \tag{3.57}$$

This functional form, which had already been derived by A. D. Becke [240] on top of Slater's $X\alpha$ approximation [54], is "the simplest conceivable dimensionally consistent expression" for exchange. To account for linear response at small generalized gradients, the parameter $\mu$ is chosen in such a way that the second-order gradient term in the exchange potentials cancels exactly with the respective correlation term in this limit. In a second step, the integrated *Lieb-Oxford Bound* [241] for a completely spin-polarized density

$$\begin{aligned} E_X^{GGA,SP}[\rho,0] \;&=\; \sqrt[3]{2}\int \rho\cdot\epsilon_x^{LDA}(\rho)\cdot F\left(\frac{s}{\sqrt[3]{2}}\right)\, d\mathbf{r}^3 \\ &\geq\; E_{XC}^{GGA,SP} \;\geq\; -1.679\int[\rho]^{\frac{4}{3}}\, d\mathbf{r}^3, \end{aligned} \tag{3.58}$$

which is a lower bound derived from first principles for the exchange and the correlation energy as a whole, can be used to find a conditional equation for the parameter $\kappa$. Indeed, the *local Lieb-Oxford* inequality

$$\rho(\mathbf{r})\cdot\epsilon_x^{LDA}(\rho)\cdot F\left(\frac{s}{\sqrt[3]{2}}\right) \;\geq\; -1.333\cdot[\rho(\mathbf{r})]^{\frac{4}{3}} \qquad \text{for all } \mathbf{r}\in\mathbb{R}^3 \tag{3.59}$$

ensures the fulfillment of the integrated Lieb-Oxford inequality (3.58) for **any** density and at the same time uniquely determines the parameter $\kappa$. Both the value for $\mu$ and for $\kappa$ thereby derived from first principles are consistent with the previously empirically found values of A. D. Becke [240].

**RPBE:** Upon publication of the PBE functional, Zhang *et al.* [242] pointed out that the *local* Lieb-Oxford inequality (3.59) is a **sufficient** but **not a necessary** condition for the fulfillment of the *integral* Lieb-Oxford inequality. Accordingly, they proposed an alternative formulation of the PBE functional, which is referred to as *revised PBE* (revPBE). This functional differs from the original just by the value of $\kappa$, which is determined by fitting total atomic energies

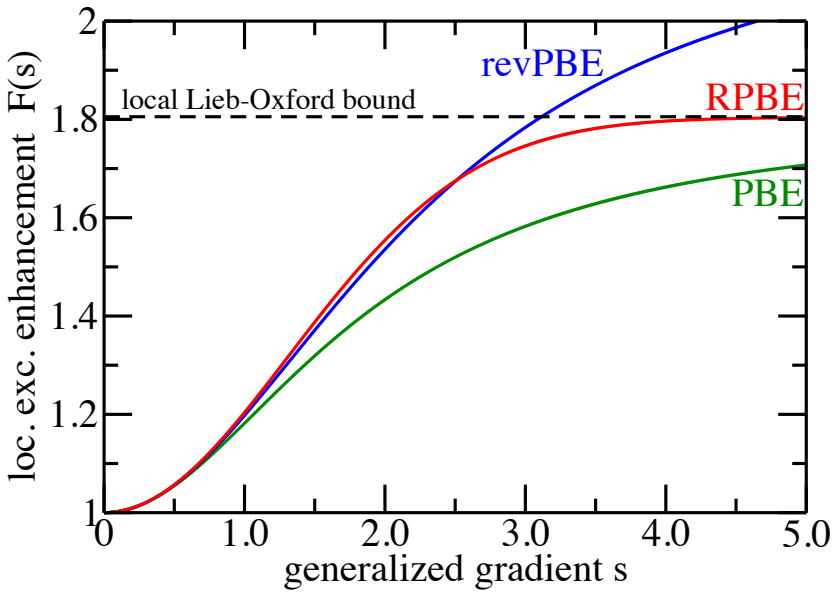


Figure 3.12: Plot of the local exchange enhancement factor $F(s)$ for the PBE, the revPBE and the RPBE functionals as function of the generalized gradient $s$. Additionally, the value of the local Lieb-Oxford bound is also indicated as a reference.

(from He to Ar) of exchange-only revPBE calculations to respective exchange-only *Optimized Exchange Potential* simulations [243]. This approach results in significantly improved molecular atomization energies [242] and chemisorption energies [93], but on the other side it may also worsen the description of other physical properties, e.g. lattice constants [93], with respect to the PBE functional. In addition, the fulfillment of the integrated Lieb-Oxford bound is not ensured by construction[16] anymore, since the local exchange enhancement factor $F(s)$ violates the local Lieb-Oxford bound for large generalized gradients, as shown in Fig. 3.12. To account for this deficiency, Hammer *et al.* [93] proposed a further revised formulation of PBE, the RPBE functional: It features a different functional form for the local exchange enhancement factor

$$F_{RPBE}(s) = 1 + \kappa \left(1 - e^{-\frac{\mu s^2}{\kappa}}\right), \tag{3.60}$$

which still satisfies linear response at small generalized gradients. In this limit the RPBE functional additionally mimics the revPBE functional, whereas it does not infringe the local Lieb-Oxford bound for large generalized gradients but levels off instead. As a consequence, it results in equally improved (and also worsened) molecular characteristics as the revPBE functional without violating the physics included in the PBE functional. Strictly speaking, the choice in between Eq. (3.57) and Eq. (3.60) as functional form for $F(s)$ is arbitrary up to the discussed extent and has hitherto not been further substantiated by *sum-rules*. Thus the systematic differences that appear between PBE and RPBE

[16] In practice, however, the integrated Lieb-Oxford inequality is also fulfilled in revPBE calculations.

calculations can be regarded as a measure for the uncertainty due to the use of approximative GGA functionals constructed according to the PBE scheme. However, this interpretation has to be handled with care: The value of $\kappa$ employed in the revPBE and RPBE functional is determined somehow arbitrarily by fitting to first principles data for first and second row elements. Accordingly, it is not too surprising that these functionals perform well for these elements and worse for elements that have not been accounted for in the fitting process. There is still enough room for the legitimate suspicion that an alternative determination of $\kappa$, e.g., by fitting to the whole periodic table, would lead to an RPBE functional that mimics the PBE functional almost exactly.

### 3.3.3 Results & Discussion

The key characteristics of the oxygen molecule have been determined in exactly the same fashion as previously discussed in Sec. 3.2.1 for the Quantum Chemical methods. Accordingly, Potential Energy Curves (PECs) were calculated for various bond lengths, starting at 0.75 Å and ending at 1.5 Å in steps of 0.05 Å. Fitting this data with a *Morse Potential* (3.4) first yields the equilibrium bond length $d_{\mathrm{eq}}$ as well as the equilibrium total energy $E_{\mathrm{eq}}$ and then, in a second step (3.7), also the vibrational frequencies $\omega_o$. Furthermore, the binding energy $E_{\mathrm{b}}$ of the oxygen molecule was calculated as specified in Eq. (3.5), whereby the thereto necessary total energy of a single oxygen atom was simulated with the exact same calculation parameters[17] employed for the molecule. Additionally, Zero Point Energy corrected binding energies (3.8) have been computed on the basis of the vibrational frequencies determined before. Eventually, the triplet-singlet energy gaps were computed by subtracting the total equilibrium energy of the triplet spin-polarized calculations from the total energy of the spin-unpolarized calculations at the (triplet) equilibrium bond length. Again, Zero Point Energy corrections (3.9) have been applied as well, whereby the necessary vibrational frequencies for the excited state were determined by fitting a Morse Potential to a spin-unpolarized PEC in the exact same way as done for the triplet state before.

#### The Ground State Properties:

As substantiated in Tab. 3.13, the performed DFT simulations yield fairly accurate results for both the equilibrium bond length and the vibrational frequency of the oxygen molecule, although they are not as precise as the respective Quantum Chemical calculations. All functionals result in bond lengths that are slightly too large, whereby the LDA, which typically underestimates bond lengths, lies closest to the experimental value of the equilibrium oxygen-oxygen distance. Thereby the PBE and the PW91 functional generate identical results within the given accuracy due to their inherent affinity, whereas the RPBE functional produces negligibly inferior results. Nevertheless, the achieved accuracy

[17] Due to the fact that neither the number of Plane Waves in the basis set expansion, nor the exchange-correlation potential depends upon the number of electrons included in the simulations, no *Basis Set Superposition Error* (BSSE) and no size consistency or extensivity problems arise in this case.

| $d_{\mathrm{eq}}$ (Å) | $\omega_o$ (cm $^{-1}$) | Reference | |
|---|---|---|---|
| 1.218 | 1632 | DFT, LDA | this work |
| 1.230 | 1565 | DFT, PW91 | this work |
| 1.230 | 1565 | DFT, PBE | this work |
| 1.232 | 1550 | DFT, RPBE | this work |
| 1.204 | 1586 | MRCI | this work |
| 1.207 | 1580 | experiment | [184] |
| 1.211 | – | DFT, LDA | [244] |
| 1.223 | – | DFT, LDA | [245] |
| 1.215 | 1642 | DFT, LDA | [186] |
| 1.210 | 1592 | DFT, LDA | [246] |
| 1.218 | – | DFT, PW91 | [247] |
| 1.224 | 1502 | DFT, PW91 | [246] |
| 1.224 | 1527 | DFT, PBE | [246] |
| 1.229 | 1597 | DFT, RPBE | [246] |
| 1.239 | – | DFT, BP86 | [223] |
| 1.240 | 1518 | DFT, BLYP | [186] |
| 1.236 | 1464 | DFT, BLYP | [246] |

Table 3.13: Equilibrium bond length $d_{\mathrm{eq}}$ and vibrational frequency $\omega_o$ of the $O_2$ molecule in its triplet ground state for various exchange-correlation functionals: All values were determined by fitting data achieved with an energy cut-off of 400 eV and a Gaussian smearing width of 0.01 eV to a Morse Potential (3.4) as discussed in Sec. 3.2.1.

with respect to the experiment of 10 mÅ for $d_{\mathrm{eq}}$ and of 30 wavenumbers for $\omega_o$ is excellent. Similarly, the correspondence to comparable DFT data found in literature is exemplary.

Unfortunately, the achieved values for the binding energy shown in Tab. 3.14 are not that satisfying: With respect to the experimental value the LDA is wrong by more than 2.0 eV (40%), PW91 and PBE by 1.0 eV (20%) and RPBE still by more than 0.5 eV (10%), although the total energy of an isolated oxygen atom was explicitly included in the latter functional's construction. These errors are not caused by numerical faults or by an incomplete convergence of the calculations, as the comparison to DFT data found in literature shows. The values for the binding energy cited in Tab. 3.14 have been achieved with various, individually converged calculational setups, which include the use of atomic orbital basis sets and of miscellaneous—also all-electron—codes. Since the thereby occurring deviations with respect to the binding energies computed in this work are in the order of 50 meV (1% of the experimental value for $E_{\mathrm{b}}$), a systematical numerical error source can be de facto excluded in this case. Rather, the origin of this discrepancy between theory and experiment has to be sought in the approximative nature of the employed GGA functionals. Especially the exchange interaction seems to play a prominent role in this context, as the result for the RPBE functional suggests. As exhaustively discussed before, it just differs from the PBE functional in the *local exchange enhancement factor* $F(s)$, but it yields almost half its error in spite of that. This hypothesis is also encouraged by

| $E_b$ (eV) | Reference | |
|---|---|---|
| -7.359 [7.258] | DFT, LDA [with ZPE] | this work |
| -6.135 [6.038] | DFT, PW91 [with ZPE] | this work |
| -6.042 [5.945] | DFT, PBE [with ZPE] | this work |
| -5.671 [5.574] | DFT, RPBE [with ZPE] | this work |
| -5.030 [4.933] | MRCI (PEC) [with ZPE] | this work |
| -5.116 | experiment | [191] |
| -5.123 | experiment | [192] |
| -7.572 | DFT, LDA | [186] |
| -7.590 | DFT, LDA, ZPE | [92] |
| -7.577 | DFT, LDA, ZPE | [248] |
| -7.10–7.30 | DFT, LDA, no ZPE | [93] |
| -7.428 | DFT, LDA, no ZPE | [246] |
| -6.202 | DFT, PW91, ZPE | [92] |
| -5.864 | DFT, PW91, ZPE | [248] |
| -5.966 | DFT, PW91 | [247] |
| -5.84–6.06 | DFT, PW91, no ZPE | [93] |
| -6.074 | DFT, PW91, no ZPE | [246] |
| -6.245 | DFT, PBE, ZPE | [92] |
| -6.149 | DFT, PBE, no ZPE | [242] |
| -5.81–5.99 | DFT, PBE, no ZPE | [93] |
| -6.099 | DFT, PBE, no ZPE | [246] |
| -5.51–5.59 | DFT, RPBE, no ZPE | [93] |
| -5.646 | DFT, RPBE, no ZPE | [246] |
| -5.754 | DFT, revPBE, no ZPE | [242] |
| -5.53–5.63 | DFT, revPBE, no ZPE | [93] |
| -5.933 | DFT, BLYP | [186] |
| -5.782 | DFT, BLYP, ZPE | [248] |
| -5.750 | DFT, BLYP, no ZPE | [246] |
| -5.205 | DFT, B3LYP, ZPE | [248] |

Table 3.14: Binding energy $E_b$ of the $O_2$ molecule as defined in Eq. (3.5) for various exchange-correlation functionals (Zero-Point-Energy (ZPE) corrected values given in brackets): All calculations have been performed with an energy cut-off of 400 eV and a Gaussian smearing width of 0.01 eV at the respective equilibrium bond lengths $d_{eq}$ given in Tab. 3.13. For the ZPE Corrections as defined in Eq. (3.8), the respective frequencies $\omega_o$ specified in Tab. 3.13 have been used.

the outcome of calculations [248] employing the B3LYP functional [99], which includes a portion[18] of exact Hartree-Fock exchange.
Although the presented considerations allow to nail down the error source, its exact reasons are not yet satisfactorily elucidated. Thereto one has to realize first that the main error does not occur in the description of the oxygen molecule, whose equilibrium bond length and whose vibrational frequency (see Tab. 3.13)

[18] As discussed in Sec. 2.2.2.3, the construction of the B3LYP functional involves a fitting process to the so called G1/G2 molecules [100, 101]. Since these sets also include the oxygen atom and the respective molecule, the amelioration achieved with the B3LYP functional could also be partially related to the fitting process itself.

are in excellent agreement with the experiment. The error rather arises in the simulation of the oxygen atom. Its $^3$P ground state electronic structure is rather peculiar, since—in contrast to the triplet state of the respective molecule—the valence orbitals are not filled with a single spin species: As a matter of fact, the two $2p_x/2p_y$ orbitals of the threefold degenerate $2p$ set are occupied—without loss of generality—by a single spin up electron each, whereas the remaining $2p_z$ orbital is fully occupied[19]. The presence of an unequal number of spin up and spin down electrons in the valence shell of the non-interacting reference system results in a lifted degeneracy for the $2p$ orbitals due to the exchange interaction, which solely acts on electrons that share the same spin. Accordingly, the half-filled $2p_x/2p_y$ orbitals are considerably lowered in energy, whereas the fully occupied $2p_z$ orbital is not. Please notice that this is an additional manifestation of static correlation that has not yet been encountered in the simulation of the oxygen molecule: Previously, there either was just one spin species present in the degenerate valence Molecular Orbitals or there was an equal number of spin up and spin down electrons.

At first, it might seem surprising that DFT is able to describe complex extended systems as bulks and surfaces correctly, but generates significant errors when applied to apparently simpler systems as diatomic molecules and single atoms. As a matter of fact, "strong correlation" effects play often an important role for such not fully coordinated systems. Only recently, the inability of DFT to account for such phenomena has been studied more systematically [249] and traced back to basically two deficiencies of the nowadays available exchange-correlation energy functionals [250], namely the so called *static correlation* error and the *delocalization* error. Promising new functionals [251] that correct for these two flaws by construction are unfortunately only available for hydrogen but not yet for multi-electron systems.

**The Excited State Properties:**

Eventually, the triplet-singlet energy gaps $\Delta E_{\mathrm{ts}}$ have been studied for the various functionals (see Tab. 3.15). With respect to the experimental value for the $^1\Delta_g$ state, the computed gaps are too large by 2% for LDA, around 10% for PW91/PBE, and by more than 15% for RPBE. The fact that the RPBE functional, which performed best for the binding energy, now yields the worst result for the triplet-singlet gap (and vice versa for the LDA), might seem puzzling at first, but has its origin in the structure of the spin-unpolarized ansatz. The respective non-interacting reference system that has been defined in Eq. (3.41) can also be expressed as:

[19] This fact results in a huge portion of static correlation, since solely the combination of Slater Determinants in which the down electron is either in the $2p_x$ or in the $2p_y$ or in the $2p_z$ orbital, yield a wave function that is also an eigenfunction of the total spin operator (see Sec. A).

| $\Delta E_{\mathrm{ts}}$ (eV) | Reference | |
|---|---|---|
| 1.017 [1.016] | DFT, LDA | this work |
| 1.091 [1.090] | DFT, PW91 | this work |
| 1.126 [1.125] | DFT, PBE | this work |
| 1.156 [1.155] | DFT, RPBE | this work |
| 0.966 [0.961] | MRCI | this work |
| 0.98 | experiment $\left({}^1\Delta_g\right)$ | [184] |
| 1.624 | experiment $\left({}^1\Sigma_g^+\right)$ | [174] |
| 1.1 | DFT, PW91 | [252] |
| 1.138 | DFT, PBE | [246] |
| 1.171 | DFT, RPBE | [246] |
| | Spin-polarized Singlet | |
| 0.43 | DFT, PW91 | [253] |
| 0.392 | DFT, PBE | [246] |
| 0.393 | DFT, RPBE | [246] |
| 0.40 | DFT, BP86 | [223] |

Table 3.15: Triplet-Singlet Energy gap $\Delta E_{\mathrm{ts}}$ of the oxygen molecule for various exchange-correlation functionals (Zero Point Energy (ZPE) corrected values given in brackets): All calculations have been performed with an energy cut-off of 400 eV and a Gaussian smearing width of 0.01 eV at the respective equilibrium bond lengths $d_{\mathrm{eq}}$ given in Tab. 3.13. For the ZPE Corrections as defined in Eq. (3.9) the respective frequencies $\omega_o$ as specified in Tab. 3.13 for the triplet ground state as well as analogously computed but not listed frequencies for the singlet state, have been used.

$$\Psi_{\mathrm{Un.Pol.}} = \frac{1}{\sqrt{2}} \Bigg[ \overbrace{\frac{1}{2}\left(\phi_x\phi_x \mp \phi_y\phi_y\right)\left(|\uparrow\downarrow\rangle - |\downarrow\uparrow\rangle\right)}^{\Psi_1^s/\Psi_1^s} \pm \underbrace{\frac{1}{2}\left(\phi_x\phi_y + \phi_y\phi_x\right)\left(|\uparrow\downarrow\rangle - |\downarrow\uparrow\rangle\right)}_{\Psi_3^s} \Bigg]. \quad (3.61)$$

Thus it includes equal portions both of the ${}^1\Delta_g$ state and of the second excited singlet ${}^1\Sigma_g^+$ state, whose respective wave functions $\Psi_1^s/\Psi_2^s$ and $\Psi_3^s$ have been introduced in Sec. 3.1. Accordingly, one would expect the electronic optimization to yield a singlet-triplet gap that is halfway in between the respective experimental gaps for the ${}^1\Delta_g$ and the ${}^1\Sigma_g^+$ state, which—most surprisingly—is not the case. The reason for this can be found in an odd anomaly of nearly all [251] hitherto known exchange-correlation functionals. In contrast to the Schrödiger Hamiltonian the Kohn-Sham Hamiltonian does generally not act linearly on the respective non-interacting reference wave functions, if fractional occupation numbers and/or fractional spins are employed [250]. As a consequence, the total energy with respect to the number of electrons is a convex and continuously differentiable function and not, as it should be, a piecewise linear one (see Fig. 3.13). Therefore, the energy of systems with fractional charges is generally underestimated and an unphysical delocalization of electrons is thus

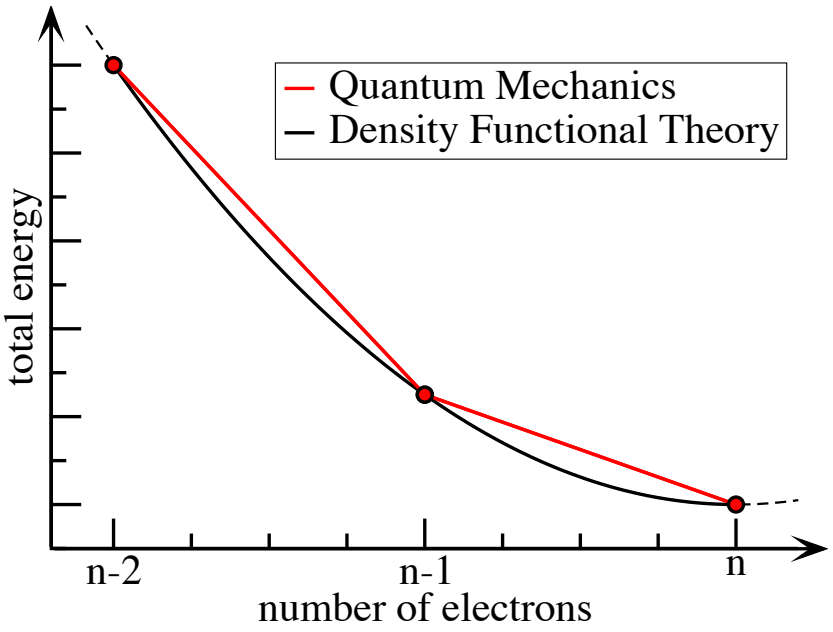


Figure 3.13: Sketch of the total energy for a system of nuclear charge $n$ as function of the fractional number of electrons present: Both the exact quantum mechanical result and the curve obtained when using one of the current exchange-correlation energy functionals are shown. Please notice that both methods yield the same result for an integer number of electrons.

typically favored by all functionals. With respect to the triplet-singlet gaps computed in this work, the discussed deficiency results in energy values that are significantly lower than the two singlet states' average due to the fact that the non-interacting reference wave function (3.61) consists of "half" the $^1\Delta_g$ and "half" the $^1\Sigma_g^+$ state. Furthermore, this current limitation of DFT foredooms any approach to decompose the obtained total energy of the spin-unpolarized state into the correct singlet states' energies, as for instance possible due to the linearity of the Hartree-Fock Hamiltonian in the *projected* UHF method introduced in Sec. 3.2.2. In spite of this deficiency, spin-projection methods can still be found in literature [223, 224], although not with respect to the spin-unpolarized calculation. Rather, a spin-polarized calculation of the singlet state is performed, whereby the two (one spin up and one spin down) valence electrons are distributed on one of the two valence orbitals $\phi_x$ and $\phi_y$ each, as previously done in this work for the simulation of the $^1\Sigma_g^+$ state with the UHF method. Due to the inherent spin-contamination, such spin-polarized calculations result in too small singlet energies (see Tab. 3.15), which are even smaller than the corresponding UHF energies given in Tab. 3.5. Accordingly, also after applying the spin-projection method, the computed triplet-singlet gap is still far too small, e.g. 0.811 eV [223], with respect to the $^1\Sigma_g^+$ singlet state it should describe. Therefore—and without any further formal justification—it is interpreted as being the triplet-singlet gap with respect to the lower lying $^1\Delta_g$ state.

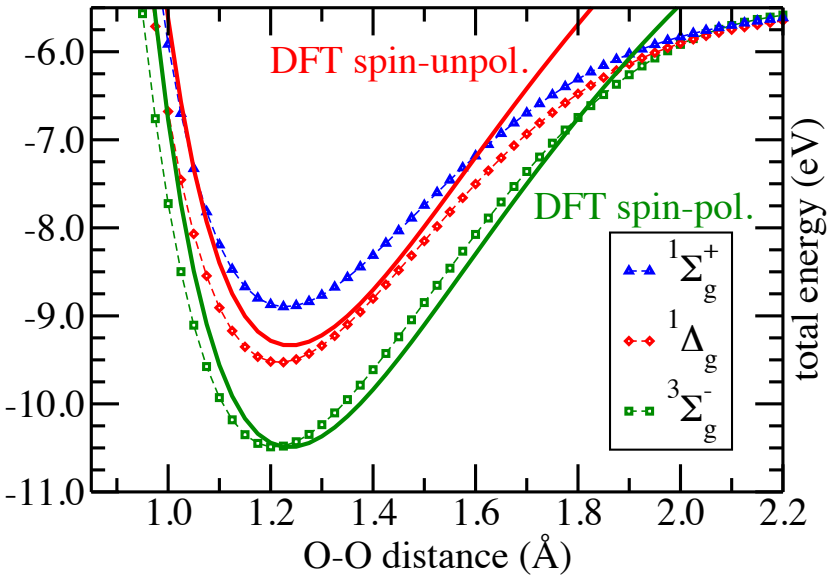


Figure 3.14: Relevant section of the Potential Energy Curves for the oxygen molecule as determined by DFT with the RPBE functional (solid lines) in a spin-polarized (triplet) and a spin-unpolarized (singlet) calculation: Additionally, the respective MRCI data is shown as dashed lines, whereby these curves have been energetically shifted so that the respective triplet calculations exhibit the exact same equilibrium energy. The complete data set for both approaches ranges from 0.7 to 3.5 Å, whereby the single points are separated by 0.025 Å from each other.

Last but not least, Zero Point Energy Corrections have been applied to the triplet-singlet gaps (see Tab. 3.15): As already found for the Quantum Chemical calculations in Sec. 3.2.2, the influence of these corrections is negligible in this context due to the similar functional form of the triplet's and the singlet's Potential Energy Curve, which are both shown in Fig. 3.14 and which are also discussed in detail in the next paragraph.

**Potential Energy Curves:**

Naturally the question arises, how legitimate DFT is for the purpose of describing the oxygen dissociation at metal surfaces, if it already disappoints in the calculation of the binding energy for an isolated oxygen molecule and introduces a rather large systematic uncertainty in the simulation of the singlet state. Although this topic is going to be critically discussed with respect to the Al(111)/O2 system as a whole in Sec. 4.2, there is an important fact that can be pointed out by now: The oxygen molecule in its triplet ground state is well described by DFT in the equilibrium and near-equilibrium region, as the obtained precise bond lengths and vibrational frequencies prove. This is further substantiated by Fig. 3.14, in which the PECs yield by the RPBE functional on a dense grid (starting at 0.75 Å and ending at 3.5 Å in steps of 0.025 Å) are

compared to the respective PECs generated by the MRCI calculations before. Beside a minute shift to larger bond lengths, the spin-polarized curve mimics the Quantum Chemical ground state neatly, at least up to an oxygen-oxygen distance of 1.8 Å. For larger bond elongations, however, the two curves come apart due to the erroneous description of the $^3$P+$^3$P dissociation limit of two isolated oxygen atoms, i.e., due to the wrong binding energy predicted in DFT.

For the singlet state the situation is similar: In the near-equilibrium region the PEC obtained by spin-unpolarized RPBE calculations is situated in between the PECs yield by MRCI for the $^1\Delta_g$ and for the $^1\Sigma_g^+$ state respectively due to the reasons discussed before. For bond elongations larger than 1.6 Å, where the Quantum Chemical curves approach each other and one would thus expect a better correspondence of DFT and MRCI, the computed RPBE curve lies significantly higher in energy and, even worse, shows qualitative differences with respect to the MRCI curves. Instead of approaching the triplet state in the limit of large oxygen-oxygen distances, the spin-unpolarized calculation exhibits an almost constant gap with respect to the spin-polarized PEC. Again, this behavior is caused by the employed ansatz for the singlet state: A spin-unpolarized simulation forces the magnetization density to vanish at any point in space. Accordingly, the correct $^3$P+$^3$P dissociation limit of two isolated triplet oxygen atoms, which only in combination yield an effective singlet configuration, cannot be achieved. Instead, the spin-unpolarized simulations approach the energy of two isolated oxygen atoms that are in their excited $^1$D singlet state each.

# Chapter 4

# Reaction Dynamics of the $O_2$/Al(111) System

## 4.1 Introduction

Metal oxidation processes are of outstanding importance in various industrial fields which range from combustion catalysis to microelectronics. Accordingly, this research field has attracted huge scientific interest—both from experimentalists and theorists—over the last decades. Although the most fundamental rules [254] underlying such processes were understood quite early, there still exist some not yet elucidated phenomena, even for systems that appear utterly simple at first sight. One of the most prominent and intriguing examples for them is the oxidation of the lowest energy (111) surface of aluminum, which exhibits quite a number of peculiar features:

(*a*) Experimental findings [3] show that the dissociative adsorption probability for the clean aluminum surface is approximately 1% at room temperature, but no state-of-the-art theoretical investigation found any evidence pointing in this direction until recently, as will be discussed below.

(*b*) Further experiments [255] found solely single oxygen atoms—in an average distance of more than 80 Å—after exposing the clean surface to oxygen. Various hypotheses, which range from hot adatom diffusion [255] over migration into sub-surface states [256] to cannonball abstraction dynamics [257], have been proposed to explain these findings. There are both investigations that support and investigations that oppose each one of these models: As a matter of fact, even the validity of the original experiments was questioned [258]. Modern theoretical methods seem ideal to finally settle this controversy: However, there is no chance to consistently clarify this mechanism as long as point (a) is still unresolved.

(*c*) Last but not least, a larger exposure of the aluminum surface to oxygen leads to the the growth of an oxide film, which then inhibits further corrosion. Although the overall mechanism for the formation of this $Al_2O_3$ stoichiometry has been elucidated by qualitative kinetic considerations [259],

the dynamics underlying the key steps of this process still has to be understood. Again, an unambiguous comprehension of point (a) and (b) is required beforehand.

Accordingly, the experimental *Sticking Coefficient* $S_0$, i.e. the probability of molecular dissociative adsorption as function of the initial translational energy, will serve as a starting point for this work. As first measured by Österlund *et al.* [3], it exhibits a typical "S"-shape (see Fig. 4.1) for the $O_2$/Al(111) system. This fact suggests that the underlying dynamics is *activated* [48], i.e. that **each** possible pathway towards dissociation is energetically hindered by a barrier on the respective Potential Energy Surface (PES). However, an almost complete absence of such barriers has been found in theoretical investigations based upon adiabatic DFT methods regardless of the functional actually employed [2, 5]. As a consequence, Molecular Dynamics simulations on thereby derived Potential Energy Surfaces yield a constant Sticking Coefficient of 100% even for thermal molecules, as shown in Fig. 4.1. A possible explanation for this dramatic discrepancy between experiment and theory could be the occurrence of a non-adiabatic spin-flip in the dissociation dynamics: Whereas the initially separated molecule-surface system is in an overall spin triplet state (see Sec. 3.1), the oxidized surface is in an overall spin singlet state [246], so that a spin-transition must occur along the dissociation pathway. Because of the fact that such transitions are governed by selection rules, which at least in the case of the free oxygen molecule are extremely discriminating (see Sec. 3.2.2), the molecule cannot relax into its singlet state as soon as this configuration becomes energetically favorable during the adsorption process (see Fig. 4.1). Rather, the oxygen may still stay in its triplet state, which actually is an excited state at this point of the dynamics, for a certain amount of time in spite of that. In this case, the motion

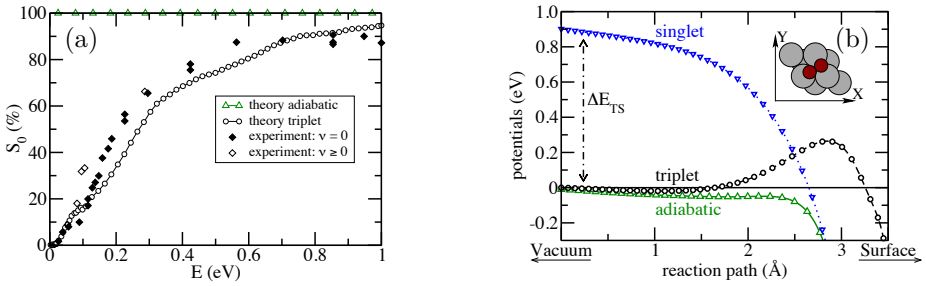


Figure 4.1: (a) Sticking Coefficient $S_0$ at normal incidence calculated by MD on the adiabatic (△) and on the triplet (○) PES respectively. At least 2000 trajectories have been computed for each marker. The also shown experimental data (⧫, ◊) is from Ref. [3]. The Minimum Energy Pathway in the triplet state and the corresponding adiabatic and singlet potentials for dissociation over the fcc site, with the molecular axis aligned parallel to the surface, are shown in Fig. (b) to exemplify the involved barriers. The addressed geometry, which is sketched in the inlet, will be used throughout this chapter for this purpose (see Fig. 4.3 and 4.5). Also, all total energies are given relatively to the total energy of a triplet molecule in the vacuum limit hereinafter.

of the oxygen molecule is determined by the Potential Energy Surface associated with the triplet state, until the system finally relaxes to its singlet ground state. Such a **non-adiabatic** spin-flip transition, which is known to enhance reaction rates in low-dimensional systems [260, 261] as well, cannot be described by a single **adiabatic** Potential Energy Surface, as if the system could relax to the respective ground state instantaneously. To account for the described breakdown of the Born-Oppenheimer approximation, Behler *et al.* [4, 6] calculated a **diabatic** triplet PES for this system, in the calculation of which both the number and the spin alignment of the oxygen electrons is kept constant. On this special PES (see Sec. 4.2), there are indeed barriers present for each possible pathway towards dissociation so that respective Molecular Dynamics simulations relying on this potential yield an "S"-shaped Sticking Coefficient in more than qualitative agreement with the experimental one (see Fig. 4.1). Although this appealing concordance of theory and experiment provides for a strong indirect evidence that the discussed spin transition indeed plays a crucial role in this process, there are, however, still some final uncertainties to settle:

- First, one has to realize that describing this process in terms of a single diabatic triplet PES is—although successful—an incorrect approach as a matter of principle: By this means, the oxygen molecule can never reach the correct final reduced singlet state, since no charge transfer or spin flips were accounted for in the calculation of the PES. As a consequence, the near-surface dynamics of the molecule, during which the relaxation into the singlet state eventually takes place, is erroneously described by this simple MD model. However, this flaw can be straightened out by simulating the dynamics on multiple Potential Energy Surfaces in terms of *Tully's Fewest Switches Surface Hopping* (SH) algorithm (see Sec. 2.4.3.2). By this means, the non-adiabatic transitions between the triplet state, i.e. the electronic ground state at large molecule-surface distances, and the singlet state, i.e. the final electronic ground state of the reaction, are explicitly accounted for. The effects of this approach can be estimated qualitatively by examining the location of the triplet-singlet curve crossing, which represents the effective barrier in the Surface Hopping approach, as done exemplarily in Fig. 4.1 for the Minimum Energy Pathway over the fcc site. Slow molecules, which are not able to reach the crossing point, will be repelled by the barrier on the triplet PES already at large oxygen-surface distances, where transitions to the singlet state are energetically forbidden. Slightly faster molecules, which are able to reach the crossing point but not to surmount the barrier, may relax into the singlet state and dissociate on the associated PES. In contrast thereto, this type of molecules is repelled back in the simple MD description due to the higher barrier that the triplet PES exhibits. Fast molecules, which can overcome the barrier anyhow, can dissociate in both approaches. Accordingly, the Surface Hopping method should result in a slight increase of the Sticking Coefficient $S_0$ at medium kinetic energies, without altering its already correct qualitative behavior. A more in-depth and quantitative analysis of this kind of simulations will be presented throughout this chapter. Thereby, the influence of the employed Potential Energy Surfaces (see Sec. 4.2) and the influence of the coupling between them (see Sec. 4.3) on the outcome of such calculations are also discussed in detail to shed some light on the

undergoing electronic processes.

- Even if the correct description of the non-adiabatic transitions for this process succeeds, there is still a possible error source left: As a matter of fact, all Potential Energy Surfaces used in this work were derived under the *frozen substrate approximation*, i.e. under the assumption that the aluminum bulk is immobile during the dissociation process. While this approximation can be expected to hold for large molecule-surface distances, it is foredoomed to fail at small distances: There, the dissociation event frees the adsorption energy of the oxygen molecule, which is even higher than the cohesive energy of the aluminum [246]. Accordingly, a strong motion of the first bulk layers is induced. This kind of effects cannot be hold responsible for the erroneous Sticking Coefficient in the adiabatic calculation, since an increased mobility of the substrate generally [48] increases the dissociation probability in inactivated systems due to the additional energy dissipation channels provided by the bulk's degrees of freedom. For the simulation of the near-surface dynamics, however, these effects are of vital importance. Accordingly, their role will be investigated in Sec. 4.4.6.2 and 4.4.6.1 both by means of an approximative *Surface Oscillator* model and by means of *ab initio MD*.

- Eventually, there is a final uncertainty that is not easy to settle: The absence of barriers on the adiabatic PES could be an artifact of the approximative GGA exchange-correlation functional used. Indeed, there is some evidence pointing in this direction: The comparison [262] of DFT calculations performed with the B3LYP functional (see Sec. 2.2.2.3) to respective PBE calculations for the interaction of an oxygen molecule with a 22-atom aluminum cluster shows that a barrier arises in the simulations with the hybrid functional. However, the cited work is affected by a series of uncertainties due to the massive calculational effort associated with such simulations. Thus the number of atoms chosen for the cluster, the size of the basis set and last but not least the amount of geometries inspected therein do not allow to clear this severe doubt definitely: If indeed barriers would arise for each possible dissociation pathway by the incorporation of a certain amount of exact exchange, the experimental Sticking Coefficient $S_0$ could then be reproduced adiabatically, i.e. without invoking a failure of the Born-Oppenheimer approximation. Consequently, this issue has to be solved as soon as possible to gain a true comprehension of the ongoing chemical process. Since the huge numerical costs associated with such hybrid functional calculations are still prohibitive, a different pathway for the assessment of this problem has been chosen in this work (see Sec. 4.4.4 and 4.4.5): Surface Hopping simulations have been used to find unambiguous, easily measurable fingerprints for the non-adiabaticity of this process so that a subsequent experiment can clarify the true nature of the barriers.

Accordingly, we will first discuss the calculational fundaments on which our simulations rely in Sec. 4.2 and Sec. 4.3. Then, Surface Hopping simulations for the determination of the Sticking Coefficient, which was already decently reproduced by the use of a single triplet PES, are presented in Sec. 4.4.1 to analyze the role that the switches actually play in the early PES dynamics. Further

insight is gained in Sec. 4.4.3, where simulations with respect to experimentally found features of the process that hitherto lack explanation are discussed. On the basis of the by then obtained insights, two kind of experiments, which can definitely verify the non-adiabaticity of this process, are proposed in Sec. 4.4.4 and 4.4.5. Last but not least, results achieved within a *Surface Oscillator* model and from *ab initio* MD simulations will be presented in Sec. 4.4.6 to validate the frozen substrate approximation for the previously discussed quantities in hindsight. Also, these calculations give an outlook on what to expect from the near surface dynamics.

## 4.2 The Potential Energy Surfaces

### 4.2.1 Calculational Details

The Potential Energy Surfaces employed in this work were all calculated by Dr. Jörg Behler in the framework of his Ph.D. thesis [246] at the Fritz-Haber Institute in Berlin. In this previous work, the atomic orbital based DMol$^3$ code [263] was used for the DFT simulations of the combined oxygen-aluminum system. Since this code allows for periodic boundary conditions [264], a $(3 \times 3)$ aluminum slab with seven layers and a vacuum stratum of 30 Å was used[1] for the simulations. As a matter of fact, the DMol$^3$ specific *all* basis set was used for the oxygen and the *dnd* (double numerics plus *d*-functions) basis set was used for the aluminum, whereby the respective numerical integrations were performed over the default mesh associated with these basis sets. Furthermore, a *cut-off radius* of 9 Bohr for the atomic orbitals, a $4 \times 4 \times 1$ **k**-point mesh and a Fermi-type smearing with a width of 0.1 eV have been employed. Extensive convergence studies with respect to these parameters can be found in [246].

For the description of exchange and correlation, the RPBE functional [93] was used for all the calculations the herein presented Potential Energy Surfaces rely on. As previously discussed in Sec. 3.3.3, this functional provides the by far best results for the oxygen molecule of all LDA and GGA functionals. As a matter of fact, Potential Energy Surfaces calculated with the PBE functional are not able to reproduce the experimental results as satisfactorily as the herein used RPBE based Potential Energy Surfaces can [6].

Additionally, the original DFT code was altered [5] to allow for *constrained* total energy simulations, in which the number of spin up and spin down electrons can be fixed to a certain arbitrary value for both the oxygen and the aluminum subsystem individually: To force the system to assume such an excited non-equilibrium occupation pattern, the relative *partial* Fermi energies of the oxygen molecule and of the aluminum surface have to be artificially shifted with respect to each other. Projection operators, which act only on one of the two subsystems respectively, have been used to achieve this goal. However, these operators depend upon the underlying electronic structure, i.e. on the necessary shift in partial Fermi energies. Thus this projection has to be repeated for each single step of the electronic minimization to ensure the self-consistency of the

[1] Due to the fact that DMol$^3$ utilizes a localized atomic orbital basis set, the vacuum size can be arbitrarily enlarged without increasing the numerical costs of the calculation.

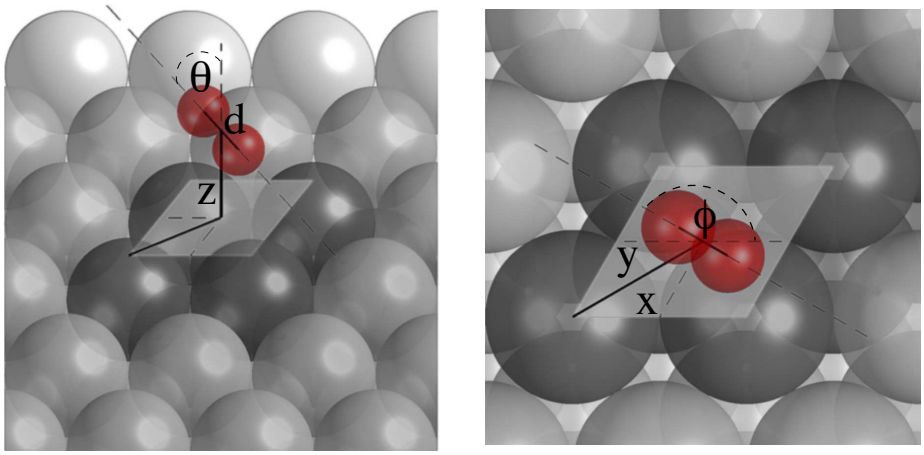


Figure 4.2: The oxygen molecule's degrees of freedom and their respective denotation both in a three-dimensional side view and a two-dimensional projected top view.

DFT calculations. By this means, various **diabatic** Potential Energy Surfaces, where the oxygen molecule is in a triplet, singlet or ionic state for instance, can be specifically addressed. For the three Potential Energy Surfaces inspected in this work (see Sec. 4.2.2), the total energies of more than 2000 different geometries of the system (almost 4000 geometries for the triplet PES) have been calculated each. Thereby, the inspected phase space was restricted to molecule-surface distances $z$ in between 1.0 and 6.0 Å, where the dynamics that actually triggers the dissociation occurs. For the same reason, solely geometries with oxygen-oxygen distances $d$ in between 1.0 and 2.4 Å were addressed, whereas the complete phase space was explored by random sampling for the remaining four degrees of freedom of the oxygen molecule, i.e. the center of mass coordinates $x$ and $y$ in the surface plane, the polar inclination angle $\theta$ with respect to the surface's normal and the azimuthal inclination angle $\phi$ with respect to the $x$-axis (see Fig. 4.2). The surface's and bulk's degree of freedom were, as mentioned before, assumed to be unaffected from the oxygen and were thus neither varied nor optimized. Actually, the geometry of a relaxed isolated slab, as yielded by an optimization of the surface geometry without any oxygen in the supercell, was used in the calculations.

In a second step, the harvested data for the individual electronic states was interpolated by a *Neural Network*, as extensively discussed in Sec. 2.3.1, to obtain a full six-dimensional smooth and continuously differentiable Potential Energy Surface each. Thereto, the previously successfully employed code of Soenke Lorenz [128] has been used and refined to fit the requirements of this chemical process best. In particular, a generic set of **eleven** *symmetry functions* [125], which serve as an input to the first layer of the network instead of the degrees of freedom shown in Fig. 4.2, has been introduced. These symmetry functions map the geometric coordinates uniquely but additionally incorporate—as the name suggests—the symmetries of the system. By this means geometries that differ in the actual values of the coordinates but which factually represent the

same geometry are mapped to the exact same total energies. For instance, the exchange of the oxygen atoms with each other or a translation along a lattice vector in the input does not influence the total energy value the Neural Network yields. To exploit this symmetry consistency in the simulation of the dynamics as well, the exact same code used for the fitting was embodied in the Molecular Dynamics and Surface Hopping code to access the Potential Energy Surfaces and their derivatives.

Technically, the quality of the fits was evaluated by inspecting the network's ability to reproduce total energies for geometries not presented to the network in the fitting procedure before. Thereby [246], mean absolute deviations in the order of 15 meV have been found for configurations with a total energy smaller than 1 eV and deviations in the order of 50 meV have been found for configurations with a larger total energy. Additionally, the validity of the fits was checked by comparing *ab initio (constrained) MD* simulations to Molecular Dynamics runs on the Neural Network's potentials. At reasonable molecule-surface distances, where the frozen substrate approximation still holds (see Sec. 4.4.6), the two methods yield almost exactly [246] the same trajectories.

### 4.2.2 The Inspected Electronic States

At first, the electronic states that are involved in the reaction have to be identified: In the initial stage, the oxygen molecule is in its triplet vacuum ground state. Thus this electronic configuration, whose PES coincides with the early part of the adiabatic Potential Energy Surface, is the first **diabatic** PES that has to be inspected. Conversely, in the final state, i.e. after the dissociative adsorption has occurred, the oxygen is in a charged singlet configuration $O_2^{\text{ion}}$, which is the respective electronic ground state at this point of the dynamics (see Fig. 4.3). Accordingly, the thereto associated **diabatic** PES, which coincides with the late part of the adiabatic Potential Energy Surface, is responsible for the late dynamics of the reaction. However, these two Potential Energy Surfaces, which are related to the initial and the final state of the reaction respectively, are not sufficient to describe the mid part of the dynamics: As a matter of fact, both the singlet $^1\Delta_g$ and the singlet $^1\Sigma_g^+$ state lie between[2] the triplet ground state and the first ionized state in the vacuum limit. Thus the two Potential Energy Curves associated with these states are expected to cross the triplet PES before the ionic potential can cross it, i.e. at larger molecule-surface distances. As a consequence, their role in the mid part of the dynamics of the dissociation process should be more significant than the one of the ionic PES, especially at small incident kinetic energies.

For an exact description of this process, it would obviously be preferable to include all the discussed states in the Surface Hopping simulations. However, this is not easily feasible: First, there are cumbersome issues in the specific addressing of the two diabatic singlet (see Sec. 3.3.3) and of the diabatic charged

[2]Please notice that the ionic state does not refer to a setup with a charged oxygen and a neutral aluminum surface, but to a setup, in which charge transfer has occurred from the surface to the molecule so that neither of them is neutral. Consequently, the energy gap in between this ionic state and the triplet ground state can be estimated to 3.8 eV [246] on the basis of both the oxygen molecule's electron affinity and the aluminum surface's workfunction [82].

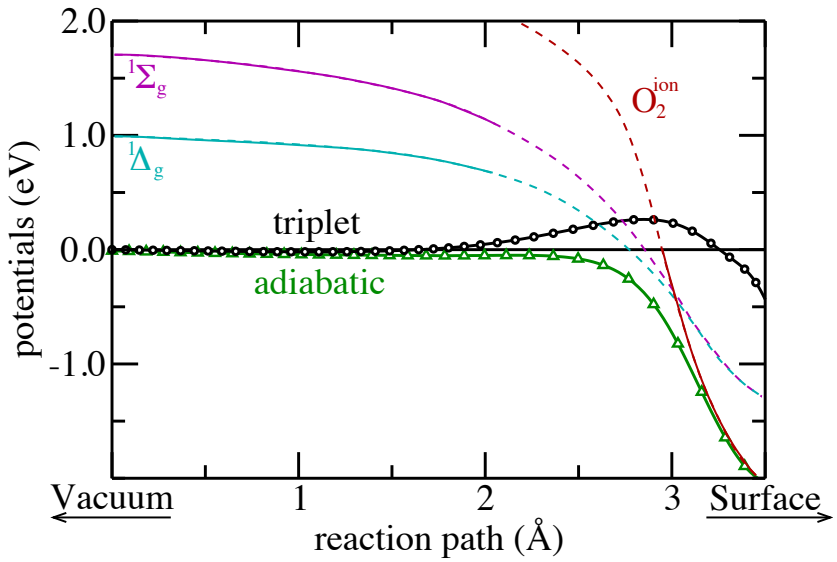


Figure 4.3: Schematic plot of the involved Potential Energy Surfaces along the Minimum Energy Path in the triplet state for dissociation in parallel alignment over the fcc site: Beside the triplet and the adiabatic PESs, which have been determined by means of DFT and Neural Network interpolation, also the expected functional form of the potentials associated with the first two excited singlet states and the ionic state is shown.

states [246] in periodic DFT calculations. Secondly, already the calculation of a single PES is computationally extremely expensive, so that we had to limit our research to three Potential Energy Curves, the electronic nature of which is critically discussed in the following.

**The Adiabatic Potential Energy Surface**

Although the **adiabatic** Potential Energy Surface is not directly used as a distinct electronic state in the final Surface Hopping simulations, it serves as a reference for the two other inspected Potential Energy Curves. Furthermore, it is very useful for the estimation of the coupling between these other states (see Sec. 4.3). As the name **adiabatic** PES implies, no constraint is employed in the underlying *spin-polarized* calculations so that the electronic structure can relax to the lowest total energy configuration for all inspected geometries. Thereby, a charge transfer and a thereto associated spin rearrangement occurs, as substantiated by a *Mulliken* [265] and a *Hirshfeld* [266] analysis in Fig. 4.4. These plots also show that the adiabatic calculations predict such a charge transfer not only at small molecule-surface distances, where it is indeed expected to occur, but also in the vacuum limit, where the occurrence of such a partial charge transfer is unphysical. This artifact in the DFT calculations is caused by the incorrect convexity of all hitherto known functionals (see Sec. 3.3.3). Accordingly, the energy of configurations with a fractional charge is underestimated and thus charge separation [250] is erroneously favored.

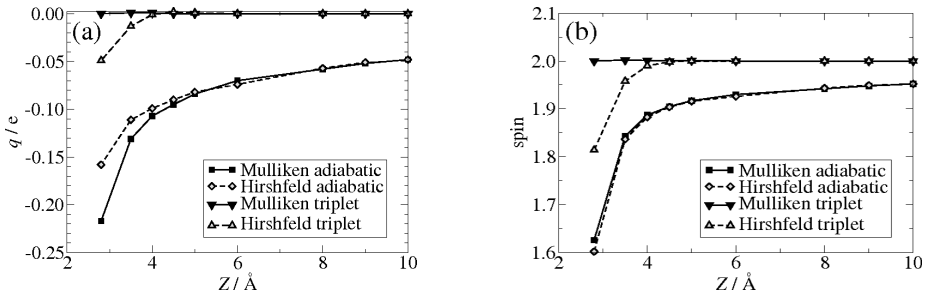


Figure 4.4: Charge (a) and spin (b) of the oxygen molecule as function of the molecule-surface distance $Z$ as yielded by adiabatic and by spin-constrained triplet DFT calculations respectively. In each case, the results of both a *Mulliken* [265] and of a *Hirshfeld* [266] analysis are shown. All calculations are performed with the PBE functional for an oxygen molecule which is aligned parallel to the surface over the fcc site. Image by courtesy of J. Behler [246].

### The Triplet Potential Energy Surface

The second inspected Potential Energy Surface is the **triplet** PES, which relies on *constrained spin-polarized* calculations in which both a possible charge transfer and a possible spin rearrangement are suppressed. As a consequence, the oxygen molecule is forced to assume the same triplet electronic state it exhibits as a ground state if isolated. Simultaneously, the number of spin up and spin down electrons is kept equal for the aluminum surface so that this subsystem is in a singlet state. The thereto employed *spin-constrained* DFT method successfully addresses this specific electronic arrangement, as respective *Mulliken* [265] and *Hirshfeld* [266] analyses substantiate (see Fig. 4.4). In contrast to the also shown adiabatic calculations, both the spin and the charge of the oxygen molecule are preserved both for large and for small molecule-surface distances. Also, no spurious charge transfer occurs in the vacuum limit. As a consequence, the triplet PES lies slightly higher in energy than the adiabatic PES in this limit.

### The Singlet Potential Energy Surface

The description of the excited states, even if done approximatively, is the by far most cumbersome task. As already seen in Sec. 3.3.3, already the excited singlet states of the isolated oxygen molecule, which serve as a starting point for the following considerations, cannot be correctly addressed individually within DFT: neither the $^1\Delta_g$ nor the $^1\Sigma_g^+$ state. However, a mixture

$$\Psi_{\text{unpol}} = \frac{1}{\sqrt{2}} \left( \Psi_\Delta + \Psi_\Sigma \right) \tag{4.1}$$

of both, the total energy of which lies in between the energies of the correct states, can be accessed by means of *spin-unpolarized* DFT. Due to the convexity of the exchange-correlation functional also discussed in Sec. 3.3.3, the simulated singlet-triplet gap ($\approx$ 1.2 eV) for such a mixture of states is closer to the experimental gap ($\approx$ 1.0 eV) for the $^1\Delta_g$ than to the one ($\approx$ 1.6 eV) for the $^1\Sigma_g^+$ state. A *constrained spin-unpolarized* DFT calculation of the oxygen-aluminum

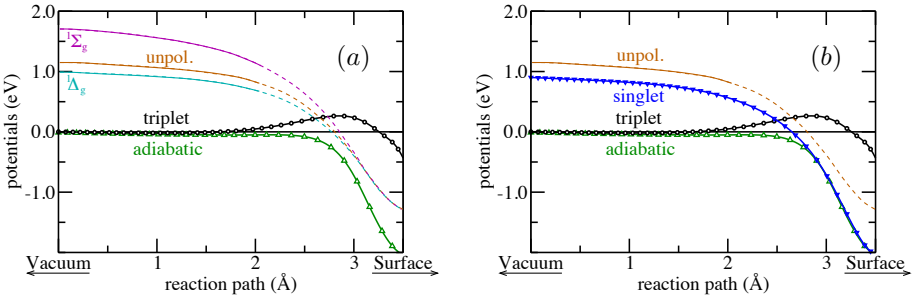


Figure 4.5: Schematic plot of the Potential Energy Surfaces along the Minimum Energy Path in the triplet state for dissociation in parallel alignment over the fcc site: Beside the triplet and the adiabatic PESs, which have been determined by means of DFT and Neural Network interpolation, also the expected functional form of the potentials associated with the first two excited singlet states are shown. In Fig. (*a*), these potentials are compared to the potential a *constrained spin-unpolarized* DFT calculation would yield. In contrast thereto, *constrained* and *unconstrained* spin-unpolarized DFT calculations, i.e. the singlet PES, are compared in Fig. (*b*).

system, in which the oxygen is forced to assume the electronic configuration it exhibits in a spin-unpolarized calculation if isolated, would thus also yield a PES that lies in between the Potential Energy Surfaces of the $^1\Delta_g$ and the $^1\Sigma_g^+$ state. As shown schematically in Fig. 4.5a, the thereby introduced error is not that significant in the barrier region: Upon dissociation, the two excited singlet states of the oxygen molecule collapse[3] into each other, since the symmetry of the molecule is thereby broken (see Sec. 3.1). As a consequence, the energetic gap in between these states is gradually diminished when approaching the surface so that the respective crossing points with the triplet PES are expected to lie close to each other. Thus also a *constrained spin-unpolarized* calculation should yield an acceptable approximation to the real crossing points.
Unfortunately, such a *constrained spin-unpolarized* approach cannot describe the correct final state of the system, since any charge transfer is suppressed between the oxygen and the aluminum in the underlying DFT calculations. To reach the charged final state of the oxygen in spite of that, an *unconstrained spin-unpolarized* PES has been used in this work to model the singlet states. By this means, the singlet spin character can still be guaranteed, while charge transfer effects are explicitly allowed. Formally, the wave function of the thereby addressed electronic state consists of three parts

$$\Psi_s = A \cdot \left( \frac{1}{\sqrt{2}} \left( \Psi_\Delta + \Psi_\Sigma \right) \right) + B \cdot \Psi_{\text{ion}}, \tag{4.2}$$

whereby the mixing coefficients $A$ and $B$ describe the amount of charge transfer and thus depend upon the simulated geometry. As shown in Fig. 4.5b, the

[3] As a matter of fact, the influence of the surface will first break the rotational symmetry of the oxygen molecule and thus lift the twofold degeneracy of the $^1\Delta_g$ state. For the sake of simplicity, this effect is not shown in Fig. 4.5a. Upon dissociation, however, both singlet states collapse into the $^3$P+$^3$P ground state of two isolated oxygen atoms, as discussed in Sec. 3.1.

thereby calculated PES, referred to as *singlet* PES hereinafter, coincides with the adiabatic PES at small molecule-surface distances and thus indeed describes the correct final state of the reaction. However, the appealing simplicity of a single PES that incorporates multiple excited states requires a price to be paid: Though the singlet PES mimics the *constrained spin-unpolarized* Potential Energy Curve at larger distances, it also experiences a shift towards lower energies due to the occurring charge transfer. Again, this charge transfer erroneously takes place even at large separations so that the simulated triplet-singlet gap is diminished to 0.9 eV [246] on this PES. Furthermore, also the crossing point with the triplet PES might be underestimated by this means.

In Fig. 4.6 the characteristics of these **six-dimensional** Potential Energy Surfaces are exemplified in so called *Elbow plots*, i.e. two-dimensional cuts for a fixed lateral center-of-mass position ($x$,$y$) and a fixed orientation ($\phi$,$\theta$) over the surface. There, the potentials for both a parallel and a perpendicular orientation of the molecular axis with respect to the surface are shown. Again, all plots are done for the dissociation over the fcc site, as sketched in Fig. 4.1 before. Although these contour plots show just a tiny section of the whole available phase space, this specific geometry exhibits some typical features of the six-dimensional Potential Energy Surfaces, which shall be discussed point by point:

- The adiabatic PES exhibits almost no barriers: neither for the parallel nor for the perpendicular orientation. Also, the offered dissociation channel is pretty broad so that special dynamic effects, as a hindered dissociation due to the vibrational degrees of freedom for instance, can be excluded in advance for this PES.

- In contrast thereto, the triplet PES exhibits a wide range of barriers: For the parallel orientation, the barrier is located in the early part of the PES at more than 2.0 Å distance from the surface, whereas for the perpendicular orientation the barrier lies a little bit closer to the surface, just at the seam of the early and the late PES. Accordingly, a slightly vibrational enhanced dissociation can be expected for the latter geometry [48]. Furthermore, this finding suggests that the triplet surface is strongly energetically and geometrically corrugated, as will be substantiated statistically in Sec. 4.4.1 and 4.4.3.

- The singlet PES does not exhibit any barrier at all and offers the widest dissociation channel of all calculations, regardless of the actual orientation. Also, this Potential Energy Surface is the smoothest of all inspected surfaces.

- Furthermore, certain geometric effects can be identified by comparing the potential for both orientations to each other: Regardless of the actual electronic state, a reaction in the perpendicular orientation is always less favorable due to a simple geometric effect: The dissociation is basically governed [1] by the hybridization of the aluminum states with the oxygen's $2\pi^*$ orbitals, which are perpendicular to the molecular axis. Accordingly, less hybridization is possible if the molecule hits the surface with its axis aligned to the surface normal. In addition, also the final state is less

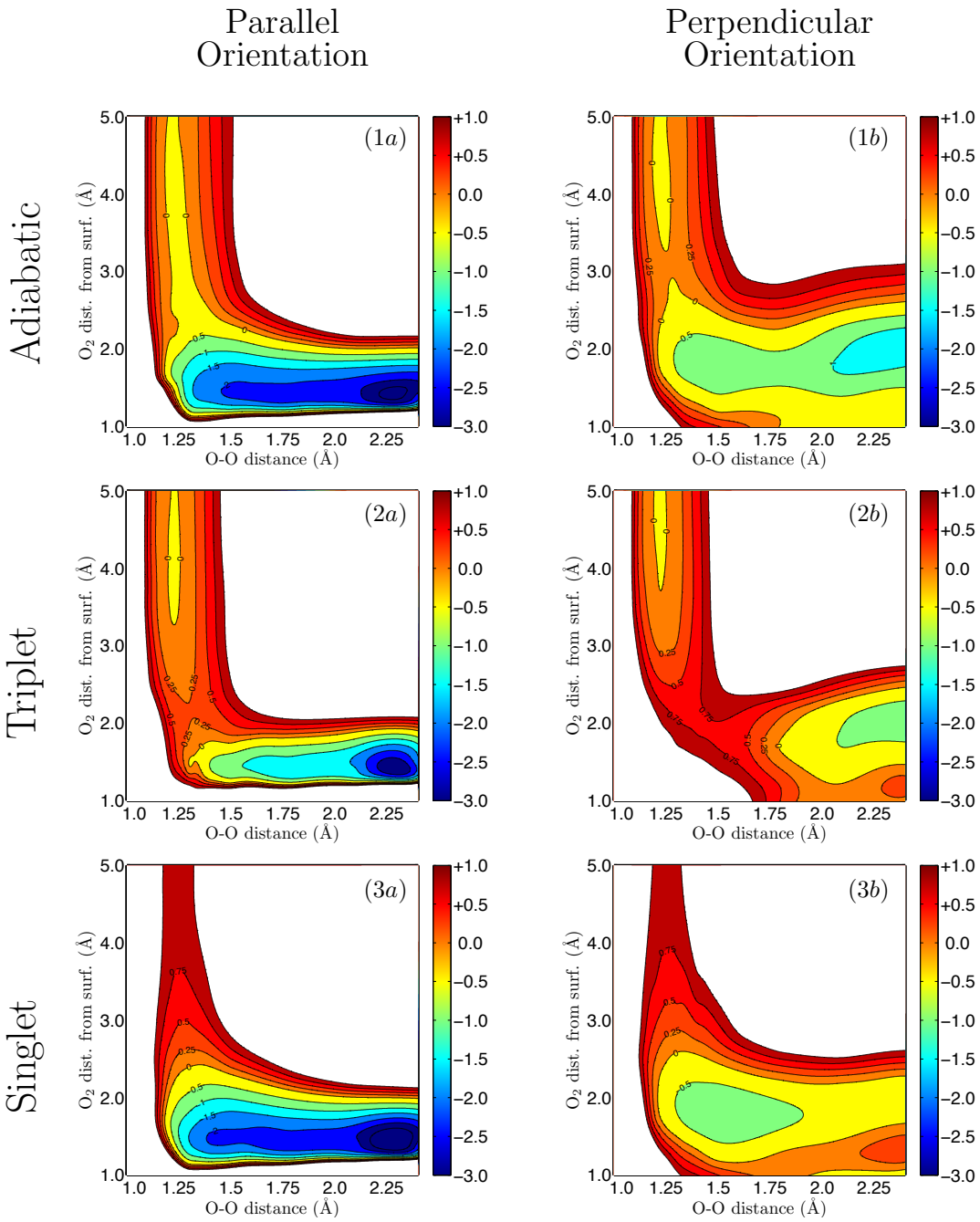


Figure 4.6: Elbow plots above the fcc site for the $O_2$/Al(111) system as yielded by an adiabatic (Fig. 1), a spin-constrained triplet (Fig. 2) and a spin-unpolarized singlet (Fig. 3) DFT calculation both for parallel ($a$) and perpendicular ($b$) alignment of the molecular axis with respect to the surface.

energetically advantageous in this geometry, since a successful dissociation event on these Elbow Plots results in the emission of a single oxygen atom from the surface by constraint.

- For the dissociation in perpendicular orientation, the mentioned emitted single oxygen atom adopts its triplet ground state: As a consequence, the adiabatic PES and the singlet PES do not resemble[4] each other in this limit. In the parallel orientation however, the two Potential Energy Surfaces are almost identical in the respective late parts as expected.

## 4.3 The Coupling

In addition to the Potential Energy Surfaces, which determine how the classical trajectories evolve, also the coupling between the inspected electronic states, which determines how the density matrix evolves along these trajectories, must be fed to *Tully's Fewest Switches Algorithm* beforehand. Thereto, two different approaches, which are antithetical in their derivation and constitute a lower and an upper bound for the unknown exact coupling, will be introduced in this section.

First, one has to realize that the triplet and the singlet Potential Energy Surfaces span a **diabatic** basis set as defined in Sec. 2.1.1: The respective triplet and singlet spinors $\chi_t$ and $\chi_s$, which are kept constant during the calculation of the respective Potential Energy Surfaces, ensure the orthogonality of the wave functions at each point in space. This statement holds in spite of the fact that the respective triplet and singlet spatial parts $\phi_t$ and $\phi_s$ might overlap due to the adiabatic charge transfer, as best seen in the calculation of the *non-adiabatic coupling vector*

$$\begin{aligned}\mathbf{d}_{ts} = \langle \Psi_t | \nabla | \Psi_s \rangle &= \langle \phi_t \cdot \chi_t | \nabla | \phi_s \cdot \chi_s \rangle \\ &= \langle \phi_t | \nabla | \phi_s \rangle \cdot \underbrace{\langle \chi_t | \chi_s \rangle}_{=0} + \langle \phi_t | \phi_s \rangle \cdot \langle \chi_t | \underbrace{\nabla | \chi_s \rangle}_{=0} = 0, \end{aligned} \tag{4.3}$$

which vanishes exactly at each point in space. As a consequence, the evolution of the density matrix, which is described by Eq. (2.115) in the *Surface Hopping* method, must be governed by the *non-diagonal* elements of the Hamiltonian matrix

$$V_{ts} = \langle \Psi_t | \mathcal{H}_e | \Psi_s \rangle , \tag{4.4}$$

which are the only terms left. For the herein simulated, previously discussed electronic states (see Sec. 4.2.2), the non-diagonal elements thus take the form

$$V_{ts} = A \cdot \left( \frac{1}{\sqrt{2}} \left( \langle \Psi_t | \mathcal{H}_e | \Psi_\Delta \rangle + \langle \Psi_t | \mathcal{H}_e | \Psi_\Sigma \rangle \right) \right) + B \cdot \langle \Psi_t | \mathcal{H}_e | \Psi_{\text{ion}} \rangle . \tag{4.5}$$

In the vacuum limit, where no charge transfer is supposed to happen, the coupling can be simplified to:

$$V_{ts} \approx \frac{1}{\sqrt{2}} \left( \langle \Psi_t | \mathcal{H}_e | \Psi_\Delta \rangle + \langle \Psi_t | \mathcal{H}_e | \Psi_\Sigma \rangle \right) . \tag{4.6}$$

[4] Rather, the triplet PES, which describes the triplet state of the oxygen molecule but not the triplet state of a single oxygen atom, exhibits a similar topology in this limit.

However, the only term in the Hamiltonian $\mathcal{H}_e$ that does not vanish in Eq. (4.6) in spite of the orthogonal spinors, is the *Spin-Orbit Coupling* $V_{\mathrm{SOC}}$, as extensively discussed in Sec. 3.2.2:

$$V_{ts} = \frac{1}{\sqrt{2}} \left( \langle \Psi_t | \, V_{\mathrm{SOC}} \, | \Psi_\Delta \rangle + \langle \Psi_t | \, V_{\mathrm{SOC}} \, | \Psi_\Sigma \rangle \right). \tag{4.7}$$

The first of the two coupling terms in Eq. (4.7), i.e. the coupling of the triplet state to the first excited $^1\Delta_g$ singlet state, vanishes[5] in first order approximation. Thus solely the second term, i.e. the coupling of the triplet state to the second excited $^1\Sigma_g^+$ singlet state, contributes to the coupling element in the vacuum limit. As discussed in Sec. 3.2.2, this non-diagonal matrix element, which has been found to be approximately 15 meV for the isolated oxygen molecule, is a linear, slowly decreasing (almost constant) function of the oxygen-oxygen distance, even up to huge separations. If even such a factual dissociation into two oxygen atoms does not affect this coupling element significantly, also the influence of the surface on this term should be negligible—at least for large and medium molecule-surface distances, where the crossing seam lies. Thus the discussed coupling element of the isolated oxygen molecule is supposed to be a suitable approximation for the combined oxygen-aluminum system in the early PES region.

Still, the influence of the adiabatic charge transfer, i.e. the gradual mixing of the ionic state $\Psi_{\mathrm{ion}}$ to the excited state $\Psi_s$, has been neglected in this derivation: To study such effects, one first has to inspect the influence of an undergoing charge transfer on the Spin-Orbit Coupling terms. For a partially ionic excited state, the normalization of the wave function (4.2) implies that the actual contributions from the Spin-Orbit Coupling are scaled by the respective mixing coefficient $A$ in Eq. (4.5). However, a maximal charge transfer of a quarter of an electron, which corresponds to an occupation probability $|B|^2 = 0.25$ of the ionic state, has been found in adiabatic calculations at the crossing seam (see Fig. 4.4). Accordingly, the absolute value of the mixing coefficient for the singlet state $|A| = \sqrt{1 - |B|^2}$ should also be larger than 0.85 in any case so that ubiquitous contributions from the Spin-Orbit Coupling can be expected, regardless of the additional contributions arising from charge transfer. Most importantly, this supplementary coupling with the ionic state, which is described by the third term in Eq. (4.5), is orders of magnitude larger than the Spin-Orbit Coupling, as will be discussed below. Consequently, the non-diagonal matrix element

$$V_{\mathrm{min}} = \frac{1}{\sqrt{2}} \langle \Psi_t | \, V_{\mathrm{SOC}} \, | \Psi_\Sigma \rangle \,, \tag{4.8}$$

in which all charge transfer effects are neglected, constitutes a **lower bound** for the total coupling present in the system.

With respect to the molecule's degrees of freedom, this minimal coupling only depends on the oxygen-oxygen distance: Accordingly, it is almost constant along the whole Minimum Energy Path up to the barrier and is weakly decreasing

[5] As elucidated in Sec. 3.2.2, there is no direct coupling between the $^3\Sigma_g^-$ state and the $^1\Delta_g$ state. Solely, an indirect coupling is possible through the $^3\Pi_g$ state, which is at least two orders of magnitude smaller than the direct coupling to the $^1\Sigma_g^+$ state.

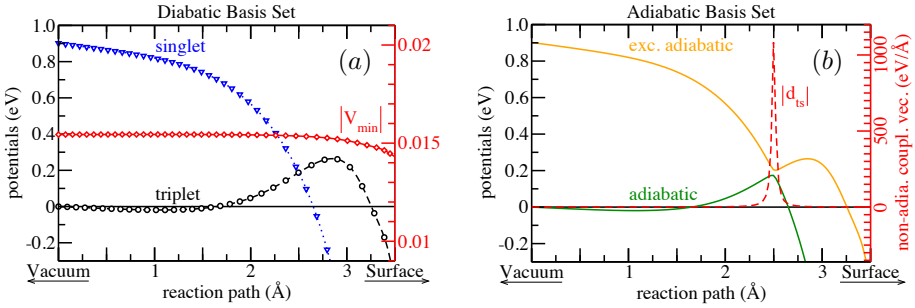


Figure 4.7: Potential Energy Surfaces for a coupling $V_{\mathrm{min}}$ along the Minimum Energy Path in the triplet state for dissociation in parallel alignment over the fcc site: Plot $(a)$ shows the potentials and the non-diagonal coupling element in the diabatic representation, whereas plot $(b)$ shows the potentials and the non-adiabatic coupling vector in the adiabatic representation. Please notice that a different scaling, as denoted on the respective right axes, has been used for $V_{\mathrm{min}}$ and $|\mathbf{d}_{ts}|$.

afterwards, as soon as the oxygen atoms move apart (see Fig. 4.7a). Beside this diabatic representation of the potentials, also the respective adiabatic potentials are shown in Fig. 4.7b: For their computation, the **diabatic** Hamiltonian matrix

$$\mathbb{H} = \begin{pmatrix} \langle \Psi_t | \mathcal{H}_e | \Psi_t \rangle & \langle \Psi_t | \mathcal{H}_e | \Psi_s \rangle \\ \langle \Psi_s | \mathcal{H}_e | \Psi_t \rangle & \langle \Psi_s | \mathcal{H}_e | \Psi_s \rangle \end{pmatrix} \approx \begin{pmatrix} E_t & V_{\mathrm{min}} \\ V_{\mathrm{min}}^* & E_s \end{pmatrix} \tag{4.9}$$

serves as a starting point. If diagonalized, the eigenvalues

$$E_{\mathrm{adia}}^{1/2} = \frac{1}{2}\left(E_s + E_t\right) \pm \frac{1}{2}\sqrt{E_s^2 - 2E_sE_t + E_t^2 + 4V_{\mathrm{min}}^* V_{\mathrm{min}}} \tag{4.10}$$

yield the respective ground and first excited state in an **adiabatic** representation. As can be seen in Fig. 4.7b, the adiabatic potentials and the diabatic ones are pretty similar in the minimal coupling model: Even the *effective barrier* in the respective representations, i.e. the crossing point of the diabatic potentials and the barrier of the adiabatic ground state, is almost the same for both basis sets, since the broadness of the avoided crossing is minute ($2V_{\mathrm{min}} \approx 0.03$ eV). Additionally, the absolute value of the non-adiabatic coupling vector $\mathbf{d}_{ts}$, which can be calculated by determining the eigenvectors during the diagonalization procedure, is shown in Fig. 4.7b as well. As usual, it is strongly localized at the avoided crossing of the two curves.

These adiabatic potentials in Fig. 4.7b reveal a fundamental inconsistency of the minimal coupling model: As a matter of fact, the thereby calculated adiabatic ground state potential does not resemble the adiabatic ground state PES yielded by the DFT simulations at all. Evidently, the employed minimal coupling is too small to reproduce the effects that lead to an unactivated adiabatic PES in the *ab initio* simulations. However, this finding can be efficiently exploited to define an **upper bound** for the coupling, which incorporates **all** charge transfer effects. Under the assumption that the adiabatic ground state yielded by the diagonalization and the adiabatic ground state yielded by DFT must be identical

$$E_{\mathrm{adia}}^{DFT} \stackrel{!}{=} \frac{1}{2}\left(E_s + E_t\right) - \frac{1}{2}\sqrt{E_s^2 - 2E_sE_t + E_t^2 + 4V_{\mathrm{max}}^* V_{\mathrm{max}}} \quad , \tag{4.11}$$

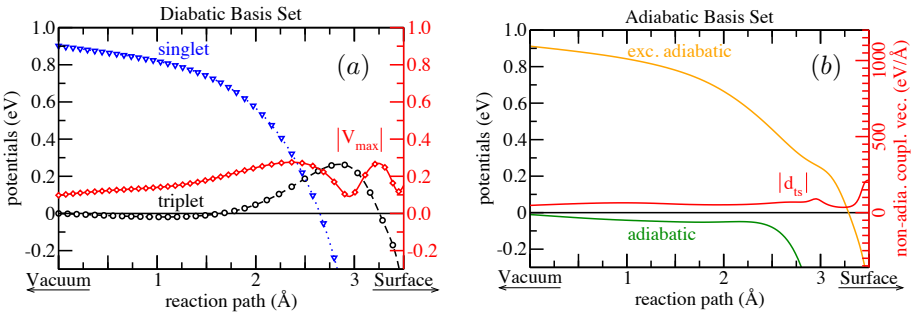


Figure 4.8: Potential Energy Surfaces for a coupling $V_{\max}$ along the Minimum Energy Path in the triplet state for dissociation in parallel alignment over the fcc site: Plot $(a)$ shows the potentials and the non-diagonal coupling element in the diabatic representation, whereas plot $(b)$ shows the potentials and the non-adiabatic coupling vector in the adiabatic representation. Please notice that a different scaling, as denoted on the respective right axes, has been used for $V_{\max}$ and $|\mathbf{d}_{ts}|$.

the absolute value of the coupling term can be determined by inverting the diagonalization

$$|V_{\max}| = \pm\sqrt{E_s E_t - E_s E_{\text{adia}}^{DFT} - E_t E_{\text{adia}}^{DFT} + \left(E_{\text{adia}}^{DFT}\right)^2} \quad . \tag{4.12}$$

In contrast to the one-dimensional minimal coupling, this maximal coupling term is a true six-dimensional function of the oxygen coordinates, since the inverse diagonalization (4.12) can be evaluated at each point in space for which respective triplet, singlet and adiabatic potential values are available. Accordingly, this coupling also depends on the respective rotational and center of mass degrees of freedom so that it does not exhibit such a constant behavior (see Fig. 4.8a) along the Minimum Energy Path as the Spin-Orbit Coupling did before. Please notice that this maximal coupling does not vanish in the vacuum limit as one would expect. As already discussed in Sec. 4.2.2, the adiabatic calculations exhibit a spurious charge transfer even at huge molecule-surface distances so that the respective adiabatic PES always lies slightly lower in energy than the triplet one does. As a consequence, even the coupling determined by Eq. (4.12), which heavily relies on the adiabatic calculation, does not vanish in this limit.

The respective adiabatic representation of the potentials in Fig. 4.8b is very useful to investigate the limits of our approach: There, the strong, non-vanishing coupling translates into a non-adiabatic coupling vector $\mathbf{d}_{ts}$ which is not localized anymore, but which is a completely atypical, almost constant function along the whole reaction path. Furthermore, also the barrier has vanished, so that the ground state potential resembles the adiabatic PES exactly, as required by construction. However, there is no barrier present on the excited PES either so that calculations for this basis set lead to a constant dissociation probability of 100% (see Sec. 4.4.1) once again. Such a drastic inconsistency between the two representations goes well beyond the usual tunneling effects found in Surface Hopping algorithms [7]. This phenomenon is especially remarkable due

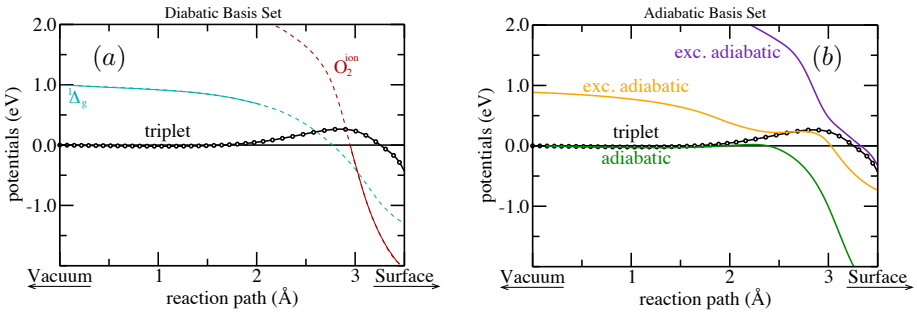


Figure 4.9: Effect of the inclusion of the charge transfer state in the determination of the adiabatic potentials: Both figures show a schematic plot of the Potential Energy Surfaces along the Minimum Energy Path in the triplet state for dissociation in parallel alignment over the fcc site. In Fig. (*a*), the diabatic potentials for the triplet, the first excited $^1\Delta_g$ singlet and the ionic state are shown. Conversely, Fig. (*b*) shows the adiabatic representation of these potentials, which have been constructed by diagonalization. Thereto, non-diagonal matrix elements in the order of magnitude of the Spin-Orbit Coupling (see Sec. 3.2.2) and in the order of magnitude of the charge-transfer based coupling (see Fig. 4.8) have been used for the coupling of the triplet to the singlet state and for the coupling of the ionic state to the neutral states respectively.

to the fact that in the case of a strong coupling an adiabatic representation should typically be more appropriate [154], which is obviously not the case for this system. As a matter of fact, this disagreement[6] with previous theoretical studies is caused by the deficient description of this reaction in terms of a two-level system, as discussed below. Unfortunately, we cannot easily extend our approach to a multitude of excited states due to the deficiencies associated with the calculation of the oxygen's excited states in DFT (see Sec. 3.3 and [246]). In spite of that, we can qualitatively discuss the effects such multiple exited states would have on our model: If we extended our system to include the first excited $^1\Delta_g$ singlet state and an ionic state for instance, the barrier would not vanish in the adiabatic representation of the potentials either, as shown schematically in Fig. 4.9: Due to the fact that the coupling of the triplet state with the $^1\Delta_g$ PES is orders of magnitude smaller than the coupling of both the neutral states to the ionic state, the first excited adiabatic state is shifted towards the adiabatic ground state and thus resembles the diabatic triplet state closest. Consequently, the barrier previously present in the triplet state is now mostly reproduced by the first excited adiabatic state, to which almost any trajectory that bypasses the first avoided crossing seam will switch due to the minuscule Spin-Orbit Coupling of the triplet and the singlet state. Still, a minute barrier is also present on the adiabatic ground state PES. If we compare these three constructed adiabatic potentials with the two-level system associated with the

[6] Actually, this finding has its roots in a different definition of "correctness": Most previous theoretical studies [154] compared diabatic and adiabatic simulations with full quantum-mechanical simulations under the assumption that the employed manifold of states and potentials is complete and exact. In our case, this is certainly not the case: Accordingly, we search for the representation of a two-level system that resembles a multi-state system closest.

maximal coupling in Fig. 4.8, it becomes obvious why Surface Hopping simulations fail in the adiabatic representation of our two-states model. Due to the strong maximal coupling, the adiabatic ground and the second excited adiabatic state of Fig. 4.9 are simulated, but not the first excited adiabatic state in which the barrier occurs. Thus, for this peculiar two-state system, we must revert to the diabatic representation, in which the two-level system resembles the manifold of potentials involved in the process closest. The price to pay is that the effective barriers in the simulations are slightly overestimated, since tunneling effects, which would be inherently incorporated in an adiabatic representation, are neglected in the diabatic representation.

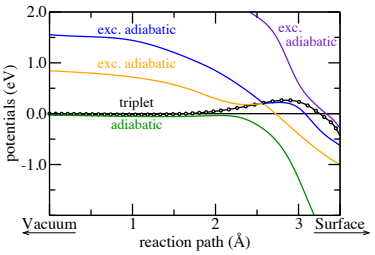


Fig. 4.10: Schematic plot of the discussed adiabatic potentials.

Eventually, the presented *Gedankenexperiment* sheds some light on the mysterious absence of barriers in the adiabatic ground state. One has to realize that all the excited states within the inspected energy interval matter in the computation of the adiabatic representation: If we additionally included the hitherto omitted $^1\Sigma_g^+$ singlet state in our previous considerations, the resulting adiabatic ground state would be further lowered in energy, as shown schematically in Fig. 4.10. The therein plotted adiabatic potentials have been computed on the basis of the qualitative diabatic potentials shown in Fig. 4.3, whereby constant non-diagonal matrix elements that are in the same order of magnitude of the Spin-Orbit Coupling (see Sec. 3.2.2) and of the charge-transfer based coupling (see Fig. 4.8) have been used for the coupling of the triplet to the singlet states and for the coupling of the ionic state to the neutral states respectively. This model indeed results in an **unactivated** adiabatic ground state PES that resembles the adiabatic DFT calculations. As discussed previously, the coupling between the neutral states and the ionic state is orders of magnitude stronger than the coupling in between the individual neutral states. Accordingly, the triplet and the singlet states are strongly repelled from the ionic potential but just weakly repelled from each other. As a consequence, the neutral states would be squeezed together and lie energetically on top of each other so that they piecewise reproduce the barrier present on the diabatic triplet PES (see Fig. 4.10). Thus—in spite of the unactivated ground state—Surface Hopping simulations would **not** lead to a dissociation probability of 100%, since there is a huge probability to switch to one of the activated excited potentials at the respective avoided crossings. Although the depicted scenario is credible and consistent with all the hitherto known facts, it is also purely hypothetical and should be further substantiated by simulations. Unfortunately, addressing all these *constrained* excited states in an *ab initio* calculation is still a formidable problem: On the one hand, the high-level Quantum Chemistry methods discussed in Sec. 3.2 are able to tackle the complex electronic correlation underlying such excited states, but are numerically too expensive to also include a realistic model of the metal surface, e.g. a large cluster of aluminum atoms. On the other hand, DFT is efficient enough to provide for a realistic description of the molecule-metal system, but the currently available semi-local exchange-correlation functionals fail to de-

scribe the excited states individually (see Sec. 3.3.1). Consequently, even very advanced methods such as *Time Dependent DFT* [115] or the solution of the *Bethe-Salpeter* equation [110] are foredoomed to fail as long as they rely on these functionals.

Last but not least, it should be noted that the exact phase of the coupling cannot be determined by the proposed inverse diagonalization either. Fortunately, this does not matter in a two-level system, where the same amount of phase shift has to occur for a transition from the ground to the excited state and vice versa. For multi-level systems, however, the phase of the coupling could be relevant, since a different phase shift can occur for transitions to different states, e.g. from the triplet to the singlet and from the triplet to the ionic state. In this case, the respective phase shift would influence coherence and respective interference effects significantly. However, the proposed method to determine the coupling is also not easily applicable to such multi-state systems. As a matter of fact, both the *constrained* diabatic Potential Energy Surfaces as well as some of the excited *adiabatic* potentials are thereto needed in advance. Thus it would be more advisable in such a case to use an *ab initio* Surface Hopping method in which both the Potential Energy Surfaces and the respective couplings are computed *on the fly* [267].

## 4.4 Results & Discussion

### 4.4.1 The Sticking Coefficient

The first property of the system that has been investigated is the *Sticking Coefficient* $S_0$ at normal incidence: Thereto the oxygen molecule was set up in its vacuum triplet state at a (center of mass) distance of 5.0 Å from the surface. Furthermore, the calculated equilibrium bond length was chosen as the starting oxygen-oxygen distance for all trajectories. The remaining initial conditions, i.e. the polar angle $\theta$, the azimuthal angle $\phi$ and the center of mass coordinates over the unit cell $x$ and $y$, were all chosen at random, so that the phase space is equally probed during the simulations: As shown in Fig. 4.11, this results in a higher probability to encounter a molecule in the parallel orientation ($\theta = \pi/2$) than in the perpendicular orientation ($\theta = 0$) due to the fact that there is more phase space for the azimuthal angle $\phi$ available in a parallel orientation. Additionally, a certain amount of kinetic energy $E$, in dependence of which the dissociation probability is inspected, is assigned to the translational (center of mass) velocity that is perpendicular to the surface. No further kinetic energy is allocated on the remaining degrees of freedom.

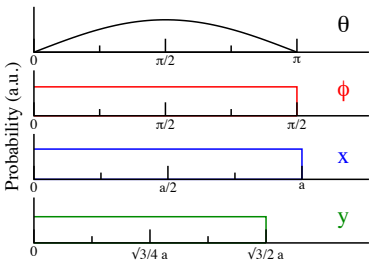


Fig. 4.11: Probability distribution of the initial conditions.

In the dynamics' simulations a multitude[7] of trajectories (> 8000) was computed

[7] In the Surface Hopping method we have to average over the available phase space **and**

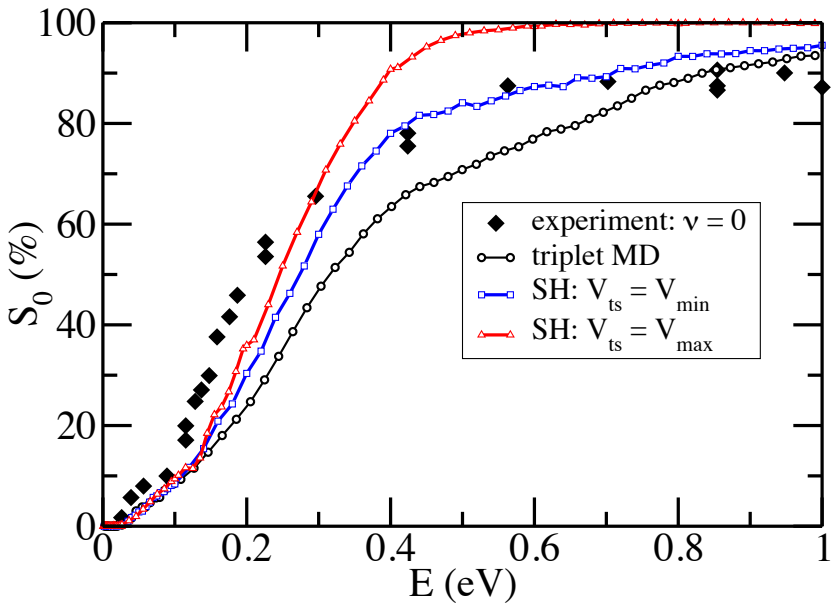


Figure 4.12: Sticking Coefficient as computed by Molecular Dynamics (MD) on the triplet Potential Energy Surface and by Tully's Surface Hopping method (SH) on both the triplet and the singlet PES. Neither vibrational nor rotational energy was assigned to the molecule in the initial conditions. The respective experimental data [3] is shown as well.

for each examined value of the translational energy. Thereby, the smallest kinetic energy that has been inspected was 2 meV and the largest energy was 1.0 eV. As can be seen in Fig. 4.12, this energy window was examined in steps of 20 meV, whereby even smaller intervals were chosen at smaller incident energies. To ensure a correct integration of the trajectory as well as of the density matrix evolution, the DLSODA routine [268, 269], i.e. a self-adaptive integration algorithm, which relies on the *Adams predictor-corrector scheme* [120] for stiff problems and on *Backward Differentiation* [130] for nonstiff problems, was chosen. In either case, a *LU decomposition* [120] is used to solve the arising linear equation system. Instead of fixing the integration step, the maximal allowed relative error has been set to $10^{-8}$ for the generalized coordinates, the associated velocities and for the density matrix elements, as done in previous works [149, 148]. Consequently, pretty small integration time steps of 0.15 fs result on average for both the diabatic and the adiabatic representation. In terms of energy conservation, these time steps translate into an average total energy error of less than $20 \cdot 10^{-9}$ eV for the complete individual trajectories. Conversely, deviances in the trace of the density matrix in the order of $10^{-9}$ have been found.

In a first step, we will discuss the outcome of such calculations for both the

over each single initial condition (see Sec. 2.4.3.2), so that a larger number of trajectories is needed than in a simple MD approach to reach a certain accuracy.

minimal $V_{\min}$ and the maximal possible values $V_{\max}$ of the coupling. To gain a better insight into the actual effect of the non-adiabatic transitions, the Sticking Coefficient as yielded by a pure MD run on the triplet PES is shown in Fig. 4.12 as well. The phenomena that have been previously postulated in the qualitative discussion (see Sec. 4.1) have been indeed found in the simulations:

($a$) With respect to the triplet MD calculations, nothing happens regardless of the actual coupling value for small incident energies ($< 0.1$ eV): The molecules are repelled at such large distances from the surface that they are not even able to reach the crossing point.

($b$) For medium incident energies ($< 0.8$ eV but $> 0.1$ eV), a significant increase of the dissociation probability is found. Molecules, which are not able to overcome the barrier in the triplet state but which are able to reach the crossing seam to the singlet state, are now allowed to dissociate. Obviously, this increase of the Sticking Coefficient is more pronounced in the case of a maximal coupling than in the case of a minimal coupling.

($c$) For even larger incident energies, the MD and the SH approach yield similar results: If the molecules are able to overcome the barrier anyway, it does not matter if a switch to the singlet state occurs or not.

It might seem surprising that the Surface Hopping method does not affect the Sticking Coefficient for slow molecules. At an incident energy of 50 meV for instance, a small portion of molecules is able to overcome the barrier and thus to dissociate even on the triplet PES alone. Accordingly, one would instinctively expect that there are also crossing points with the singlet state below the 50 meV region in which this barrier lies. This is indeed the case: However, these crossing points lie behind the peak of the barrier and do thus not increase the Sticking Coefficient, as exemplarily shown for the dissociation over the bridge site in Fig. 4.13. More systematically, these effects can be studied by inspecting the barrier distribution on the six-dimensional Potential Energy Surfaces. Thereto, a *Climbing-Image Nudged Elastic Band* method [26, 270, 271] was implemented to calculate the **Minimum Energy Path** in two-dimensional elbow plots (see Fig. 4.6 for instance). Beforehand, the initial and the final point of the reaction path have to be found. Whereas the starting coordinates are identical (5.0 Å for the molecule-surface distance and an equilibrium oxygen-oxygen bond length) for all the inspected elbow plots, the final positions vary from case to case. Thus, a crude bisection algorithm is used to search for a local minimum in the late part of the PES first. As a matter of fact, no such minimum exists in certain purely repulsive geometries, e.g., when the molecular axis is perpendicularly aligned to the surface over the top site, so that no reaction path can be computed for such geometries. Contrariwise, if an appropriate final point is found, the *reaction path* is modeled by so called discrete *images*, i.e. set of coordinates, which

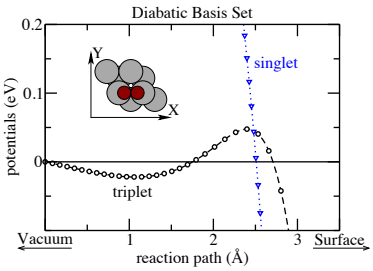


Figure 4.13: Diabatic potentials along the Minimum Energy Path for the also shown geometry.

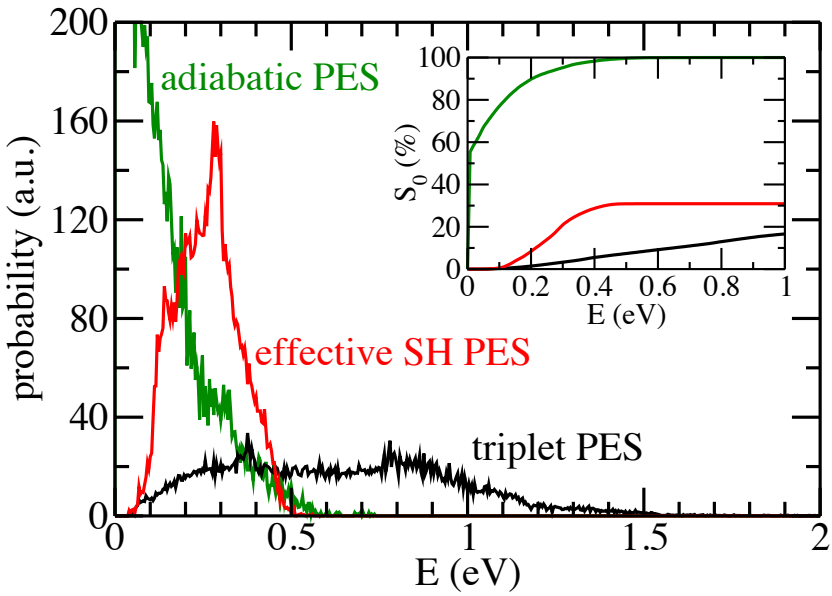


Figure 4.14: Area normalized histograms of the barriers found with the Nudged Elastic Band approach: The respective distributions on the adiabatic and on the triplet PES are shown. Additionally, the *effective barriers*, i.e. the barriers found for the ground state in the adiabatic representation of the triplet and singlet PES for a vanishing coupling, are plotted as well. The inlet shows the integrated barrier distributions, which correspond to the Sticking Coefficient in the sudden approximation ("hole model").

are initially set up equidistantly on the straight line connecting the initial and the final state. These individual images are now successively relaxed in a very peculiar way. They solely feel the portion of force from the potential that is perpendicular to the actual reaction path, i.e. the straight line connecting the respective image to its nearest neighbors. Additionally, each image is coupled to its nearest neighbors by a spring force that hence acts along the reaction path. Solely the first and the last image are not relaxed but kept fixed at the position of the previously determined initial and final state. After a few iterations, the images have relaxed to the Minimum Energy Path of the system, whereby the spring forces ensure its continuity [26]. At this point, the force acting on the image that exhibits the highest energy value is changed: Not the spring forces, but the full forces of the underlying potential act on it now, whereby the component along the reaction path is inverted [270]. This strategy ensures that this special image "climbs" up to the top of the barrier so that its actual energy value can be determined accurately. Furthermore, the spring forces acting on the other images can be adapted [271] so that they gather around the barrier to map this region of the PES more precisely.

In our case, a 20 images Nudged Elastic Band method has been employed to inspect the Minimum Energy Path in a huge number ($> 350,000$) of configurations, whereby a climbing image scheme has been used to determine the

respective barriers accurately. As a matter of fact, this procedure has been applied to both the adiabatic and the diabatic triplet PES. Additionally, also the ground state in the adiabatic representation of the triplet and the singlet PES has been inspected in the limit of a vanishing coupling ($V_{ts} = 10^{-5}$ eV). For such a tiny value of the coupling, also the respective gap arising at the avoided crossing in the adiabatic representation is minute (see Fig. 4.7). Accordingly, a thereby constructed adiabatic ground state is used to model the *effective* barriers that the molecules encounter in the diabatic Surface Hopping simulations in the limit of large couplings, as if each molecule would switch from the diabatic triplet into the diabatic singlet state as soon as it reaches the crossing point. The resulting barrier distributions in Fig. 4.14 show that the adiabatic PES is unactivated for the large majority of configurations, and that even in the case of a hindered dissociation the arising barriers are typically smaller than 0.5 eV. In contrast thereto, the triplet PES exhibits exclusively activated entrance channels with a broad distribution of barriers that ranges from approximately 40 meV to more than 1.5 eV. On the respective effective PES for the Surface Hopping, the value of the occurring barriers is drastically reduced to 0.5 eV at most. However, the lowest occurring barriers are not modified due to the reasons discussed before (see Fig. 4.13). Furthermore, the inlet of Fig. 4.14 shows the integrated barrier distribution, which corresponds to the Sticking Coefficient in the sudden approximation. In this so called "hole model" both the rotational and the lateral surface motion are suppressed during the reaction and the respective degrees of freedom are kept fixed to their initial conditions. The comparison to the six-dimensional Sticking Coefficient in Fig. 4.12, in the computation of which the motion of all six molecular degrees of freedom is accounted for, clearly shows the importance of dynamical effects for this system, especially on the strongly corrugated triplet PES.
The finding mentioned above, i.e. that the dissociation probability is not altered by the inclusion of non-adiabatic effects at small incident translational energies, could lead to the erroneous conclusion that non-adiabatic effects do **not** play a role in the dynamics in this energy window at all. As substantiated in Fig. 4.15, the number of switches per computed trajectory indeed depends upon the incident translational energy and vanishes in the limit of slow molecules. The number of switches occurring per successful **dissociation** event, however, is almost constant over the whole range of inspected translational energies. More figuratively, one can understand this behavior on the basis of the Minimum Energy Path over the bridge site shown in Fig. 4.13: In this case, the dissociation probability is indeed solely determined by the triplet PES. Nevertheless, if a molecule is able to overcome the barrier, it will bypass the crossing seam with the singlet state as well. Since in the late part of the trajectory the singlet state is energetically favorable, a switch to this ground state will occur sooner or later. Thus, for such low energy molecules, switches still occur on top or after the barrier and thus determine the late part of the trajectory significantly. Furthermore, Fig. 4.15 substantiates that the chosen couplings are indeed lower and upper bounds to the true coupling: For a successful dissociation event, at least one switch, i.e. one transition from the triplet into the singlet state has to occur. In our simulations with the minimal coupling, considerably less than one switch per dissociation event is found. Accordingly, only a portion of these trajectories reach the correct final singlet state upon dissociation. Conversely, considerably more than one switch per dissociation event is found in the case of

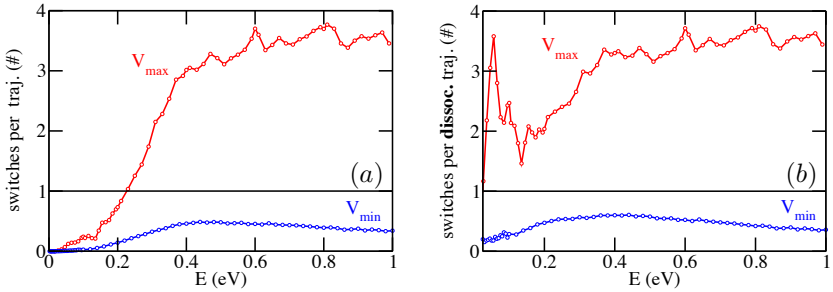


Figure 4.15: Number of Switches per computed trajectory ($a$) and per successfully dissociated trajectory ($b$) for both a maximal and a minimal coupling of the Potential Energy Surfaces. Neither vibrational nor rotational energy was assigned to the molecules in the initial conditions.

a maximal coupling.

In this context, it is also instructive to compare simulations that have been performed in the diabatic or adiabatic representation respectively. As shown in Fig. 4.16, there is almost no difference in the Sticking Coefficient for the two representations in the case of a minimal coupling: The avoided crossing in the adiabatic representation just vaguely lowers the effective barrier (see Fig. 4.7) and thus slightly enhances the dissociation probability for kinetic energies up to 0.4 eV. For larger incident energies, however, the dissociation probability is slightly lowered in the adiabatic representation in spite of that fact: One has to realize that for a successful dissociation the molecule has to get rid of its translational energy or otherwise it will be scattered back. Due to the frozen substrate approximation the only possible mechanism available is to redistribute the available energy onto the other degrees of freedom. As discussed in Sec. 2.4.3.2, *surface hops*, which occur more often in a diabatic basis set by definition, favor such a redistribution along the non-adiabatic coupling vector and thus favor the dissociation as well. Whereas the discussed differences in the two representations are rather subtle for the minimal coupling, a drastic discrepancy occurs when the maximal possible coupling is employed. As extensively discussed before (see Sec. 4.3), the calculation in the adiabatic representation leads to a dissociation probability of 100% in the case of the maximal coupling, as MD simulations do on the adiabatic PES that was used to construct this coupling element. Accordingly, solely calculations in the diabatic representation will be presented hereinafter.

### 4.4.2 The Vibrational Enhancement

Still, the influence of the vibrational degrees of freedom has not been accounted for in the hitherto presented calculations. As a matter of fact, the oxygen molecule exhibits a significant *Zero Point Energy* of approximately 0.1 eV (see Sec. 3.2.2). This characteristics of the oxygen molecule can be modelled approximatively by assigning the respective energy to the vibrational degree of freedom when setting up the initial conditions. Thereto, the molecule's coordinates are

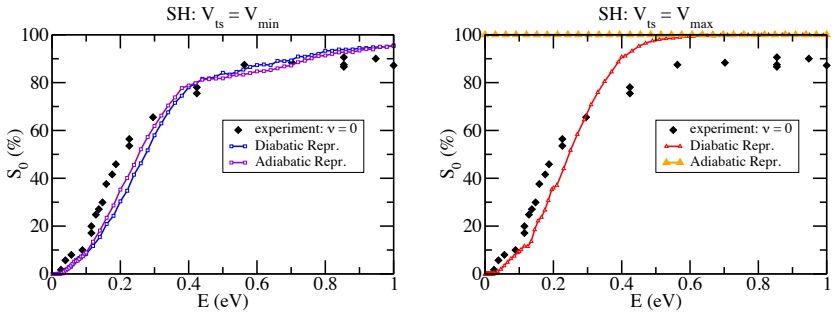


Figure 4.16: Sticking Coefficient as computed by Tully's Surface Hopping method (SH) in the diabatic and adiabatic representation: Neither vibrational nor rotational energy was assigned to the molecule in the initial conditions. The respective experimental data [3] is shown as well.

first determined at random as discussed before (see Fig. 4.11). Then, a simple *bisection* method is used to compute the maximal possible bond elongation and maximal possible bond compression at the chosen initial vibrational energy. Again, a dice is thrown[8] to decide which oxygen-oxygen distance in between the maximal bond elongation and the maximal bond compression is actually used as initial condition. The remaining vibrational energy, i.e. the portion of chosen vibrational energy that is not consumed by the potential energy term, is allocated as kinetic energy on the vibrational degree of freedom of the molecule. As shown in Fig. 4.18, the amount of vibrational energy thereby assigned to the molecules affects the dissociation probability significantly. For small incident translational energies, already the Zero Point Energy more than doubles the Sticking Coefficient, while the respective increase at larger kinetic energies is less pronounced but still present. This phenomenon occurs regardless of the employed coupling and even in the case of triplet MD simulations so that it must have its roots in the topology of the triplet PES. This might seem surprising at first, since such a strong vibrational enhancement is typically [48] caused by barriers that lie in the late part of the elbow plots, which is not typically the case on the triplet PES (see Sec. 4.2).

Nevertheless, the occurring vibrational enhancement can be understood by inspecting the triplet PES more closely. During the dynamics, the vibrational frequency of the oxygen molecule does not stay constant at its vacuum value $\omega_0$ but depends on the other degrees of freedom, especially on the molecule-surface distance. As a matter of fact, the vibrational frequency $\omega(\mathbf{s})$ is softened while approaching the surface along a reaction coordinate $\mathbf{s}$ (see Fig. 4.17). As a consequence, the energy $\hbar\omega(\mathbf{s})\left(\nu+\frac{1}{2}\right)$ associated with the vibrational state $\nu$ also decreases along the reaction path so that the surplus of energy with re-

[8] As a consequence, each bond length in the available vibrational phase space is equally likely as initial condition. This is—as a matter of principle—an incorrect procedure: On average, a classical oscillator is most likely found at its maximal deflection, whereas a quantum mechanical oscillator is most likely found at its minimal deflection. However, it has been found that these details in the initial conditions do not influence the outcome of the calculations at all.

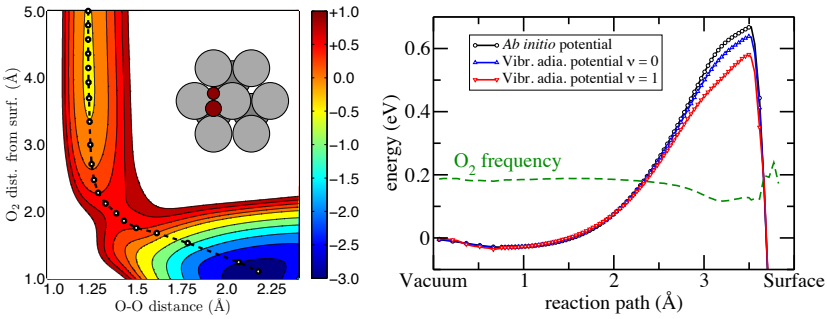


Figure 4.17: The elbow plot for the triplet Potential Energy Surface is shown in the left image: Additionally, the Minimum Energy Path (dashed line) with the individual images (circles) of the Nudged Elastic Band method are plotted. In the right graph, the corresponding vibrational frequency $\hbar\omega(\mathbf{s})$ of the oxygen along this pathway as well as the vibrational adiabatic potentials are shown. Both figures refer to the geometry over the bridge site sketched in the inlet.

spect to the initially assigned value of $\hbar\omega_0\left(\nu+\frac{1}{2}\right)$ is steadily redistributed on the other degrees of freedom. Formally, this phenomenon can be described by *vibrationally adiabatic potentials*

$$V^{\nu}_{\text{vib. adia.}} = V_t(\mathbf{s}) + (\hbar\omega(\mathbf{s}) - \hbar\omega_0)\cdot\left(\nu+\frac{1}{2}\right), \tag{4.13}$$

which are adjusted to intrinsically include this flow of energy from the vibrational degree of freedom into the others. Although the quantization of the vibrational states enters the derivation [272] of the vibrationally adiabatic potentials $V^{\nu}_{\text{vib. adia.}}$ explicitly, the use of Eq. (4.13) is not restricted to full quantum mechanical dynamics simulations. Due to the fact that the vibration is the fastest degree of freedom of the system, it is also an *adiabatic invariant* in the classical motion, so that Eq. (4.13) also applies to classical trajectories [134] as inspected herein.

As shown in Fig. 4.17 for a sample geometry, the decrease of the vibrational frequency indeed results in a lowered effective barrier on the vibrationally adiabatic potentials. These reduced barriers explain the strong vibrational enhancement found in the simulations (see Fig. 4.18). When the first excited vibrational state is simulated, this phenomenon may reduce the barrier so significantly in certain geometries that it even vanishes. Consequently, the Sticking Coefficient does not vanish in the limit of zero incident translational energy either. Rather, steering effects [147], which allow a molecule to find the non-activated pathway at low incident energies, become active and lead to a remarkable increase of dissociation events. Unfortunately, the respective available experimental data is not sufficient to confirm or to contradict the simulated steering phenomena. However, a vibrational enhancement of the dissociation, which—as far as one can tell—is in qualitative agreement with our calculations, has been found there, too. As a matter of fact, the vibrational enhancement might be artificially amplified in the simulations due to the classical description of the nuclear motion, in which

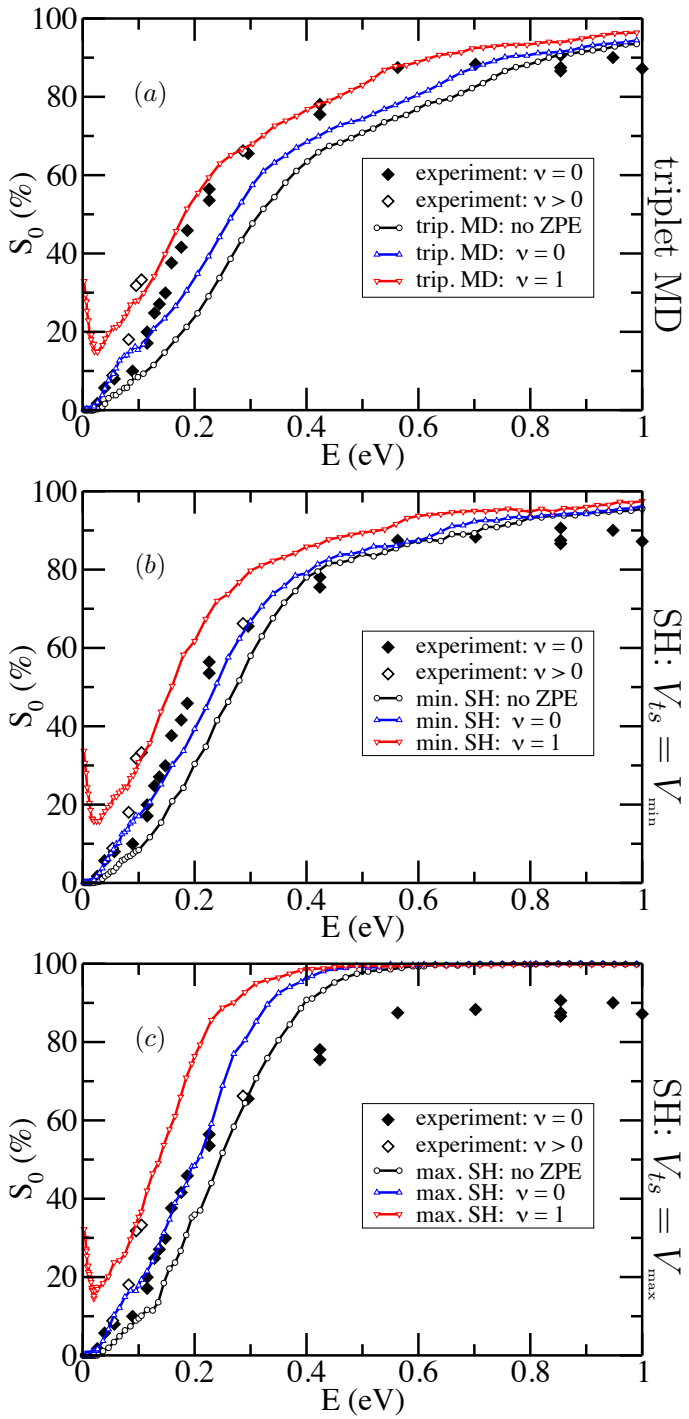


Figure 4.18: Sticking Coefficient $S_0$ as calculated by Molecular Dynamics on the triplet PES ($a$) and by Tully's Fewest Switches Surface Hopping with minimal ($b$) and maximal coupling ($c$) of the triplet and singlet PES. In each graph, the results of calculations with no initial vibration energy (no ZPE) and of calculations with the energy of the vibrational ground ($\nu = 0$) and the first excited ($\nu = 1$) state are shown.

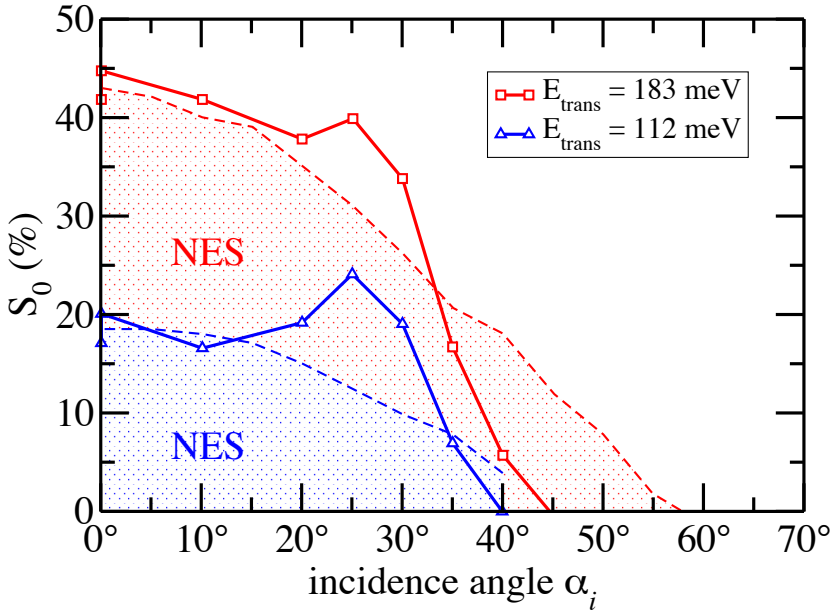


Figure 4.19: Experimentally [3] determined Sticking Coefficient $S_0$ as function of the incidence angle $\alpha_i$: Both the results for an incident total kinetic energy of 0.112 eV and of 0.183 eV are plotted. These measurements were performed with an azimuthal angle corresponding to a direction 7° away from the $[11\bar{2}]$ direction. Additionally, the respective Normal Energy Scaling (4.14) of the experimental Sticking Coefficient at normal incidence is shown as shaded area.

the Zero Point Energy is not conserved during the dynamics. Thus even this portion of energy can be withdrawn from the vibrational degree of freedom and then promote dissociation, especially at low incident energies. This artificial energy transfer also explains why Surface Hopping simulations with no initial Zero Point Energy seem better suited to reproduce the experimental data for translational energies below 0.1 eV, whereas Surface Hopping simulations with the initial Zero Point Energy are more appropriate for the rest of the inspected energy window. In spite of this fact, the Zero Point Energy was assigned to the molecules as initial condition in all calculations that are presented hereinafter, if not explicitly specified otherwise.

As mentioned before, this vibrational enhancement is not a non-adiabatic effect, but can be understood on the basis of MD simulations on the triplet PES alone. However, these are also the last experimental measurements we are able to explain without the introduction of non-adiabatic transitions, as will be seen in the next sections.

### 4.4.3 The Normal Energy Scaling

As discussed in the previous sections, the outstanding majority of barriers occurs on the early part of the triplet Potential Energy Surface. Consequently, one

would expect [48] that for an off-normal incidence of the molecules the Sticking Coefficient solely depends on the portion of kinetic energy $E_\perp$ associated with the velocity component that is perpendicular to the surface. Formally, this assumption, which is usually referred to as *Normal Energy Scaling* (NES), allows to express the Sticking Coefficient for an off-normal incidence $S_0\left(E, \alpha_i\right)$ in terms of the Sticking Coefficient for the normal incidence at $\alpha_i = 0$

$$S_0\left(E, \alpha_i\right) \approx S_0\left(E_\perp, 0\right) = S_0\left(E\cos^2\left(\alpha_i\right), 0\right), \tag{4.14}$$

whereby a scaling in dependence of the incidence angle $\alpha_i$ with respect to the surface normal is performed. However, the experiments of Österlund *et al.* [3] show that this assumption is not fulfilled: In the cited work, the dissociation probability was also measured in dependence of the incidence angle for both a constant total translational energy of 0.112 and 0.183 eV respectively, whereby the chosen azimuthal incidence angle corresponds to a direction 7° away from the $[11\bar{2}]$ direction. Actually, the thereby found Sticking Coefficient strongly deviates from the Sticking Coefficient constructed by a Normal Energy Scaling of the respective normal incidence data, as shown in Fig. 4.19. Instead of following the monotonic decay of the NES, the dissociation probability exhibits a pronounced maximum at approximately 25° from normal incidence, whereas it decays faster than the NES for angles that are larger than 35°. Further experiments by Weiße *et al.* [11] yielded similar although not equal[9] results: In this work, the in-plane reflectivity $R(E, \alpha_i)$ has been measured for a total translational energy of 0.09, 0.17, 0.3 and 0.4 eV respectively. Again, an increase of dissociation occurs at approximately 22°, whereby the dip found in the reflectivity is most pronounced at an incidence energy of 0.17 eV. Still, significant effects are also found for an incidence energy of 0.09 and 0.3 eV respectively, whereas the measurement at 0.4 eV does not exhibit such features. Basically, this study suggests that such a peculiar behavior of the Sticking Coefficient is also found in a larger energy window and at different azimuthal angles.

Beside these experimental findings that just support the measurements performed before by Österlund *et al.* [3], Weiße *et al.* [11] also proposed a possible mechanism that could lead to this completely atypical dependence of the Sticking Coefficient on the incidence angle. It is a well known fact, that **potential wells** act like a converging lens on incoming trajectories [147]. As shown schematically for a fictitious potential in Fig. 4.20, any trajectories that hit a potential well on its sidewall are deflected from their original direction towards the well's center. If by any chance there is a high barrier at the "focal point", i.e. in front of the potential well, molecules at a normal incidence ($a$) will be steered towards this barrier. With respect to a PES with the same barriers but without any wells, this steering results in a reduction of the dissociation probability, since incident molecules at a normal incidence ($a$) will encounter large barriers more often due to the steering. For the described arrangement of potential wells and barriers, a connatural effect occurs for trajectories ($b$) at

[9] First, the exact azimuthal angle with respect to the crystal has apparently not been measured and is thus most probably not identical with the one used in the previous measurements of Österlund *et al.* [3]. Secondly, solely the in-plane reflectivity of the molecular beam has been determined. However, also the out-of-plane reflectivity has to be known to determine the absolute value of the respective dissociation probability. The qualitative findings of this work remain valid in spite of that.

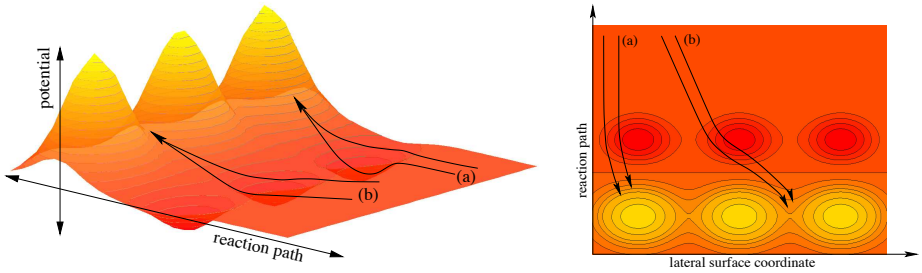


Figure 4.20: Two and three-dimensional sketch of the dynamics of slow molecules on a fictitious Potential Energy Surface that exhibits both activation barriers and physisorption wells. Thereby, the PES is strongly corrugated with respect to the lateral surface coordinate. Accordingly, the highest barrier as well as the deepest potential well are found in front of a specific surface site. The trajectories ($a$) sketch the possible dynamics of molecules at normal incidence, whereas the trajectories ($b$) depict the dynamics at off-normal incidence.

off-normal incidence. Again, the potential well acts like a converging lense on the incoming trajectories. However, due to the different incidence angle, the focal point does not lie at the position of the highest, but at the position of the lowest barrier (see Fig. 4.20). Thus, an increase of dissociation with respect to the normal incidence case will result for a specific incidence angle due to the steering. Weiße *et al.* [11] also further substantiated the validity of the proposed mechanism on the basis of classical and quantum dynamics simulations on a three-dimensional semi-empirical model PES, the actual parameters of which were adjusted to yield the best possible agreement with the experiment. For a parallel orientation of the molecule's axis with the surface normal, this procedure results in a minimal barrier of 0.05 eV and a maximal barrier of 0.15 eV, whereas barriers of approximatively 2 eV arise in the perpendicular orientation. Furthermore, the simulations resulted in a qualitative agreement with the experiment for potential well depths in between 50 and 100 meV. All these parameters seem reasonable: First, the barriers are in the same order of magnitude as the barriers found on our triplet PES. Secondly, the potential well is shallow enough to explain [11] why such a physisorbed state has hitherto not been found experimentally.

As plausible as the proposed model might seem at first glance in this reduced dimensionality scenario, the actual dynamics occurring on a six-dimensional PES is much more complicated. As a matter of fact, the described effect depends on a variety of factors, which all have to collude in a particular way to actually result in such an increase of dissociation at off-normal incidence. The first fundamental prerequisite for this effect is the occurrence of physisorption wells, which have to be localized[10] and not equally distributed with respect to the surface degrees of freedom. To investigate this issue, the Minimum Energy Paths computed previously with the *Nudged Elastic Band* method on the triplet PES

[10] A physisorption valley, i.e. a continuous potential well with the same location and depth over all surface sites, would not lead to any steering at all.

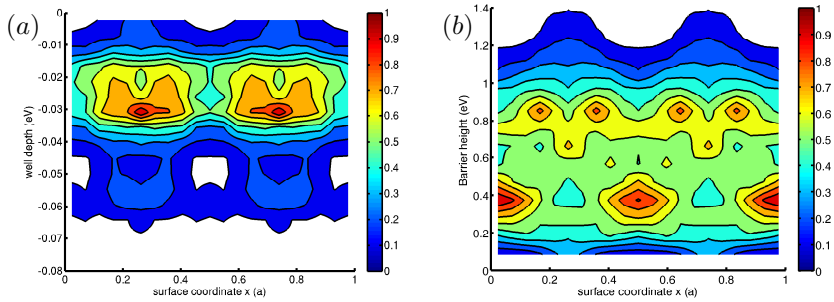


Figure 4.21: Fig. (*a*) shows the probability distribution for the physisorption wells on the triplet PES in dependence of their depth and their location with respect to the lateral surface coordinate $x$. Conversely, Fig. (*b*) shows the probability distribution for the barriers found on the triplet PES in dependence of their height and their location with respect to the lateral surface coordinate $x$. For the calculation of both normalized histograms the data previously achieved with the Nudged Elastic Band method was used.

have been inspected for such energy minima in between the vacuum region and the barrier position. The resulting probability distribution with respect to the well depth and the lateral surface coordinate $x$ is shown in Fig. 4.21, whereby a summation has occurred over all other degrees of freedom of the molecule. Indeed, such localized physisorption wells can be found at a lateral coordinate of approximately a quarter and three quarters of the lattice constant respectively. However, they are not as deep ($\approx 30$ meV) as the ones determined in the semi-empirical calculations before. This is not too surprising, though: The employed semi-local GGA functionals do not account for non-local effects such as the long-range *Van-der-Waals* attraction, which is generally responsible for the largest portion of the physisorption interaction. Furthermore, the wells are not only too shallow but also slightly too close[11] to the surface with respect to the semi-empirical data. These apparently insignificant and negligible deficiencies of the DFT functional will have a huge impact on our calculations, as will be discussed below.

Furthermore, a peculiarly corrugated barrier distribution, in which the highest barriers are found in front of the physisorption wells and considerably lower barriers are found in the region between them, is required for the occurrence of such a steering effect as described above: Indeed, if we compute a histogram of the barriers found on the triplet PES with respect to their height and their lateral surface coordinate $x$, we find such a barrier arrangement. As shown in Fig. 4.21, the most probable barrier found in front of the wells is at approximately 0.65 eV, whereas in the region between the wells the most probable

[11] While slightly too short bond lengths are typically found for *Van-der-Waals* systems if addressed with the PW91 functional [273], slightly too large bond lengths are typically found with PBE [104]. In comparison to PBE, the RPBE functional solely exhibits a larger local exchange enhancement factor at large generalized gradients—as does PW91 (see Sec. 3.3.2). Thus the found shortening of the physisorption distance on our RPBE-PES seems reasonable. Unfortunately, no systematic studies for the RPBE functional could be found in literature with respect to this issue.

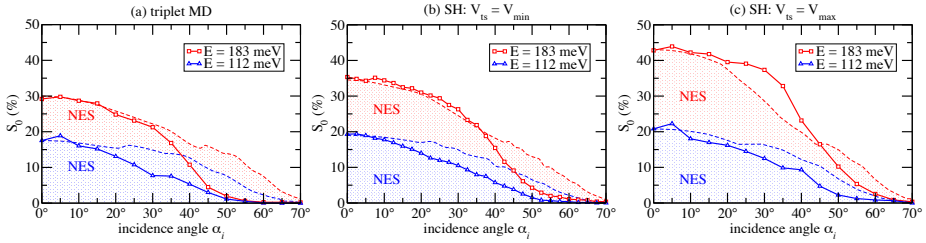


Figure 4.22: Sticking Coefficient as function of the incidence angle $\alpha_i$: Fig. (*a*) shows the results of MD simulations on the triplet PES, whereas Fig. (*b*) and (*c*) show the results of Surface Hopping simulations for a minimal and a maximal coupling respectively. For correspondence to the experiment, an azimuthal angle of 7° with respect to the $[11\bar{2}]$ direction has been chosen for all calculated trajectories. As a reference, the respective *Normal Energy Scaled* Sticking Coefficient, as derived from the normal incidence data labeled as "trip. MD: $\nu = 0$", "min. SH: $\nu = 0$" and "max. SH: $\nu = 0$" in Fig. 4.18, is shown as shaded area in all plots.

barrier is found at approximately 0.38 eV. However, no steering effects will be active for molecules that are able to surmount such high barriers. Therefore, we have to focus on the low energy region below 0.2 eV, in which steering effects are indeed significant. There, the barrier's distribution changes completely: In this energy window, the lowest energy barriers are situated directly in front of the physisorption wells and thus a basic requirement of the proposed model is not met. As a consequence, Molecular Dynamics simulations on the triplet PES do not show any increase of the dissociation probability for an off-normal incidence. Rather, the Sticking Coefficient seems to obey the Normal Energy Scaling at small incidence angles (see Fig. 4.22). Thus, neither an adiabatic calculation, which predicts a 100% of dissociation regardless of the incidence angle due to the absence of barriers, nor the triplet MD simulations are able to reproduce these experiments—not even qualitatively.

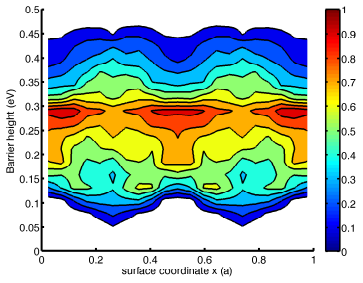


Fig. 4.23: Probability distribution of the barriers in SH simulations.

The *Surface Hopping* calculations, however, succeed at least partially where the other approaches failed before. As can be seen in Fig. 4.22, the simulations with Tully's Fewest Switches algorithm indeed predict an increase of the dissociation probability at off-normal incidence with respect to the NES, at least for an incident translational energy of 183 meV. With respect to the coupling, solely minute effects are found for the minimal possible coupling, while an evident increase is found for the maximal one. Again, this phenomenon can be understood by analyzing the previously computed *effective* distribution of barriers that are encountered in such Surface Hopping simulations. The thereto employed *effective* PES for

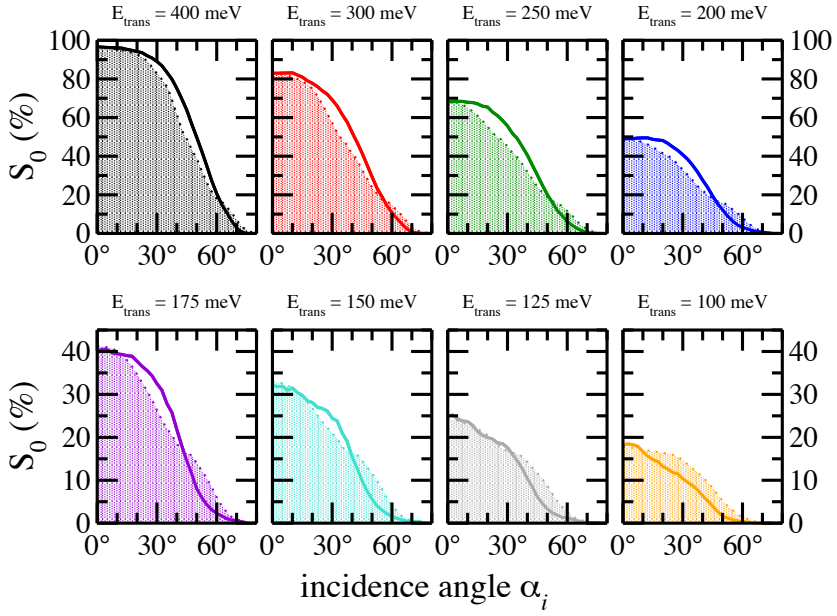


Figure 4.24: Systematic study of the Sticking Coefficient in dependence of the incidence angle $\alpha_i$, which has been computed by Tully's Fewest Switches Surface Hopping for the maximal possible coupling. For correspondence to the experiment, an azimuthal angle of 7° with respect to the $[11\bar{2}]$ direction has been chosen for all calculated trajectories. As a reference, the respective *Normal Energy Scaled* Sticking Coefficient, as derived from the normal incidence data labeled "max. SH: $\nu = 0$" in Fig. 4.18c, is shown as shaded area. Please note that a different scaling of the abscissae has been used for the first and the second row.

the combined triplet-singlet system is much less *energetically* corrugated than the triplet PES: As already discussed on the basis of Fig. 4.14, it exhibits a significantly narrower barrier distribution around a pronounced maximum at approximately 0.3 eV. Geometrically, however, also this PES is strongly corrugated, as substantiated in the barrier histogram in Fig. 4.23 with respect to the lateral surface coordinate $x$. In contrast to the triplet PES, the lowest possible energy barriers in the energy window in between 0.1 and 0.3 eV are indeed situated in the middle of the physisorption wells and not in front of them so that the proposed steering mechanism can become active. Still, the simulations reproduce the experiments at most qualitatively so that further systematic studies (see Fig. 4.24) have been performed over a wide range of incident translational energies to understand the occurring discrepancies.

As a first step, we are going to explain why the "peak" of the Sticking Coefficient is shifted towards larger angles in the simulations and why it is situated at almost 35° and not at the experimental value of less than 25°. As becomes evident from the fictitious PES shown in Fig. 4.20, the angle at which the peak lies is determined by the geometry of the Potential Energy Surface, i.e. by the right-angled triangle spanned between the potential well and the lowest as well as the

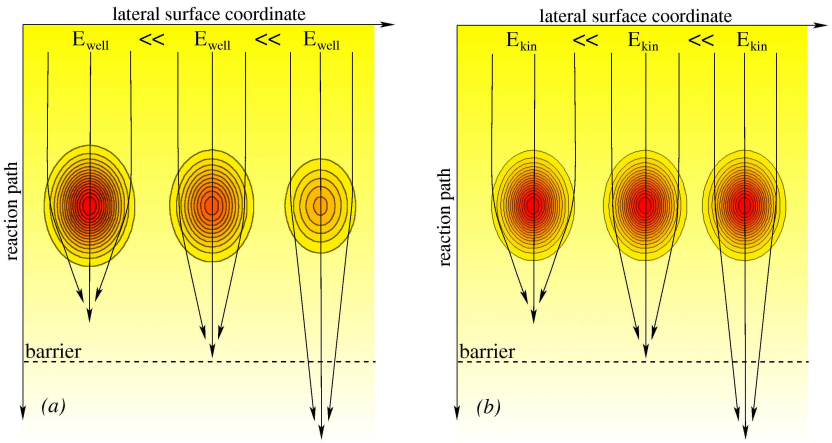


Figure 4.25: Sketch of the steering processes induced by potential wells as function of the well's depth ($a$) and as function of the incident kinetic energy ($b$).

highest barrier. With respect to the semi-empirical PES, the potential wells on the *ab initio* PES lie too close to the surface by approximately 0.25 Å so that the respective triangle is compressed: Accordingly, the angle at which the steering amplifies the dissociation probability most is shifted towards larger values. Still, these purely geometrical considerations do not explain why the simulations do not result in a pronounced peak of the Sticking Coefficient but in a diffuse enhancement of the dissociation probability with respect to the NES. First one has to realize that such potential wells exhibit a "focal length" in dependence of their depth $E_{\mathrm{well}}$, as shown in Fig. 4.25: A deep well accounts for strong steering effects so that a manifold of parallel incident trajectories is focused to a point that is located shortly after the well. Contrariwise, a shallow well focuses such trajectories to a point that is farther away. As schematically shown previously in Fig. 4.20, the strongest enhancement of the dissociation probability occurs if the most favorable incident angle and the focal length match so that the focal point of the well lies exactly at the position of the lowest barrier. In such a case all incident trajectories are steered towards this lowest barrier when approaching the surface. However, such a peculiar geometry is unstable with respect to the incidence angle, since even a minute tilt of the molecular beam brings the system out of focus. As a consequence, the resulting peak in the Sticking Coefficient is highly localized at a specific angle in such a system.

In the scenario described above, the most favorable incidence angle, which is determined by the respective position of the lowest barrier with respect to the potential well, and the focal length of the well, which is determined by its depth, have to match. While the semi-empirical simulations suggest [11] that this severe constraint might be fulfilled in the real system, it is surely not fulfilled on the computed system of *ab initio* Potential Energy Surfaces, which are known to exhibit physisorption wells that are both too shallow and too close to the surface. Consequently, a manifold of parallel incident trajectories is not focused to the lowest barrier, but to a point beyond the barrier region (see Fig. 4.25). Thus

solely few molecules hit the lowest barrier exactly, while the majority of the incident trajectories is steered towards slightly higher barriers that lie next to the lowest barrier. In such an out-of-focus system, small changes of the incidence angle are less relevant: A small tilt away from the most favorable angle does not result in an increase of the encountered barrier for almost all trajectories as in the perfectly focused system. Rather, some trajectories, which do not hit the lowest barrier at the most favorable incidence angle, are now indeed steered towards the lowest barrier in the tilted geometry. Contrariwise, the trajectories that are steered towards the lowest barrier at the most favorable incidence angle, experience a higher barrier in the tilted geometry. As a consequence, the peak in the Sticking Coefficient is less pronounced and blurred with respect to the incidence angle for such an out-of-focus system—exactly as it is in the Surface Hopping simulations.

In the previous considerations, however, we have completely neglected the role of the incident translational energy. As a matter of fact, slow molecules are deflected more strongly by a potential well, whereas fast molecules are less deflected. As schematically shown in Fig. 4.25, the actual "focal length" of a physisorption well does thus not solely depend on its depth, but also on the translational energy of the incident trajectories. Accordingly, it should be possible to counterbalance the lack of well depth on the *ab initio* PES by decreasing the kinetic energy in the simulations so that a "perfectly focused" configuration is achieved. As a consequence, a sharp pronounced peak of the Sticking Coefficient should appear in the simulations as well. However, no such effect is observed in the calculations at all (see Fig. 4.24). On the contrary, no enhancement of the dissociation probability is found for incident energies below 150 meV in the simulations, whereas a peak is still found for incident energies as low as 90 meV in the experiments. One has to realize that the lowered translational energy might counterbalance the lack of well depth but not the too low distance in between the wells and the barriers, which actually determines the most favorable incidence angle. Since this angle is considerably larger in the simulations at any incident energy, there is significantly less kinetic energy available that can be used to overcome the barrier. At a total translational incidence energy of 150 meV for instance, solely $150\ \text{meV} \cdot \cos^2(35^\circ) \approx 100$ meV are stored in the velocity component perpendicular to the surface. For this or even smaller energy values, however, there is again a higher probability to find a lower barrier in front of the well than beside it (see Fig. 4.23). Accordingly, the proposed steering mechanism cannot be active at such little incidence energies in the simulations, since the required peculiar corrugation of the PES is not met in the energy regime below 0.1 eV. Conversely, this mechanism would still be active at total incidence energies as low as $100\ \text{meV}/\cos^2(25^\circ) \approx 123$ meV, if the steering was already active at 25° as it is in the experiment. Although this estimated energy value is not as low as the one for which a peak is detected in the measurements, it is still considerably closer to the experiment than the value found in the simulations.

Obviously, our simple optical considerations cannot describe this effect on an exact quantitative basis for various reasons: First, the real potential wells do not exhibit a perfectly circular shape (see Fig. 4.21) and do thus not behave like perfect lenses as assumed in the model system. Accordingly, the steering

process is affected by some intrinsic aberration. Furthermore, all the discussed parameters, i.e. the well depth, the lowest and the highest barrier as well as their respective distances, cannot be accurately described by fixed values that are assumed to be valid for the whole six-dimensional PES. Rather, this parameters are statistically distributed for the various configurations, since a huge number of similar but not equal barrier-well topologies occurs in the various elbow plots. Last but not least, the role of the other[12] degrees of freedom, i.e. the vibrational and the rotational motion, have not been accounted for in the presented considerations, although they play a role in the simulated six-dimensional dynamics. In spite of all these shortcomings, both the experiments and the simulations, as well as the occurring deviations between them, can be described more than qualitatively on the basis of this simple model. Furthermore, not just this peculiar peak, but all features of the experimental measurements are consistent with the proposed mechanism: The strong decay of the Sticking Coefficient at large angles for instance is also caused by the well's steering. As becomes evident from Fig. 4.20, the incident molecules are steered towards larger barriers, if the chosen incident angle deviates from the most favorable angle. This characteristic is also present in the simulations (see Fig. 4.24), although it is again less pronounced, since the deviances on the PES result in a less focused steering as described above.

In spite of the fact that the experiment is solely reproduced qualitatively, but not quantitatively by the simulations, the found increase is still a formidable achievement: Since the whole mechanism relies heavily on various distinct features of the PES that all have to collude in a particular way, the presented results further emphasize the quality of the employed Potential Energy Surfaces. But even more importantly, these calculations provide a strong evidence that non-adiabatic triplet-singlet transitions are active in this system, since the respective increase of dissociation at a certain incidence angle cannot be reproduced by simple Molecular Dynamics simulations: neither on the adiabatic nor on the triplet PES. In this context it is important to point out that the missing enhancement in the MD simulations is not only caused by the defective location or depth of the potential wells, the description of which is known to be erroneous in DFT, but by the respective barrier distributions, for which DFT is known to be accurate. Even if the potential wells were described exactly, we do thus not expect any increase of the dissociation to occur in pure (triplet) MD simulations on one PES. Conversely, the Surface Hopping simulations on multiple Potential Energy Surfaces are expected to yield a pronounced peak of the dissociation probability—as it occurs in the experiment—if the potential wells were described exactly. Since the height as well as the broadness of this peak would depend upon the employed non-diagonal matrix elements, the comparison of the simulations to the experiment would allow to estimate the real amount of coupling occurring in the system. Unfortunately, this is not possible on the basis of our simulations, which just exhibit a qualitative agreement with the measurements. Still, one might argue that the maximal coupling seems to be more appropriate, since such a pronounced peak as found in the experiments

[12] In this section, all presented probability distributions (Fig. 4.21 and 4.23) have been computed with respect to the surface coordinate $x$ in order to achieve clarity and consistency. However, also histograms for an arbitrary lateral surface coordinate that differs from $x$ exhibit comparable probability distributions.

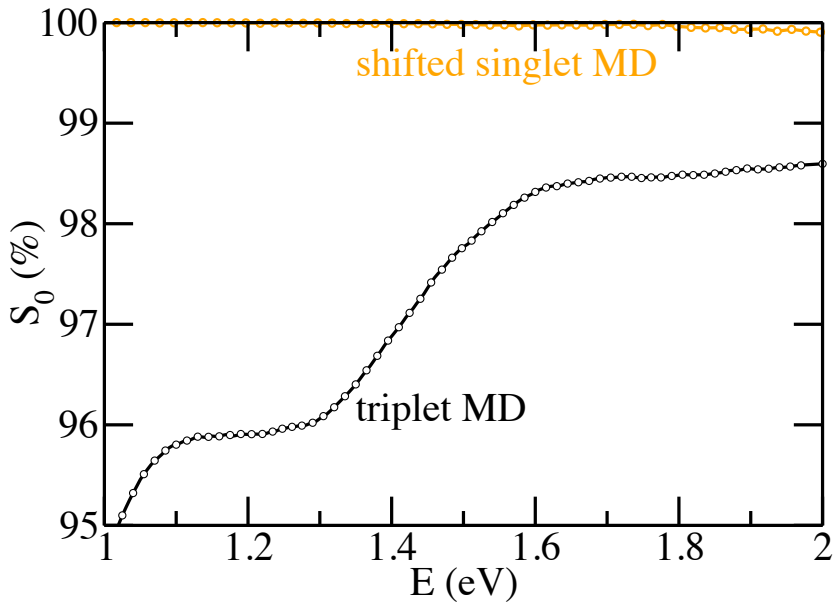


Figure 4.26: Sticking Coefficient at high incident translational energies as computed by Molecular Dynamics (MD) on the triplet Potential Energy Surface. Whereas the Zero Point Energy has been assigned to the vibrational degree of freedom, no rotational energy was assigned to the simulated molecules in the initial conditions. Additionally, the Sticking Coefficient for singlet oxygen as yielded by MD simulations on the singlet PES is shown as well. To allow for a correct comparison of simulations that start in the triplet and in the singlet state respectively, the Sticking Curve for the singlet state has been shifted by the value of the triplet-singlet gap $E_{ts} = 0.937$ eV towards larger energies.

cannot be reproduced by simulations in which a significant portion of the trajectories stays on the triplet PES, as it is the case when the minimal coupling is used (see Fig. 4.15).

### 4.4.4 High Energy Effects

Up to now, we have concentrated on effects occurring at relatively low incident energies where the Sticking Coefficient varies most. However, also the high energy regime above 1 eV exhibits some interesting features. As can be seen in Fig. 4.26 and Fig. 4.27, the Sticking Coefficient approaches, but does not reach a value of 100% even at such high incident energies—neither in the MD simulations on the triplet PES, nor in the Surface Hopping simulations. Before we discuss these data sets, however, we will focus on the also shown outcome of reference MD simulations on the singlet PES, which serve as a starting point for the understanding of the ongoing dynamics. Thereby, one has to keep in mind that MD simulations on the triplet and MD simulations on the singlet PES are not directly comparable to each other: Due to the large triplet-singlet gap $E_{ts}$, the molecules that start in the singlet state with a well defined kinetic energy $E$

will exhibit a significantly larger kinetic energy of approximately $E + E_{ts}$ at the barrier's position than respective molecules that start in the triplet state with the exact same kinetic energy $E$. To approximatively account for this effect, the Sticking Coefficient yielded by MD simulations on the singlet PES has been shifted towards larger energies by the value of $E_{ts}$ in Fig. 4.26. As shown in that figure, the resulting dissociation probability stays nearly constant at 100% for all inspected kinetic energies due to the almost purely attractive underlying PES. Only in certain peculiar geometric setups, e.g. for a perpendicular arrangement over the top site (see Sec. 4.2.2), the dissociation is completely hindered on the singlet PES by the chosen geometry. Within the respective elbow plot, i.e. for fixed rotational and lateral surface coordinates, there is no local or global energy minimum that corresponds to a dissociated adsorbed state (see Sec. 4.4.1). Accordingly, the molecules are repelled from the surface regardless of their kinetic energy, as long as the rotational and lateral surface coordinates are kept fixed. In the six-dimensional dynamics, however, trajectories with such disadvantageous initial conditions can assume a more favorable geometry while approaching the surface and thus dissociate in spite of that. Such a relaxation process does not occur instantaneously but requires a certain amount of time, which is actually limited by the dynamics: The residence time in the surface's vicinity, where such a relaxation with a subsequent dissociation can occur, decreases the higher the incident translational energy is. As a consequence, the Sticking Coefficient as computed by MD simulations on a singlet PES falls *almost linearly* from 100% to 99.89% in the inspected kinetic energy interval. Please note that the described effect has its origin in the geometry of the system[13] and that it does thus not depend on the actual electronic state. Accordingly, this effect occurs and influences also the MD simulations on the triplet PES. For this electronic state, however, the described mechanism is not the dominant factor that determines the shape and the values of the Sticking Coefficient (see Fig. 4.26), as will be discussed below.

In contrast to the discussed reference calculations for the singlet state, the dissociation probability for MD simulations on the triplet PES does not decrease, but increases the larger the incident energy is. Thereby, ten times more molecules are repelled in these calculations than in MD simulations on the singlet PES, even at the largest inspected incident energy. This sizeable amount of reflected molecules cannot be explained on the basis of the geometric effects found for the dynamics in the singlet state before. But even more importantly, this finding, which suggests that barriers with a height well above 2.0 eV must be present on the triplet PES, seems to contradict the previously determined barrier distribution shown in Fig. 4.14, in which the highest barrier found for the triplet PES lies at approximately 1.5 eV. One has to realize that this barrier distribution has been obtained from the calculation of the Minimum Energy Paths in a large series of two-dimensional elbow plots. As the name suggests, such a Minimum Energy Path describes the optimal trajectory in a given elbow plot, as if each of the involved inner degrees of freedom of the molecule could relax to its most

[13]The influence of such geometries enters the calculation of the barrier distributions in Fig. 4.14 only by the area normalization, since the Nudged Elastic Band method is not applicable without a well defined final state. However, triplet and singlet PES are affected by such geometric effects in an equal measure so that the respective barrier distributions are still comparable.

favorable configuration instantaneously and independently from the center-of-mass motion. For small kinetic energies this is a justified assumption, at least as long the respective dynamic processes occur on the same timescale. However, this approximation breaks down for the fast velocities addressed in these simulations, in which the translational energy is at least ten times larger than the assigned vibrational energy. For the narrow dissociation channels present on the triplet PES (see Sec. 4.2.2 and Fig. 4.6), such deviations from the optimal path result in a huge increase of the actual potential energy values that the molecules experience during the dynamics. Accordingly, these molecules also encounter considerably larger barriers than the ones determined by inspecting the Minimum Energy Paths before. Thereby, this effect is counterbalanced when the incident kinetic energy is further increased: On the one hand, there is more energy available to overcome the barrier; on the other hand, the barriers that have to be overcome also grow higher. Consequently, the resulting Sticking Coefficient almost levels off for kinetic energies larger than 1.5 eV. Nevertheless, there is a certain amount of trajectories which are not able to dissociate at all even in this limit. More figuratively, these oxygen molecules crash against the aluminum surface and are repelled back into the vacuum, before the individual oxygen atoms are able to move apart. Still, it might seem surprising that no similar effect has been found for the dynamics in the singlet state before: As discussed in Sec. 4.2.2 and exemplified in Fig. 4.6, the singlet PES typically offers much wider dissociation channels, for which deviations from the optimal path do not significantly alter the actual potential energy values that the molecules experience during the dynamics.

On the basis of the discussed MD simulations, we are now able to understand the outcome of the Surface Hopping simulations shown in Fig. 4.27 as well. Thereby, the transition probability from the triplet to the singlet state is the crucial factor that determines on which PES the molecules move when approaching the surface. Thereby, the minimal coupling provides only for a minute transition probability so that the associated Surface Hopping simulations yield a Sticking Coefficient that resembles the one of the MD simulations on a triplet PES. With respect to these calculations, the few occurring surface hops still result in a small increase of the dissociation probability. However, the respective enhancement of the dissociation probability becomes smaller the faster the molecules are. To affect the simulated Sticking Coefficient at all, a transition to the singlet PES has to occur either at the crossing seam or at least briefly after, before the oxygen is possibly scattered back on the triplet PES. The thereto available time window becomes shorter the larger the kinetic energy of an incident trajectory is. As a consequence, less and less switches occur at large translational energies, so that the resulting Sticking Coefficient for the minimal coupling almost coincides with the one yielded by MD simulations on the triplet PES. In the theory of non-adiabatic processes, such a situation, in which the nuclear motion is so fast that practically no electronic relaxation takes place, is usually referred to as the *diabatic* limit (see Sec. 2.1.1). However, the occurrence of transitions does not depend on the length of the available time window alone, but also on the strength of the coupling. Accordingly, the Surface Hopping calculations for a maximal coupling have not yet reached this diabatic limit. Rather, almost all trajectories switch to the singlet PES when it becomes energetically favorable so that the resulting Sticking Coefficient resembles the one yielded by MD simulations

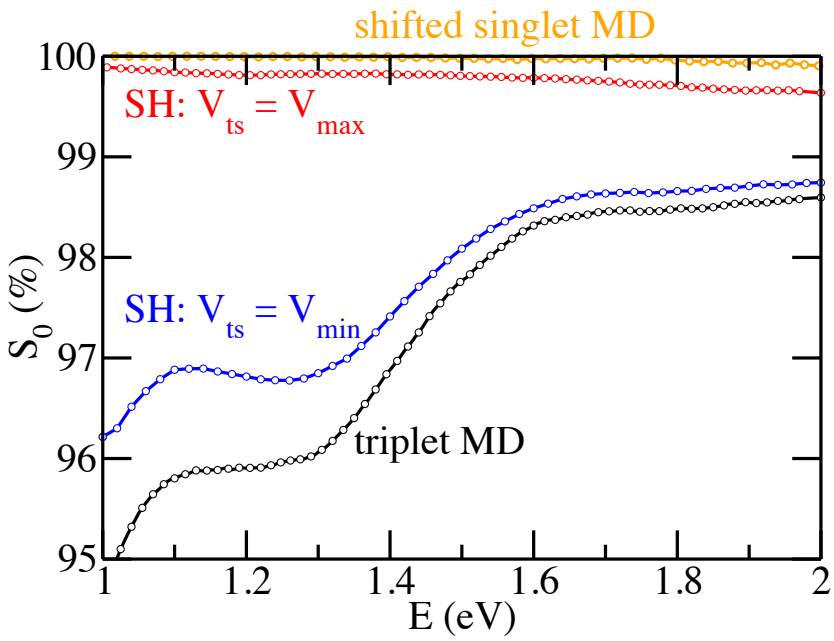


Figure 4.27: Sticking Coefficient at high incident translational energies as computed by Tully's Surface Hopping method (SH) for a minimal and a maximal coupling of the triplet and the singlet PES. Whereas the Zero Point Energy has been assigned to the vibrational degree of freedom, no rotational energy was assigned to the simulated molecules in the initial conditions. Additionally, the results of MD simulations already shown in Fig. 4.26 have been included as a reference.

on the singlet PES. Still, the time window that is available for the transition becomes shorter at large incidence energies for the maximal coupling as well. As a consequence, a minority of the molecules does not switch to the singlet PES fast enough, i.e. before being repelled on the triplet PES by the mechanism described above. Thus—in spite of the large coupling—the resulting Sticking Coefficient exhibits a linear decay to values well below the curve associated with the singlet PES alone. Thereby, the actual amount of molecules, which are reflected on the triplet PES, is still significantly larger than the amount of molecules that are reflected by the geometric effects active and dominant on the singlet PES alone, as a comparison of the respective Sticking Coefficients shows.

With respect to the experiment, all these "high energy" simulations seem to overestimate the dissociation probability, the few available measurements of which seem to lie all around 90% [3]. This finding is rather surprising, since at first one would expect the simulations to underestimate the dissociation probability due to the *frozen substrate approximation*, i.e the inability of the surface to adsorb some of the incident kinetic energy by phonon creation. Basically, such inelastic scattering processes would decelerate the incident molecules [169] and thus increase the time window that is available for the transition to the singlet ground state in the surface's vicinity (see Sec. 4.4.6 for an in-depth discussion

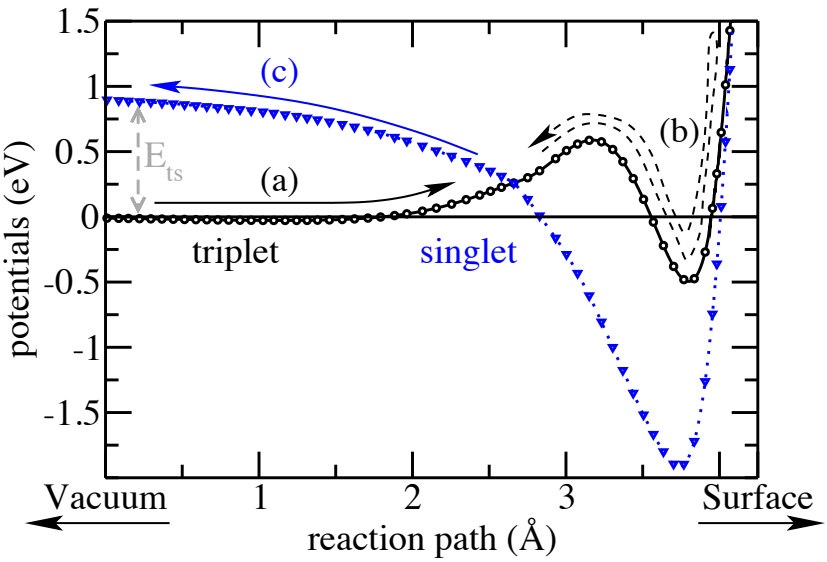


Figure 4.28: Sketch of a possible reaction pathway that can lead to the reflection of an oxygen molecule in its singlet state, if high energy triplet molecules are shot at the surface. The shown triplet and singlet potentials originate from a trajectory with an incident kinetic energy of 1.5 eV that is indeed reflected in the singlet state. For clarity solely the first part of the potentials, along which the trajectory evolves from the vacuum to the turning point, have been plotted. The scenarios ($a$), ($b$) and ($c$) are discussed in the text.

of these effects). Therefore, the found deviances from the experiment can only be caused by some flaws of the Potential Energy Surfaces: First, less strict accuracy requirements (see Sec. 4.2.1) have been employed in the construction of the respective high energy regions of the Potential Energy Surfaces. Secondly, even some higher excited states, which are not accounted for in this work (see Sec. 4.2.2), could influence the dynamics in this energy region as well. However, one has to bear in mind that the found relative errors are not dramatically high but lie all in the range between 5 and 10%. Such an accuracy is hard to reach in the respective experiments, since the production of a molecular beam with that large incident energies and the subsequent measurement [274] of the Sticking Coefficient is still a formidable problem.

Nevertheless, the presented considerations allow to propose an experimental setup that permits to unambiguously detect the occurrence of non-adiabatic transitions in this system: Its starting point is again a molecular beam of triplet oxygen molecules with large kinetic energies $E > E_{ts}$ that is shot ($a$) at the clean aluminum (111) surface, as sketched in Fig. 4.28. In contrast to the previously discussed measurements, we will not focus on the molecules that actually dissociate anymore but on the trajectories that are reflected back into the vacuum. As discussed above, some of the incident trajectories, which do

not switch[14] to the singlet state, will be scattered back ($b$) on the triplet PES. On their way back into the vacuum, there is still a minute but finite probability that these repelled molecules switch to the singlet PES, especially while and before bypassing the crossing seam for the second time. As a consequence, such trajectories lead to a minuscule amount of molecules that are reflected in their singlet state ($c$). Thereby, this clearly non-adiabatic scattering process converts **nuclear** kinetic energy into **electronic** potential energy. Obviously, energy conservation requires the initial kinetic energy of the molecules to be larger than the triplet-singlet gap $E_{ts}$ of the isolated oxygen molecule to make such a process occur at all. Thereby, three different possible transitions, which all depend on the coupling and on the kinetic energy in a different fashion, play a significant role in the dynamics:

($i$) First, a transition **must not** occur while the molecules approach the surface. As became evident in the discussion of the Sticking Coefficient at high incidence energies before, the persistence on the triplet PES is required to achieve a significant amount of reflected molecules at all. Thereby, the employed non-diagonal matrix elements play a significant role: For the minimal coupling, the trajectories almost suffer no surface hops at all, whereas for the maximal coupling switches occur almost instantaneously, as soon as the singlet state becomes energetically favorable. Furthermore, the initially assigned translational energy affects this transition as well, but not that significantly. The actual time span elapsed in between the crossing seam and the turning point at these kinetic energies is too long to affect the relaxation into the singlet ground state for the maximal coupling, even at the highest inspected kinetic energies. Conversely, this time span is still too short to significantly destabilize the triplet state and so to enhance the transitions to the ground state in the case of the minimal coupling, even at the lowest inspected kinetic energies.

($ii$) Secondly, a transition from the triplet to the singlet state **must** occur after the backscattering event, but most probably while or before the crossing seam is bypassed, i.e. in the region where the singlet state is still the ground state. Please note that this is exactly the same transition as discussed in point ($i$), with one crucial difference: While such a switch is unwanted before the backscattering, it is desirable afterwards. Accordingly, its occurrence depends on the coupling and on the kinetic energy in precisely the same (inverse) way as discussed in point ($i$) before.

($iii$) Last but not least, a relaxation from the singlet state back to the triplet ground state **must not** take place while the molecules leave the crossing seam behind and travel back into the vacuum. Although surface hops typically occur only in the proximity of the respective crossing points, they can in principle take place anywhere along the pathway. Especially, such electronic relaxations affect the calculations with a maximal coupling,

[14] Conversely, the incident molecules can switch into the singlet state and then be repelled on this PES while approaching the surface. On their way back into the vacuum, the molecules then end up in a singlet state if no switch occurs when bypassing the crossing seam for the second time. Although such trajectories have been found in the simulations as well, they only provide for a minute portion of the found backscattered singlet molecules, since the singlet PES is way more attractive than the triplet PES (see Fig. 4.27 and the discussion related thereto).

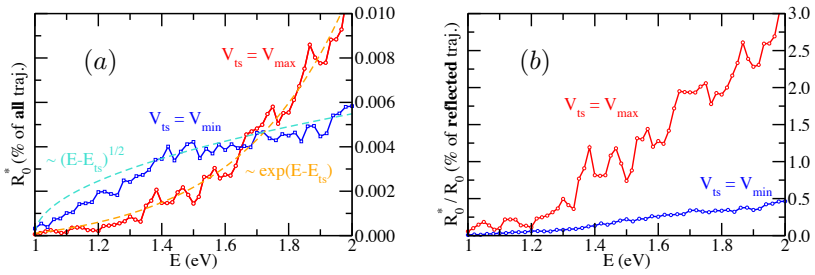


Figure 4.29: Fig. ($a$) shows the percentage of molecules $R_0^*$ that are reflected in the singlet state with respect to the total number of incident trajectories simulated, whereas Fig. ($b$) shows the fraction of molecules $R_0^*/R_0$ that are reflected in the singlet state with respect to all the reflected molecules, regardless of their electronic state. All data has been gained with Surface Hopping simulations with a minimal and a maximal coupling respectively, whereby the Zero Point Energy has been assigned to the vibrational degree of freedom, but no rotational energy was assigned to the simulated molecules in the initial conditions. Please note that more than 5 million trajectories have been computed for each data point shown to achieve such a high, sub-per mill accuracy as needed in this case.

which does not level off to a minute value in the vacuum limit. But even in the case of a minimal coupling, the molecules must leave the crossing seam behind as fast as possible so that the singlet state becomes stable as soon as possible. Thereby, the amount of kinetic energy $E_{ts}$ that the molecules lose while climbing the singlet PES critically prolongates the time span in which such a relaxation to the triplet ground state is probable. As a consequence, this transition strongly depends on the initially assigned translational energy. For instance, an increase of its value from $E_{ts}+0.1 \approx 1.0$ eV to $E_{ts} + 0.2 \approx 1.1$ eV results in twice as much kinetic energy available while leaving the surface as singlets. Again, this effect is stronger for the maximal coupling, for which the transition probability does not virtually vanish in the vacuum limit.

As shown in Fig. 4.29, backscattered singlet oxygen molecules are indeed predicted by the Surface Hopping simulations as soon as the incident kinetic energy is larger than the triplet-singlet gap in the vacuum $E_{ts}$. In a first step, we will discuss Fig. 4.29a, in which the percentage of molecules that are scattered back in their singlet state $R_0^*$ with respect to all the **incident** molecules is shown. To understand this plot, it is crucial to realize that the required absence of switches of type ($i$) and the required occurrence of switches of type ($ii$)—which both depend on the coupling and on the kinetic energy in the same fashion—cancel each other out in the simulation of this **absolute** yield $R_0^*$. As a consequence, Fig. 4.29a allows to study how transitions of type ($iii$) actually depend on the coupling and on the incident kinetic energy. For a minimal coupling, the absolute yield of singlet molecules resembles the behavior of $\sqrt{E - E_{ts}}$, as if there

was indeed only a **confined** and narrow region

$$\Delta z \approx \dot{z} \cdot \Delta t \approx \sqrt{\frac{2(E - E_{ts})}{M}} \cdot \Delta t \tag{4.15}$$

that has to be bypassed as fast as possible to avoid a relaxation into the ground state. This is not the case for the maximal coupling, for which such a transition into the ground state is virtually assured at the lower kinetic energy range. Thus the thereto associated absolute yield rises exponentially, as typically occurs for systems in which the coupling of the individual electronic states is active over an **extended** region [7].
To analyze the feasibility of such an experiment, the **relative** yield $R_0^*/R_0$, i.e. the fraction of molecules that are scattered back in their singlet state $R_0^*$ with respect to all the **reflected** molecules $R_0$, is also of utmost importance. As shown in Fig. 4.29b, it exhibits a strong dependence on the employed coupling that has not been found for the total yield before. One has to realize that the transitions of type $(i)$ do not enter the calculation of this relative yield so that the transitions of type $(ii)$ have no partner they can cancel out with anymore. Consequently, the relative yield exhibits the exact same strong dependence on the coupling we have found for the Sticking Coefficient at high energies before. Again, a relaxation into the singlet state in step $(ii)$ is much more probable in the case of a maximal coupling than in the case of a minimal coupling, for which the diabatic limit has almost been reached in the dynamics.

Eventually, the final question is whether the proposed experiment is feasible in the lab: As a matter of fact, we are pretty confident that the presented simulations only yield a lower bound for the actual amount of singlet molecules that are produced during such high energy scattering processes, since the calculations generally seem to overestimate[15] the dissociation probability. However, the respective relative errors are all smaller than 10% so that yields in the same order of magnitude of the simulations are expected in the measurements as well. As a consequence, the experiment itself has to struggle with certain difficulties: First, the total yield of singlet molecules $R_0^*$ is minuscule. As a matter of fact, only one out of ten-thousand incident trajectories leads to a backscattered singlet oxygen in the best case. Accordingly, a huge amount of molecules has to be shot at the surface to get a signal, let alone an acceptable accuracy in the experiment. Thereby, the overwhelming majority of the incident molecules will dissociate and thus gradually cover the surface. As a consequence, the most basic assumption of the inspected model, i.e. that the oxygen hits a clean surface, is not guaranteed anymore. To avoid such a contamination, the measurement can be split up over time in distinct sessions, in between which the aluminum surface is replaced or cleaned again. Please note that this approach might increase the necessary experimental effort considerably, since the production of clean aluminum surfaces is an utterly cumbersome process [275, 276]. This is additionally aggravated by the fact, that also the accurate detection of singlet oxygen—usually done through the $a \rightarrow X$ phosphorescence of molecular oxygen at 1270 nm [277]—is a complex procedure as well, although noteworthy improvements have been achieved in this field in the last decades [174]. Actually,

[15] As discussed in Sec. 4.4.6.2, this consideration remains valid in spite of the herein employed *frozen substrate approximation*.

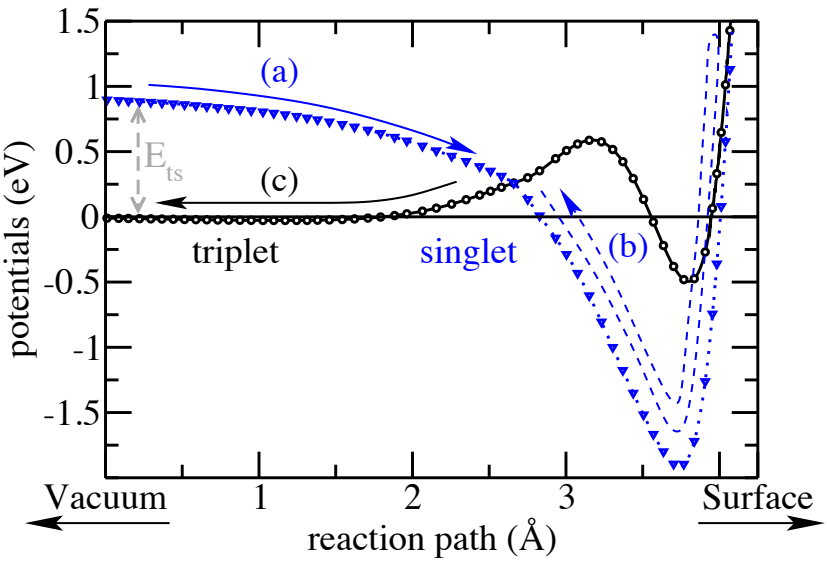


Figure 4.30: Sketch of a possible reaction pathway that can lead to triplet molecular oxygen in the reflection channel, even if singlet molecules are shot at the surface. For clarity, the triplet and singlet potentials already employed for the sketch in Fig. 4.28 have been used in this plot, too. The scenarios (*a*), (*b*) and (*c*) are discussed in the text.

the described mechanism seems to offer a possibility to circumvent the direct detection of singlet oxygen by phosphorescence: Due to the non-adiabaticity of the inspected process, in which an amount $E_{ts}$ of nuclear kinetic energy is converted into electronic potential energy, the singlet molecules must exhibit significantly less kinetic energy than respective triplet molecules in the reflection channel. As a consequence, it might be sufficient to measure the center-of-mass velocity distribution in reflection to discriminate between triplet and singlet molecules. However, such an approach is still far from being fail-proof. As a matter of fact, the simulations suggest that the oxygen molecules—regardless of the actual electronic state they end up—exhibit a broad distribution of kinetic energies upon reflection, since the backscattering process provides for a reallocation of the incident translational energy onto the rotational and vibrational degrees of freedom. Thus, also specific information about the actual vibrational and rotational state[16] of the molecules might be required to unambiguously determine their electronic state. Thereby, these kinetic energy distributions will be further blurred by the certainly occurring energy transfer to the surface, which will be discussed in Sec. 4.4.6. To draw a bottom line: In principle, the proposed experiment should be feasible, but even more certainly it will be a hard task, in which the respective experimenter has to struggle with more than one formidable challenge.

[16]Unfortunately, such a measurement is not trivial, since REMPI [19] does not work for the oxygen molecule. Thus only time of flight (TOF) measurements seem to be realistic up to now.

### 4.4.5 The Dynamics of Singlet $O_2$

The fundamental idea underlying the previous chapter is that the non-adiabatic character of the inspected reaction can be directly proven by detecting the conversion of **nuclear** kinetic energy into **electronic** potential energy. Conversely, also the inverse process, i.e. the conversion of **electronic** potential energy into **nuclear** kinetic energy, should provide for unambiguous experimental evidence that such non-adiabatic spin transitions play a major role in the dynamics. To actually measure these effects, a molecular beam consisting of oxygen molecules in their singlet state must be shot at the aluminum surface, as sketched in step (*a*) of Fig. 4.30. Most probably, the molecules will stay[17] in the singlet state, which then has become the ground state, when bypassing the crossing seam. Still, there is a minute but finite possibility that the molecules are repelled on the singlet PES in step (*b*). Such backscattered molecules can then switch to the triplet ground state while bypassing the crossing seam for the second time when leaving the surface. As a consequence, a certain amount of molecules will end up in the triplet state in the vacuum limit (*c*), where they can be experimentally detected.

Although extensively discussed before (see Fig. 4.26 and the discussion related thereto), MD simulations on the individual Potential Energy Surfaces will serve as a starting point for our considerations again and shall thus be shortly recalled: As shown in Fig. 4.31, the dynamics in the singlet state alone leads to a Sticking Coefficient of virtually 100% at low incident energies. The almost complete absence of barriers on the singlet PES and the wide dissociation channels it typically offers are responsible for this behavior. At larger incident energies, the dissociation probability exhibits a weak decrease, as best seen in the inlet of Fig. 4.31. For such fast molecules there is less time available to geometrically relax before being repelled. At least, however, the amount of dissociating molecules is 99.9% on this PES. Conversely, triplet oxygen molecules that hit the surface with a comparable[18] kinetic energy are more likely repelled, as respective MD simulations on the triplet PES show. The thereby resulting Sticking Coefficient first increases for larger incident energies due to the larger barriers present on the triplet PES, which can be as high as 1.5 eV even on the Minimum Energy Pathways (see Fig. 4.14). At the largest inspected velocities, however, the Sticking Coefficient levels off at a constant value well below 100%, since such fast incident molecules are not able to follow the narrow dissociation channels this corrugated PES offers. In any case, however, the probability for a backscattering event is orders of magnitude higher in the triplet state. This fact is of particular importance for the Surface Hopping Calculations discussed below, in which we will focus on the total Reflection Coefficient $R_0 = 100\% - S_0$ as well as on the portion of reflected molecules $R_T/R_0$ that leaves the surface in the triplet state after being backscattered.

In the case of a minimal coupling, we find a total Reflection Coefficient $R_0$ that

[17] Conversely, the molecules can also switch to the triplet state and can then be backscattered on the thereto associated potential. Such processes also play a role in the dynamics, as will be seen below.

[18] To account for the fact that the singlet molecules gain a considerable amount of kinetic energy $E_{ts}$ while approaching the surface, the Sticking Coefficient for the triplet MD simulations has been shifted by $E_{ts}$ towards smaller energies.

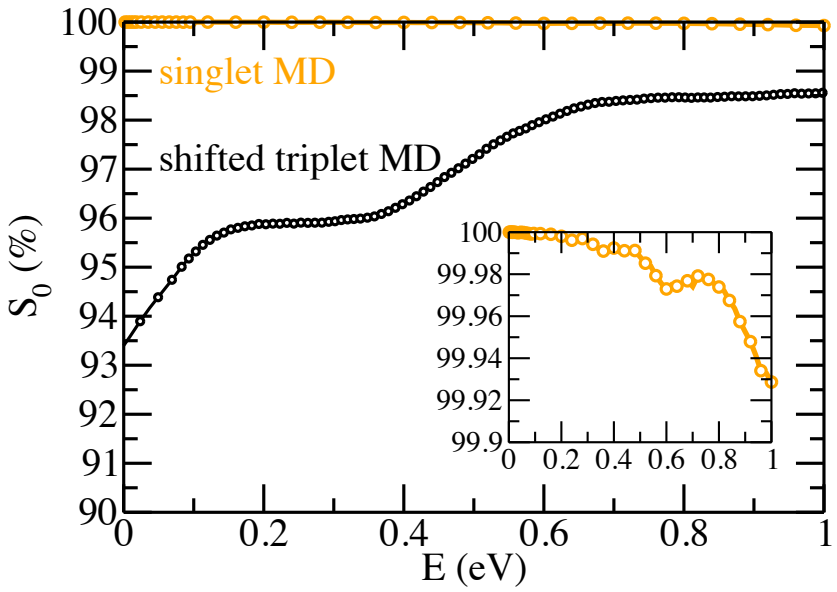


Figure 4.31: Sticking Coefficient $S_0$ as computed by Molecular Dynamics (MD) on the singlet Potential Energy Surface. Whereas the Zero Point Energy has been assigned to the vibrational degree of freedom, no rotational energy was assigned to the simulated molecules in the initial conditions. Additionally, the Sticking Coefficient yielded by MD simulations on the triplet PES is shown as well. To allow for a correct comparison of simulations that start in the singlet and in the triplet state respectively, the Sticking Curve for the triplet state has been shifted by the value of the triplet-singlet gap $E_{ts} = 0.937$ eV towards smaller energies.

mimics the one yielded by MD simulations on the singlet PES (see Fig. 4.32): Not too surprisingly, the oxygen tends to stay in its electronic state for such a minuscule value of the coupling. This behavior is additionally aggravated by the fact that such singlet molecules gain a considerable amount of kinetic energy $E_{ts}$ before reaching the crossing seam: Consequently, the *diabatic limit*, in which no switches occur at all, is almost reached in the presented calculations. However, the shown Surface Hopping simulations for such singlet molecules do not coincide with the MD simulations on the singlet PES, as was the case for the Surface Hopping simulations of triplet molecules and MD simulations on the triplet PES in the diabatic limit before (see Fig. 4.27). Rather, the respective Reflection Coefficients are separated by an almost constant shift, which is caused by the inherent limitations of the MD simulations: One has to realize that during the backscattering event the available kinetic energy is partially reallocated on all available molecular degrees of freedom. As a consequence, the backscattered molecules may not have enough translational energy to climb up the singlet PES again. In the MD simulations, in which the motion is constrained to the singlet PES, such molecules will be dynamically trapped for a short time in the surface's vicinity, until they finally find a route towards dissociation. In the Surface Hopping simulations, however, such backscattered molecules may also

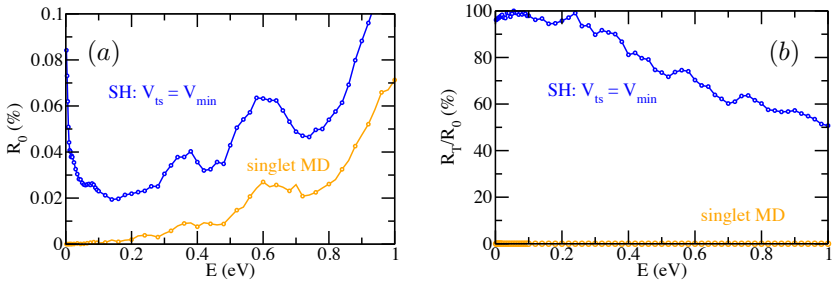


Figure 4.32: Fig. (*a*) shows the Reflection Coefficient $R_0$ as computed by Tully's Surface Hopping method (SH) for a minimal coupling of the triplet and the singlet Potential Energy Surfaces. Whereas the Zero Point Energy has been assigned to the vibrational degree of freedom, no rotational energy was assigned to the simulated molecules in the initial conditions. Additionally, the Reflection Coefficient yielded by MD simulations on the singlet PES is shown as reference. Conversely, Fig. (*b*) shows the respective relative yields of reflected triplet molecules $R_T/R_0$.

switch to the triplet PES if they are able to reach the crossing seam again. In this electronic state, considerably less translational energy is needed to escape the surface and thus more molecules—but not all actually repelled molecules—are able to reach the vacuum. The probability of such a transition also depends on the velocity of the molecules at the crossing seam. Consequently, the relative yield $R_T/R_0$ decreases linearly from almost 100% to approximately 50% in the inspected kinetic energy range, as can be seen in Fig. 4.32.

Furthermore, the shown Reflection Coefficient for the minimal coupling exhibits an intriguing characteristic at incident energies below 0.1 eV, for which virtually no backscattered molecules have been found in the singlet MD simulations before. Most peculiarly, the Reflection Coefficient increases exponentially in this interval the lower the incident translational energy is, while the relative triplet yield $R_T/R_0$ remains constant at almost 100%. Again, electronic transitions, which become more likely at these low kinetic energy values, are responsible for this effect: Some of the incident trajectories suffer an electronic relaxation to the triplet state at the crossing seam (or even before) and are then backscattered on the thereto associated potential. At these small incident energies the reflection probability is orders of magnitude higher on the triplet PES than on the singlet PES. Consequently, even a minute increase in the transition probability—as it occurs when the incident velocity is decreased—amplifies the amount of backscattered molecules significantly. Still, such processes occur only in exceptional cases due to the extremely low value of the coupling: If this was not the case, the Surface Hopping simulations would closely resemble the shifted triplet MD calculations, which actually yield a Reflection Coefficient that is almost an order of magnitude higher (see Fig. 4.31).

In the case of a maximal coupling, the exact same mechanisms are active again: At large incident energies, approximately 1% of the incident molecules are repelled. These molecules almost completely result from backscattering events

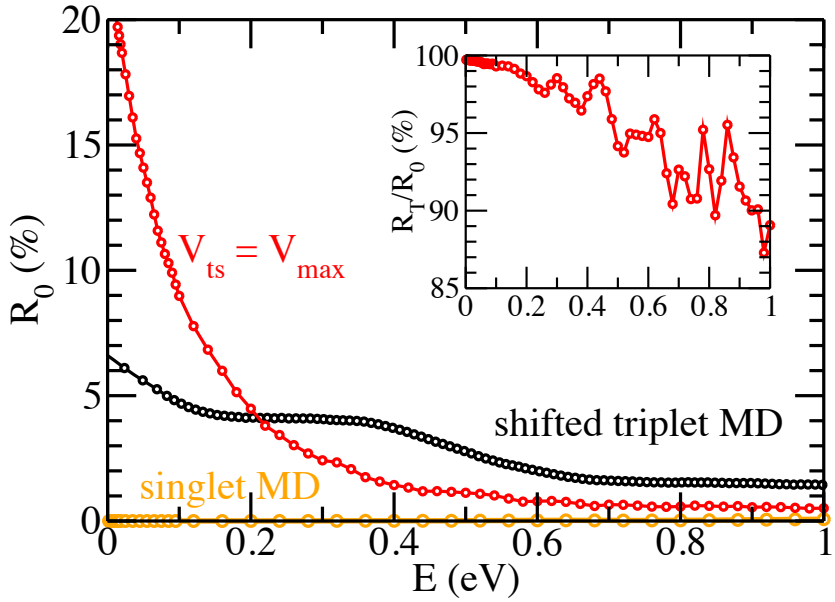


Figure 4.33: Reflection Coefficient $R_0$ and relative triplet yield $R_T/R_0$ as computed by Tully's Surface Hopping method (SH) for a maximal coupling of the triplet and the singlet Potential Energy Surfaces. Whereas the Zero Point Energy has been assigned to the vibrational degree of freedom, no rotational energy was assigned to the simulated molecules in the initial conditions. Additionally, the Reflection Coefficients yielded by MD simulations on the singlet and the triplet PES respectively, which were already shown in Fig. 4.31, are plotted as reference.

on the singlet PES, as discussed for the minimal coupling before. In contrast thereto, however, a switch to the triplet state does not only occur for a few selected trajectories, but for almost all reflected molecules, as soon as they reach the crossing seam for the second time while travelling back into the vacuum. As a consequence, significantly more molecules are able to escape the surface if the maximal coupling is employed. Also, the relative yield of triplet molecules becomes considerably higher therefore.
When the incident energy is decreased, the Reflection Coefficient increases exponentially again: As also discussed for the minimal coupling before, this effect results from switches onto the more repulsive triplet PES that become more likely at small incident energies. With respect to the previous calculations shown in Fig. 4.32, however, this effect is considerably more pronounced for the maximal coupling and dominates the behavior of the Reflection Coefficient in the inspected energy range. Although transitions are generally more probable for high coupling values, such a huge enhancement of the Reflection Coefficient as actually found in the calculations cannot be explained on the basis of the coupling value alone: Even if all molecules switched to the triplet state at the crossing seam, one would expect the resulting Reflection Coefficient to resemble the respective triplet MD simulations at most, but not to exceed them—as it occurs in the Surface Hopping simulations. To understand this effect the occur-

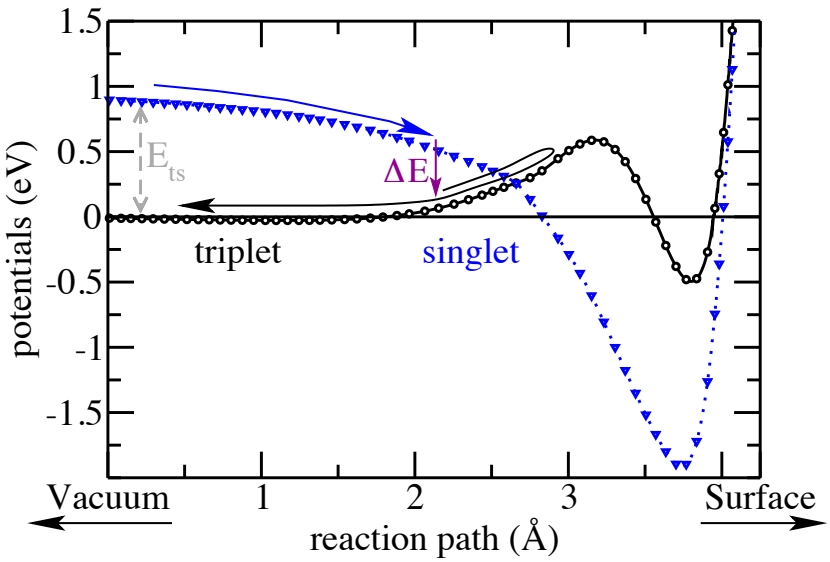


Figure 4.34: Sketch of a possible reaction pathway that can lead to the reflection of oxygen molecules in the triplet state, even if singlet molecules are shot at the surface. Due to the early relaxation to the triplet PES, not the complete released potential energy $\Delta E$ is converted into translational kinetic energy so that the oxygen is not able to overcome the barrier on the triplet PES.

ring non-adiabatic switches have to be scrutinized more accurately: As a matter of fact, such transitions do not only occur at the exact position of the crossing point but can also occur in its proximity (see Fig. 4.34), especially in the case of such a high and extended coupling. If such a relaxation takes place before the crossing seam is reached, the surplus of potential energy $\Delta E$, i.e. the energy gap in between the two electronic states at the actual position, is then redistributed on all degrees of freedom in the direction of the non-adiabatic coupling vector (see Sec. 2.4.3.2), along which the forces associated to such a non-adiabatic transition typically [140, 141] act. Consequently, not all the released potential energy $\Delta E$ is assigned to the translational velocity perpendicular to the surface, but parts of it are also assigned to the vibrational, rotational and lateral center-of-mass motions. This fact had not been accounted for in the construction of the reference Reflection Coefficient on the triplet PES. By just shifting the original data towards smaller energies, we inherently assumed that while approaching the surface the whole triplet-singlet gap energy $E_{ts}$ is converted into kinetic energy that promotes dissociation, i.e. primarily into velocity associated to the molecule-surface distance. This presumption, which is approximatively valid as long as the molecules move on one PES or solely switch at the crossing point, is violated in the case of such a non-adiabatic energy reallocation. Accordingly, a molecule that suffered such a relaxation will impinge on the surface with a translational energy well below $E + E_{ts}$ and thus be more likely reflected.

How strong this effect actually influences the dynamics depends primarily on the amount of energy $\Delta E$ that is reallocated, i.e. the position at which the relaxation

takes place (see Fig. 4.34). For high velocities and small coupling values, such transitions take place—if they occur at all—almost exclusively at the crossing point. In this case, almost no potential energy $\Delta E$ is reallocated during the switching procedure and such effects are negligible. Conversely, switches might occur earlier, as soon as the singlet state becomes destabilized by the surface, if a high coupling in combination with low incident energies is used. For instance, a singlet molecule that exhibits an initial kinetic energy $E$ of 0.2 eV typically gains[19] only 0.3 eV (30% of $E_{ts}$) translational energy: Thus it impinges on the surface with approximately 0.5 eV and not with $E + E_{ts} \approx 1.1$ eV as assumed before. Such a slow oxygen molecule, however, is more likely repelled by the barriers present on the triplet PES. Thereby, the actual reflection probability on the triplet PES is additionally amplified by two purely dynamical effects:

- The vibrational, rotational and lateral center-of-mass motion, to which additional kinetic energy is assigned in the transition, are not only less effective in promoting the dissociation as the perpendicular center-of-mass motion but can even hinder it under certain conditions (see Sec. 4.4.1, 4.4.2 and 4.4.3).
- Intuitively, one would expect that for such high coupling values a relaxation to the singlet state occurs almost immediately after bypassing the crossing seam, as soon as the singlet state becomes the ground state. However, such a relaxation is not as likely as one would naively suppose. In contrast to the reflection probability on the triplet PES alone, which primarily depends on the incident translational energy perpendicular to the surface, the transition probability depends on the velocity of **all** degrees of freedom. With respect to all of them, the total kinetic energy is still considerably higher than the triplet-singlet gap $E_{ts}$ so that such a relaxation is even in the case of a maximal coupling not very likely (see Sec. 4.4.4).

These peculiar non-adiabatic effects in the dynamics manifest themselves also in the respective kinetic energy distributions the triplet molecules exhibit after being reflected, as shown in Fig. 4.35. There, the kinetic energy the molecules gain during the described singlet-triplet conversion process is plotted with respect to the initial translational velocity. At the lowest incident energies, the released electronic potential energy $E_{ts}$ is reallocated onto the translational, vibrational and rotational degrees of freedom in almost equal parts. When the incidence energy is increased, the actual portion assigned to the translational energy decreases almost linearly: On the one hand, molecules that gain a significant amount of translational energy $\Delta E_{\text{trans}}$ also impinge on the surface with a larger translational energy $E + \Delta E_{\text{trans}}$ and are thus able to overcome the barriers on the triplet PES more easily. Accordingly, such molecules are not reflected and do thus not enter the statistics underlying Fig. 4.35. This mechanism is of particular importance in the calculations that employ the maximal coupling. On the other hand, molecules that gain a significant amount of kinetic energy $E_{\text{trans}}$ while staying on the singlet PES are also able to escape the surface in the singlet state and do therefore not enter the statistics underlying Fig. 4.35 either. This effect is of particular importance for the calculations that employ the minimum coupling, especially at large incidence energies.

[19] For an in-depth analysis of the actual energy transfer occurring onto the various degrees of freedom, see Fig. 4.35 and the discussion related thereto.

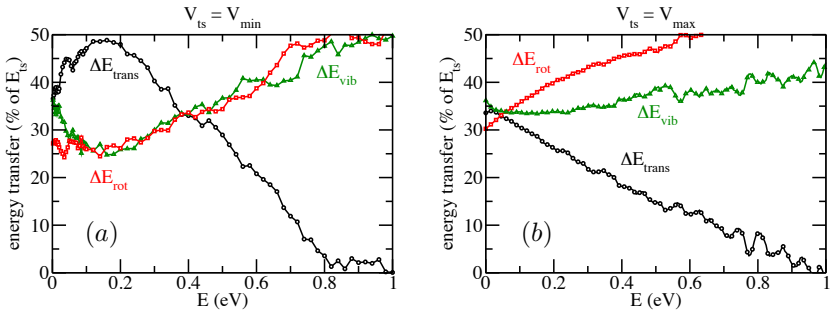


Figure 4.35: Fig. (*a*) and (*b*) show the average kinetic energy singlet molecules gain when being converted to triplet molecules in the backscattering process at the aluminum surface for a minimal and a maximal coupling respectively. Please note that this data has been derived from the average kinetic energy these molecules exhibit back in the vacuum. Accordingly, the plot does not only include the energy rearrangement due to the non-adiabatic transition, but also the adiabatic energy reallocation that occurs during the backscattering dynamics.

Additionally, the actual amount of translational energy gained in the process exhibits a maximum at low incident energies, whereby the respective peak is particularly pronounced in the case of a minimal coupling. As mentioned before, slow molecules will actually suffer a relaxation to the triplet ground state earlier, i.e. at larger distances from the crossing seam so that the actual amount of potential energy $\Delta E$ redistributed during the non-adiabatic transitions is larger (see Fig. 4.34). In the case of a maximal coupling, all molecules—regardless of their incident energy—tend to relax to the triplet ground state as soon as the singlet state becomes destabilized. As a consequence, the respective peak is almost irrecognizable.

In this section, we have again presented an experimental setup that allows to unambiguously nail down the occurrence of non-adiabatic transitions in the aluminum-oxygen system. Although such measurements are well feasible [278], it might seem cumbersome to use a molecular beam of singlet molecules for the detection of the non-adiabaticity, if similar evidence can be achieved by the scattering of high-energy triplet molecules, as discussed in Sec. 4.4.4. With respect to the previously discussed experimental setup, however, the setup proposed in this section is superior in many aspects:

- First, the amount of reflected molecules is significantly higher and can be as large as 20% in the case of a maximal coupling. But even for simulations with a minimal coupling, we found absolute yields $R_0$ as high as 0.1% (see Fig. 4.33) and thus an order of magnitude larger than what could be found in the previous section at all, even in simulations that employ the maximal coupling (see Fig. 4.29).
- Analogously, also the inspected relative yields of interest are significantly higher: While relative singlet fractions of a few percent were found in the case of the high energy scattering at most, the amount of triplet molecules stays well above 50% for the singlet scattering in any case.

Furthermore, the actual detection of the non-adiabatic energy conversion is less error-prone: There is no need to use the $a \rightarrow X$ phosphorescence of molecular oxygen at 1270 nm [277] to analyze the relative amount of triplet and singlet molecules that are backscattered. Rather, it is sufficient to measure the actual kinetic energy the molecules exhibit after being reflected by the surface. If any of the degrees of freedom exhibits an energy that is not compatible with the translational energy the molecular beam initially exhibits, a switch must have happened. Especially at low incidence energies, it might thus be sufficient to measure[20] the translational, the vibrational or the rotational state of the reflected molecules to unambiguously detect a significant amount of triplet oxygen through the respective kinetic energy **gain**. Contrariwise, the actual velocity of all molecular degrees of freedom has to be measured in the high-energy scattering case to make sure a **loss** of kinetic energy has occurred at all. This fact does not only simplify the detection of the non-adiabaticity but even the realization of the experiment as a whole. Even if the molecular beam does not consists purely of singlet molecules, the energy conservation law allows to clearly distinguish molecules that initially were in the triplet state from molecules that were in the singlet state.

### 4.4.6 The Frozen Substrate Approximation and its Limits

As mentioned several times in the previous sections, only the six degrees of freedom of molecular oxygen have been accounted for in the dynamics' simulations hitherto presented in this work, whereas all the bulk and surface atoms were kept fixed at the equilibrium positions of a clean aluminum (111) surface. This commonly applied *frozen substrate approximation* allows to significantly reduce the number of degrees of freedom the Potential Energy Surfaces depend on (see Sec. 2.3). However, this approximation might also bias the simulation of the dynamics. In particular, the thereby neglected motion of the aluminum atoms provides for an energy dissipation channel, which allows the incident molecules to get partially rid of of their kinetic energy [169]. Therefore, certain molecules, which would be backscattered from the surface under the frozen substrate approximation, dissociate after being trapped in the surface's proximity due to the energy loss to the bulk, if the motion of the aluminum is accounted for. To study such effects and to estimate the error the frozen substrate approximation has introduced in our previous results, two different approaches, which will be discussed in the following, have been employed.

#### 4.4.6.1 Ab Initio Molecular Dynamics

As discussed in the previous sections, many peculiarities of this system can be understood on the basis of the topology of the early PES, where the barriers, the crossing points and the physisorption wells are located. Especially, this statement holds for the calculation of the Sticking Coefficient, of the thereto related vibrational enhancement and of its deviation from the Normal Energy Scaling (see Sec. 4.4.1, 4.4.2 and 4.4.3). Since all the relevant steps in these

[20] Unfortunately, such a measurement is not trivial, since REMPI [19] does not work for the oxygen molecule. Thus only time of flight (TOF) measurements seem to be realistic up to now.

| | |
|---|---|
| Slab setup | $3 \times 3$ unit cell with 7 layers (63 atoms) |
| Slab-to-slab distance | 15 Å |
| Functional | RPBE |
| Cut-off energy | 350 eV |
| **k**-points | $4 \times 4 \times 1$ Γ-centered mesh |
| Smearing Method | First Order Methfessel-Paxton [279] |
| Smearing Width | 0.1 eV |
| PREC [228] | "Medium" |
| Ionic Time Step | 1.0 fs |

Table 4.1: Supercell setup and numerical settings used in the *ab initio* MD simulations with VASP

simulations occur at pretty large molecule-surface distances, one expects the motion of the surface atoms to be indeed negligible in these cases. To substantiate this credible presumption, *ab initio* Molecular Dynamics simulations (see Sec. 2.3), in which the motion of the aluminum atoms is explicitly included, have been performed with VASP [227, 228]. Thereby, the nuclear trajectories are propagated like in Molecular Dynamics algorithms in steps of 1 fs with a *predictor-corrector* algorithm. In each of these steps, an electronic structure calculation is carried out to determine the forces that actually act on the nuclei. For the sake of consistency, the supercell chosen for these simulations (see Tab. 4.1) is much the same as the one employed for the electronic structure calculations [246] the Neural Network is based on. However, the numerical settings used for the *ab initio MD* are certainly not accurate enough to reproduce each single detail of the electronic structure. In spite of that, various test runs[21] have shown that the actual Potential Energy Surface and the thereto associated forces are correctly reproduced with these settings. Unfortunately, it is not easily possible to constrain the oxygen molecule to a certain spin state in such a Plane Wave based code as VASP. As a consequence, only the motion on the adiabatic spin-polarized PES could be addressed with the *ab initio* MD simulations.

These calculations showed that a significant energy transfer to the surface does indeed not occur until pretty late in the dynamics, for instance at approximately 300 fs in the exemplary trajectory shown in Fig. 4.36. At this point, however, the oxygen molecule is separated from the surface by less than 2 Å and has thus bypassed the region in which the great majority of the barriers lies (see Sec. 4.2). A significant amount of energy is set free only thereafter, as soon as the oxygen atoms start to move apart. During this process, more and more kinetic energy is also transferred to the aluminum atoms. Similar results have been found for several other trajectories, in which different initial conditions for the orientation, for the lateral surface coordinates and for the incident kinetic energy had been chosen. Consequently, our initial presumption, i.e. that the

[21] As a matter of fact, extensive calculations have been performed for the aluminum bulk, the clean aluminum (111) surface and the combined oxygen-aluminum system. Thereby, the dependence of various quantities, e.g. the lattice constant, the work function, and the adsorption energies, on the numerical and geometrical settings have been investigated. In spite of that, these calculations are not reviewed in this work, since the found results do not deviate from previous findings [246].

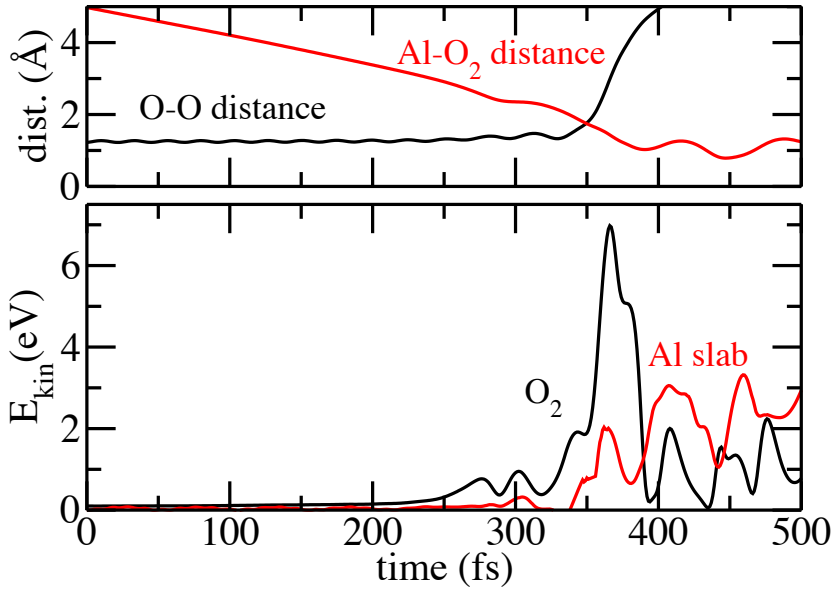


Figure 4.36: Trajectory of an oxygen molecule with an initial translational energy of 0.1 eV and no vibrational energy as computed by *ab initio MD*: In the upper plot, the time evolution of the molecular oxygen bond length and of the molecule-surface distance are shown, whereas the respective kinetic energies of the molecule and of the slab are plotted in the lower figure.

motion of the aluminum is not drastically altering the dynamics on the early PES, is substantiated. Unfortunately, however, these calculations do not allow to estimate the actual error that the frozen substrate approximation introduces into the Surface Hopping calculations of the Sticking Coefficient. Due to the fact that only the adiabatic ground state is accessible in VASP, all molecules dissociate—regardless of the energy transfer to the bulk.

#### 4.4.6.2 Surface Oscillator Simulations

To actually estimate the influence the frozen substrate approximation has on the non-adiabatic dynamics, a so called *Surface Oscillator* [280] has been used. In this model, which has been successfully employed several times before [9, 170, 281], the motion of the surface atoms can be approximately accounted for in hindsight, i.e. on the basis of Potential Energy Surfaces derived within the frozen substrate approximation. Thereto, the aluminum slab is also permitted to oscillate as a whole in a harmonic potential

$$V_{SO}\left(\tilde{z}\right) = \frac{\hbar\omega}{2}\tilde{z}^2, \tag{4.16}$$

as sketched in Fig. 4.37. Consequently, the actual molecule-surface distance does then not solely depend on the cartesian center-of-mass coordinate $z$ of the oxygen anymore but also on the amplitude of the Surface Oscillator $\tilde{z}$. Thus both the diagonal and the non-diagonal potential matrix elements (see Sec. 2.4.3.2,

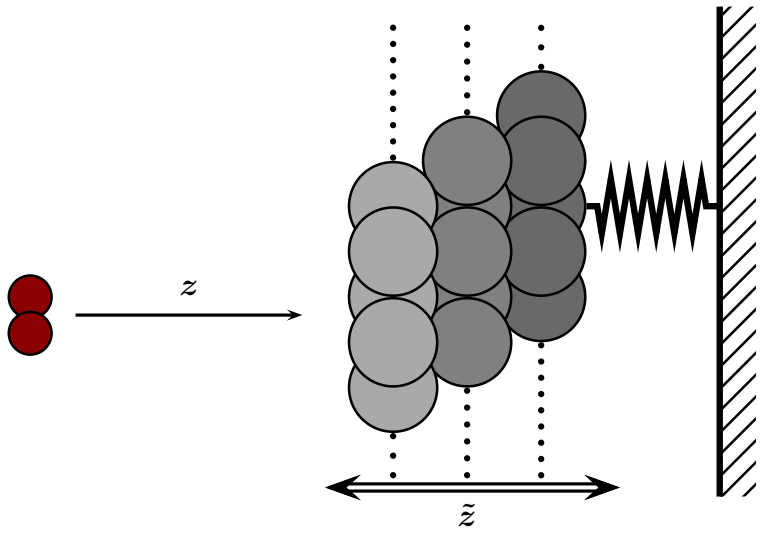


Figure 4.37: Sketch of the one-dimensional Surface Oscillator model.

4.2 and 4.3) that enter the Surface Hopping simulations have to be formally adjusted to reflect this additional dependence:

$$V_{ij}\left(x, y, z, d, \theta, \phi\right) \xrightarrow{\text{Surface Oscillator}} V_{ij}\left(x, y, [z - \tilde{z}], d, \theta, \phi\right). \tag{4.17}$$

Furthermore, an auxiliary harmonic potential, which does not depend on the electronic state, is added to each of the diagonal elements of the potential matrix

$$V_{ii}^{7D}\left(x, y, [z - \tilde{z}], d, \theta, \phi, \tilde{z}\right) = V_{ii}\left(x, y, [z - \tilde{z}], d, \theta, \phi\right) + V_{SO}\left(\tilde{x}\right), \tag{4.18}$$

whereas no additional coupling term is added to the non-diagonal elements. Analogously, this model can be extended to also allow for an oscillation of the slab with respect to the lateral surface coordinates $x$ and $y$, as done in this work. Although such a Surface Oscillator does not yield any additional information about the actual motion of the individual aluminum atoms, it effectively incorporates the energy transfer effects in between the slab and the molecule into the simulations [280]. As previous studies showed [282, 283, 284], this additional energy dissipation channel is best modeled by choosing a value of 70% of the experimental Debye frequency ($\approx 34$ meV [47]) of the bulk for the frequency $\omega$ in the harmonic potential (4.16). Since in the real system a multitude of aluminum atoms—each of which is able to take up a certain amount of energy—is present, three[22] times the mass of such a single aluminum atom is assigned to the Surface Oscillator to take account of finite size effects [149, 168, 148]. Last but not least, appropriate initial conditions have to be chosen for the Surface

[22] As a matter of fact, a whole series of calculations, in which the mass and the frequency of the oscillator was varied, has been performed. However, no significant quantitative differences have been found in these studies. Consequently, the setup that results in the strongest energy transfer, i.e. a three dimensional oscillator with three times the mass of a single aluminum atom, is used in the presented calculations to serve as an upper bound for the effects that have to be expected.

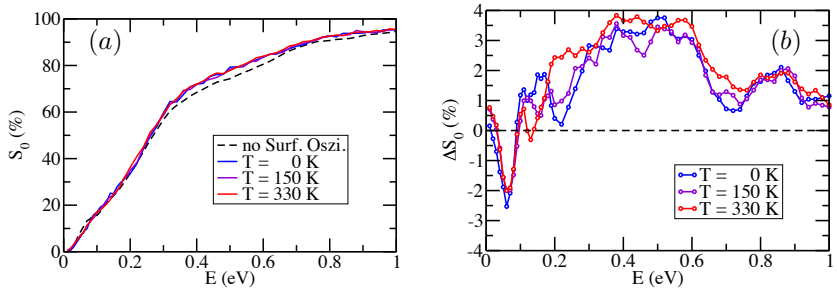


Figure 4.38: Fig. (*a*) shows the Sticking Coefficients yielded from MD simulations on the triplet PES: Both the results of calculations on the basis of the frozen substrate approximation and of calculations with a three-dimensional Surface Oscillator at various temperatures are plotted. Fig. (*b*) additionally shows the absolute difference $\Delta S_0$ between the calculations with and without this additional energy dissipation channel.

oscillator as well: As done for the vibrational degree of freedom of the oxygen molecule before (see Sec. 4.4.1), the amplitude of the oscillator and its velocity are chosen at random under the constraint that the total energy of the subsystem is equal to a given energy value. Three different energy values, which correspond to a temperature of 0 K, 150 K and 330 K respectively, have been used in the presented simulations to embrace the whole temperature range at which such experiments are typically performed [3, 11, 255, 258].

As shown in Fig. 4.38 for MD simulations on the triplet PES, the Surface Oscillator does not affect the Sticking Coefficient at normal incidence significantly. Generally, the additionally offered energy dissipation channel results in a slight increase of the dissociation probability, as one would intuitively expect (see Sec. 4.4.6). At low incident energies but not at the lowest[23] ones, however, also a decrease in the Sticking Coefficient is found: One has to realize that due to Newton's third law, commonly summarized as *actio est reactio* [285]—the molecules already lose a certain part of their energy to the oscillator while climbing up the barrier on the triplet PES, before actually impinging on the surface. For such slow molecules even a relatively small depletion of kinetic energy results in a strongly diminished Sticking Coefficient. Please note that the same phenomenon, i.e. the energy transfer to the Surface Oscillator, has a twofold effect on the dynamics: If a significant loss occurs before the barrier is surmounted, the dissociation probability decreases, as it is the case for slow molecules. Contrariwise, if a significant loss occurs only after the barrier, the dissociation probability increases, as it is the case for fast molecules. At medium energies, however, the impact such a Surface Oscillator has on the simulations is determined by the detailed balance of these two effects. For our strongly corrugated triplet PES the absolute difference in the Sticking Coefficient $\Delta S_0$ is thus not a smooth monotonic function of the incidence energy, but rather

[23] For the lowest kinetic energy the dissociation probability increases again, at least for non-zero temperatures: In this case, the Surface Oscillator holds more energy than the actually impinging molecule so that a minute energy transfer from the surface to the molecule occurs by exactly the same mechanism as described above.

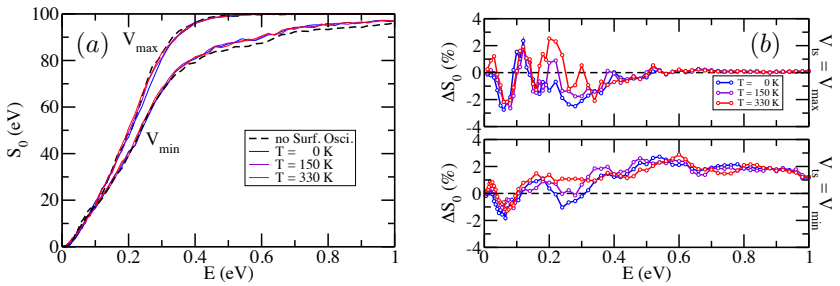


Figure 4.39: Fig. (*a*) shows the Sticking Coefficients yielded from Surface Hopping simulations with the minimal and the maximal coupling respectively: Both the results of calculations on the basis of the frozen substrate approximation and of calculations with a three-dimensional Surface Oscillator at various temperatures are plotted. Fig. (*b*) additionally shows the absolute difference $\Delta S_0$ between the calculations with and without this additional energy dissipation channel.

exhibits a defined structure.

Also in the Surface Hopping simulations, the results of which are shown in Fig. 4.39, no significant influence of the Surface Oscillator has been found: neither for the minimal, nor for the maximal coupling. In both cases, the Sticking Coefficient decreases at low incident energies when the Surface Oscillator is included in the calculations. Not too surprisingly, the calculations with a minimal coupling resemble the MD simulations on a single PES at larger velocities. The calculations with a maximal coupling, however, differ from the other simulations and yield almost no increase of the Sticking Coefficient at all. For this high value of the coupling, the molecules switch to the singlet state almost immediately when bypassing the crossing seam. On the thereto associated PES, the Sticking Coefficient is virtually 100% even under the frozen substrate approximation (see Sec. 4.4.5). Consequently, the Surface Oscillator cannot further promote the dissociation after the barrier has been surmounted. Before the crossing seam is reached, however, the Surface Oscillator can still withdraw some kinetic energy from the impinging molecules and thus make their repulsion more likely. In the minimal coupling case this effect is still noticeable, but is not that pronounced, since the switches to the singlet PES do not occur immediately at the crossing seam. Accordingly, the Surface Oscillator can still promote the dissociation on the late triplet PES for molecules that did not suffer an electronic transition. Furthermore, the Surface Oscillator increases the transition probability to the singlet PES by slowing the molecules down.

Last but not least, the calculations for the high energy scattering case presented in Sec. 4.4.4 and the calculations for the singlet scattering presented in Sec. 4.4.5 have been repeated[24] too. Whereas for the high energy scattering the yields of interest are decreased by a factor of two at most, the singlet scatter-

[24] Due to the high numerical costs associated to such simulations, a single temperature value, i.e. 330 K, has been inspected. As it is the case in the experiment [3] and in the previously presented calculations, no significant dependence on the Surface Oscillator's initial energy is expected anyway.

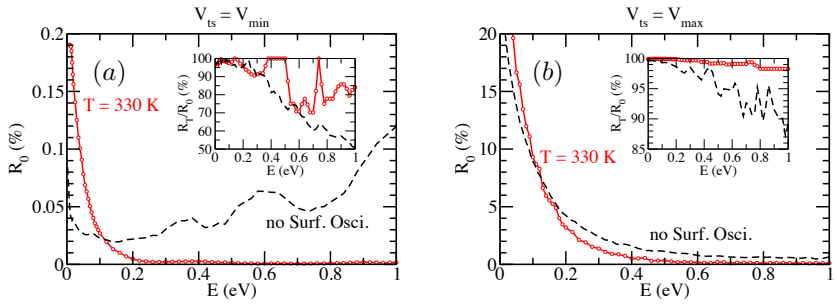


Figure 4.40: Singlet Oxygen Scattering: Reflection Coefficient $R_0$ and relative triplet yield $R_T/R_0$ as computed by Tully's Surface Hopping method for a minimal coupling ($a$) and a maximal coupling ($b$). Both the results of calculations on the basis of the frozen substrate approximation and of calculations with a three-dimensional Surface Oscillator initialized at room temperature are plotted. Please note that the wiggles in the shown relative yields are caused by the deficient statistics and have no physical origin.

ing simulations exhibit a more interesting behavior, as shown in Fig. 4.40. At large incidence energies, the actual reflection probability is strongly decreased when the Surface Oscillator is employed. The few molecules that were previously backscattered on the singlet PES are now able to dissociate due to the additional energy dissipation channel. At low incidence energies, however, the Reflection Coefficient increases. Singlet molecules that relax to the triplet state before bypassing the crossing seam are now even more likely repelled, since they can additionally lose portions of their kinetic energy to the Surface Oscillator while climbing the barrier. Accordingly, also the respective relative yield increases and is larger than 50% in any case. This simulations demonstrate that the proposed singlet scattering experiments to assess the occurrence of non-adiabatic transitions in this system are feasible. As a matter of fact, the expected yield of triplet molecules is not suppressed by a possible energy transfer to the surface. Conversely, the minute yields for the high-energy scattering are even further diminished when the frozen substrate approximation is abandoned. This fact could make the realization of such an experiment extremely problematic, as in principle discussed before (see Sec. 4.4.4).

# Chapter 5

# Conclusion & Outlook

In this work, the enigmatic mechanisms underlying the dissociative adsorption of molecular oxygen at the aluminium (111) surface have been eventually unveiled on the basis of *first principles* simulations alone. Unquestionably, the key to the unraveling of the ongoing processes is the consideration of non-adiabatic triplet-singlet transitions. These effects have never been explicitly accounted for in simulations of this system's dynamics before. By extending these previous approaches, we were not only able to reproduce and explain the dissociation probability to a great detail, but we were also able to shed some light on more complex phenomena, e.g. the deviation of the Sticking Coefficient from the Normal Energy Scaling. This effect does not depend on the occurrence of non-adiabatic transitions alone, but also relies on the topologies of the triplet and of the singlet Potential Energy Surface, which have to collude in a peculiar fashion. In spite of the fact that even physisorption wells, which are typically not correctly described by the employed semi-local exchange-correlation functionals, play a decisive role in this case, our simulations yielded a more than acceptable accordance with the experiments. Impressively enough, the calculations presented in this work are compatible with all nowadays known measurements performed for this system—except the maybe most puzzling one, which has hitherto only been shortly mentioned in the introduction (see Sec. 4.1): After exposing a clean aluminum surface to oxygen atmosphere, single oxygen atoms in an average distance of more than 80 Å [255] from each other have been found by *Scanning Tunneling Microscopy*. Various antithetic models—even the invalidity [258] of the original experiment itself—have been suggested as a possible explanation of this baffling finding. Up to now, evidences that support as well as evidences that undermine each one of this proposals have been found so that this dispute has not been settled yet in spite of the huge scientific effort [286, 287, 288, 289, 258, 257, 256, 290, 4, 5, 6, 10] invested in its solution.

As a matter of fact, we also tried to solve this riddle with the simulation techniques employed in this work. Thereto, the cartesian coordinates that the single oxygen atoms exhibit after the dissociative adsorption have been statistically analyzed for distinct incident energies. As can be seen in Fig. 5.1 and 5.2, a peculiar dependence is found in the respective distributions. Hyperthermal molecules generally tend to dissociate with the molecular axis oriented parallel to the surface, whereby the single atoms are located over the fcc hollow and

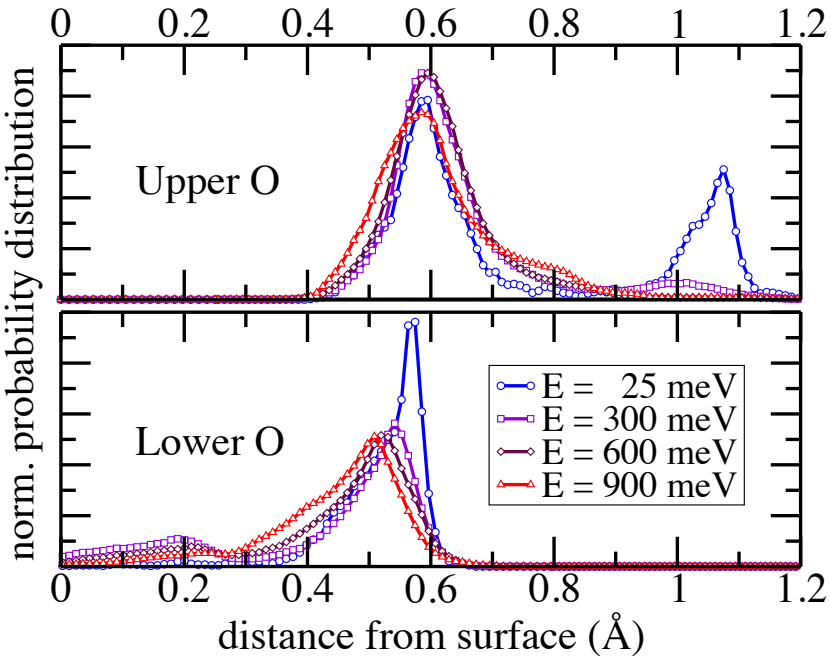


Figure 5.1: Distribution of distances that the single oxygen molecules exhibit with respect to the surface after the dissociation event at an oxygen-oxygen distance of 2.0 Å. Distinct histograms have been computed for the "upper" oxygen atom, which is farther away from the surface, and the "lower" oxygen atom that lies closer.

the top site respectively. In contrast thereto, thermal molecules prefer a different orientation. Indeed, a significant amount of oxygen is found in a tilted geometry, in which the lower lying atom, i.e. the one closer to the surface, is located over the top site and the higher lying atom is located over the hcp hollow site. On the basis of these data one might thus conclude, that an abstraction or cannonball-like dissociation mechanism originates the peculiar experimental results. Such an interpretation, however, is by far too bold. All these coordinates are yielded at the bond breaking condition, i.e. at an oxygen-oxygen distance of 2.0 Å, at which also the interpolation of the Potential Energy Surfaces almost ends. At this point the individual oxygen atoms are not at rest yet, but exhibit a significant kinetic energy of more than 5 eV they have first to get rid of (see Sec. 4.4.6.1). Thereby, the actual interaction with the distinct aluminum atoms of the surface starts to play a significant role in this late part of the dynamics. This motion, however, cannot be accurately described within a Surface Oscillator model, even if we extended our Potential Energy Surfaces to map larger oxygen-oxygen distances as well. Consequently, the frozen substrate approximation has to be abandoned when searching for the origin of this phenomenon. For this purpose the use of an adiabatic *ab initio MD* algorithm, which leads to the dissociation of all impinging molecules, is certainly[1] not the

[1]Indeed, purely adiabatic *ab initio MD* trajectories from the vacuum to the surface have been investigated previously [256] as well. Nevertheless, the results of such studies are at least questionable: A method that yields a completely incorrect Sticking Coefficient for thermal

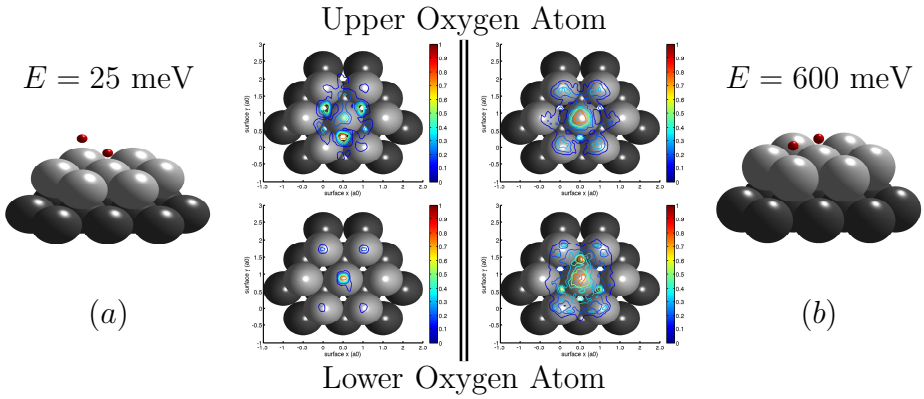


Figure 5.2: Two-dimensional histograms of the lateral surface coordinates that the oxygen molecules exhibit after the dissociation event at an oxygen-oxygen distance of 2.0 Å. Both the distribution for oxygen impinging at thermal energies ($a$) and the distribution for hyperthermal molecules ($b$) is shown. Additionally, the respective most probable "dissociation" geometry found in the simulations is sketched as well.

best choice. Rather, an *ab initio Surface Hopping* method, in which the various Potential Energy Surfaces and their respective couplings are computed *on the fly*, must be used. Such techniques have already been implemented before, e.g. on the basis of Quantum Chemical algorithms [291, 292], but also in the framework of Density Functional Theory [267]. These approaches have hitherto never been applied to such extended systems as the one this work is focused on due to their prohibitive numerical cost that even exceeds the one of *ab initio MD* simulations. Therefore, these techniques are nowadays successfully used in the investigation of comparatively small molecules on the basis of relatively few trajectories [293, 294]. In future, the growth of computing power will allow such simulations to be performed also for such extended systems as the one inspected in this work. Certainly, no high statistic accuracy on the basis of millions of trajectories, as required in the simulations presented in Sec. 4.4.4 and 4.4.5 for instance, will be achievable by *ab initio Surface Hopping* techniques soon. The mysterious results found in the STM experiments, which are apparently caused by one dominant mechanism during the dissociative adsorption, will however finally find their explanation due to such calculations much earlier.

The way for such future *ab initio Surface Hopping* simulations has been paved and critically discussed in this work. Thereby, the outstanding agreement found with a wide range of experiments substantiates the validity of our approach. However, there is room left for improvement: In particular, it would be desirable to include into the simulations at least three excited states of the oxygen, i.e. the $^1\Delta_g$, the $^1\Sigma_g^+$ and the ionic state, since they all differ significantly in their coupling to the triplet ground state. Although we did our best to account for this fact by introducing a lower and an upper bound for the non-diagonal matrix elements, the herein employed description of the excited states in terms of a "mean" singlet PES will and is already subject to refinement in future

molecules will most probably not yield the correct dissociation mechanism in the late part of the dynamics either.

studies [295]. The indispensable prerequisite thereto, however, is that the electronic states of interest are correctly addressable by Density Functional Theory, which is not the case for the singlet states yet (see Sec. 3.3). In this context, the development of new exchange-correlation functionals [251] that correct for the self-interaction of the electrons and the thereto associated static correlation error will certainly play a crucial role. Such considerations led to the hypothesis [262] that future functionals might also correctly describe the dynamics of the system without the invocation of any electronic transitions at all, i.e. on the basis of one activated adiabatic PES alone. As discussed in Sec. 4.1 before, this conjecture is highly speculative. In spite of that, such considerations drew our attention to a severe lack in the previous studies: Therein, no method had been proposed to verify that such hindered spin transitions indeed play a crucial role for the inspected system. This work fills this gap by suggesting two different experimental setups in Sec. 4.4.4 and Sec. 4.4.5, which should both be able to unambiguously assess the occurrence of non-adiabatic transitions during the dissociative adsorption.

Eventually, the question arises if such hindered spin transitions are solely relevant for the system discussed in this work or if such a mechanism is active in other reactions[2] at surfaces, too. As a matter of fact, such effects are common and well known [296] in the gas-phase chemistry of a variety of molecules, whereas they have hitherto neither been widely inspected nor detected in heterogeneous reactions. Typically, the surface behaves as a spin (electron and momentum) bath that makes reactions that are strongly hindered in the gas phase possible at all [21]. The herein inspected substrate, however, constitutes a special case that cannot be generally regarded as such a spin bath, since it exhibits a minute Spin-Orbit Coupling [296] due to the light atomic mass of aluminum. As measurements of the molecular oxygen's reactivity at aluminum clusters [278] substantiate, such triplet-singlet conversions are therefore drastically impeded. This finding suggests that comparable effects can be expected for other, likewise light elements. At the silicon (001) surface for instance, a pronounced dependence on the spin transition has been found [297] for the dissociative adsorption of oxygen as well. For reactions with heavier elements, e.g. at transition metal surfaces, such hindered spin transition are thus expected to be a secondary effect that certainly plays a role in the dynamics, but does not completely determine it—as it is the case for the herein inspected system. In principle, the experiments proposed and the simulation techniques employed in this work allow to assess the role of non-adiabatic effects in such more complex systems, too. The studies presented in this work for the dissociative adsorption of oxygen at the aluminum (111) surface, which can be regarded as a model system for spin transitions, will serve as a valuable reference for such future investigations.

[2]The oxygen molecule is perfectly suited for the identification of such effects, since its triplet-singlet transition is strongly forbidden in the gas phase. Similar phenomena might also occur for more complex molecules whose transition is comparably hindered [296].

# Appendix A

# The Many-Electron Spin Problem

## A.1 The Spin Operators $\mathbf{S}^2$ and $S_z$

The spin operators $\mathbf{S}_i^2$ and $S_i^z$ for one single electron $i$ have the following properties [142]:

$$S_i^{\mathbf{z}} |\uparrow\rangle_i = +\frac{\hbar}{2} |\uparrow\rangle_i \qquad \mathbf{S}_i^2 |\uparrow\rangle_i = \frac{3}{4}\hbar^2 |\uparrow\rangle_i$$
$$S_i^{\mathbf{z}} |\downarrow\rangle_i = -\frac{\hbar}{2} |\downarrow\rangle_i \qquad \mathbf{S}_i^2 |\downarrow\rangle_i = \frac{3}{4}\hbar^2 |\downarrow\rangle_i$$

Accordingly, ladder operators $S_i^{\pm} = S_i^{\mathbf{x}} \pm \mathrm{i} S_i^{\mathbf{y}}$ that fulfill

$$S_i^+ |\uparrow\rangle_i = 0 \qquad S_i^+ |\downarrow\rangle_i = \hbar |\uparrow\rangle_i \qquad S_i^+ |\uparrow\rangle_j = |\uparrow\rangle_j S_i^+$$
$$S_i^- |\uparrow\rangle_i = \hbar |\downarrow\rangle_i \qquad S_i^+ |\downarrow\rangle_i = 0 \qquad S_i^- |\uparrow\rangle_j = |\uparrow\rangle_j S_i^-$$

can be introduced.

In the many-electron problem the spin of an electron $i$ couples to the spin of an electron $j$. Hence combinations of the single electron ladder operators, namely $S_i^+ S_j^-$ and $S_i^- S_j^+$, occur in the calculation of the total spin. The action of these two-electron operators on all possible two-component spinors is:

$$S_i^+ S_j^- |\uparrow\rangle_i |\uparrow\rangle_j = 0 \qquad S_i^- S_j^+ |\uparrow\rangle_i |\uparrow\rangle_j = 0$$
$$S_i^+ S_j^- |\uparrow\rangle_i |\downarrow\rangle_j = 0 \qquad S_i^- S_j^+ |\uparrow\rangle_i |\downarrow\rangle_j = \hbar^2 |\downarrow\rangle_i |\uparrow\rangle_j$$
$$S_i^+ S_j^- |\downarrow\rangle_i |\uparrow\rangle_j = \hbar^2 |\uparrow\rangle_i |\downarrow\rangle_j \qquad S_i^- S_j^+ |\downarrow\rangle_i |\uparrow\rangle_j = 0$$
$$S_i^+ S_j^- |\downarrow\rangle_i |\downarrow\rangle_j = 0 \qquad S_i^- S_j^+ |\downarrow\rangle_i |\downarrow\rangle_j = 0$$

On this basis the total multi-electron spin operators $\mathbf{S}^2$ and $S^{\mathbf{z}}$ can be introduced

by taking the vectorial sum of the single electron spins [142]:

$$\begin{aligned} S^{\mathbf{z}} &= \left(\textstyle\sum_i \mathbf{S}_i\right)|^{\mathbf{z}} &&= \sum_i S_i^{\mathbf{z}}, \qquad (A.1)\\ \mathbf{S}^2 &= \left(\textstyle\sum_i \mathbf{S}_i\right)^2 &&= \sum_i \mathbf{S}_i^2 + 2\sum_i \sum_{j>i} \mathbf{S}_i \cdot \mathbf{S}_j \\ &&&= \sum_i \mathbf{S}_i^2 + \sum_{i\neq j} \mathbf{S}_i \cdot \mathbf{S}_j \\ &&&= \sum_i \mathbf{S}_i^2 + \sum_{i,j} \mathbf{S}_i \cdot \mathbf{S}_j \left(1-\delta_{ij}\right). \end{aligned}$$

The scalar product $\mathbf{S}_i \cdot \mathbf{S}_j$ that appears in the last sum can be further simplified by employing the ladder operators introduced in the beginning:

$$\mathbf{S}_i \cdot \mathbf{S}_j = S_i^{\mathbf{x}} S_j^{\mathbf{x}} + S_i^{\mathbf{y}} S_j^{\mathbf{y}} + S_i^{\mathbf{z}} S_j^{\mathbf{z}} = \frac{1}{2}\left(S_i^+ S_j^- + S_i^- S_j^+\right) + S_i^{\mathbf{z}} S_j^{\mathbf{z}}.$$

Accordingly, the total spin operator $\mathbf{S}^2$ can now be written as

$$\mathbf{S}^2 = \sum_i \mathbf{S}_i^2 + \sum_{i,j} S_i^{\mathbf{z}} S_j^{\mathbf{z}} \left(1-\delta_{ij}\right) + \frac{1}{2}\sum_{i,j}\left(S_i^+ S_j^- + S_i^- S_j^+\right)\left(1-\delta_{ij}\right). \qquad (A.2)$$

For a simple spinor $\chi = \left(|\uparrow\rangle_1 \cdot |\downarrow\rangle_2 \cdots |\downarrow\rangle_n\right)$ that describes $n^\uparrow$ spin up electrons and $n^\downarrow$ spin down electrons ($n = n^\uparrow + n^\downarrow$ electrons in total) the single terms in Eq. (A.2) can be expressed as:

$$\begin{aligned} \sum_i \mathbf{S}_i^2 \chi &= n\frac{3}{4}\hbar^2\chi, \qquad (A.3)\\ \sum_{i,j} S_i^{\mathbf{z}} S_j^{\mathbf{z}} \left(1-\delta_{ij}\right)\chi &= \sum_{i,j} S_i^{\mathbf{z}} S_j^{\mathbf{z}} \chi - \sum_i \left(S_i^{\mathbf{z}}\right)^2 \chi \\ &= \sum_i S_i^{\mathbf{z}} \frac{\hbar}{2}\left(n^\uparrow - n^\downarrow\right)\chi - \frac{\hbar^2}{4} n\chi \\ &= \left(\frac{\hbar^2}{4}\left(n^\uparrow - n^\downarrow\right)^2 - \frac{\hbar^2}{4} n\right)\chi, \qquad (A.4)\\ \frac{1}{2}\sum_{i,j}\left(S_i^+ S_j^- + S_i^- S_j^+\right)\left(1-\delta_{ij}\right)\chi &= \frac{1}{2}\sum_{i\neq j}\left(S_i^+ S_j^- + S_i^- S_j^+\right)\chi \\ &= \frac{\hbar^2}{2}\sum_{i\neq j} \mathfrak{F}_{ij}\,\chi. \qquad (A.5) \end{aligned}$$

Thereby the *spin-flip* operator $\mathfrak{F}_{ij}$ was introduced in Eq. (A.5): Whereas all other operators in Eq. (A.3) and (A.4) do not change the spinor they act on, the spin-flip operator pairwise flips the spins of the electrons $i$ and $j$ if their respective spin alignment is antiparallel:

$$\begin{aligned} \mathfrak{F}_{ij}\,\chi &= \frac{1}{\hbar^2}\left(S_i^+ S_j^- + S_i^- S_j^+\right)\chi \qquad (A.6)\\ &= \begin{cases} |\uparrow\rangle_1 \cdots |\uparrow\rangle_i \cdots |\downarrow\rangle_j \cdots |\downarrow\rangle_n & \text{for } \chi = |\uparrow\rangle_1 \cdots |\downarrow\rangle_i \cdots |\uparrow\rangle_j \cdots |\downarrow\rangle_n \\ |\uparrow\rangle_1 \cdots |\downarrow\rangle_i \cdots |\uparrow\rangle_j \cdots |\downarrow\rangle_n & \text{for } \chi = |\uparrow\rangle_1 \cdots |\uparrow\rangle_i \cdots |\downarrow\rangle_j \cdots |\downarrow\rangle_n \\ 0 & \text{else for all } i \neq j \end{cases}. \end{aligned}$$

Thus only eigenfunctions of $\mathfrak{F}_{ij}$ can be eigenfunctions of $\mathbf{S}^2$, as can easily be seen by inserting (A.3), (A.4) and (A.5) into Eq. (A.2):

$$\mathbf{S}^2\chi = \frac{\hbar^2}{4}\left(2n + \left(n^{\uparrow} - n^{\downarrow}\right)^2 + 2\sum_{i\neq j}\mathfrak{F}_{ij}\right)\chi. \tag{A.7}$$

More general operators for the coupling of the orbital angular momentum with the spin $(J^2, J_z)$ can be derived in a similar manner as well [142].

## A.2 Generic Eigenfunctions of $\mathbf{S}^2$

Since electrons are fermions, their wave function $\Psi$ has to be totally antisymmetric, i.e., it changes its sign upon exchange of two electrons. Formally this exchange is performed by the two-particle permutation operator

$$\begin{aligned}\mathfrak{P}_{ij}\ \Psi\left(\mathbf{r}_1,\ldots\mathbf{r}_i,\ldots\mathbf{r}_j,\ldots\mathbf{r}_n\right) &= \quad \Psi\left(\mathbf{r}_1,\ldots\mathbf{r}_j,\ldots\mathbf{r}_i,\ldots\mathbf{r}_n\right)\\ &= \quad -\Psi\left(\mathbf{r}_1,\ldots\mathbf{r}_i,\ldots\mathbf{r}_j,\ldots\mathbf{r}_n\right).\end{aligned} \tag{A.8}$$

Accordingly, two electrons $i$ and $j$ that share the same spin alignment—without loss of generality $|\uparrow\rangle$—must differ in their spatial part $\mathbf{x}$, since otherwise Eq. (A.8) would lead to

$$\begin{aligned}\mathfrak{P}_{ij}\ \Psi\left(\ldots,\mathbf{x}\left|\uparrow\right\rangle,\ldots,\mathbf{x}\left|\uparrow\right\rangle,\ldots\right) &= \quad \Psi\left(\ldots,\mathbf{x}\left|\uparrow\right\rangle,\ldots,\mathbf{x}\left|\uparrow\right\rangle,\ldots\right)\\ &= \quad -\Psi\left(\ldots,\mathbf{x}\left|\uparrow\right\rangle,\ldots,\mathbf{x}\left|\uparrow\right\rangle,\ldots\right)\\ &= \quad 0.\end{aligned} \tag{A.9}$$

This is the well known Pauli principle [298]. A wave function that fulfills this criterion for an $n$ electron system can be constructed by using one *Slater Determinant* [53]. Thereby each of the $n$ spinorbitals $\Phi_i(i) = \phi_i(\mathbf{r_i})\cdot\sigma_i$ consists of a spatial part $\phi_i(\mathbf{r_i})$ and a spin part $\sigma_i$:

$$\begin{aligned}\Psi_{SD}(1,\ldots,n) &= \frac{1}{\sqrt{n!}}\begin{vmatrix}\Phi_1(1) & \Phi_1(2) & \cdots & \Phi_1(n)\\ \Phi_2(1) & \Phi_2(2) & \cdots & \Phi_2(n)\\ \vdots & \vdots & \ddots & \vdots\\ \Phi_n(1) & \Phi_n(2) & \cdots & \Phi_n(n)\end{vmatrix}\\ &= \frac{1}{\sqrt{n!}}\,\epsilon^{i_1\cdots i_n}\Phi_{i_1}(1)\cdots\Phi_{i_i}(i)\cdots\Phi_{i_n}(n).\end{aligned} \tag{A.10}$$

In the last step the *Einstein summation notation* and the *Levi-Civita Symbol* $\epsilon^{1\cdots n}$ have been used.

However, not all Slater Determinants are necessarily eigenfunctions of $\mathbf{S}^2$, as can be easily shown for, e.g., certain Slater Determinants of two electrons distributed on two degenerate spatial orbitals $\phi_x$ and $\phi_y$[1]. Under the constraint of antiparallel alignment of the spins and of partial occupation of both orbitals

[1] This configuration corresponds to the configuration of the $O_2$ molecule, as described in detail in section 3.1.

two Slater Determinants can be constructed:

$$\Psi_a = \frac{1}{\sqrt{2}}\begin{vmatrix}\phi_x(1)\,|\uparrow\rangle & \phi_x(2)\,|\uparrow\rangle\\ \phi_y(1)\,|\downarrow\rangle & \phi_y(2)\,|\downarrow\rangle\end{vmatrix} = \frac{1}{\sqrt{2}}\left(\phi_x(1)\phi_y(2)\,|\uparrow\downarrow\rangle - \phi_y(1)\phi_x(2)\,|\downarrow\uparrow\rangle\right)$$

$$\Psi_b = \frac{1}{\sqrt{2}}\begin{vmatrix}\phi_x(1)\,|\downarrow\rangle & \phi_x(2)\,|\downarrow\rangle\\ \phi_y(1)\,|\uparrow\rangle & \phi_y(2)\,|\uparrow\rangle\end{vmatrix} = \frac{1}{\sqrt{2}}\left(\phi_x(1)\phi_y(2)\,|\downarrow\uparrow\rangle - \phi_y(1)\phi_x(2)\,|\uparrow\downarrow\rangle\right)$$

Since the action of $\mathfrak{F}_{12}$ on these wave functions results in

$$\mathfrak{F}_{12}\Psi_a = \Psi_b \qquad \text{and} \qquad \mathfrak{F}_{12}\Psi_b = \Psi_a,$$

neither $\Psi_a$ nor $\Psi_b$ are eigenfunctions of $\mathbf{S}^2$. Nevertheless, their linear combinations $\Psi_a \pm \Psi_b$ are eigenfunctions of both $\mathfrak{F}_{12}$ and $\mathbf{S}^2$ and correspond to a low-spin triplet state and a singlet state respectively:

$$\mathbf{S}^2\ (\Psi_a + \Psi_b) = 2\hbar^2\,(\Psi_a + \Psi_b) \qquad S_z\ (\Psi_a + \Psi_b) = 0$$

$$\mathbf{S}^2\ (\Psi_a - \Psi_b) = 0 \qquad S_z\ (\Psi_a - \Psi_b) = 0$$

A correct calculation of such electronic states hence deserves a method that includes at least the two relevant Slater Determinants $\Psi_a$ and $\Psi_b$ in the construction of the wave function. However, such an electronic configuration is an exception to the rule: The most common ground states addressed in electronic structure simulations, i.e. the closed shell and the high-spin configuration, are described correctly by one Slater Determinant, as shown in the next two sections.

### A.2.1 High-Spin Configurations

In so called high-spin configurations all electrons are aligned parallel and thus lead to Slater Determinants of the form

$$\begin{aligned}\Psi_{SD}^{HS}(1,\ldots,n) &= \frac{1}{\sqrt{n!}}\,\epsilon^{i_1\cdots i_n}\phi_{i_1}(1)\,|\uparrow\rangle\cdots\phi_{i_i}(i)\,|\uparrow\rangle\cdots\phi_{i_n}(n)\,|\uparrow\rangle\\ &= \frac{1}{\sqrt{n!}}\begin{vmatrix}\phi_1 & \phi_1 & \cdots & \phi_1\\ \phi_2 & \phi_2 & \cdots & \phi_2\\ \vdots & \vdots & \ddots & \vdots\\ \phi_n & \phi_n & \cdots & \phi_n\end{vmatrix}|\uparrow\rangle_1\,|\uparrow\rangle_2\cdots|\uparrow\rangle_n\,.\end{aligned}$$

Obviously the application of $\mathfrak{F}_{ij}$ as defined in Eq. (A.6) yields

$$\mathfrak{F}_{ij}\Psi_{SD}^{HS}(1,\ldots,n) = 0,$$

since no antiparallel spins are present. Hence the high-spin Slater Determinant $\Psi_{SD}^{HS}$ is indeed an eigenfunction to the spin operators (A.7) and (A.1):

$$\mathbf{S}^2\Psi_{SD}^{HS} = \frac{\hbar^2}{4}n(n+2)\ \Psi_{SD}^{HS} \qquad S_z\Psi_{SD}^{HS} = \frac{\hbar}{2}n\ \Psi_{SD}^{HS}$$

### A.2.2 Closed Shell Configurations

Now we investigate those $n$ electron configurations, in which $n/2$ spatial orbitals are occupied with both a spin up and a spin down electron each[2]. This leads to

[2] We call this configuration "closed-shell", since according to Hund's second rule [172] just closed shell systems exhibit such an occupation pattern in their ground state. However, also an excited state of an open shell system may exhibit the same occupation characteristics.

Slater Determinants of the form

$$\begin{aligned}\Psi_{SD}^{CS} &= \frac{1}{\sqrt{n!}}\begin{vmatrix} \phi_1|\uparrow\rangle(1) & \phi_1|\uparrow\rangle(2) & \cdots & \phi_1|\uparrow\rangle(n) \\ \phi_1|\downarrow\rangle(1) & \phi_1|\downarrow\rangle(2) & \cdots & \phi_1|\downarrow\rangle(n) \\ \phi_2|\uparrow\rangle(1) & \phi_2|\uparrow\rangle(2) & \cdots & \phi_2|\uparrow\rangle(n) \\ \vdots & \vdots & \ddots & \vdots \\ \phi_{\frac{n}{2}}|\downarrow\rangle(1) & \phi_{\frac{n}{2}}|\downarrow\rangle(2) & \cdots & \phi_{\frac{n}{2}}|\downarrow\rangle(n) \end{vmatrix} \\ &= \frac{1}{\sqrt{n!}}\,\epsilon^{i_1\cdots i_{\frac{n}{2}}}\phi_{i_1}(1)|\uparrow\rangle\cdot\phi_{i_1}(2)|\downarrow\rangle\cdots\phi_{i_{\frac{n}{2}}}(n-1)|\uparrow\rangle\cdot\phi_{i_{\frac{n}{2}}}(n)|\downarrow\rangle\,.\end{aligned}$$

The action of $\mathfrak{F}_{ij}$ on two electrons sharing the same spatial orbital, electron 1 and 2 for instance, results in

$$\begin{aligned}\mathfrak{F}_{12}\Psi_{SD}^{CS} &= \mathfrak{F}_{12}\frac{1}{\sqrt{n!}}\,\epsilon^{i_1\cdots i_{\frac{n}{2}}}(\phi_{i_1}(1)|\uparrow\rangle\cdot\phi_{i_1}(2)|\downarrow\rangle\cdots) \\ &= \frac{1}{\sqrt{n!}}\,\epsilon^{i_1\cdots i_{\frac{n}{2}}}(\phi_{i_1}(1)|\downarrow\rangle\cdot\phi_{i_1}(2)|\uparrow\rangle\cdots) \\ &= \mathfrak{P}_{12}\frac{1}{\sqrt{n!}}\,\epsilon^{i_1\cdots i_{\frac{n}{2}}}(\phi_{i_1}(1)|\uparrow\rangle\cdot\phi_{i_1}(2)|\downarrow\rangle\cdots) \\ &= -\frac{1}{\sqrt{n!}}\,\epsilon^{i_1\cdots i_{\frac{n}{2}}}(\phi_{i_1}(1)|\uparrow\rangle\cdot\phi_{i_1}(2)|\downarrow\rangle\cdots) \\ &= -\Psi_{SD}^{CS}.\end{aligned}$$

In this special case the action of $\mathfrak{F}_{12}$ corresponds to a permutation $\mathfrak{P}_{12}$ (A.8) and hence leads to a change in the sign of the wave function. On the contrary $\mathfrak{F}_{ij}\Psi_{SD}^{CS}$ vanishes if the electrons $i$ and $j$ do not share the same spatial orbital:

$$\begin{aligned}\mathfrak{F}_{13}\Psi_{SD}^{CS} &= \mathfrak{F}_{13}\frac{1}{\sqrt{n!}}\,\epsilon^{i_1\cdots i_{\frac{n}{2}}}(\phi_{i_1}(1)|\uparrow\rangle\cdot\phi_{i_1}(2)|\downarrow\rangle\cdot\phi_{i_2}(3)|\uparrow\rangle\cdots) \\ &= \frac{1}{\sqrt{n!}}\,\epsilon^{i_1\cdots i_{\frac{n}{2}}}(\phi_{i_1}(1)|\uparrow\rangle\cdot\phi_{i_1}(2)|\uparrow\rangle\cdot\phi_{i_2}(3)|\downarrow\rangle\cdots) \\ &= 0\end{aligned}$$

In this special case—without loss of generality demonstrated for electron 2 and 3—the electron pairs $(1,2)$ as well as $(3,4)$ share the same quantum numbers. Consequently, the Pauli principle (A.9) demands the respective wave function to vanish.

Eventually, the action of the spin operators (A.7) and (A.1) on such closed-shell wave functions is

$$\mathbf{S}^2\Psi_{SD}^{CS} = 0 \qquad\qquad S_z\Psi_{SD}^{CS} = 0,$$

as intuitively expected for such configurations.

# Appendix B

# Convergence Studies

## B.1 Quantum Chemical Calculations

To ensure the convergence of the data discussed in Sec. 3.2 for the oxygen molecule, an extensive series of simulations for each of the presented Quantum Chemistry methods has been performed. Thereby both the employed basis set and the numerical convergence and integration parameters have been varied systematically. In a next step, all relevant properties of the molecule have been determined for each of these convergence studies in exactly the same fashion as discussed in Sec. 3.2 to inspect the molecular properties' dependence on the various calculational setups. The thereby employed basis sets [176, 177, 178, 179, 180] and their abbreviations used hereinafter are:

- **VDZ:** Correlation Consistent Double-Zeta Dunning Basis Set
- **VTZ:** Correlation Consistent Triple-Zeta Dunning Basis Set
- **VQZ:** Correlation Consistent Quadruple-Zeta Dunning Basis Set
- **V5Z:** Correlation Consistent Quintuple-Zeta Dunning Basis Set
- **V6Z:** Correlation Consistent Sextuple-Zeta Dunning Basis Set
- **Aug. pCV5Z:** Correlation Consistent Quintuple-Zeta Dunning Basis Set with additional diffusive, polarized and core-valence split basis functions
- **pV5Z:** Correlation Consistent Quintuple-Zeta Dunning Basis Set with additional polarized basis functions (Gaussian only)

Each of these basis sets has been used for all the Quantum Chemical methods that have already been discussed in detail in Sec. 3.2:

- **UHF:** Unrestricted Hartree-Fock
- **ROHF:** Restricted Open Shell Hartree-Fock
- **MCSCF:** Multiconfiguration SCF
- **CASSCF:** Complete Active Space SCF
- **FVCI:** Full Valence Configuration Interaction with single and double excitations
- **CISD:** Configuration Interaction with single and double excitations
- **MRCI:** Multireference Configuration Interaction with single and double excitations

Additionally, two further *Configuration Interaction with single and double excitations* simulation setups with slightly different constraints on the MOs' occupation have been employed:

**CISD ($2\pi$):** In this setup the excitations of both the $2\pi$ and $2\pi^*$ orbital are explicitly addressed, whereas the electrons in the $2\sigma_p$ and $2\sigma_s$ orbital are just *internally* correlated [175]. Furthermore, the $1\sigma_s$ and the $1\sigma_s^*$ orbitals are "frozen" to the outcome of the underlying Hartree-Fock calculation. Therefore, these simulations are situated in between the CISD calculations, which additionally allow for excitations in the $2\sigma_s$ orbital, and the FVCI calculations, which explicitly correlate just the $2\pi^*$ valence electrons.

**CISD ($1\sigma$):** In this setup the electrons in **all** orbitals, even the four electrons in the $1\sigma_s$ and $1\sigma_s^*$ orbitals, are explicitly correlated. Thus the comparison of these calculations with the CISD simulations allows to estimate the role that the core orbitals play.

The influence of the core orbitals was also studied for the MRCI method in the V5Z basis set by first "unfreezing" the $1\sigma_s$ and $1\sigma_s^*$ electrons in the underlying CASSCF calculation and by then explicitly addressing all single and double excitations out of these MOs. These calculations are denoted by "V5Z ($1\sigma$)" in Tab. B.2 and B.3.

Furthermore, the influence of the numerical parameters, i.e. the integral and convergence thresholds, has been inspected for the MRCI/V5Z calculations as well. Whereas all other presented calculations have been performed with MOLPRO's default thresholds (see Tab. B.1), the simulations denoted with "V5Z (s.t.)" employ thresholds which are at least two order of magnitudes smaller than the respective default values (also see Tab. B.1).

**Results:**

- The V5Z basis set ensures convergence for the triplet ground state properties of the oxygen—i.e. the equilibrium bond length $d_{\mathrm{eq}}$ and the vibrational

| Thresholds | Default | (s.t.) |
|---|---|---|
| Numerical zero | $10^{-12}$ | $10^{-14}$ |
| Threshold for one-electron integrals[1] | $10^{-12}$ | $10^{-14}$ |
| Threshold for the neglect of two-electron integrals | $10^{-12}$ | $10^{-14}$ |
| Convergence threshold for energy | $10^{-6}$ | $10^{-12}$ |
| Convergence threshold for orbital gradient in MCSCF | $10^{-2}$ | $10^{-6}$ |
| Convergence threshold for step length in MCSCF orbital optimization | $10^{-3}$ | $10^{-6}$ |
| Threshold for symmetry in gradient | $10^{-6}$ | $10^{-6}$ |
| Convergence threshold for CI coefficients in MCSCF and reference vector in CI | $10^{-5}$ | $10^{-7}$ |
| Convergence threshold for coefficients in CI and CCSD | $10^{-4}$ | $10^{-6}$ |

Table B.1: Numerical parameters and integration thresholds in atomic units (if applicable) used in MOLPRO [175]: Both the program's default values employed for the majority of the calculations and the drastically reduced thresholds employed for the (s.t.) runs are given.

[1] Not used at present [175].

frequency $\omega_0$—to a large extent: A further enlargement of the number of basis functions in the V6Z and Aug. pCV5Z simulations results in deviations of less than 1 mÅ and less than 3 $cm^{-1}$ ($\ll$ 1 meV) respectively.

- Not too surprisingly, larger uncertainties have been found for the total equilibrium energies $E_{eq}$: With respect to the V5Z basis set fluctuations in the order of magnitude of 200 meV still occur if the number of basis functions is further increased. For the explicit correlation of the core electrons even higher uncertainties ($>$ 1.0 eV) can arise, as the CISD ($1\sigma$) calculations show.

- For the Counterpoise (and Zero Point Energy) corrected binding energy $E_b$ maximal uncertainties of 10 meV for the single Determinant calculations and 30 meV for the multiple Determinant ones have been found in the V5Z basis set. However, these deviations correspond to relative errors of less than 1% with respect to the experimental value of 5.12 eV (see Sec. 3.2.2).

- For the Zero Point Energy corrected excitation energies $\Delta E^{\Delta}_{TS}$ and $\Delta E^{\Sigma}_{TS}$ listed in Tab. B.3 the V5Z simulations are converged up to an accuracy of 5 meV for the $^1\Delta_g$ state and 10 meV for the $^1\Sigma^+_g$ state. In terms of relative errors these energies correspond to deviations of less than 1% of the respective experimental excitation energies (0.98 and 1.62 eV as discussed in Sec. 3.2.2).

- Single reference CI calculations in the VDZ basis set do not converge for elongated molecular bond lengths and are thus neither listed in Tab. B.2 nor in Tab. B.3.

- The CISD ($2\pi$) calculations result in precisely the same simulated oxygen features as the CISD calculations, with a single exception: The triplet-

singlet energy gap $\Delta E^{\Sigma}_{\mathrm{TS}}$, where excitations out of the $2\sigma_s$ orbital indeed play a role.

- The inclusion of core electron correlation for the CISD and MRCI method does still lower the total energy by almost 2 eV. However, all other molecular properties are not altered significantly. In fact the error introduced by ignoring the core electron correlation is at most in the order of magnitude of the basis set error:

  | | | |
  |---|---|---|
  | 3 mÅ | for | $d_{\mathrm{eq}}$, |
  | 20 $\mathrm{cm}^{-1}$ | for | $\omega_0$ and |
  | 10 meV | for | $\Delta E^{\Delta}_{\mathrm{TS}}$ and $\Delta E^{\Sigma}_{\mathrm{TS}}$. |

  This statement also holds for the binding energy: There, in addition, the "basis set error" and the "core correlation error" have opposite signs and this fact results in a positive error cancellation.

- Also a drastic reduction of the integration thresholds (see Tab. B.1) in the V5Z (s.t.) calculations alters the total equilibrium energy and the vibrational frequency by at most the same amount as an enlargement of the basis set to the V6Z level would. All other simulated molecular properties are considerably less affected.

To draw a bottom line: The V5Z calculations exhibit more than satisfying convergence for our purpose of calculating Spin-Orbit transition probabilities in the near-equilibrium region. Calculations with even higher accuracy, to achieve a smaller absolute error for the binding energy for instance, can be performed by correlating the core electrons explicitly. In this case also a larger basis set—V6Z and higher—has to be employed to assure the convergence of the data. However, the error in the binding energy generated by truncating the Configuration Interaction method to single and double excitations is almost two orders of magnitude larger than the error generated by neglecting the core correlation [189]. Thus, in a first step, additional triple and quadruple excited Determinants have to be included to gradually approach the exact solution.

Table B.2 – Triplet Ground State Properties of the Oxygen Molecule

| Basis Set | $d_{\mathrm{eq}}$ (Å) | $E_{\mathrm{eq}}$ (eV) | $\omega_0(\mathrm{cm}^{-1})$ | $E_{\mathrm{b}}$ (eV) | +CP | +ZPE |
|---|---|---|---|---|---|---|
| UHF | | | | | | |
| VDZ | 1.15420 | -4071.70 | 2029.57 | -1.3040 | -1.2130 | -1.0867 |
| VTZ | 1.15331 | -4072.99 | 2005.70 | -1.5278 | -1.4998 | -1.3751 |
| VQZ | 1.15259 | -4073.32 | 2003.91 | -1.5564 | -1.5531 | -1.4285 |
| V5Z | 1.15260 | -4073.41 | 2001.95 | -1.5655 | -1.5653 | -1.4408 |
| V6Z | 1.15261 | -4073.43 | 2001.99 | -1.5765 | -1.5717 | -1.4472 |
| Aug. pCV5Z | 1.15266 | -4073.42 | 2001.76 | -1.5721 | -1.5738 | -1.4493 |

Continuation follows on the next page...

Table B.2 – Continued from the previous page

| Basis Set | $d_{eq}$ (Å) | $E_{eq}$ (eV) | $\omega_0$(cm$^{-1}$) | $E_b$ (eV) | +CP | +ZPE |
|---|---|---|---|---|---|---|
| ROHF | | | | | | |
| VDZ | 1.14957 | -4071.19 | 2054.55 | -1.0472 | -1.0004 | -0.8726 |
| VTZ | 1.14720 | -4072.41 | 2041.85 | -1.2804 | -1.2670 | -1.1400 |
| VQZ | 1.14599 | -4072.73 | 2044.52 | -1.3175 | -1.3117 | -1.1846 |
| V5Z | 1.14574 | -4072.82 | 2045.25 | -1.3320 | -1.3226 | -1.1954 |
| V6Z | 1.14571 | -4072.83 | 2045.68 | -1.3343 | -1.3285 | -1.2013 |
| Aug. pCV5Z | 1.14574 | -4072.82 | 2045.62 | -1.3304 | -1.3302 | -1.2030 |
| MCSCF | | | | | | |
| VDZ | 1.14957 | -4071.19 | 2054.55 | -1.0483 | -1.0004 | -0.8726 |
| VTZ | 1.14720 | -4072.41 | 2041.85 | -1.3244 | -1.2670 | -1.1400 |
| VQZ | 1.14599 | -4072.73 | 2044.52 | -1.3701 | -1.3117 | -1.1846 |
| V5Z | 1.14574 | -4072.82 | 2045.25 | -1.3865 | -1.3226 | -1.1954 |
| V6Z | 1.14571 | -4072.83 | 2045.68 | -1.3893 | -1.3285 | -1.2013 |
| Aug. pCV5Z | 1.14574 | -4072.82 | 2045.62 | -1.3856 | -1.3302 | -1.2030 |
| CASSCF | | | | | | |
| VDZ | 1.21854 | -4073.92 | 1522.47 | -3.7783 | -3.7422 | -3.6473 |
| VTZ | 1.21488 | -4075.09 | 1529.14 | -4.0044 | -3.9621 | -3.8668 |
| VQZ | 1.21293 | -4075.40 | 1537.56 | -4.0401 | -3.9968 | -3.9010 |
| V5Z | 1.21255 | -4075.48 | 1539.58 | -4.0465 | -4.0049 | -3.9090 |
| V6Z | 1.21244 | -4075.49 | 1540.66 | -4.0493 | -4.0096 | -3.9137 |
| Aug. pCV5Z | 1.21244 | -4075.48 | 1540.99 | -4.0456 | -4.0110 | -3.9150 |
| FVCI | | | | | | |
| VTZ | 1.18264 | -4083.82 | 1784.60 | -3.8706 | -3.7342 | -3.6231 |
| VQZ | 1.17833 | -4084.91 | 1803.71 | -3.9619 | -3.9041 | -3.7919 |
| V5Z | 1.17720 | -4085.28 | 1808.36 | -3.9958 | -3.9697 | -3.8572 |
| V6Z | 1.17677 | -4085.41 | 1810.78 | -4.0160 | -4.0025 | -3.8898 |
| Aug. pCV5Z | 1.17714 | -4085.36 | 1808.49 | -4.0082 | -3.9912 | -3.8787 |
| CISD ($2\pi$) | | | | | | |
| VTZ | 1.19303 | -4084.05 | 1692.94 | -4.1041 | -3.9699 | -3.8645 |
| VQZ | 1.18843 | -4085.14 | 1713.37 | -4.1957 | -4.1389 | -4.0323 |
| V5Z | 1.18724 | -4085.51 | 1718.28 | -4.2301 | -4.2045 | -4.0975 |
| V6Z | 1.18679 | -4085.64 | 1720.83 | -4.2505 | -4.2373 | -4.1302 |
| Aug. pCV5Z | 1.18717 | -4085.59 | 1718.55 | -4.2427 | -4.2261 | -4.1192 |
| CISD | | | | | | |
| VTZ | 1.19303 | -4084.05 | 1692.94 | -4.1041 | -3.9699 | -3.8645 |
| VQZ | 1.18843 | -4085.14 | 1713.37 | -4.1957 | -4.1389 | -4.0323 |
| V5Z | 1.18724 | -4085.51 | 1718.28 | -4.2301 | -4.2045 | -4.0975 |
| V6Z | 1.18679 | -4085.64 | 1720.83 | -4.2505 | -4.2373 | -4.1302 |
| Aug. pCV5Z | 1.18717 | -4085.59 | 1718.55 | -4.2427 | -4.2261 | -4.1192 |

Continuation follows on the next page...

Table B.2 – Continued from the previous page

| Basis Set | $d_{eq}$ (Å) | $E_{eq}$ (eV) | $\omega_0$(cm$^{-1}$) | $E_b$ (eV) | +CP | +ZPE |
|---|---|---|---|---|---|---|
| CISD ($1\sigma$) | | | | | | |
| VTZ | 1.18941 | -4084.66 | 1708.75 | -4.1390 | -3.9448 | -3.8384 |
| VQZ | 1.18529 | -4086.65 | 1728.79 | -4.1474 | -4.0703 | -3.9627 |
| V5Z | 1.18341 | -4087.36 | 1738.80 | -4.1751 | -4.1207 | -4.0124 |
| V6Z | 1.18272 | -4087.77 | 1741.49 | -4.1742 | -4.1404 | -4.0320 |
| Aug. pCV5Z | 1.18308 | -4088.62 | 1741.14 | -4.1017 | -4.0845 | -3.9762 |
| MRCI | | | | | | |
| VDZ | 1.21623 | -4080.94 | 1552.81 | -4.3029 | -4.0085 | -3.9117 |
| VTZ | 1.20960 | -4084.48 | 1562.36 | -4.5490 | -4.4187 | -4.3214 |
| VQZ | 1.20511 | -4085.58 | 1581.13 | -4.6500 | -4.5951 | -4.4966 |
| V5Z | 1.20398 | -4085.95 | 1585.51 | -4.6879 | -4.6629 | -4.5641 |
| V6Z | 1.20353 | -4086.08 | 1588.08 | -4.7093 | -4.6962 | -4.5973 |
| Aug. pCV5Z | 1.20396 | -4086.03 | 1585.87 | -4.7001 | -4.6837 | -4.5849 |
| V5Z ($1\sigma$) | 1.20102 | -4087.84 | 1606.44 | -4.6601 | -4.6074 | -4.5074 |
| V5Z (s.t.) | 1.20443 | -4085.96 | 1592.42 | -4.6880 | -4.6630 | -4.5638 |

Table B.2: Simulated triplet ground state key features of the oxygen molecule: The equilibrium bond length $d_{eq}$, the equilibrium total energy $E_{eq}$, the vibrational frequency $\omega_0$ and the binding energy $E_b$ with additional Counterpoise (CP) corrections and Zero Point Energy (ZPE) corrections are listed for a whole series of different methods and basis sets (see text). For the MRCI method the results of two supplementary runs, one including the core orbitals ($1\sigma$) and one with smaller integration thresholds (s.t.) are also listed. All properties have been determined with the methods described in Sec. 3.2.1.

Table B.3 – Excitation Energies for the Oxygen Molecule

| Basis Set | $\Delta E_{TS}^{\Delta}$ (eV) | +ZPE | $\Delta E_{TS}^{\Sigma}$ (eV) | +ZPE |
|---|---|---|---|---|
| UHF | | | | |
| VDZ | 2.2969 | 2.2969 | – | – |
| VTZ | 2.3168 | 2.3174 | – | – |
| VQZ | 2.3217 | 2.3226 | – | – |
| V5Z | 2.3219 | 2.3229 | – | – |
| V6Z | 2.3219 | 2.3229 | – | – |
| Aug. pCV5Z | 2.3219 | 2.3229 | – | – |

Continuation follows on the next page...

Table B.3 – Continued from the previous page

| Basis Set | $\Delta E_{\mathrm{TS}}^{\Delta}$ (eV) | +ZPE | $\Delta E_{\mathrm{TS}}^{\Sigma}$ (eV) | +ZPE |
|---|---|---|---|---|
| ROHF | | | | |
| VDZ | 1.7909 | 1.7894 | – | – |
| VTZ | 1.7406 | 1.7390 | – | – |
| VQZ | 1.7272 | 1.7255 | – | – |
| V5Z | 1.7232 | 1.7215 | – | – |
| V6Z | 1.7221 | 1.7204 | – | – |
| Aug. pCV5Z | 1.7211 | 1.7194 | – | – |
| MCSCF | | | | |
| VDZ | 1.2928 | 1.2922 | 2.5730 | 2.5717 |
| VTZ | 1.2897 | 1.2891 | 2.5591 | 2.5579 |
| VQZ | 1.2881 | 1.2875 | 2.5536 | 2.5524 |
| V5Z | 1.2869 | 1.2863 | 2.5501 | 2.5489 |
| V6Z | 1.2869 | 1.2863 | 2.5496 | 2.5484 |
| Aug. pCV5Z | 1.2868 | 1.2862 | 2.5495 | 2.5483 |
| CASSCF | | | | |
| VDZ | 0.9545 | 0.9480 | 1.4737 | 1.4624 |
| VTZ | 0.9613 | 0.9550 | 1.4866 | 1.4757 |
| VQZ | 0.9622 | 0.9560 | 1.4883 | 1.4775 |
| V5Z | 0.9619 | 0.9557 | 1.4877 | 1.4770 |
| V6Z | 0.9619 | 0.9557 | 1.4877 | 1.4770 |
| Aug. pCV5Z | 0.9618 | 0.9556 | 1.4876 | 1.4769 |
| FVCI | | | | |
| VTZ | 1.1161 | 1.1180 | 1.9697 | 1.9738 |
| VQZ | 1.1008 | 1.1025 | 1.9603 | 1.9641 |
| V5Z | 1.0935 | 1.0951 | 1.9529 | 1.9566 |
| V6Z | 1.0904 | 1.0920 | 1.9499 | 1.9536 |
| Aug. pCV5Z | 1.0918 | 1.0934 | 1.9510 | 1.9547 |
| CISD ($2\pi$) | | | | |
| VTZ | 0.9460 | 0.9460 | 1.6302 | 1.6425 |
| VQZ | 0.9303 | 0.9304 | 1.6168 | 1.6287 |
| V5Z | 0.9229 | 0.9229 | 1.6082 | 1.6199 |
| V6Z | 0.9200 | 0.9200 | 1.6048 | 1.6165 |
| Aug. pCV5Z | 0.9211 | 0.9211 | 1.6058 | 1.6175 |
| CISD | | | | |
| VTZ | 0.9460 | 0.9460 | 1.5909 | 1.6028 |
| VQZ | 0.9303 | 0.9304 | 1.5743 | 1.5858 |
| V5Z | 0.9229 | 0.9229 | 1.5646 | 1.5760 |
| V6Z | 0.9200 | 0.9200 | 1.5608 | 1.5721 |
| Aug. pCV5Z | 0.9211 | 0.9211 | 1.5620 | 1.5733 |

Continuation follows on the next page...

Table B.3 – Continued from the previous page

| Basis Set | $\Delta E_{\mathrm{TS}}^{\Delta}$ (eV) | +ZPE | $\Delta E_{\mathrm{TS}}^{\Sigma}$ (eV) | +ZPE |
|---|---|---|---|---|
| CISD ($1\sigma$) | | | | |
| VTZ | 0.9479 | 0.9479 | 1.5953 | 1.6072 |
| VQZ | 0.9285 | 0.9285 | 1.5737 | 1.5852 |
| V5Z | 0.9207 | 0.9207 | 1.5636 | 1.5750 |
| V6Z | 0.9170 | 0.9170 | 1.5588 | 1.5707 |
| Aug. pCV5Z | 0.9154 | 0.9154 | 1.5556 | 1.5670 |
| MRCI | | | | |
| VDZ | 1.0364 | 1.0303 | 1.6091 | 1.5975 |
| VTZ | 0.9897 | 0.9843 | 1.6733 | 1.6627 |
| VQZ | 0.9739 | 0.9688 | 1.6387 | 1.6286 |
| V5Z | 0.9663 | 0.9613 | 1.6218 | 1.6119 |
| V6Z | 0.9633 | 0.9584 | 1.6118 | 1.6019 |
| Aug. pCV5Z | 0.9644 | 0.9595 | 1.6080 | 1.5981 |
| V5Z ($1\sigma$) | 0.9650 | 0.9609 | 1.6107 | 1.6007 |
| V5Z (s.t.) | 0.9660 | 0.9600 | 1.6112 | 1.5998 |

Table B.3: Excitation energies $\Delta E_{\mathrm{TS}}^{\Delta}$ and $\Delta E_{\mathrm{TS}}^{\Sigma}$ from the triplet ground state of the oxygen molecule into the excited $^1\Delta_g$ and the $^1\Sigma_g^+$ state respectively: Zero Point Energy corrected values (ZPE) are also listed. For the MRCI method the results of two supplementary runs, one including the core orbitals ($1\sigma$) and one with smaller integration thresholds (s.t.) are given as well. All energies have been determined as described in Sec. 3.2.1.

**Additional Gaussian Calculations:** As discussed extensively in Sec. 3.2.2, Unrestricted Hartree-Fock (UHF) calculations for the oxygen molecule's excited singlet states have been performed with Gaussian [199], since MOLPRO does not allow to access these states by the same simulation technique. To ensure self-consistency also the triplet ground state properties had to be recomputed with Gaussian. However, no extensive convergence tests for various basis sets have been performed in this case, since a similar behavior can be expected for both Quantum Chemical simulation packages. Thus the V5Z basis set, which in Gaussian is solely provided with additional polarized functions per default (pV5Z), has been employed directly. As shown in Tab. B.4, the reference Restricted Open-Shell Hartree-Fock (ROHF) calculations lead to the same results (within the discussed uncertainty) for both Gaussian and MOLPRO, although the basis sets are not completely identical. The UHF triplet-singlet gaps, which are listed as well, are discussed extensively in Sec. 3.2.2.

## B.2 Density Functional Theory Calculations

In this section the convergence of the Density Functional Theory simulations of $O_2$ with respect to the various calculational parameters is inspected. Thereto

| | | UHF | ROHF | MOLPRO |
|---|---|---|---|---|
| $d_{\mathrm{eq}}$ | (Å) | 1.15247 | 1.14558 | 1.14574 |
| $E_{\mathrm{eq}}$ | (eV) | -4073.41 | -4072.81 | -4072.82 |
| $\omega_0$ | ($\mathrm{cm}^{-1}$) | 1997.02 | 2040.78 | 2045.25 |
| $E_{\mathrm{b}}$ | (eV) | -1.5671 | -1.3223 | -1.3320 |
| $E_{\mathrm{b}}$, +CP | (eV) | -1.5652 | -1.3216 | -1.3226 |
| $E_{\mathrm{b}}$, +CP, +ZPE | (eV) | -1.4410 | -1.1947 | -1.1954 |
| $\Delta E_{\mathrm{TS}}^{\Delta}$ | (eV) | 2.3211 | 1.7239 | 1.7232 |
| $\Delta E_{\mathrm{TS}}^{\Delta}$,+ZPE | (eV) | 2.3221 | 1.7222 | 1.7215 |
| $\Delta E_{\mathrm{TS}}^{C}$ | (eV) | 0.7548 | – | – |
| $\Delta E_{\mathrm{TS}}^{C}$,+ZPE | (eV) | 0.7551 | – | – |
| $\Delta E_{\mathrm{TS}}^{\Sigma}$ | (eV) | 1.5096 | – | – |
| $\Delta E_{\mathrm{TS}}^{\Sigma}$,+ZPE | (eV) | 1.5099 | – | – |

Table B.4: Results for the Unrestricted (UHF) and Restricted Open Shell (ROHF) Hartree-Fock simulations performed with Gaussian [199] in the V5Z basis set with additional polarization functions. Additionally, the results of the Restricted Open Shell Hartree-Fock calculations performed with MOLPRO in the V5Z basis set already given in Tab. B.2 and Tab. B.3 are listed for comparison.

the key characteristics of the oxygen molecule have been determined in the exact same fashion as described in Sec. 3.2.1 and Sec. 3.3.2 for a whole series of simulations, each with a slightly altered calculation setup. Although the basic concept is the same as in Sec. B.1, the studied parameters and their effect on the results of the simulations differ from the ones discussed before due to the profoundly divergent nature of the Quantum Chemical/Atomic Orbital and the Density Functional Theory/Plane Waves approach.

This fact becomes evident already in the first calculation parameter that has been inspected for the simulation of the oxygen molecule with VASP, which is the size and the geometry of the employed monoclinic unit cell (see Fig. 3.11), as described by the basic vectors:

$$\begin{aligned} a &= 1.1 \cdot l, \\ b &= 1.3 \cdot l, \\ c &= 1.7 \cdot l. \end{aligned}$$

Thereby the lattice parameter $l$ was systematically varied from 5.0 Å to 12.5 Å in steps of 2.5 Å, but the ratio of the edge lengths (and the respective angles) were kept constant. Although the equilibrium molecular bond length of the oxygen molecule is almost an order of magnitude smaller, such a huge unit cell

is necessary, since VASP employs periodic boundary conditions and hence describes a three-dimensional, infinite array of such identical unit cells. Conversely, the size of the single unit cell determines the distance between the oxygen molecule and its periodic replicas. To address the electronic structure of an isolated oxygen molecule, the lattice parameter must be chosen large enough so that interactions between the oxygen molecule and its periodic clones virtually vanish. From a numerical performance point of view, however, the volume of the unit cell should be preferably minute, since it significantly influences the memory usage of such calculations: For a fixed cut-off energy, a larger unit cell results in smaller reciprocal lattice vectors and as a consequence, in more terms in the wave function expansion (3.44).

As substantiated in Tab. B.5, the equilibrium characteristics of the oxygen molecule, i.e. the molecular bond length and the vibrational frequency, are converged well below experimental accuracy at a lattice parameter value of 10.0 Å. This also applies to the triplet-singlet energy gap, whereas the binding energy still shows oscillations in the meV range. With respect to the systematic error introduced by the approximative exchange-correlation functionals, however, this uncertainty is absolutely negligible. Noteworthy enough, all equilibrium characteristics besides the vibrational frequency are already converged at a lattice parameter of 7.5 Å. The correct simulation of the vibrational frequency, though, demands a larger super cell due to its higher sensitivity on the shape of the Potential Energy Curve. At large bond elongations the distance between the single oxygen atoms and their periodic replicas in the adjacent cells is shortened along

| | $l$ (Å) | $d_{\mathrm{eq}}$ (Å) | $E_{\mathrm{eq}}$ (eV) | $\omega_0$ (cm$^{-1}$) | $E_{\mathrm{b}}$ (eV) | $\Delta E_{\mathrm{TS}}$ (eV) |
|---|---|---|---|---|---|---|
| LDA | 5.0 | 1.21734 | -10.44 | 3259.04 | -7.478 [7.274] | 0.9716 [0.9686] |
| | 7.5 | 1.21770 | -10.45 | 3969.17 | -7.485 [7.237] | 0.9702 [0.9660] |
| | 10.0 | 1.21772 | -10.46 | 1631.63 | -7.485 [7.384] | 0.9702 [0.9697] |
| | 12.5 | 1.21769 | -10.45 | 1631.83 | -7.489 [7.387] | 0.9702 [0.9697] |
| PW91 | 5.0 | 1.23059 | -9.72 | 2925.73 | -6.254 [6.071] | 1.0457 [1.0424] |
| | 7.5 | 1.23102 | -9.75 | 3555.60 | -6.262 [6.040] | 1.0443 [1.0389] |
| | 10.0 | 1.23104 | -9.74 | 1556.44 | -6.262 [6.165] | 1.0442 [1.0434] |
| | 12.5 | 1.23100 | -9.75 | 1556.69 | -6.265 [6.168] | 1.0442 [1.0434] |
| PBE | 5.0 | 1.22932 | -9.90 | 2948.86 | -6.034 [5.849] | 1.1272 [1.1237] |
| | 7.5 | 1.22975 | -9.83 | 3589.15 | -6.042 [5.818] | 1.1257 [1.1195] |
| | 10.0 | 1.22977 | -9.82 | 1564.67 | -6.043 [5.945] | 1.1257 [1.1247] |
| | 12.5 | 1.22938 | -9.83 | 1566.98 | -6.049 [5.951] | 1.1258 [1.1246] |
| RPBE | 5.0 | 1.23129 | -10.44 | 2885.35 | -5.662 [5.481] | 1.1579 [1.1533] |
| | 7.5 | 1.23174 | -10.47 | 3508.87 | -5.670 [5.451] | 1.1563 [1.1498] |
| | 10.0 | 1.23176 | -10.46 | 1550.42 | -5.671 [5.574] | 1.1563 [1.1548] |
| | 12.5 | 1.23172 | -10.48 | 1550.65 | -5.674 [5.577] | 1.1563 [1.1552] |

Table B.5: Molecular bond length $d_{\mathrm{eq}}$, total equilibrium energy $E_{\mathrm{eq}}$, vibrational frequency $\omega_0$, binding energy $E_{\mathrm{b}}$ and triplet-singlet energy gap $\Delta E_{\mathrm{TS}}$ (Zero Point Energy corrected values in brackets) for the oxygen molecule as function of the lattice parameter $l$. All calculations have been performed with an energy cut-off of 400 eV and a Gaussian smearing of 0.01 eV.

| | $E_{\mathrm{co}}$ (eV) | $d_{\mathrm{eq}}$ (Å) | $E_{\mathrm{eq}}$ (eV) | $\omega_0(\mathrm{cm}^{-1})$ | $E_{\mathrm{b}}$ (eV) | $\Delta E_{\mathrm{TS}}$ (eV) |
|---|---|---|---|---|---|---|
| LDA | 300 | 1.21892 | -10.46 | 1587.86 | -7.596 [7.497] | 0.9831 [0.9819] |
| | 350 | 1.21822 | -10.43 | 1621.85 | -7.529 [7.428] | 0.9628 [0.9623] |
| | 400 | 1.21772 | -10.45 | 1631.63 | -7.485 [7.384] | 0.9702 [0.9697] |
| | 450 | 1.21747 | -10.45 | 1632.82 | -7.466 [7.365] | 0.9734 [0.9728] |
| PW91 | 300 | 1.23343 | -9.76 | 1504.51 | -6.379 [6.285] | 1.0596 [1.0583] |
| | 350 | 1.23181 | -9.72 | 1544.90 | -6.308 [6.212] | 1.0362 [1.0361] |
| | 400 | 1.23104 | -9.74 | 1556.44 | -6.262 [6.165] | 1.0442 [1.0434] |
| | 450 | 1.23076 | -9.75 | 1557.88 | -6.241 [6.144] | 1.0476 [1.0468] |
| PBE | 300 | 1.23213 | -9.83 | 1512.41 | -6.157 [6.062] | 1.2445 [1.2415] |
| | 350 | 1.23053 | -9.80 | 1553.04 | -6.088 [5.991] | 1.1172 [1.1161] |
| | 400 | 1.22977 | -9.82 | 1564.67 | -6.042 [5.945] | 1.1257 [1.1247] |
| | 450 | 1.22951 | -9.83 | 1566.08 | -6.021 [5.924] | 1.1293 [1.1283] |
| RPBE | 300 | 1.23440 | -10.48 | 1496.75 | -5.788 [5.695] | 1.1945 [1.1920] |
| | 350 | 1.23261 | -10.45 | 1538.38 | -5.717 [5.622] | 1.1468 [1.1451] |
| | 400 | 1.23176 | -10.46 | 1550.42 | -5.671 [5.574] | 1.1563 [1.1548] |
| | 450 | 1.23148 | -10.47 | 1551.95 | -5.649 [5.552] | 1.1603 [1.1592] |

Table B.6: Molecular bond length $d_{\mathrm{eq}}$, total equilibrium energy $E_{\mathrm{eq}}$, vibrational frequency $\omega_0$, binding energy $E_{\mathrm{b}}$ and triplet-singlet energy gap $\Delta E_{\mathrm{TS}}$ (Zero Point Energy corrected values in brackets) for the oxygen molecule as function of the energy cut-off $E_{\mathrm{co}}$. All calculations have been performed with a Gaussian smearing of 0.01 eV in the monoclinic unit cell discussed before with a lattice parameter of 10 Å.

the molecular axis, since the atoms get closer to the unit cell's borders.

In the next step, the dependence of the calculations on the cut-off energy $E_{\mathrm{co}}$ has been studied. For a fixed unit cell geometry this parameter basically determines the size of the basis set, i.e. the number of plane waves that are employed in the expansion (3.44). As seen in Tab. B.6, both the molecular bond length and the vibrational frequency are converged again well below experimental accuracy at a cut-off value of 400 eV. At this specific value the binding energy exhibits an error of approximately 20 meV, whereas the triplet-singlet energy gap might still vary by about 5 meV. The corresponding relative errors for both quantities are significantly smaller than 1%, so that these results can also be regarded as converged with respect to an energy cut-off of 400 eV.

Eventually, the dependence of the calculations on the employed Gaussian smearing was inspected for a wide range of broadening widths $\sigma_s$ (see Tab. B.7). As this data highlights, neither the equilibrium bond lengths nor the vibrational frequencies are affected by the broadening, even if it is varied by **three** orders of magnitude. This is not too surprising, though, since the smearing procedure solely allows for the spill out of electronic charge in $\sigma_s$-near-degenerate, vacant orbitals with the same spin. For the triplet ground state electronic structure of the equilibrium oxygen molecule there is no such vacancy available, since the spin up valence orbitals—without loss of generality—are all completely filled with one spin species. Therefore the Pauli principle prevents such a spill out in

| | $\sigma_s$ (eV) | $d_{eq}$ (Å) | $E_{eq}$ (eV) | $\omega_0$(cm$^{-1}$) | $E_b$ (eV) | $\Delta E_{TS}$ (eV) |
|---|---|---|---|---|---|---|
| LDA | 0.100 | 1.21772 | -10.45 | 1631.63 | -7.573 [7.472] | 0.9194 [0.9189] |
| | 0.050 | 1.21772 | -10.45 | 1631.63 | -7.612 [7.510] | 0.9476 [0.9471] |
| | 0.010 | 1.21772 | -10.45 | 1631.63 | -7.485 [7.384] | 0.9702 [0.9697] |
| | 0.005 | 1.21772 | -10.45 | 1631.63 | -7.485 [7.384] | 0.9730 [0.9727] |
| | $10^{-3}$ | 1.21772 | -10.45 | 1631.63 | -7.485 [7.384] | 1.0730 [1.0730] |
| | $10^{-4}$ | 1.21772 | -10.45 | 1631.63 | -7.485 [7.384] | 1.0730 [1.0726] |
| PW91 | 0.100 | 1.23104 | -9.74 | 1556.44 | -6.747 [6.650] | 0.9934 [0.9926] |
| | 0.050 | 1.23104 | -9.74 | 1556.44 | -6.785 [6.688] | 1.0216 [1.0208] |
| | 0.010 | 1.23104 | -9.74 | 1556.44 | -6.262 [6.165] | 1.0442 [1.0434] |
| | 0.005 | 1.23104 | -9.74 | 1556.44 | -6.262 [6.165] | 1.1448 [1.1428] |
| | $10^{-3}$ | 1.23104 | -9.74 | 1556.44 | -6.262 [6.165] | 1.1979 [1.1968] |
| | $10^{-4}$ | 1.23104 | -9.74 | 1556.44 | -6.262 [6.165] | 1.2006 [1.1992] |
| PBE | 0.100 | 1.22977 | -9.82 | 1564.67 | -6.716 [6.619] | 1.0749 [1.0739] |
| | 0.050 | 1.22977 | -9.82 | 1564.67 | -6.526 [6.429] | 1.1031 [1.1021] |
| | 0.010 | 1.22977 | -9.82 | 1564.67 | -6.042 [5.945] | 1.1257 [1.1247] |
| | 0.005 | 1.22977 | -9.82 | 1564.67 | -6.042 [5.945] | 1.2141 [1.2118] |
| | $10^{-3}$ | 1.22977 | -9.82 | 1564.67 | -6.043 [5.946] | 1.2871 [1.2860] |
| | $10^{-4}$ | 1.22977 | -9.82 | 1564.67 | -6.042 [5.945] | 1.2477 [1.2461] |
| RPBE | 0.100 | 1.23176 | -10.46 | 1550.42 | -6.390 [6.293] | 1.1055 [1.1044] |
| | 0.050 | 1.23176 | -10.46 | 1550.42 | -5.671 [5.574] | 1.1337 [1.1326] |
| | 0.010 | 1.23176 | -10.46 | 1550.42 | -5.671 [5.574] | 1.1563 [1.1548] |
| | 0.005 | 1.23176 | -10.46 | 1550.42 | -5.671 [5.574] | 1.3065 [1.3044] |
| | $10^{-3}$ | 1.23176 | -10.46 | 1550.42 | -5.671 [5.574] | 1.3339 [1.3328] |
| | $10^{-4}$ | 1.23176 | -10.46 | 1550.42 | -5.671 [5.574] | 1.3340 [1.3323] |

Table B.7: Molecular bond length $d_{eq}$, total equilibrium energy $E_{eq}$, vibrational frequency $\omega_0$, binding energy $E_b$ and triplet-singlet energy gap $\Delta E_{TS}$ (Zero Point Energy corrected values in brackets) for the oxygen molecule as function of the smearing broadness $\sigma_s$. All calculations have been performed with an energy cut-off of 400 eV in the monoclinic unit cell discussed before with a lattice parameter of 10 Å.

energetically adjacent orbitals from the beginning. The electronic structure of the oxygen atom, and hence the calculated binding energy, however, depend on the chosen smearing width. In the particular triplet $^3$P ground state of the oxygen atom the threefold degenerate $2p$ valence orbitals are occupied by—again without loss of generality—three spin up and one spin down electrons. The latter one tends to spread over all three degenerate orbitals for too large $\sigma_s$ values, which results in an artificial occupation of one third of an electron in each one of the spin down $2p$ orbitals. To avoid this effect and thus to gain converged binding energies, a Gaussian smearing broadness of 10 meV or less must be employed in the simulation of an oxygen molecule.

A connatural effect occurs in the simulation of the triplet-singlet energy gap, only the other way round: As scrutinized in Sec. 3.3.1, the excited singlet state is best described by a non-interacting reference system (3.41) that indeed exhibits fractional occupation numbers. Thus, in this particular case, both the spin up and the spin down valence electrons present in the valence shell shall spread

| | $\epsilon_C^{LDA}$ | $d_{\mathrm{eq}}$ (Å) | $E_{\mathrm{eq}}$ (eV) | $\omega_0(\mathrm{cm}^{-1})$ | $E_{\mathrm{b}}$ (eV) | $\Delta E_{\mathrm{TS}}$ (eV) |
|---|---|---|---|---|---|---|
| LDA | std. | 1.21772 | -10.45 | 1631.63 | -7.485 [7.384] | 0.9702 [0.9697] |
| | VWN | 1.21772 | -10.49 | 1631.83 | -7.359 [7.258] | 1.0167 [1.0162] |
| PW91 | std. | 1.23104 | -9.74 | 1556.44 | -6.262 [6.165] | 1.0442 [1.0434] |
| | VWN | 1.23103 | -9.79 | 1556.69 | -6.135 [6.038] | 1.0911 [1.0903] |
| PBE | std. | 1.22977 | -9.82 | 1564.67 | -6.042 [5.945] | 1.1257 [1.1247] |
| | VWN | 1.22977 | -9.82 | 1564.67 | -6.042 [5.945] | 1.1257 [1.1247] |
| RPBE | std. | 1.23176 | -10.46 | 1550.42 | -5.671 [5.574] | 1.1563 [1.1548] |
| | VWN | 1.23176 | -10.46 | 1550.42 | -5.671 [5.574] | 1.1562 [1.1548] |

Table B.8: Molecular bond length $d_{\mathrm{eq}}$, total equilibrium energy $E_{\mathrm{eq}}$, vibrational frequency $\omega_0$, binding energy $E_{\mathrm{b}}$ and triplet-singlet energy gap $\Delta E_{\mathrm{TS}}$ (Zero Point Energy corrected values in brackets) for the oxygen molecule: Results for calculations employing the Padeé interpolation and for calculations employing the *Vosko-Wilk-Nusair interpolation* (VWN) for the LDA correlation are listed.

equally over the whole twofold degenerate valence $2\pi^*$ orbitals of the oxygen molecule. A too low value of $\sigma_s$, i.e. lower than 10 meV, prevents this spill out and leads to an undesired segregation of the electrons into one of the two $2\pi^*$ valence orbitals. Accordingly, the thereby reduced exchange interaction results in too large simulated triplet-singlet energy gaps.
To achieve a correct description of both the excited singlet state and the binding energy at one and the same level of theory, a compromise has to be made in the selection of the smearing broadness: All results presented in this work have been performed with a Gaussian broadening of 0.01 eV, which yields converged binding energies for all functionals due to the correct segregation of the single spin down electron to one orbital in the simulation of the oxygen atom. Furthermore, the chosen broadness results in an electronic structure of the excited singlet state that exhibits an almost uniform occupation pattern in the valence orbitals: In the RPBE calculations, for instance, there are 0.50016 electrons in the one and 0.49984 electrons in the other valence orbital for each spin species. Finally, it has to be said that all presented results have been achieved under the condition that the electronic optimization stops as soon as both the total and the band structure energy difference between two self-consistency cycles is smaller than $E_{\mathrm{diff}} = 10^{-6}$ eV. This value ensures very accurate results, as calculations with a breaking condition that is an order of magnitude smaller[2] demonstrate.

In a next step also the influence of the *Vosko-Wilk-Nusair interpolation* [238] of the *Ceperly-Alder* data [88] in the calculation of the LDA correlation potential with respect to VASP's standard Padé type [299] interpolation scheme has been inspected as shown in Tab. B.8. Although this special technique should enhance spin-polarized simulations [228], virtually any amelioration is found for the PBE and RPBE calculations. Solely the binding energy and the triplet-singlet gap are slightly better when either the LDA or the PW91 functional is

[2]The data obtained by calculations with an $E_{\mathrm{diff}}$ value of $10^{-7}$ eV is not shown, since it is identical to the hitherto presented data.

| Pseudopot. | | $d_{eq}$ (Å) | $E_{eq}$ (eV) | $\omega_0$(cm$^{-1}$) | $E_b$ (eV) | $\Delta E_{TS}$ (eV) |
|---|---|---|---|---|---|---|
| LDA | soft | 1.28564 | -9.94 | 1666.51 | -6.915 [6.812] | 1.0163 [1.0158] |
| | std. | 1.21772 | -10.49 | 1631.83 | -7.359 [7.258] | 1.0167 [1.0162] |
| | hard | 1.20110 | -10.60 | 1623.84 | -7.513 [7.412] | 1.0222 [1.0216] |
| all-e$^-$ [246] | | 1.210 | – | 1592 | -7.428 | – |
| PW91 | soft | 1.31387 | -9.08 | 1551.10 | -5.835 [5.739] | 1.0787 [1.0780] |
| | std. | 1.22977 | -9.82 | 1564.67 | -6.135 [6.038] | 1.0911 [1.0903] |
| | hard | 1.21552 | -9.87 | 1543.84 | -6.175 [6.078] | 1.0980 [1.0974] |
| all-e$^-$ [246] | | 1.224 | – | 1502 | -6.074 | – |
| PBE | soft | 1.29477 | -9.43 | 1627.47 | -5.637 [5.536] | 1.1053 [1.1046] |
| | std. | 1.22977 | -9.82 | 1564.67 | -6.042 [5.945] | 1.1257 [1.1247] |
| | hard | 1.21446 | -9.92 | 1555.35 | -6.078 [5.981] | 1.1471 [1.1460] |
| all-e$^-$ [246] | | 1.224 | – | 1527 | -6.099 | 1.138 |
| RPBE | soft | 1.29662 | -10.08 | 1615.87 | -5.266 [5.165] | 1.1358 [1.1350] |
| | std. | 1.23176 | -10.46 | 1550.42 | -5.671 [5.574] | 1.1563 [1.1548] |
| | hard | 1.21656 | -10.56 | 1540.90 | -5.702 [5.606] | 1.1772 [1.1761] |
| all-e$^-$ [246] | | 1.229 | – | 1597 | -5.646 | 1.171 |

Table B.9: Molecular bond length $d_{eq}$, total equilibrium energy $E_{eq}$, vibrational frequency $\omega_0$, binding energy $E_b$ and triplet-singlet energy gap $\Delta E_{TS}$ (Zero Point Energy corrected values in brackets) of the oxygen molecule for various pseudopotentials. Please note that the calculations for hard pseudopotentials have been performed at a cut-off energy of 650 eV. Additionally, the outcome of all-electron calculations found in literature is listed as a reference.

employed. Whereas the reason for this improvement in the LDA calculations due to a refined interpolation is self-evident, at first it remains unclear why this enhancement occurs just for the PW91 and not for all GGA functionals: Linear response at small generalized gradients, a functional characteristic of major importance that the LDA, the PBE and the RPBE functional fulfill exactly by construction, is realized just roughly in the PW91 functional due to the approximative cancellation of respective correlation and exchange terms (see Sec. 3.3.2). As these calculations suggest, the *Vosko-Wilk-Nusair interpolation* improves this cancellation and thereby the accuracy of the PW91 functional as a whole. Accordingly, all further simulations for the LDA and PW91 functionals have been performed with the Vosko-Wilk-Nusair interpolation.

Last but not least, the error introduced by the pseudopotential approximation was studied by comparing the hitherto presented "standard" pseudopotential results to the outcome of all-electron calculations performed by J. Behler [246]. Additionally, simulations that respectively employ "softer" and "harder" pseudopotentials, which are also provided by the VASP suite, have been performed, as the data in Tab. B.9 shows. The oxygen molecule's key features are described rather precisely within the hitherto employed pseudopotential, since average deviations of 6 mÅ for the lattice constant, 50 cm$^{-1}$ for the vibrational frequencies, 50 meV for the binding energy and 17 meV for the triplet-singlet gaps occur with respect to the all-electron calculations. Although the use of the

harder pseudopotential can slightly improve the simulations, the final average error is still in the same order of magnitude as before. For the binding energy, however, the harder pseudopotential even worsens the results due to the fact that the calculations for the oxygen atom—in contrast to the ones for the oxygen molecule—are not yet completely converged at the employed cut-off energy of 650 eV. Thus the minute gain in accuracy due to a harder pseudopotential does not justify the thereby induced huge increase in numerical effort in our case.

# Bibliography


[1] K. Honkala and K. Laasonen. Oxygen Molecule Dissociation on the Al(111) Surface. *Phys. Rev. Lett.*, 84:705, 2000.

[2] Y. Yourdshahyan, B. Razaznejad, and B. I. Lundqvist. Adiabatic potential-energy surfaces for oxygen on Al(111). *Phys. Rev. B*, 65:75416, 2002.

[3] L. Österlund, I. Zorić, and B. Kasemo. Dissociative sticking of $O_2$ on Al(111). *Phys. Rev. B*, 55:15452, 1997.

[4] J. Behler, B. Delley, S. Lorenz, K. Reuter, and M. Scheffler. Dissociation of $O_2$ at Al(111): The Role of Spin Selection Rules. *Phys. Rev. Lett.*, 94:036104, 2005.

[5] J. Behler, B. Delley, K. Reuter, and M. Scheffler. Nonadiabatic potential-energy surfaces by constrained density-functional theory. *Phys. Rev. B*, 75:115409, 2007.

[6] J. Behler, K. Reuter, and M. Scheffler. Nonadiabatic effects in the dissociation of oxygen molecules at the Al(111) surface. *Phys. Rev. B*, 77:115421, 2008.

[7] J. C. Tully. Molecular dynamics with electronic transitions. *J. Chem. Phys.*, 93:1061, 1990.

[8] C. Bach, C. Carbogno, and A. Groß. Mixed Quantum–Classical Treatment of Reactions at Surfaces with Electronic Transitions. *Israel J. Chem.*, 45:46, 2005.

[9] C. Carbogno, A. Groß, and M. Rohlfing. Ab initio investigation of the laser induced desorption of iodine from KI(100). *Appl. Phys. A*, 88:579, 2007.

[10] C. Carbogno, J. Behler, A. Groß, and K. Reuter. Fingerprints for spin-selection rules in the interaction dynamics of $O_2$ at Al(111). *Phys. Rev. Lett.*, 101:096104, 2008.

[11] O. Weiße, C. Wesenberg, M. Binetti, E. Hasselbrink, C. Corriol, G. R. Darling, and S. Holloway. Incidence angle dependence of scattering and dissociation of $O_2$ on Al(111): Possible weakly bound molecular precursors. *J. Chem. Phys.*, 118:8010, 2003.

[12] *Nobel Lecture in Chemistry.* http://www.nobel.se, 1901.

[13] *Nobel Lecture in Chemistry.* http://www.nobel.se, 1932.

[14] *Nobel Lecture in Chemistry.* http://www.nobel.se, 1909.

[15] *Nobel Lecture in Chemistry.* http://www.nobel.se, 1918.

[16] *Nobel Lecture in Chemistry.* http://www.nobel.se, 1950.

[17] *Nobel Lecture in Chemistry.* http://www.nobel.se, 1986.

[18] F. Pirani, D. Cappelletti, F. Vecchiocattivi, L. Vattuone, A. Gerbi, M. Rocca, and U. Valbusa. A simple and compact mechanical velocity selector of use to analyze/select molecular alignment in supersonic seeded beams. *Rev. of Sci. Inst.*, 75:349, 2004.

[19] M. N. R Ashfold and J. D. Howe. Multiphoton spectroscopy of molecular species. *Annu. Rev. Phys. Chem.*, 45:57, 1994.

[20] *Nobel Lecture in Chemistry.* http://www.nobel.se, 1999.

[21] *Nobel Lecture in Chemistry.* http://www.nobel.se, 2007.

[22] H. Eyring. The Activated Complex in Chemical Reactions. *J. Chem. Phys.*, 3:107, 1935.

[23] *Nobel Lecture in Chemistry.* http://www.nobel.se, 1992.

[24] G. L. Closs, L. T. Calcaterra, N. J. Green, K. W. Penfield, , and J. R. Miller. Distance, stereoelectronic effects, and the Marcus inverted region in intramolecular electron transfer in organic radical anions. *J. Phys. Chem.*, 90:3673, 1986.

[25] *Nobel Lecture in Chemistry.* http://www.nobel.se, 1998.

[26] G. Henkelman and H. Jónsson. A dimer method for finding saddle points on high dimensional potential surfaces using only first derivatives. *J. Chem. Phys.*, 111:7010, 1999.

[27] L. Verlet. Computer "Experiments" on Classical Fluids. *Phys. Rev.*, 159:98, 1967.

[28] M. Tanaka and M. Aida. Ab initio MO and quasi-classical direct ab initio MD studies on the nitrogen inversion of trimethylamine. *Chem. Phys. Lett.*, 417:316, 2006.

[29] A. Groß and A. Dianat. Hydrogen dissociation dynamics on precovered Pd surfaces: Langmuir is still right. *Phys. Rev. Lett.*, 98:206107, 2007.

[30] A. Groß and M. Scheffler. Ab initio quantum and molecular dynamics of the dissociative adsorption of hydrogen on Pd(100). *Phys. Rev. B*, 57:2493, 1998.

[31] B. M. Garraway and K.-A. Suominen. Wave-packet dynamics: new physics and chemistry in femto-time. *Rep. Prog. Phys.*, 58:365, 1995.

[32] M. Rieger, J. Rogal, and K. Reuter. Effect of Surface Nanostructure on Temperature Programmed Reaction Spectroscopy: First-Principles Kinetic Monte Carlo Simulations of CO Oxidation at $RuO_2(110)$. *Phys. Rev. Lett.*, 100:016105, 2008.

[33] K. A. Fichthorn and W. H. Weinberg. Theoretical foundations of dynamical Monte Carlo simulations. *J. Chem. Phys.*, 95:1090, 1991.

[34] D. Menzel and R. Gomer. Desorption from metal surfaces by low–energy electrons. *J. Chem. Phys.*, 41:3311, 1964.

[35] P. A. Redhead. Interaction of slow electrons with chemisorbed oxygen. *Can. J. Phys.*, 42:886, 1964.

[36] M. Head-Gordon and J. C. Tully. Molecular dynamics with electronic friction. *J. Chem. Phys.*, 103:10137, 1995.

[37] B. Gergen, H. Nienhaus, W. H. Weinberg, and E. W. McFarland. Chemically induced electronic excitations at metal surfaces. *Science*, 294:2521, 2001.

[38] J. T. Kindt, J. C. Tully, M. Head-Gordon, and M. A. Gomez. Electron–hole pair contribution to scattering, sticking and surface diffusion. *J. Chem. Phys.*, 109:3629, 1998.

[39] M. Bonn, S. Funk, Ch. Hess, D. N. Denzler, C. Stampfl, M. Scheffler, M. Wolf, and G. Ertl. Phonon- Versus Electron-Mediated Desorption and Oxidation of CO on Ru(0001). *Science*, 285:1042, 1999.

[40] M. Quack and J. Stohner. Influence of Parity Violating Weak Nuclear Potentials on Vibrational and Rotational Frequencies in Chiral Molecules. *Phys. Rev. Lett.*, 84:3807, 2000.

[41] J. Thyssen, J. K. Laehrdahl, and P. Schwerdtfeger. Fully Relativistic Coupled Cluster Treatment for Parity-Violating Energy Differences in Molecules. *Phys. Rev. Lett.*, 85:3105, 2000.

[42] P. Pyykko. Relativistic effects in structural chemistry. *Chem. Rev.*, 88:563, 1988.

[43] W. Kutzelnigg. *Einführung in die Theoretische Chemie*. Verlag Chemie, 1975.

[44] N. C. Handy and A. M. Lee. The adiabatic approximation. *Chem. Phys. Lett.*, 252:425, 1996.

[45] M. Born and J. R. Oppenheimer. *Ann. Physik*, 84:457, 1927.

[46] H. S. Friedrich. *Theoretical Atomic Physics*. Springer, 2005.

[47] N. W. Ashcroft and N. D. Mermin. *Festkörperphysik*. Oldenbourg, 1. edition, 2001.

[48] A. Groß. *Theoretical Surface Science*. Springer, 2003.

[49] K. R. Naqvi and W. B. Brown. The non-crossing rule in molecular quantum mechanics. *Int. J. Quantum. Chem.*, 6:271, 1972.

[50] F. T. Smith. Diabatic and adiabatic representations for atomic collision problems. *Phys. Rev.*, 179:111, 1969.

[51] C. A. Mead and D. G. Truhlar. Conditions for the definition of a strictly diabatic electronic basis for molecular systems. *J. Chem. Phys.*, 77:6090, 1982.

[52] W. Ritz. Über eine neue Methode zur Lösung gewisser Variationsprobleme der mathematischen Physik. *J. Reine Angew. Math.*, 135:1, 1909.

[53] J. C. Slater. The Theory of Complex Spectra. *Phys. Rev.*, 34:1293, 1929.

[54] J. C. Slater. A Simplification of the Hartree-Fock Method. *Phys. Rev.*, 81:385, 1951.

[55] F. Jensen. *Introduction to Computational Chemistry*. Wiley, 2002.

[56] D. Feller and E. R. Davidson. Basis Sets for Ab Initio Molecular Orbital Calculations and Intermolecular Interactions. In *Rev. Comput. Chem. Vol. 1*. 1990.

[57] J. C. Slater. Atomic Shielding Constants. *Phys. Rev.*, 36:57, 1930.

[58] S. F. Boys. *Proc. Roy. Soc. (London) A*, 200:542, 1950.

[59] F. Bloch. Über die Quantenmechanik der Elektronen in Kristallgittern. *Z. Physik*, 52:555, 1928.

[60] J. C. Grossman and L. Mitas. High Accuracy Molecular Heats of Formation and Reaction Barriers: Essential Role of Electron Correlation. *Phys. Rev. Lett.*, 79:4353, 1997.

[61] J. Pranata. The ene reaction: Comparison of results of Hartree-Fock, Møller-Plesset, CASSCF, and DFT calculations. *Int. J. Quantum. Chem.*, 62:509, 1997.

[62] R. Newton. *Scattering Theory of Waves and Particles*. Springer, 1982.

[63] V. Bach, E. H. Lieb, M. Loss, and J. P. Solovej. There are no unfilled shells in unrestricted Hartree-Fock theory. *Phys. Rev. Lett.*, 72:2981, 1994.

[64] H. Nakatsuji. Structure of the exact wave function. *J. Chem. Phys.*, 113:2949, 2000.

[65] J. C. Slater. Molecular Energy Levels and Valence Bonds. *Phys. Rev.*, 38:1109, 1931.

[66] C. Møller and M. S. Plesset. Note on an Approximation Treatment for Many-Electron Systems. *Phys. Rev.*, 46:618, 1934.

[67] C. W. Bauschlicher, Jr. and S. R. Langhoff. Full CI benchmark calculations on $N_2$, NO, and $O_2$: A comparison of methods for describing multiple bonds. *J. Chem. Phys*, 86:5595, 1987.

[68] D. L. Strout and G. E. Scuseria. A coupled-cluster study of the electron affinity of the oxygen atom. *J. Chem. Phys.*, 96:9025, 1992.

[69] C. W. Bauschlicher, Jr., S. R. Langhoff, H. Partridge, and P. R. Taylor. On the electron affinity of the oxygen atom. *J. Chem. Phys*, 85:3407, 1986.

[70] C. W. Bauschlicher, Jr. and P. R. Taylor. Benchmark full configuration-interaction calculations on $H_2O$, F, and $F^-$. *J. Chem. Phys*, 85:2779, 1986.

[71] C. W. Bauschlicher, Jr. and P. R. Taylor. Full CI studies of the collinear transition state for the reaction $F + H_2 \rightarrow HF + H$. *J. Chem. Phys*, 86:858, 1987.

[72] R. G. Parr and W. Yang. *Density-Functional Theory of Atoms and Molecules*. Oxford Science Publications, 1989.

[73] L. H. Thomas. The calculation of atomic fields. *Proc. Camb. Phil. Soc.*, 23:542, 1927. [Reprinted in March (1975)].

[74] E. Fermi. Un Metodo Statistice per la Determinazione di Alcune Proprietá dell' Atomo. *Rend. Accad.*, Lincei 6:602, 1927.

[75] P. Hohenberg and W. Kohn. Inhomogeneous Electron Gas. *Phys. Rev.*, 136:B864, 1964.

[76] W. Kohn and L. J. Sham. Self-Consistent Equations Including Exchange and Correlation Effects. *Phys. Rev.*, 140:A1133, 1965.

[77] P. A. M. Dirac. *Proc. Royal Soc. A*, 123:714, 1929.

[78] P. A. M. Dirac. Note on exchange phenomena in the Thomas atom. *Proc. Cambridge Phil. Soc.*, 26:376, 1930.

[79] C. F. von Weizäcker. *Z. Physik*, 96:431, 1935.

[80] Y. A. Wang, N. Govind, and E. A. Carter. Orbital-free kinetic-energy density functionals with a density-dependent kernel. *Phys. Rev. B*, 60:16350, 1999.

[81] Y. A. Wang, N. Govind, and E. A. Carter. Erratum: Orbital-free kinetic-energy density functionals with a density-dependent kernel [Phys. Rev. B 60, 16 350 (1999)]. *Phys. Rev. B*, 64:089903, 2001.

[82] J. F. Janak. Proof that $\partial E/\partial n_i = \epsilon_i$ in density-functional theory. *Phys. Rev. B*, 18:7165, 1978.

[83] J. T. Chayes, L. Chayes, and M. B. Ruskai. Density functional approach to quantum lattice systems. *J. Statist. Phys.*, 38:493, 1985.

[84] M. Levy. Electron densities in search of Hamiltonians. *Phys. Rev. A*, 26:1200, 1982.

[85] E. H. Lieb. Density Functionals for Coulomb Systems. *Int. J. Quantum. Chem.*, 24:243, 1983.

[86] J. P. Perdew and A. Zunger. Self-interaction correction to density-functional approximations for many-electron systems. *Phys. Rev. B*, 23:5048, 1981.

[87] M. Levy and J. P. Perdew. The constrained search formulation of density functional theory. In R. M. Dreizler and J. da Providencia, editors, *Density Functional Methods in Physics*, page 11. Plenum, New York, 1985.

[88] D. M. Ceperly and B. J. Alder. Ground state of the electron gas by a stochastic method. *Phys. Rev. Lett.*, 45:566, 1980.

[89] M. C. Payne, M. P. Teter, D. C. Allan, T. A. Arias, and J. D. Joannopoulos. Iterative minimization techniques for ab initio total-energy calculations: molecular dynamics and conjugate gradients. *Rev. Mod. Phys.*, 64:1045, 1992.

[90] C. Lee, W. Yang, and R. G. Parr. Development of the Colle-Salvetti correlation-energy formula into a functional of the electron density. *Phys. Rev. B*, 37:785, 1988.

[91] J. P. Perdew, J. A. Chevary, S. H. Vosko, K. A. Jackson, M. R. Pederson, D. J. Singh, and C. Fiolhais. Atoms, molecules, solids, and surfaces: Applications of the generalized gradient approximation for exchange and correlation. *Phys. Rev. B*, 46:6671, 1992.

[92] J. P. Perdew, K. Burke, and M. Ernzerhof. Generalized Gradient Approximation Made Simple. *Phys. Rev. Lett.*, 77:3865, 1996.

[93] B. Hammer, L. B. Hansen, and J. Nørskov. Improved adsorption energetics within density-functional theory using revised Perdew-Burke-Ernzerhof functionals. *Phys. Rev. B*, 59:7413, 1999.

[94] J. P. Perdew and K. Schmidt. In V. Van Doren, C. Van Alsenoy, and P. Geerlings, editors, *Density Functional Theory and Its Application to Materials*. Springer, 2000.

[95] A. E. Mattsson. Density Functional Theory: In Pursuit of the "Divine" Functional. *Science*, 298:759, 2002.

[96] S. Kurth, J. P. Perdew, and P. Blaha. Molecular and Solid-State Tests of Density Functional Approximations: LSD, GGAs, and Meta-GGAs. *Int. J. Quantum. Chem.*, 75:889, 1999.

[97] M. Städele, J. A. Majewski, P. Vogl, and A. Görling. Exact Kohn-Sham Exchange Potential in Semiconductors. *Phys. Rev. Lett.*, 79:2089, 1997.

[98] J. Harris. Adiabatic-connection approach to Kohn-Sham theory. *Phys. Rev. A*, 29:1648, 1984.

[99] A. D. Becke. Density-functional thermochemistry. III. The role of exact exchange. *J. Chem. Phys.*, 98:5648, 1993.

[100] J. A. Pople, M. Head-Gordon, D. J. Fox, K. Raghavachari, and L. A. Curtiss. Gaussian-1 theory: A general procedure for prediction of molecular energies. *J. Chem. Phys.*, 90:5622, 1989.

[101] L. A. Curtiss, C. Jones, G. W. Trucks, K. Raghavachari, and J. A. Pople. Gaussian-1 theory of molecular energies for second-row compounds. *J. Chem. Phys.*, 93:2537, 1990.

[102] C. Adamo and V. Barone. Toward reliable density functional methods without adjustable parameters: The PBE0 model. *J. Chem. Phys.*, 110:6158, 1999.

[103] J. Paier, M. Marsman, and G. Kresse. Why does the B3LYP hybrid functional fail for metals? *J. Chem. Phys.*, 127:024103, 2007.

[104] J. Harl and G. Kresse. Cohesive energy curves for noble gas solids calculated by adiabatic connection fluctuation-dissipation theory. *Phys. Rev. B*, 77:045136, 2008.

[105] I. Frank, J. Hutter, D. Marx, and M. Parrinello. Molecular dynamics in low-spin excited states. *J. Chem. Phys.*, 108:4060, 1998.

[106] M. Filatov and S. Shaik. Application of spin-restricted open-shell Kohn-Sham method to atomic and molecular multiplet states. *J. Chem. Phys.*, 110:116, 1999.

[107] S. Grimme and M. Waletzke. A combination of Kohn-Sham density functional theory and multi-reference configuration interaction methods. *J. Chem. Phys.*, 111:5645, 1999.

[108] J. Gräfenstein and D. Cremer. Can density functional theory describe multi-reference systems? Investigations of carbenes and organic biradicals. *Phys. Chem. Chem. Phys.*, 2000:2091, 2000.

[109] L. V. Slipchenko and A. I. Krylov. Singlet-triplet gaps in diradicals by the spin-flip approach: A benchmark study. *J. Chem. Phys.*, 117:4694, 2002.

[110] M. Rohlfing. Excited electronic states and optical spectra of solids, surfaces and molecules. Habilitationsschrift, Mathematisch-Naturwissenschaftliche Fakultät der Westfälischen Wilhelms-Universität Münster, 2000.

[111] M. Rohlfing and S. G. Louie. Excitons and optical spectrum of the Si(111)-(2x1) surface. *Phys. Rev. Lett.*, 83:856, 1999.

[112] J.C. Grossmann, M. Rohlfing, L. Mitas, S. G. Louie, and M. L. Cohen. High accuracy many–body calculation approaches for excitation in molecules. *Phys. Rev. Lett.*, 86:472, 2001.

[113] P. Rinke, A. Qteish, J. Neugebauer, C. Freysoldt, and M. Scheffler. Combining GW calculations with exact-exchange density-functional theory: an analysis of valence-band photoemission for compound semiconductors. *New J. Phys.*, 7:126, 2005.

[114] A. Qteish, P. Rinke, M. Scheffler, and J. Neugebauer. Exact-exchange-based quasiparticle energy calculations for the band gap, effective masses, and deformation potentials of ScN. *Phys. Rev. B*, 74:245208, 2006.

[115] E. K. U. Gross, J. F. Dobson, and M. Petersilka. In R. F. Nalewajski, editor, *Topics in Current Chemistry: Density Functional Theory II*, page 81. Springer, Berlin, 1996.

[116] M. Lindenblatt and E. Pehlke. Ab Initio Simulation of the Spin Transition during Chemisorption: H/Al(111). *Phys. Rev. Lett.*, 97:216101, 2006.

[117] M. E. Casida, C. Jamorski, K. C. Casida, and D. R. Salahub. Molecular excitation energies to high-lying bound states from time-dependent density-functional response theory: Characterization and correction of the time-dependent local density approximation ionization threshold. *J. Chem. Phys.*, 108:4439, 1998.

[118] S. T. Epstein, A. C. Hurley, R. E. Wyatt, and R. G. Parr. Integrated and Integral Hellmann—Feynman Formulas. *J. Chem. Phys.*, 47:1275, 1967.

[119] P. Pulay. Ab initio calculation of force constants and equilibrium geometries in polyatomic molecules. *Mol. Phys.*, 17:197, 1969.

[120] W. H. Press, B. P. Flannery, S. A. Teukolsky, and W. T. Vetterling. *Numerical Recipes: The Art of Scientific Computing*. Cambridge University Press, Cambridge (UK) and New York, 2nd edition, 1992.

[121] H. F. Busnengo, A. Salin, and W. Dong. Representation of the 6D potential energy surface for a diatomic molecule near a solid surface. *J. Chem. Phys.*, 112:7641, 2000.

[122] Thomas B. Blank, Steven D. Brown, August W. Calhoun, and Douglas J. Doren. Neural network models of potential energy surfaces. *J. Chem. Phys.*, 103:4129, 1995.

[123] W. S. McCulloch and W. Pitts. A logical calculus of the ideas immanent in nervous activity. *Bull. Math. Biophys.*, 5:115, 1943.

[124] F. Rosenblatt. The perceptron: A probabilistic model for information storage and organization in the brain. *Psychol. Rev.*, 65:386, 1958.

[125] J. Behler, S. Lorenz, and K. Reuter. Representing molecule-surface interactions with symmetry-adapted neural networks. *J. Chem. Phys.*, 127:014705, 2007.

[126] Y. LeCun and L. Botton and G. B. Orr and K.-R. Müller. *Efficient BackProp*, volume 1524 of *Lecture Notes in Computer Science*. Springer, 1998.

[127] G. B. Orr and K.-R. Müller, editors. volume 1524 of *Lecture Notes in Computer Science*. Springer, 1998.

[128] S. Lorenz, A. Groß, and M. Scheffler. Representing high-dimensional potential-energy surfaces for reactions at surfaces by neural networks. *Chem. Phys. Lett.*, 395:210, 2004.

[129] J. Behler and M. Parrinello. Generalized Neural-Network Representation of High-Dimensional Potential-Energy Surfaces. *Phys. Rev. Lett.*, 98:146401, 2007.

[130] D. W. Heermann. *Computer simulation methods in theoretical physics*. Springer, 1986.

[131] K.Y. Sanbonmatsu and C.-S. Tung. High performance computing in biology: Multimillion atom simulations of nanoscale systems. *J. Struct. Biol.*, 157:470, 2007.

[132] D. L. Ensigna, P. M. Kassona, and V. S. Pande. Heterogeneity Even at the Speed Limit of Folding: Large-scale Molecular Dynamics Study of a Fast-folding Variant of the Villin Headpiece. *J. Mol. Biol.*, 374:806, 2007.

[133] G. C. Schatz. Quantum Effects in Gas Phase Bimolecular Chemical Reactions. *Annu. Rev. Phys. Chem.*, 39:317, 1988.

[134] A. Groß and M. Scheffler. Role of zero-point effects in catalytic reactions involving hydrogen. *J. Vac. Sci. Technol. A*, 15:1624, 1997.

[135] R. E. Tuzun, B. G. Sumpter, and D. W. Noid. On the correspondence between classical and quantum mechanics in macromolecular systems: Too much classical chaos. *Macromol. Theory Simul.*, 7:203, 1998.

[136] W. Heisenberg. Über den anschaulichen Inhalt der quantentheoretischen Kinematik und Mechanik. *Z. Physik*, 43:172, 1927.

[137] W. Brenig, T. Brunner, A. Groß, and R. Russ. Numerically stable solution of coupled channel equations: The local reflection matrix. *Z. Phys. B.*, 93:91, 1993.

[138] W. Brenig and R. Russ. Numerically stable solution of coupled channel equations: The local transmission matrix. *Surf. Sci.*, 315:195, 1994.

[139] W. Brenig A. Groß and R. Russ. Numerically stable solution of coupled channel equations: The wave-function. *Z. Phys. B.*, 97:311, 1995.

[140] M. F. Herman. Generalization of the geometric optical series approach for nonadiabatic scattering problems. *J. Chem. Phys.*, 76:2949, 1982.

[141] M. F. Herman. Nonadiabatic semiclassical scattering. I. Analysis of generalized surface hopping procedures. *J. Chem. Phys.*, 81:754, 1984.

[142] F. Schwabl. *Quantenmechanik*. Springer, 5. edition, 1998.

[143] J. A. Fleck, Jr., J. R. Morris, and M. D. Feit. Time-dependent propagation of high energy laser beams through the atmosphere. *Appl. Phys.*, 10:129, 1976.

[144] M. D. Feit, J. A. Fleck, Jr., and A. Steiger. Solution of the Schrödinger equation by a spectral method. *J. Comput. Phys.*, 47:412, 1982.

[145] T. Klüner, H.-J. Freund, V. Staemmler, and R. Kosloff. Theoretical Investigation of Laser Induced Desorption of Small Molecules from Oxide Surfaces: A First Principles Study. *Phys. Rev. Lett.*, 80:5208, 1998.

[146] I. Mehdaoui, D. Kröner, M. Pykavy, H.-J. Freund, and T. Klüner. Photo-induced desorption of NO from NiO(100): calculation of the four-dimensional potential energy surfaces and systematic wave packet studies. *Phys. Chem. Chem. Phys.*, 8:1584, 2006.

[147] A. Groß, S. Wilke, and M. Scheffler. Six-Dimensional Quantum Dynamics of Adsorption and Desorption of $H_2$ at Pd(100): Steering and Steric Effects. *Phys. Rev. Lett.*, 75:2718, 1995.

[148] C. Bach. Semiklassische Behandlung nichtadiabaischer Prozesse an Oberflächen, 2000. Diploma thesis at the Technische Universität München.

[149] C. Bach. *Simulation of nonadiabatic processes on surfaces*. PhD thesis, Technische Universität München, 2004.

[150] A. G. Redfield. *Adv. Mag. Res.*, 1:1, 1965.

[151] J. M. Jean, R. A. Friesner, and G. R. Fleming. Application of a multilevel Redfield theory to electron transfer in condensed phases. *J. Chem. Phys.*, 96:5827, 1992.

[152] N. F. Mott. *Proc. Cambridge Philos. Soc.*, 27:553, 1931.

[153] E. E. Nikitin. *Theory of Elementary Atomic and Molecular Processes in Gases*. Clarendon, Oxford, 1974.

[154] J. C. Tully. *Modern Methods for Multidimensional Dynamics Computation in Chemistry*. World Scientific, Singapore, 1998.

[155] A. Messiah. *Quantum Mechanics*. John Wiley, New York, 1962.

[156] C. C. Martens and J.-Y. Fang. Semiclassical-limit molecular dynamics on multiple electronic surfaces. *J. Chem. Phys.*, 106:4918, 1997.

[157] J. C. Tully and R. K. Preston. Trajectory Surface Hopping Approach to Nonadiabatic Molecular Collisions: The Reaction of $H^+$ with $D_2$. *J. Chem. Phys.*, 55:562, 1971.

[158] J. R. Stine and J. T. Muckerman. On the multidimensional surface intersection problem and classical trajectory "surface hopping". *J. Chem. Phys.*, 65:3975, 1976.

[159] N. C. Blais and D. G. Truhlar. Trajectory-surface-hopping study of Na(3p $^2$P) +$H_2$ $\rightarrow$ Na(3s $^2$S)+$H_2$($\nu$', $j$', $\theta$). *J. Chem. Phys.*, 79:1334, 1983.

[160] G. Parlant and E. A. Gislason. An exact trajectory surface hopping procedure: Comparison with exact quantal calculations. *J. Chem. Phys.*, 91:4416, 1989.

[161] P. J. Kuntz. Classical path surface-hopping dynamics. I. General theory and illustrative trajectories. *J. Chem. Phys.*, 95:141, 1991.

[162] F. Webster, P.J. Rossky, and R.A. Friesner. Nonadiabatic processes in condensed matter: semi-classical theory and implementation. *Comp. Phys. Comm.*, 63:494, 1991.

[163] I. H. Gersonde and H. Gabriel. Molecular dynamics of photodissociation in matrices including nonadiabatic processes. *J. Chem. Phys.*, 98:2094, 1993.

[164] D. F. Coker and L. Xiao. Methods for molecular dynamics with nonadiabatic transitions. *J. Chem. Phys.*, 102:496, 1995.

[165] A. I. Krylov, R. B. Gerber, and R. D. Coalson. Nonadiabatic dynamics and electronic energy relaxation of Cl($^2$P) atoms in solid Ar. *J. Chem. Phys.*, 105:4626, 1996.

[166] U. Müller and G. Stock. Surface-hopping modeling of photoinduced relaxation dynamics on coupled potential-energy surfaces. *J. Chem. Phys.*, 107:6230, 1997.

[167] N. Metropolis, A. Rosenbluth, M. Rosenbluth, A. Teller, and E. Teller. Equation of State Calculations by Fast Computing Machines. *J. Chem. Phys.*, 21:1087, 1953.

[168] C. Carbogno. Gemischt quantenmechanisch-klassische Beschreibung von elektronisch nichtadiabatischen Reaktionen an Oberflächen, 2004. Diploma thesis at the Technische Universität München.

[169] Tillmann Klamroth and Peter Saalfrank. Effect of substrate vibrations on the sticking of atoms at surfaces: A critical comparison of different propagation methods for the H/Cu(100) system. *J. Chem. Phys.*, 112:10571, 2000.

[170] A. Groß and C. Bach. Semiclassical treatment of charge transfer in molecule-surface scattering. *J. Chem. Phys.*, 114:6396, 2001.

[171] E. Wigner. *Nachr. Ges. Wiss. Goett., Math.-Phys. Kl.*, page 375, 1927.

[172] F. Hund. *Z. Phys.*, 33:345, 1925.

[173] H. Haken and H. C. Wolf. *Atom- und Quantenphysik: Einführung in die experimentellen und theoretischen Grundlagen.* Springer, 5. edition, 1993.

[174] C. Schweitzer and R. Schmidt. Physical Mechanisms of Generation and Deactivation of Singlet Oxygen. *Chem. Rev.*, 103:1685, 2003.

[175] H.-J. Werner, P. J. Knowles, R. Lindh, F. R. Manby, M. Schütz, P. Celani, T. Korona, G. Rauhut, R. D. Amos, A. Bernhardsson, A. Berning, D. L. Cooper, M. J. O. Deegan, A. J. Dobbyn, F. Eckert, C. Hampel, G. Hetzer, A. W. Lloyd, S. J. McNicholas, W. Meyer, M. E. Mura, A. Nicklass, P. Palmieri, R. Pitzer, U. Schumann, H. Stoll, A. J. Stone, R. Tarroni, and T. Thorsteinsson. MOLPRO, version 2006.1, a package of ab initio programs, 2006. see http://www.molpro.net.

[176] T. H. Dunning, Jr. Gaussian Basis Sets for Use in Correlated Molecular Calculations. I. The Atoms Boron through Neon and Hydrogen. *J. Chem. Phys.*, 90:1007, 1989.

[177] R. A. Kendall, T. H. Dunning, Jr., and R. J. Harrison. Electron Affinities of the First-Row Atoms Revisited. Systematic Basis Sets and Wave Functions. *J. Chem. Phys.*, 96:6796, 1992.

[178] D. E. Woon and T. H. Dunning, Jr. Gaussian basis sets for use in correlated molecular calculations. V. Core-valence basis sets for boron through neon. *J. Chem. Phys.*, 103:4572, 1995.

[179] A. K. Wilson, T. van Mourik, and T. H. Dunning, Jr. Gaussian basis sets for use in correlated molecular calculations. VI. Sextuple-zeta correlation-consistent sets for boron through neon. *J. Mol. Struc. (Theochem)*, 388:339, 1996.

[180] T. van Mourik, A.K. Wilson, and T.H. Dunning, Jr. Benchmark calculations with correlated molecular wavefunctions. XIII. Potential energy curves for He2, Ne2 and Ar2 using correlation consistent basis sets through augmented sextuple zeta. *Mol. Phys.*, 99:529, 1999.

[181] P. M. Morse. Diatomic Molecules According to the Wave Mechanics. II. Vibrational Levels. *Phys. Rev.*, 34:57, 1929.

[182] Y. Scribano and D. M. Benoit. Iterative active-space selection for vibrational configuration interaction calculations using a reduced-coupling VSCF basis. *Chem. Phys. Lett.*, 458:384, 2008.

[183] N. H. F. Beebe, E. W. Thulstrup, and A. Andersen. Configuration interaction calculations of low-lying electronic states of $O_2$, $O_2^+$, and $O_2^{2+}$. *J. Chem. Phys.*, 64:2080, 1976.

[184] G. Herzberg. *Molecular Spectra and Molecular Structure, I. Spectra of Diatomic Molecules*. van Nostrand Reinhold Company, New York, 1950.

[185] W. J. Hehre, L. Radom, P. v. R. Schleyer, and J. A. Pople. *Ab Initio Molecular Orbital Theory*. Wiley, New York, 1986.

[186] B. G. Johnson, P. M. W. Gill, and J. A. Pople. The performance of a family of density functional methods. *J. Chem. Phys.*, 98:5612, 1993.

[187] R. P. Saxon and B. Liu. Ab initio configuration interaction study of the valence states of $O_2$. *J. Chem. Phys.*, 67:5432, 1977.

[188] B. F. Minaev and V. A. Minaeva. MCSCF response calculations of the excited states properties of the $O_2$ molecule and a part of its spectrum. *Phys. Chem. Chem. Phys.*, 3:720, 2001.

[189] H. Partridge, Jr. C. W. Bauschlicher, S. R. Langhoff, and P. R. Taylor. Theoretical study of the low-lying bound states of $O_2$. *J. Chem. Phys.*, 95:8292, 1991.

[190] A. Badinski. Electronic correlation calculations of small molecules with quantum monte carlo methods, 2004. Diploma thesis at the Technische Universität Berlin.

[191] G. Herzberg. *Can. J. Phys.*, 30:185, 1952.

[192] Ed. R. C. Weast. *CRC Handbook of Chemistry and Physics (67th ed.)*. CRC Press, 1987.

[193] D. Feller and K. A. Peterson. Re-examination of atomization energies for the Gaussian-2 set of molecules. *J. Chem. Phys.*, 110:8384, 1999.

[194] J. C. Grossman. Benchmark quantum Monte Carlo calculations. *J. Chem. Phys.*, 117:1434, 2002.

[195] J. A. Pople, M. Head-Gordon, and K. Raghavachari. Quadratic configuration interaction. A general technique for determining electron correlation energies. *J. Chem. Phys.*, 87:5968, 1987.

[196] P. Krupenie. *J. Phys. Chem. Ref. Data*, 1:423, 1972.

[197] B. J. Moss, F. W. Bobrowicz, and W. A. Goddard III. The generalized valence bond description of $O_2$. *J. Chem. Phys.*, 63:4632, 1975.

[198] K. Yamaguchi, F. Jensen, A. Dorigo, and K. N. Houk. A spin correction procedure for unrestricted Hartree-Fock and Møller-Plesset wavefunctions for singlet diradicals and polyradicals. *Chem. Phys. Lett.*, 149:537, 1988.

[199] M. J. Frisch, G. W. Trucks, H. B. Schlegel, G. E. Scuseria, M. A. Robb, J. R. Cheeseman, J. A. Montgomery, Jr., T. Vreven, K. N. Kudin, J. C. Burant, J. M. Millam, S. S. Iyengar, J. Tomasi, V. Barone, B. Mennucci, M. Cossi, G. Scalmani, N. Rega, G. A. Petersson, H. Nakatsuji, M. Hada, M. Ehara, K. Toyota, R. Fukuda, J. Hasegawa, M. Ishida, T. Nakajima, Y. Honda, O. Kitao, H. Nakai, M. Klene, X. Li, J. E. Knox, H. P. Hratchian, J. B. Cross, V. Bakken, C. Adamo, J. Jaramillo, R. Gomperts, R. E. Stratmann, O. Yazyev, A. J. Austin, R. Cammi, C. Pomelli, J. W. Ochterski, P. Y. Ayala, K. Morokuma, G. A. Voth, P. Salvador, J. J. Dannenberg, V. G. Zakrzewski, S. Dapprich, A. D. Daniels, M. C. Strain, O. Farkas, D. K. Malick, A. D. Rabuck, K. Raghavachari, J. B. Foresman, J. V. Ortiz, Q. Cui, A. G. Baboul, S. Clifford, J. Cioslowski, B. B. Stefanov, G. Liu, A. Liashenko, P. Piskorz, I. Komaromi, R. L. Martin, D. J. Fox, T. Keith, M. A. Al-Laham, C. Y. Peng, A. Nanayakkara, M. Challacombe, P. M. W. Gill, B. Johnson, W. Chen, M. W. Wong, C. Gonzalez, and J. A. Pople. Gaussian 03, Revision D.01. Gaussian, Inc., Wallingford, CT, 2004.

[200] J. S. Andrews, D. Jayatilaka, R. G. A. Bone, N. C. Handy, and R. D. Amos. Spin contamination in single-determinant wavefunctions. *Chem. Phys. Lett.*, 183:423, 1991.

[201] K. J. Ritter and T. D. Wilkerson. High-resolution spectroscopy of the oxygen A band. *J. Mol. Spectrosc.*, 121:1, 1987.

[202] M. Kasha. In A. A. Frimer, editor, *Singlet Oxygen*, page 1. CRC Press: Boca Raton, 1985.

[203] P. A. M. Dirac. The Quantum Theory of the Electron. *Proc. Royal Soc. A*, 117:631, 1928.

[204] P. A. M. Dirac. A Theory of Electrons and Protons. *Proc. Royal Soc. A*, 126:360, 1929.

[205] G. Breit. The Effect of Retardation on the Interaction of Two Electrons. *Phys. Rev.*, 34:553, 1929.

[206] F. A. Parpia, C. Froese Fischer, and I. P. Grant. GRASP92: A package for large-scale relativistic atomic structure calculations. *Comput. Phys. Commun.*, 94:249, 1996.

[207] E. Engel, S. Keller, A. F. Bonetti, H. Müller, and R. M. Dreizler. Local and nonlocal relativistic exchange-correlation energy functionals: Comparison to relativistic optimized-potential-model results. *Phys. Rev. A*, 52:2750, 1995.

[208] A. Berning, M. Schweizer, H.-J. Werner, P. J. Knowles, and P. Palmieri. Spin-orbit matrix elements for internally contracted multireference configuration interaction wavefunctions. *Mol. Phys.*, 98:1823, 2000.

[209] H. A. Bethe and E. E. Salpeter. *Quantum Mechanics of One- and Two-Electron Atoms*. Berlin: Springer Verlag, 1957.

[210] S. R. Langhoff and C. W. Kern. *Modern Theoretical Chemistry*, volume 3. New York: Plenum Press, 1977.

[211] F. Schwabl. *Quantenmechanik für Fortgeschrittene*. Springer, 2. edition, 2000.

[212] L. L. Foldy and S. A. Wouthuysen. On the Dirac Theory of Spin 1/2 Particles and Its Non-Relativistic Limit. *Phys. Rev.*, 78:29, 1950.

[213] R. Klotz, C. M. Marian, S. D. Peyerimhoff, B. A. Hess, and R. J. Buenker. Calculation of spin-forbidden radiative transitions using correlated wavefunctions: Lifetimes of $b^1\Sigma^+$, $a^1\Delta$ states in $O_2$, $S_2$ and SO. *Chem. Phys.*, 89:223, 1984.

[214] B. M., O. Vahtras, and H. Ågren. Magnetic phosphorescence of molecular oxygen. A study of the $b^1\Sigma_g^+ - X^3\Sigma_g^-$-transition probability using multiconfiguration response theory. *Chem. Phys.*, 208:299, 1996.

[215] B. F. Minaev. Intensities of spin-forbidden transitions in molecular oxygen and selective heavy-atom effects. *Int. J. of Quant. Chem.*, 17:367, 1980.

[216] R. Klotz and S. D. Peyerimhoff. Theoretical study of the intensity of the spin- or dipole forbidden transitions between the $c^1\Sigma_u^-$, $A'^3\Delta_u$, $A^3\Delta_u$ and $X^3\Sigma_g^-$, $a^1\Delta_g$, $b^1\Sigma_g$ states in $O_2$. *Mol. Phys.*, 57:573, 1986.

[217] B. F. Minaev and H. Ågren. Collision-induced $b^1\Sigma_g^+ - a^1\Delta_g$, $b^1\Sigma_g^+ - X^3\Sigma_g^-$ and $a^1\Delta_g - X^3\Sigma_g^-$ transition probabilities in molecular oxygen. *J. Chem. Soc., Faraday Trans.*, 93:2231, 1997.

[218] O. Spalek, J. Kodymova, P. Stopka, and I. Micek. Experimental verification of the Einstein A-coefficient used for evaluation of $O_2(^1\Delta_g)$ concentration in the chemical oxygen-iodine laser. *J. Phys. B: At., Mol., Opt. Phys.*, 32:1885, 1999.

[219] R. M. Badger, A. C. Wright, and R. F. Whitlock. Absolute Intensities of the Discrete and Continuous Absorption Bands of Oxygen Gas at 1.26 and 1.065 $\mu$ and the Radiative Lifetime of the $^1\Delta_g$ State of Oxygen. *J. Chem. Phys.*, 43:4345, 1965.

[220] U. von Barth and L. Hedin. A local exchange-correlation potential for the spin polarized case: I. *J. Phys. C*, 5:1629, 1972.

[221] M. M. Pant and A. K. Rajagopal. Theory of inhomogeneous magnetic electron gas. *Solid State Commun.*, 10:1157, 1972.

[222] O. Gunnarsson and R. O. Jones. Extensions of the LSD approximation in density functional calculations. *J. Chem. Phys.*, 72:5357, 1980.

[223] A. A. Ovchinnikov and J. K. Labanowski. Simple spin correction of unrestricted density-functional calculation. *Phys. Rev. A*, 53:3946, 1996.

[224] J. M. Wittbrodt and H. B. Schlegel. Some reasons not to use spin projected density functional theory. *J. Chem. Phys.*, 105:6574, 1996.

[225] R. K. Nesbet. Fractional occupation numbers in density-functional theory. *Phys. Rev. A*, 56:2665, 1997.

[226] J. R. Schmidt, N. Shenvi, and J. C. Tully. Controlling spin contamination using constrained density functional theory. *J. Chem. Phys.*, 129:114110, 2008.

[227] G. Kresse and J. Furthmüller. Efficient iterative schemes for ab initio total-energy calculations using a plane-wave basis set. *Phys. Rev. B*, 54:11169, 1996.

[228] G. Kresse and J. Furthmüller. *VASP the GUIDE*. 2007. see http://cms.mpi.univie.ac.at/vasp.

[229] H. Nyquist. Certain topics in telegraph transmission theory. *Trans. Amer. Inst. Elect. Eng.*, 47:617, 1928.

[230] J. C. Phillips and L. Kleinman. New Method for Calculating Wave Functions in Crystals and Molecules. *Phys. Rev.*, 116:287, 1959.

[231] G. B. Bachelet, D. R. Hamann, and M. Schlüter. Pseudopotentials that work: From H to Pu. *Phys. Rev. B*, 26:4199, 1982.

[232] N. Troullier and J. L. Martins. Efficient pseudopotentials for plane-wave calculations. *Phys. Rev. B*, 43:1993, 1991.

[233] N. Troullier and J. L. Martins. Efficient pseudopotentials for plane-wave calculations. II. Operators for fast iterative diagonalization. *Phys. Rev. B*, 43:8861, 1991.

[234] P. E. Blöchl. Projector augmented-wave method. *Phys. Rev. B*, 50:17953, 1994.

[235] D. Vanderbilt. Soft self-consistent pseudopotentials in a generalized eigenvalue formalism. *Phys. Rev. B*, 41:7892, 1990.

[236] H. J. Monkhorst and J. D. Pack. Special points for Brillouin-zone integrations. *Phys. Rev. B*, 13:5188, 1976.

[237] N. D. Mermin. Thermal Properties of the Inhomogeneous Electron Gas. *Phys. Rev.*, 137:A1441, 1965.

[238] S. H. Vosko, L. Wilk, and M. Nusair. *Can. J. Phys.*, 58:1200, 1980.

[239] G. L. Oliver and J. P. Perdew. Spin-density gradient expansion for the kinetic energy. *Phys. Rev. A*, 20:397, 1979.

[240] A. D. Becke. Density functional calculations of molecular bond energies. *J. Chem. Phys.*, 84:4524, 1986.

[241] E. H. Lieb and S. Oxford. Improved lower bound on the indirect Coulomb energy. *Int. J. Quantum Chem.*, 19:427, 1981.

[242] Y. Zhang and W. Yang. Comment on "Generalized Gradient Approximation Made Simple". *Phys. Rev. Lett.*, 80:890, 1998.

[243] E. Engel and S. H. Vosko. Accurate optimized-potential-model solutions for spherical spin-polarized atoms: Evidence for limitations of the exchange-only local spin-density and generalized-gradient approximations. *Phys. Rev. A*, 47:2800, 1993.

[244] B. Delley. Analytic energy derivatives in the numerical local-density-functional approach. *J. Chem. Phys.*, 94:7245, 1991.

[245] J. Andzelm and E. Wimmer. Density functional Gaussian-type-orbital approach to molecular geometries, vibrations, and reaction energies. *J. Chem. Phys.*, 96:1280, 1992.

[246] J. Behler. *Dissociation of Oxygen Molecules on the Al(111) Surface*. PhD thesis, Technische Universität Berlin, 2004.

[247] M. V. Ganduglia-Pirovano and M. Scheffler. Structural and electronic properties of chemisorbed oxygen on Rh(111). *Phys. Rev. B*, 59:15533, 1999.

[248] L. A. Curtiss, K. Raghavachari, P. C. Redfern, and J. A. Pople. Assessment of Gaussian-2 and density functional theories for the computation of enthalpies of formation. *J. Chem. Phys.*, 106:1063, 1997.

[249] Aron J. Cohen, Paula Mori-Sánchez, and Weitao Yang. Fractional spins and static correlation error in density functional theory. *J. Chem. Phys.*, 129:121104, 2008.

[250] A. J. Cohen, P. Mori-Sánchez, and W. Yang. Insights into Current Limitations of Density Functional Theory. *Science*, 321:792, 2008.

[251] P. Mori-Sánchez, A. J. Cohen, and W. Yang. Discontinuous Nature of the Exchange-Correlation Functional in Strongly Correlated Systems. *Phys. Rev. Lett.*, 102:066403, 2009.

[252] S.-P. Chan, G. Chen, X. G. Gong, and Z.-F. Liu. Oxidation of Carbon Nanotubes by Singlet $O_2$. *Phys. Rev. Lett.*, 90:086403, 2003.

[253] D. C. Sorescu, K. D. Jordan, and P. Avouris. Theoretical Study of Oxygen Adsorption on Graphite and the (8,0) Single-walled Carbon Nanotube. *J. Phys. Chem. B*, 105:11227, 2001.

[254] N. Cabrera and N. F. Mott. Theory of the oxidation of metals. *Rep. Prog. Phys.*, 12:163, 1949.

[255] H. Brune, J. Wintterlin, R. J. Behm, and G. Ertl. Surface Migration of "hot" adatoms in the course of dissociative chemisorption of oxygen on Al(111). *Phys. Rev. Lett.*, 68:624, 1992.

[256] L. C. Ciacchi and M. C. Payne. "Hot-Atom" $O_2$ Dissociation and Oxide Nucleation on Al(111). *Phys. Rev. Lett.*, 92:176104, 2004.

[257] A. J. Komrowski, J. Z. Sexton, A. C. Kummel, M. Binetti, O. Weiße, and E. Hasselbrink. Oxygen Abstraction from Dioxygen on the Al(111) Surface. *Phys. Rev. Lett.*, 87:246103, 2001.

[258] M. Schmid, G. Leonardelli, R. Tscheließnig, A. Biedermann, and P. Varga. Oxygen adsorption on Al(111): low transient mobility. *Surf. Sci.*, 478:L355, 2001.

[259] P. O. Gartland. Adsorption of oxygen on clean single crystal faces of aluminium. *Surf. Sci.*, 62:183, 1977.

[260] Joachim Ankerhold and Hermann Grabert. Enhancement of Macroscopic Quantum Tunneling by Landau-Zener Transitions. *Phys. Rev. Lett.*, 91:016803, 2003.

[261] G. Ithier, E. Collin, P. Joyez, D. Vion, D. Esteve, J. Ankerhold, and H. Grabert. Zener Enhancement of Quantum Tunneling in a Two-Level Superconducting Circuit. *Phys. Rev. Lett.*, 94:057004, 2005.

[262] C. Mosch, C. Koukounas, N. Bacalis, A. Metropoulos, A. Groß, and A. Mavridis. Interaction of Dioxygen with Al Clusters and Al(111): A Comparative Theoretical Study. *J. Phys. Chem. C*, 112:6924, 2008.

[263] B. Delley. An all-electron numerical method for solving the local density functional for polyatomic molecules. *J. Chem. Phys.*, 92:508, 1990.

[264] B. Delley. From molecules to solids with the $DMol^3$ approach. *J. Chem. Phys.*, 113:7756, 2000.

[265] R. S. Mulliken. Electronic Population Analysis on LCAO[Single Bond]MO Molecular Wave Functions. I. *J. Chem. Phys.*, 23:1833, 1955.

[266] F. L. Hirshfeld. Bonded-atom fragments for describing molecular charge densities. *Theor. Chim. Acta*, 44:129, 1977.

[267] N. L. Doltsinis and D. Marx. Nonadiabatic Car-Parrinello Molecular Dynamics. *Phys. Rev. Lett.*, 88:166402, 2002.

[268] A. C. Hindmarsh. ODEPACK, A Systematized Collection of ODE Solvers. In R. S. Stepleman et al., editor, *Scientific Computing*, page 55. 1983.

[269] L. R. Petzold. Automatic Selection of Methods for Solving Stiff and Nonstiff Systems of Ordinary Differential Equations. *Siam J. Sci. Stat. Comput.*, 4:136, 1983.

[270] G. Henkelman, B. P. Uberuaga, and H. Jónsson. A climbing image nudged elastic band method for finding saddle points and minimum energy paths. *J. Chem. Phys.*, 113:9901, 2000.

[271] G. Henkelman and H. Jónsson. Improved tangent estimate in the nudged elastic band method for finding minimum energy paths and saddle points. *J. Chem. Phys.*, 113:9978, 2000.

[272] A. Gross and M. Scheffler. Influence of molecular vibrations on dissociative adsorption. *Chem. Phys. Lett.*, 256:417, 1996.

[273] D. C. Patton and M. R. Pederson. Application of the generalized-gradient approximation to rare-gas dimers. *Phys. Rev. A*, 56:R2495, 1997.

[274] D. A. King and M. G. Wells. Molecular beam investigation of adsorption kinetics on bulk metal targets: Nitrogen on tungsten. *Surf. Sci.*, 29:454, 1972.

[275] T. Fort Jr. and R. L. Wells. Adsorption of water on clean aluminum by measurement of work function changes. *Surf. Sci.*, 32:543, 1972.

[276] R. L. Wells and T. Fort Jr. Interaction of oxygen with clean aluminum surfaces by measurement of work function changes. *Surf. Sci.*, 33:172, 1972.

[277] A. A. Krasnovsky. *Jr. Biofizika*, 21:748, 1976.

[278] R. Burgert, H. Schnöckel, A. Grubisic, X. Li, S. T. Stokes, K. H. Bowen, G. F. Ganteför, B. Kiran, and P. Jena. Spin Conservation Accounts for Aluminum Cluster Anion Reactivity Pattern with $O_2$. *Science*, 319:438, 2008.

[279] M. Methfessel and A. T. Paxton. High-precision sampling for Brillouin-zone integration in metals. *Phys. Rev. B*, 40:3616, 1989.

[280] Michael Dohle, Peter Saalfrank, and T. Uzer. Dissociative sticking of diatomic molecules on cold, non-rigid surfaces: comparison of quantal and semiclassical surface oscillator models. *Surf. Sci.*, 409:37, 1998.

[281] C. Bach, T. Klüner, and A. Groß. Simulation of laser induced desorption of NO from NiO(100). *Chem. Phys. Lett.*, 376:424, 2003.

[282] M. Hand and J. Harris. Recoil effects in surface dissociation. *J. Chem. Phys.*, 92:7610, 1990.

[283] A. Groß and W. Brenig. Adiabatic versus non-adiabatic effects in the vibrational excitation in NO/Ag scattering. *Chem. Phys.*, 177:497, 1993.

[284] A. Groß and W. Brenig. Vibrational excitation in the scattering from an almost rigid surface: NO/diamond(110). *Surf. Sci.*, 302:403, 1994.

[285] I. Newton. *Philosophiae Naturalis Principia Mathematica*. Royal Society, 1687.

[286] I. P. Batra and L. Kleinman. Chemisorption of oxygen on aluminum surfaces. *J. Elec. Spec.*, 33:175, 1984.

[287] H. Brune, J. Wintterlin, J. Trost, G. Ertl, J. Wiechers, and R. J. Behm. Interaction of oxygen with Al(111) studied by scanning tunneling microscopy. *J. Chem. Phys.*, 99:2128, 1993.

[288] C. Engdahl and G. Wahnström. Transient hyperthermal diffusion following dissociative chemisorption: a molecular dynamics study. *Surf. Sci.*, 312:429, 1994.

[289] G. Wahnström, A. B. Lee, and J. Strömquist. Motion of "hot" oxygen adatoms on corrugated metal surfaces. *J. Chem. Phys.*, 105:326, 1996.

[290] A. Hellman, B. Razaznejad, and B. I. Lundqvist. Trends in sticking and adsorption of diatomic molecules on the Al(111) surface. *Phys. Rev. B*, 71:205424, 2005.

[291] M. Barbatti, G. Granucci, M. Persico, M. Ruckenbauer, M. Vazdar, M. Eckert-Maksic, and H. Lischka. The on-the-fly surface-hopping program system Newton-X: Application to ab initio simulation of the nonadiabatic photodynamics of benchmark systems. *J. Photochem. Photobio. A*, 190:228, 2007.

[292] M. Barbatti, G. Granucci, M. Ruckenbauer, J. Pittner, M. Persico, and H. Lischka. NEWTON-X: a package for Newtonian dynamics close to the crossing seam, 2008. www.univie.ac.at/newtonx.

[293] H. Langer, N. L. Doltsinis, and D. Marx. Excited-State Dynamics and Coupled Proton-Electron Transfer of Guanine. *Chem. Phys. Chem.*, 6:1734, 2005.

[294] P. R. L. Markwick and N. L. Doltsinis. Ultrafast repair of irradiated DNA: Nonadiabatic ab initio simulations of the guanine-cytosine photocycle. *J. Chem. Phys.*, 126:175102, 2007.

[295] C. Carbogno *et al.* to be published.

[296] H. Schwarz. On the spin-forbiddeness of gas-phase ion–molecule reactions: a fruitful intersection of experimental and computational studies. *Int. J. Mass Spectrom.*, 237:75, 2004.

[297] K. Kato, T. Uda, and K. Terakura. Backbond Oxidation of the Si(001) Surface: Narrow Channel of Barrierless Oxidation. *Phys. Rev. Lett.*, 80:2000, 1998.

[298] W. Pauli. *Z. Phys.*, 31:765, 1925.

[299] R. Lopez-Boada, V. Karasiev, and S. Liu. Padé approximation for the polynomial representation of the correlation energy density functional. *Chem. Phys. Lett.*, 270:443, 1997.

# Acknowledgements

First and foremost, I have to express my deep gratitude to my advisor and mentor Prof. Dr. Axel Groß, who made this work possible: He introduced me to this challenging and fascinating topic and provided for scientific guidance during its elaboration. Whenever I was stuck or doubtful myself, I could count on his wide experience and valuable professional advice. Furthermore, he also permitted me to deepen and broaden my knowledge in surface science by attending conferences and workshops on the topic. Moreover, my special thanks go to Prof. Dr. Karsten Reuter and Dr. Jörg Behler, whose work these studies are based on. Their deep knowledge and expertise in constrained DFT and in Neural Networks enriched my thesis, too. In this context, I also have to thank Prof. Dr. Matthias Scheffler for his interest in the topic and his critical reviews and annotations. Although too many to mention individually, I have to thank all my colleagues at the Institute for Theoretical Chemistry for the fruitful discussions that took place over the years. In particular, my very special thanks go to Christian Mosch, who taught me the basic tricks used in everyday Density Functional Theory. Especially, however, I have to express him my gratitude for the nice time we had while planning, testing and building up the in-house high-performance computing cluster, on which the great majority of the presented calculations have been carried out. The remaining simulations, especially in the last year, were performed on computational resources made available within the D-GRID (bwGRID) project, which provided for additional, highly appreciated, computational time.

This work also profited strongly from the support provided by my family and by my friends: First of all, I have to thank Christina Pöche, whose inner beauty annihilated all my professional sorrows during the last years. In spite of my inclination to spend hours, days and nights in front of the computer, she has always encouraged me to persist. Similarly, also my parents—Annemarie Spöttl and August Carbogno—backed me up in my intentions and offered their support whenever possible. Last but not least, I have to thank all my friends I actually found in Ulm along the way: Without them, my stay would have never been that enjoyable.

Financial grants from the *Deutsche Forschungsgemeinschaft* within the *Schwerpunktprogramm 1093: Dynamik von Elektronentransferprozessen an Grenzflächen* and within the *Ab initio description of non-adiabatic effects in dissociative adsorption at surfaces* project are deeply acknowledged. Furthermore, I want to express my gratitude to the *Wilhelm und Else Heraeus Stiftung*, which partially covered the travel expenses associated with the attendance of the annual DPG spring meetings.

This work is dedicated to my grandfather and grandmother, which regrettably died before it was finished. They certainly would have appreciated the outcome.